Modellering van niet-lineaire nanofotonische componenten
gebaseerd op fotonische kristallen

Modeling of Nonlinear Nanophotonic Components
Based on Photonic Crystals

Björn Maes

Promotor: prof. dr. ir. R. Baets
Proefschrift ingediend tot het behalen van de graad van
Doctor in de Toegepaste Wetenschappen: Natuurkunde

Vakgroep Informatietechnologie
Voorzitter: prof. dr. ir. P. Lagasse
Faculteit Ingenieurswetenschappen
Academiejaar 2004 - 2005

UNIVERSITEIT
GENT

ISBN 90-8578-016-0
NUR 959, 924
Wettelijk depot: D/2005/10.500/16

Promotor:

Prof. dr. ir. R. Baets	Universiteit Gent, INTEC

Examencommissie:

Prof. dr. ir. D. De Zutter, voorzitter	Universiteit Gent, INTEC
Prof. dr. ir. P. Bienstman, secretaris	Universiteit Gent, INTEC
Prof. dr. ir. T. Benson	University of Nottingham
Prof. dr. I. Veretennicoff	Vrije Universiteit Brussel
Prof. dr. ir. P. De Visschere	Universiteit Gent, ELIS
Prof. dr. ir. G. Morthier	Universiteit Gent, INTEC
Dr. ir. W. Bogaerts	Universiteit Gent, INTEC

Universiteit Gent
Faculteit Ingenieurswetenschappen

Vakgroep Informatietechnologie (INTEC)
Sint-Pietersnieuwstraat 41
B-9000 Gent
België

Tel.: +32-9-264.33.16
Fax: +32-9-264.35.93
http://www.intec.ugent.be

Dit werk kwam tot stand in het kader van een mandaat van Aspirant bij het Fonds voor Wetenschappelijk Onderzoek (FWO) - Vlaanderen (België)

This work was carried out in the context of a doctoral fellowship from the Fund for Scientific Research (FWO) - Flanders (Belgium)

Contents

Preface - Voorwoord

De eerste woorden, en tevens de laatste die aan het werk worden toegevoegd. Het was een lange en interessante weg, doorheen verschillende tijdzones en continenten. Moeilijke momenten gingen voorbij, maar die leidden tot nieuwe inzichten.

Naast filosofische mijmeringen is dit de uitgelezen kans om mensen te bedanken die mij hebben bijgestaan op verscheidene manieren. Dank aan Prof. Paul Lagasse die aan het hoofd staat van een dynamische vakgroep met een goede infrastructuur waar men grensverleggend onderzoek kan verrichten. Prof. Roel Baets heeft als promotor het oorspronkelijke idee voor deze thesis aangebracht. Hierdoor werd ik binnengeloodst in een bijzonder intrigerend, uitgebreid en niet-linear vakgebied. Daarnaast kreeg ik voldoende vrijheid om mij te verdiepen naar mijn eigen inzichten en ideeën. Een speciaal dankjewel is zeker aan de orde voor Prof. Peter Bienstman. Zonder zijn CAMFR-werk zou deze thesis er volledig anders uitzien. Niet alleen kon ik verder bouwen op een stevige basis, tevens was Peter altijd beschikbaar om (razendsnel!) allerhande vragen te beantwoorden en belangrijke suggesties te doen.

Verder droegen alle collega's bij (op min of meer wetenschappelijke wijze) tot een zeer aangename sfeer op de werkvloer en tijdens de andere activiteiten. De bende van de 39 zal met blijde herinneringen terugkijken op onze speciale lokatie. We zullen ons historisch bolwerk missen. Dank aan de bureaugenoten Bert, Reinhard, Alberto en Peter om problemen te helpen oplossen, discussies uit te vechten, verzuchtingen te aanhoren, etc. Om de frustraties weg te werken dank ik Kris en Lieven om zich spelletjesgewijs te laten afknallen. Ik dank ook Nina die bereid was om als thesisstudent een tijdje hetzelfde vakdomein te verkennen. Verder had ik regelmatig de onmisbare hulp nodig van Hendrik en Kristien om mijn computerproblemen op te lossen. Daar-

naast dank ik de mensen van het secretariaat, de administratie en de bibliotheek. Zij zijn altijd bereid om hulp te verstrekken.

Via conferenties en projecten ontmoette ik vele mensen die meehielpen of inspiratie leverden voor nieuwe ontwikkelingen. Hierbij moet ik zeker de volgende personen vermelden: Prof. Marc Haelterman, Simon-Pierre Gorza, Prof. Trevor Benson, Prof. Jan Danckaert, Prof. Irina Veretennicoff en Andrea Locatelli. Een speciale vermelding voor Guy Van der Sande die een mooie bijdrage geleverd heeft tot dit werk.

Buiten de werkuren heb ik het voorrecht met een leuke groep vrienden te kunnen optrekken. Ik denk hierbij aan onvergetelijke weekendjes en feestjes, squashwedstrijden en kaartavonden, café-bezoeken en video-opnames, en nog zoveel meer . . .

Daarnaast is mijn familie er steeds om mij aan te moedigen bij alle projecten die ik onderneem. Hopelijk was ik af en toe een beetje duidelijk als ik iets over mijn werk probeerde te vertellen, maar de oprechte interesse is altijd aangenaam. Tevens dank ik mijn grootouders om mij altijd een extra duwtje te geven. Mijn ouders verdienen een (grote!) pluim om een luisterend oor te zijn, en mij met raad en daad vooruit te helpen.

Ik wil nu graag Evelien in de bloemetjes zetten. Zij staat mij al enkele jaren bij, op zoveel verschillende manieren. Als het eens wat minder vlotte, kon ik steeds op haar geduld rekenen. Dank je voor het verleden, en voor onze toekomst.

Björn Maes
Gent, 17 mei 2005

Nederlandstalige Tekst

Nederlandstalige samenvatting - Dutch summary

In dit gedeelte geven we een beknopte inleiding tot en samenvatting van de belangrijkste verwezenlijkingen in dit doctoraatswerk. Voor meer achtergrond en details verwijzen we uiteraard naar de Engelstalige tekst.

1. Inleiding

1.1 Achtergrond

Nadat Maiman in 1960 de eerste laser voorstelde, ontstond een revolutie in de wetenschap en techniek. Doordat de vermogens van deze bron voldoende sterk waren, kon men het domein van de niet-lineaire optica betreden. Het eerste experiment van frequentie-verdubbeling werd reeds in 1961 uitgevoerd. Daarnaast slaagde men erin om zuivere glasvezels te vervaardigen, waardoor het licht met heel kleine verliezen propageert. Door de beschikbare bandbreedte verloopt een groot deel van onze informatietransmissie dan ook onder de vorm van lichtpulsen doorheen deze vezels.

Er is echter nog steeds een vraag naar grotere communicatiesnelheden, zoals voor het internet. Een grote vertraging in de hedendaagse netwerken treedt op wanneer een omzetting gebeurt tussen het optische en het elektronische gebied. De meeste gegevensverwerking in de knooppunten gebeurt immers nog steeds door elektronische circuits, zoals voorgesteld in figuur 1. Het is een uitdaging voor de fotonica om een zo groot mogelijk deel van de verwerkingen zelf uit te voeren.

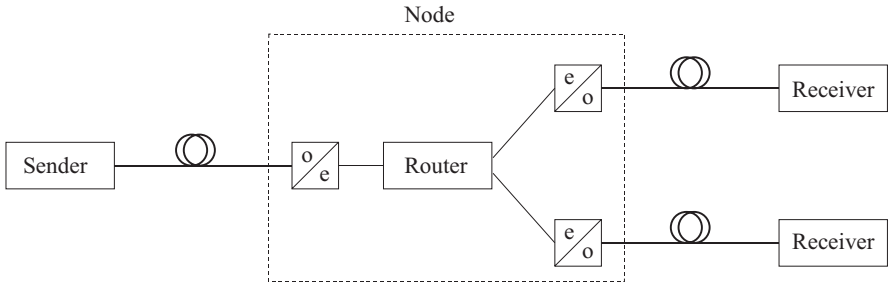

Figuur 1: Schematische voorstelling van een netwerk met elektro-optische omzettingen.

Op die manier creëren we een volledig optisch netwerk, zodat er een rechtstreeks lichtpad stroomt van zender naar ontvanger.

Om deze functies efficiënt en goedkoop uit te voeren, moeten we compacte structuren gebruiken die gefabriceerd zijn met geïntegreerde technologie. We spreken dan over fotonische geïntegreerde circuits (Photonic Integrated Circuits of PIC's). Heden ten dage worden steeds complexere en performantere PIC's gedemonstreerd.

Om optisch te schakelen, en dus licht met licht te doen interageren, moeten we de niet-lineaire effecten van materialen gebruiken. Het voordeel van de PIC's hierbij is dat heel compacte geleiders gedefinieerd worden. De sterke opsluiting van het licht zorgt ervoor dat we de zwakke niet-lineariteiten kunnen uitbuiten.

Daarnaast zorgt de kwaliteit en de golflengte-schaal van de componenten ervoor dat we nieuwe fysische effecten zoals niet-lineair gelokaliseerde modes kunnen bestuderen. Deze concepten komen voor in verscheidene gebieden van de fysica, maar worden nu vaak voor het eerst gedemonstreerd in optische laboratoria. Dergelijke innovatieve verschijnselen kunnen de basis vormen voor toekomstige toepassingen.

Fotonische kristallen (Photonic Crystals of PhC's) vertegenwoordigen een technologie met veel potentieel, zowel voor lineaire als niet-lineaire componenten. Door hun periodieke structuur, voorgesteld in figuur 2, ontstaan frequentie-gebieden waar het licht niet kan propageren. Hierdoor kunnen de kristallen functioneren als een speciaal soort spiegel, waarmee we een sterke opsluiting van de velden bekomen. Door het aanbrengen van defecten kunnen golfgeleiders en resonatoren ontstaan. Een combinatie van een resonator met geleiders aan weers-

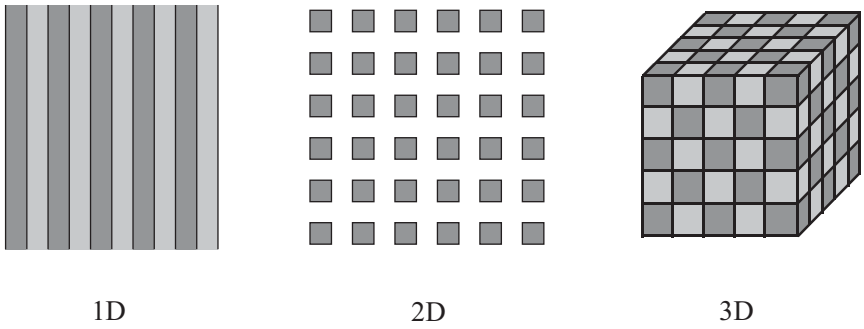

Figuur 2: Voorbeelden van 1D, 2D en 3D fotonische kristallen.

zijden is voorgesteld in figuur 3. Deze structuur kan dienst doen als een niet-lineaire schakelaar: Bij laag vermogen reflecteert het licht, bij hoog vermogen komt het licht in de rechtse golfgeleider terecht. Dergelijke compacte caviteiten zijn uitermate geschikt voor deze vorm van gegevensverwerking.

1.2 Modelleren van optische componenten

Het is duur en tijdrovend om structuren te fabriceren en te meten. Om de componenten te ontwerpen moeten we bijgevolg gebruik maken van computersimulaties. De ontwikkelde algoritmen kan men ruwweg opsplitsen in methodes die de ruimte volledig discretiseren en methodes die een meer analytische aanpak gebruiken.

De eerste categorie definieert een rooster over de structuur, zoals in figuur 4. Met een dergelijke aanpak kunnen we zeer onregelmatige componenten beschrijven. Bovendien zijn de resultaten exact als het rooster zeer fijn wordt. Een nadeel hierbij is dat elk roosterpunt een variabele introduceert, zodat bij grotere structuren de berekeningen zeer veel tijd en geheugen opslorpen.

Daarom is er nood aan technieken die anders te werk gaan. De eigenmode expansie methode bv. deelt de structuur op in stuksgewijze continue secties, zoals in figuur 5. Het veld in zo'n sectie wordt beschreven als een superpositie van de eigenmodes van de desbetreffende laag. Op die manier reduceren we het aantal parameters tot de coëfficiënten van de modes. Omdat de verschillende stukken op een efficiënte manier aaneengehecht kunnen worden, vormt dit een doeltreffende manier om een groot gamma aan lineaire componenten te berekenen.

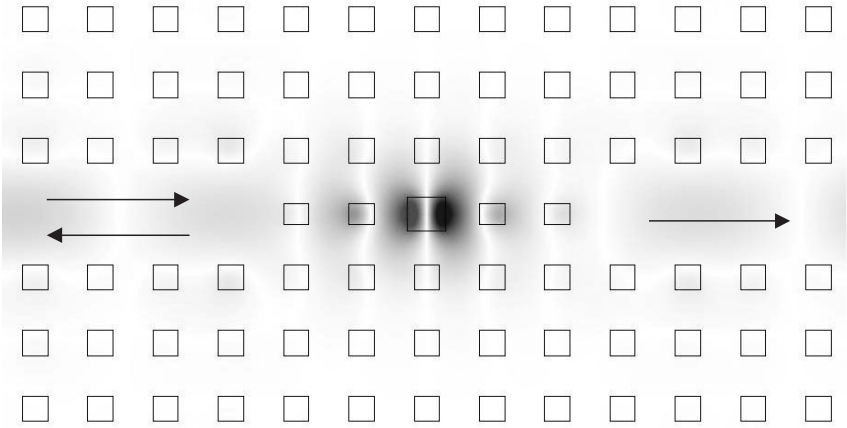

Figuur 3: Een fotonisch kristal met defecten.

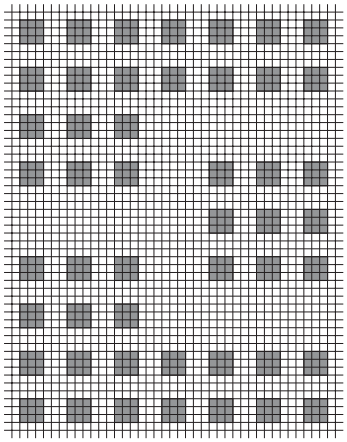

Figuur 4: Voorbeeld van een splitser met een rooster.

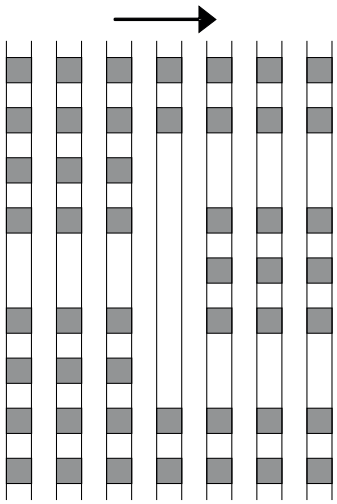

Figuur 5: De splitser met de eigenmode methode: slechts vier verschillende secties.

1.3 Overzicht van het proefschrift

Het aantal methodes om niet-lineaire effecten te berekenen is veel beperkter in vergelijking met de lineaire programma's. Mede door de interesse voor volledig optische gegevensverwerking hadden wij tot doel om efficiënte en accurate tools te ontwikkelen voor niet-lineariteiten. Hiervoor hebben we het mode expansie programma CAMFR uitgebreid voor het Kerr effect en tweede-harmonische generatie. Dit zijn de twee meest gebruikte effecten. Daarnaast hebben we deze algoritmen toegepast op verscheidene fotonische kristal structuren, om innovatieve componenten en nieuwe concepten te bestuderen.

Het proefschrift is als volgt opgebouwd. De achterliggende ideeën en methodes worden besproken in hoofdstuk 2. Onze methode voor het Kerr effect wordt uitvoerig behandeld in hoofdstuk 3. Hierbij berekenen we eindige en periodieke structuren. We vermelden o.a. een component die een Fano respons vertoont en een fotonische kristal golfgeleider die een bistabiele dispersiecurve bezit. In hoofdstuk 4 bestuderen we een eindige serie van resonatoren. Een juiste spatiëring van de caviteiten zorgt voor efficiënte schakelmogelijkheden. Daarna, in hoofdstuk 5, stellen we een nieuw soort solitonen voor in fotonische kristallen zonder defecten. Deze elektromagnetische modes creëren hun eigen golfgeleider omwille van het Kerr effect. Ons algoritme voor

tweede-harmonische generatie wordt uitgelegd in hoofdstuk 6. We berekenen hier een lange periodieke structuur, om de efficiëntie van de techniek aan te tonen. Uiteindelijk volgen de conclusies in hoofdstuk 7.

1.4 Publicaties

Het werk uitgevoerd in het kader van dit proefschrift heeft bijgedragen tot een aantal publicaties in internationale tijdschriften:

- B. Maes, P. Bienstman, R. Baets, 'Modeling of Kerr nonlinear photonic components with mode expansion', Optical and Quantum Electronics 36 (1-3): 15-24 Jan-Feb (2004).
- G. Priem, I. Notebaert, B. Maes, P. Bienstman, G. Morthier, R. Baets, 'Design of all-optical nonlinear functionalities based on resonators', IEEE Journal of Selected Topics in Quantum Electronics 10 (5): 1070-1078 Sept-Oct (2004).
- B. Maes, P. Bienstman, R. Baets, 'Bloch modes and self-localized waveguides in nonlinear photonic crystals', Journal of the Optical Society of America B 22 (3): 613-619 Mar (2005). (Also appeared as invited paper in Virtual Journal of Nanoscale Science & Technology, March 28, 2005.)
- G. Van der Sande, B. Maes, P. Bienstman, J. Danckaert, R. Baets, I. Veretennicoff, 'Nonlinear lattice model for spatially guided solitons in nonlinear photonic crystals', Optics Express 13 (5): 1544-1554 Mar (2005).
- B. Maes, P. Bienstman, R. Baets, 'Switching in coupled nonlinear photonic crystal resonators', accepted in Journal of the Optical Society of America B.
- B. Maes, P. Bienstman, R. Baets, 'Modeling second-harmonic generation with mode expansion', accepted in Journal of the Optical Society of America B.

Onze resultaten zijn gepresenteerd op verscheidene internationale conferenties:

- B. Maes, P. Bienstman, R. Baets, 'Modelling of nonlinear effects in a mode expansion context', Workshop 2D photonic crystals, Switzerland, p.I-05 (2002).

- B. Maes, P. Bienstman, R. Baets, 'Rigorous modelling of nonlinear wave-length-scale structures with mode expansion and spatial index discretisation', OWTNM (Optical Waveguide Theory and Numerical Modelling), Czech Republic, p.98 (2003).
- B. Maes, P. Bienstman, R. Baets, 'Rigorous modelling of non-linear photonic components with mode expansion and spatial index discretisation', IPR (Integrated Photonics Research), United States, p.105-107 (2003).
- B. Maes, P. Bienstman, R. Baets, 'Bloch modes and self-localized waveguides in non-linear photonic crystals', IEEE Leos Benelux Annual Symposium, The Netherlands, p.303-306 (2004).
- B. Maes, P. Bienstman, R. Baets, 'A novel photonic crystal flip-flop device', NLGW (Nonlinear Guided Waves and Their Applications), Canada, TuC45 (2004).
- B. Maes, P. Bienstman, R. Baets, 'Modeling second harmonic generation with mode expansion', OWTNM, Belgium, p.36 (2004).
- G. Van der Sande, B. Maes, P. Bienstman, J. Danckaert, R. Baets, I. Veretennicoff, 'Semi-analytical model for spatial solitons in nonlinear photonic crystals', IEEE Leos Benelux Annual Symposium, Belgium, p.303-306 (2004).
- B. Maes, G. Van der Sande, P. Bienstman, J. Danckaert, R. Baets, I. Veretennicoff, 'Self-localized Waveguides in Nonlinear Photonic Crystals', IPRA (Integrated Photonics Research and Applications), United States, p.ITuB2 (2005).
- G. Van der Sande, B. Maes, P. Bienstman, J. Danckaert, R. Baets, I. Veretennicoff, 'Nonlinear lattice model for self-localized waveguides in nonlinear photonic crystals', accepted for SPIE Optics and Optoelectronics, Poland (2005).
- B. Maes, P. Bienstman, R. Baets, 'Efficient and rigorous modeling of second-harmonic generation including moderate pump-depletion', submitted to NLGW, Germany (2005).
- S.-P. Gorza, C. Cambournac, P. Emplit, M. Haelterman, D. Taillaert, B. Maes, R. Baets, 'Identification of gap soliton through phase measurement', submitted to NLGW, Germany (2005).

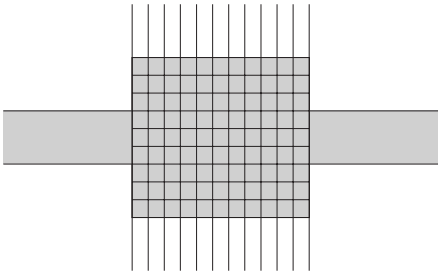

Figuur 6: Een discretisatie voorbeeld, de middelste sectie is niet-lineair.

2. Modelleren van het Kerr effect

2.1 Methode

Het Kerr effect betekent dat de brekingsindex afhankelijk wordt van de lokale veldintensiteit:

$$n(\mathbf{r}) = n_0 + n_2 I(\mathbf{r}), \tag{1}$$

met n_0 de lineaire index, n_2 de Kerr coëfficiënt en I de intensiteit. Om dit te incorporeren in een eigenmode algoritme verdelen we de niet-lineaire gedeeltes in een rooster, zoals voorgesteld in figuur 6. Doordat de interne velden vooraf niet gekend zijn, moeten we een iteratieve werkwijze hanteren: We starten van een bepaalde indexverdeling over het rooster en voeren een *lineaire* eigenmode berekening uit. Deze levert ons de intensiteiten in het centrum van elk roosterverdeling. Met behulp van vergelijking 1 kunnen we nieuwe brekingsindices bepalen. Als de nieuwe en de oude indices nagenoeg gelijk zijn, hebben we een volledig niet-lineaire oplossing. Indien dat niet zo is, moeten we een nieuwe iteratie starten. Deze werkwijze is voorgesteld in figuur 7.

Met behulp van deze methode kunnen we zowel eindige als oneindig periodieke structuren berekenen. In beide gevallen moet een bepaalde grootheid constant gehouden worden om consistente iteraties te bekomen.

Voor eindige structuren houden we eenvoudigweg de vector met extern inkomende amplitudes constant. We volgen zo de evolutie van de verstrooiingsmatrix van de component.

Bij periodieke structuren moeten we de flux of de energie constant houden. We moeten dan bij elke stap de Bloch modes van de verstrooiingsmatrix berekenen. Indien de grootte van de structuren beperkt is,

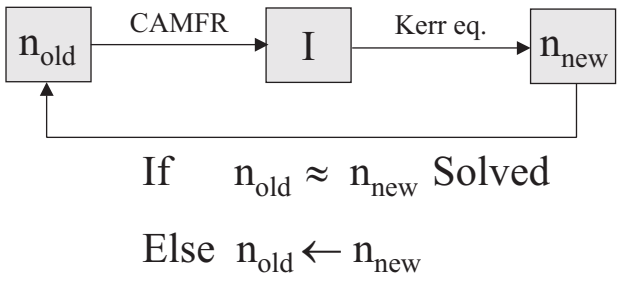

Figuur 7: Schema van het Kerr algoritme.

kan dit zeer vlot verlopen. Bovendien zijn we vaak enkel geïnteresseerd in de laagste orde mode. Op deze manier kunnen we de verschuiving van de bandenstructuur bij toenemend vermogen volgen.

We hebben met deze methode een kwantitatieve overeenkomst met de literatuur bereikt. Verder hebben we gemerkt dat we voor sommige berekeningen de indices voorzichtiger moeten aanpassen. De nieuwe indices worden dan bepaald met:

$$n'_{new} = \left(n_{new} + \alpha n_{old}\right) / \left(1 + \alpha\right), \qquad \alpha \geq 0, \tag{2}$$

waarbij n_{new} bekomen wordt uit vergelijking 1. Indien $\alpha > 0$ zijn de iteraties minder abrupt. Dit is soms nodig om convergentie te bereiken.

We merken dat we bij dit algoritme een rooster moeten introduceren, hetgeen we bij eigenmode expansie het liefst vermijden. Indien we grote niet-lineaire zones modelleren komen we dus in dezelfde problemen als andere roostermethodes. Bij fotonische kristallen is het echter vaak zo dat we enkele kleine staafjes niet-lineair moeten veronderstellen. Dit is zeker het geval bij structuren met caviteiten. Bovendien hoeven we lineaire gedeelten slechts één keer te berekenen, daar hun matrix immers vermogenonafhankelijk is. Voor periodieke structuren moet tevens slechts één periode beschouwd worden. Daar meestal enkele tientallen modes voldoende zijn en convergentie relatief vlot verloopt, spreken we over rekentijden van seconden of minuten voor de voorbeelden in dit proefschrift.

We merken tenslotte op dat de methode bidirectioneel is, wat betekent dat er modes propageren in beide richtingen. Dit stelt ons in staat om verschijnselen zoals bistabiliteit te berekenen, hetgeen in het voorbeeld in de volgende sectie opduikt.

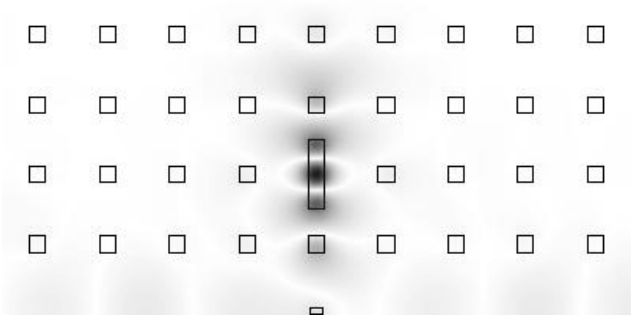

Figuur 8: Geometrie van de structuur met Fano respons. Omwille van symmetrie is slechts de bovenste helft getoond.

2.2 Fano resonantie

Zoals reeds vermeld is de simulatiemethode uitermate geschikt voor structuren met resonatoren in fotonische kristallen. We demonstreren dit aan de hand van een component die een specifiek transmissiespectrum bezit. Een dergelijk spectrum noemt men een Fano resonantie.

De geometrie is voorgesteld in figuur 8. We bemerken een resonator naast de golfgeleider, en een klein staafje in de golfgeleider zelf dat het licht gedeeltelijk reflecteert. Door interferentie tussen het directe kanaal, de golfgeleider, en de resonantie in de caviteit bekomen we een asymmetrische transmissiecurve, die we voorstellen in figuur 9. Deze respons kan tevens beschreven worden met gekoppelde mode theorie (Coupled Mode Theory of CMT), zoals getoond met de volle lijn.

In de PhC literatuur zijn Fano resonanties opgedoken in de transmissie doorheen een vrijstaande laag. De structuur die we hier voorstellen is een geïntegreerde versie met een kleine oppervlakte.

Als we de caviteit niet-lineair veronderstellen, geeft dit aanleiding tot eigenaardige transmissiecurves. Nemen we een negatieve Kerr niet-lineariteit, en kiezen we de frequentie een weinig groter dan de resonantiefrequentie $\omega_r = 0.44381(2\pi c/a)$, dan bekomen we de respons van figuur 10. Bemerk de goede overeenkomst tussen de rigoureuze simulatiemethode en de niet-lineaire CMT.

Vooreerst zien we een gebied van bistabiliteit, waar eenzelfde ingangsvermogen overeenkomt met twee mogelijke transmissies. Daarnaast is er een punt waar de curves snijden zodat beide oplossingen als het ware tezamen vallen. Deze punten zijn ontaard met betrekking

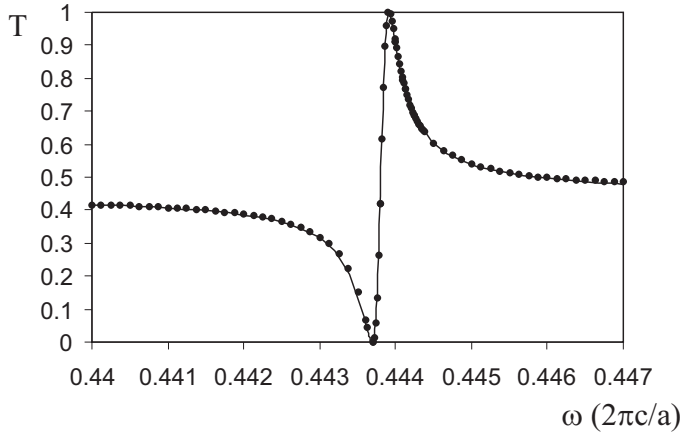

Figuur 9: Lineair transmissiespectrum met de asymmetrische Fano resonantie. Punten tonen simulatieresultaten, de lijn is bekomen door CMT.

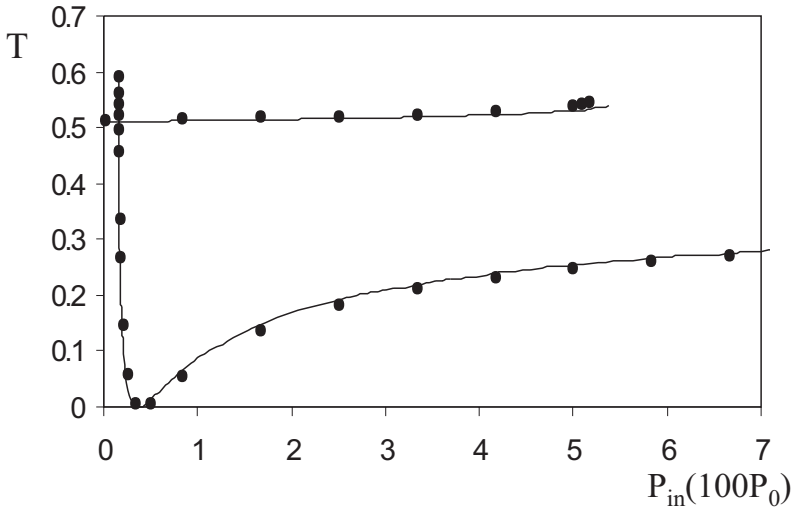

Figuur 10: Transmissie versus ingangsvermogen met $\omega = 0.4455(2\pi c/a)$ en negatieve Kerr coëfficiënt.

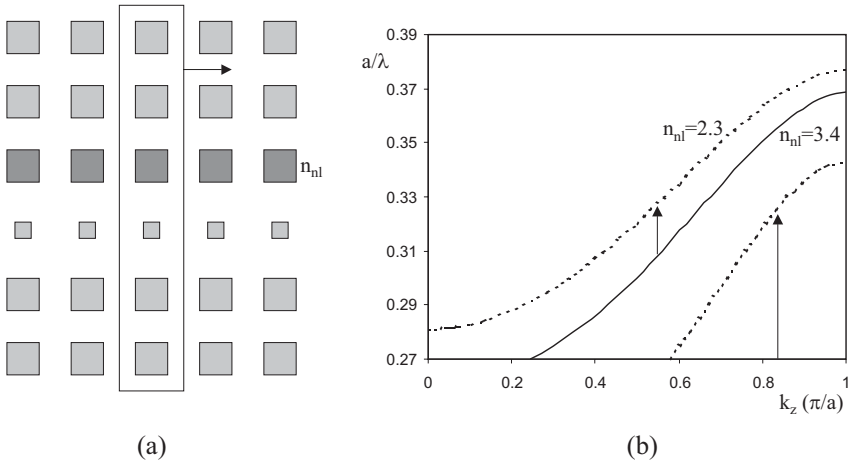

Figuur 11: (a) Geometrie van de PhC golfgeleider. De donkere staafjes zijn niet-lineair. Alleen het rechthoekje moet gebruikt worden voor niet-lineaire berekeningen. (b) Band structuur. De volle en gestreepte lijnen komen overeen met indices 3.4 en 2.3, respectievelijk, voor het niet-lineair staafje. De pijlen tonen de bewegingsrichting van de banden bij een dalende index.

tot de amplitude, maar zijn toch verschillend omdat ze een andere fase bezitten.

2.3 PhC golfgeleider

De vorige structuur was een eindige component. In deze sectie geven we bijgevolg een periodiek voorbeeld. We behandelen een verschijnsel dat reeds gekend is bij conventionele golfgeleiders. Indien de mantel niet-lineair verondersteld wordt, kan de dispersiecurve (vermogen versus effectieve index) vervormen en zelfs bistabiel worden. Er verschijnen dan twee curves: Een tak met ‘lineaire’ oplossingen waar de mode zich grotendeels in de kern bevindt. En een ‘niet-lineaire’ tak, met de mode voornamelijk gelokaliseerd in de mantel.

We onderzoeken in dit gedeelte hetzelfde fenomeen bij PhC golfgeleiders. Daar het opsluitingsmechanisme verschillend is (totale interne reflectie versus bandgap effecten) zullen specifieke eigenschappen optreden.

De geometrie is voorgesteld in figuur 11(a). De golfgeleider ontstaat door een rij staafjes met een kleinere straal. De staafjes aan één kant van deze kern worden niet-lineair verondersteld, met negatieve Kerr-

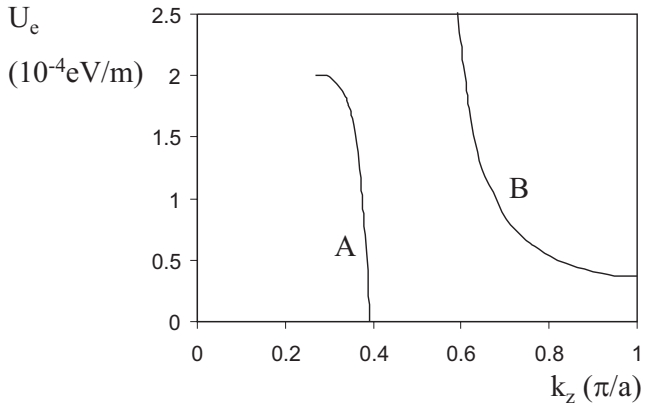

Figuur 12: Energie versus Bloch golfvector. De 'lineaire' ('niet-lineaire') tak is aangeduid met A (B).

coëfficiënt. Indien we het vermogen opdrijven, zal de index van deze niet-lineaire staafjes dalen. Bijgevolg creëren ze een nieuwe rij defecten, en uiteindelijk zelfs een nieuwe geleidende mode.

Deze redenering is in overeenstemming met de bandstructuren in figuur 11(b). In deze figuur worden de golfgeleidermodes getoond in de bandgap, voor twee verschillende indices van het niet-lineaire staafje. Bemerk dat we voor de Bloch berekeningen slechts één periode moeten beschouwen. Wanneer $n = 3.4$ hebben we de lineaire situatie: Er is één mode aanwezig. Bij $n = 2.3$ is deze mode verschoven en duikt er een tweede mode op. Deze laatste ontstaat door het extra kanaal naast de oorspronkelijke geleider. Het is zelfs zo dat de oorspronkelijke mode zich loskoppelt van de bandgap-grens. Indien we dus een frequentie kiezen aan de onderkant van de bandgap, verwachten we dat de lineaire mode bij een bepaald vermogen niet meer zal optreden.

Het voorgaande wordt gestaafd aan de hand van niet-lineaire berekeningen. De resultaten zijn voorgesteld in figuur 12. We bemerken inderdaad twee oplossingstakken. Bij lage energie is er slechts één mode beschikbaar. Deze is boven een bepaalde energiedrempel niet meer bereikbaar, waarna het systeem overschakelt op de niet-lineaire oplossing. Deze resultaten komen overeen met de bandstructuur-analyse.

Het verschillend karakter van de twee curves is geïllustreerd aan de hand van veldprofielen in figuur 13. We merken inderdaad dat de lokalisatie verschuift van het centrum naar de mantelstaafjes. Bemerk dat

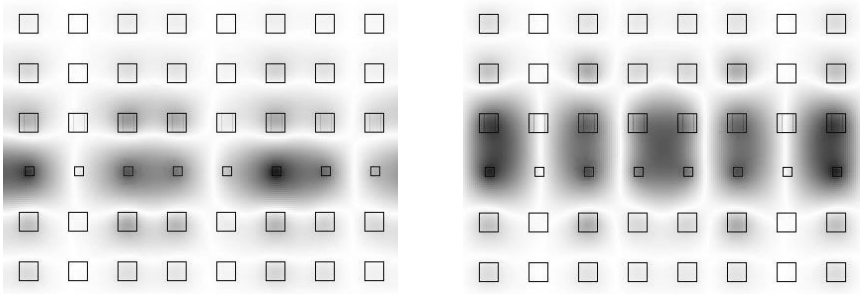

Figuur 13: Voorstelling van de velden voor de takken A en B, respectievelijk (zie figuur 12). Berekend door de Bloch mode lineair te propageren, met het indexprofiel bekomen van de niet-lineaire berekening.

deze negatieve indexverandering geen dergelijk verschijnsel oplevert voor een conventionele golfgeleider. Een verlaging van de mantelindex zorgt daar immers voor een sterkere opsluiting in de kern.

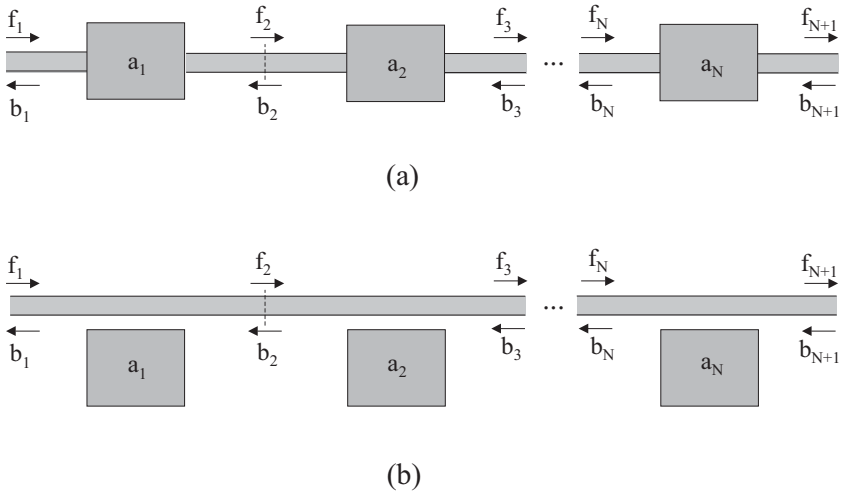

Figuur 14: Twee types van series: (a) Resonant gekoppelde structuur. (b) Zijwaarts gekoppelde structuur.

3. Gekoppelde PhC resonatoren

We hebben reeds gemerkt dat systemen met golfgeleiders en resonatoren een grote waaier aan mogelijkheden bezitten. Hun eigenschappen kunnen we aanpassen om selectieve functies te verrichten. Door de sterke opsluiting van de velden is het bovendien haalbaar om niet-lineaire effecten waar te nemen. Verschillende technologieën staan ter beschikking, zoals gedistribueerde reflectoren, ringresonatoren en fotonische kristallen. Wij zijn vooral geïnteresseerd in deze laatste daar ze het potentieel bezitten om erg compacte structuren te verwezenlijken.

Wanneer nu meerdere resonatoren worden gekoppeld, ontstaan er nieuwe mogelijkheden. Zo is men in staat om complexere en selectievere filterfuncties te bekomen. In het niet-lineaire geval ontstaan dan weer nieuwe toestanden, die vaak een vervorming inhouden van lineaire modes.

3.1 Structuur en berekeningsmethode

In dit gedeelte bestuderen we series van resonatoren. Ofwel bevinden deze zich in de golfgeleider, zoals in figuur 14(a), ofwel zijn ze geplaatst net naast de golfgeleider, voorgesteld in figuur 14(b). In het eerste geval

spreken we van een resonant gekoppelde structuur. Ver van resonantie wordt het licht gereflecteerd, op resonantie zal het licht via de caviteit in de andere golfgeleider komen. De andere geometrie noemen we de zijwaarts gekoppelde structuur. Deze vertoont een duaal gedrag: Ver van resonantie gaat het licht gewoon door de golfgeleider. Op resonantie wordt alles gereflecteerd.

Om deze series te berekenen gebruiken we CMT. Dit is een handig en accuraat schema met eenvoudige vergelijkingen, zelfs voor het niet-lineaire geval. Voor een resonant gekoppelde caviteit zien ze er, ter illustratie, als volgt uit:

$$j\omega a_1 = \left[j\left(\omega_r + \delta\omega\right) - \frac{1}{\tau}\right] a_1 + df_1 + db_2, \quad (3)$$

$$b_1 = \exp(j\phi) f_1 + da_1, \quad (4)$$

$$f_2 = \exp(j\phi) b_2 + da_1. \quad (5)$$

Bij een resonant gekoppelde serie kunnen we de toestanden berekenen door van de uitgang naar de ingang te werken. We kiezen dus een uitgangsvermogen en lopen met een transfermechanisme terug naar het ingangsvermogen.

Voor de zijwaartse serie kunnen we dit eveneens bij de lineaire toestanden. In het niet-lineaire geval hebben we een aanpassing nodig. Bij elke resonator moet een complexe derde orde polynoom opgelost worden. Dit kunnen we doen met behulp van het Newton-Raphson algoritme. Daar deze iteratieve techniek een beginschatting van de oplossing gebruikt, bemoeilijkt dit de berekeningen enigszins. Daar het echter over eenvoudige algebraïsche bewerkingen gaat, worden de oplossingen toch snel gevonden.

3.2 Niet-lineaire resonanties

We hebben ons toegespitst op het frequentie-domein en we onderzochten de types niet-lineaire modes die voorkomen in dergelijke series.

Een eerste type vormen de gapsolitonen. Deze modes corresponderen met een lineaire transmissiepiek die een intensiteitsmaximum in het centrum van de structuur bezit. Als we een frequentie kiezen die een beetje van dat maximum afwijkt, en het vermogen opdrijven (met het juiste teken van niet-lineariteit) dan kan er opnieuw een transmissiemaximum optreden. Deze niet-lineair vervormde modes zijn de solitonen. Het veld creëert dan een val voor de elektromagnetische energie, zodat het profiel meer en meer een sech-curve voorstelt. Deze so-

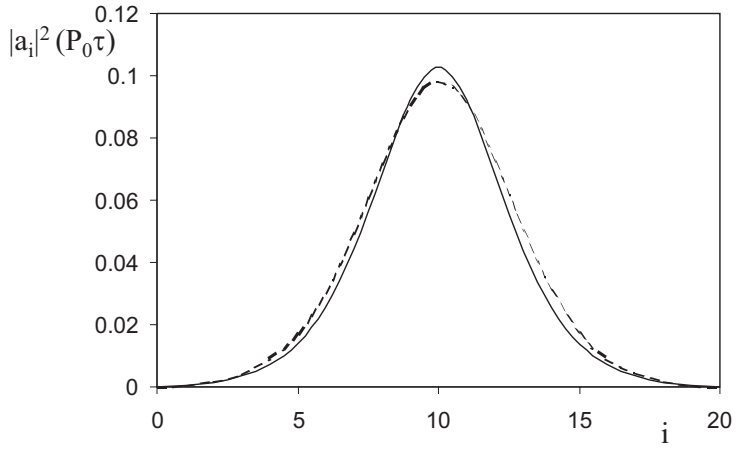

Figuur 15: Fundamenteel gapsoliton voor resonante (volle lijn) en zijwaartse (gestreepte lijn) koppeling. a_i is de amplitude van resonator nummer i. De energieprofielen volgen een sech^2-curve.

litonen komen zowel voor in resonant als zijwaarts gekoppelde series. Een voorbeeld met een rij van 21 caviteiten is getoond in figuur 15. Dergelijke solitonen zijn algemeen en komen in verscheidene situaties voor.

Een tweede, minder gekend type zijn de niet-lineaire transmissie-anomalieën. Deze variëteit is reeds vermeld in resonant gekoppelde structuren, maar nog niet in zijwaartse rijen. Hun verschijning in de transmissiecurve wordt weergegeven in figuur 16. Dit spectrum wordt getoond in functie van de dimensieloze afwijking van de resonantiefrequentie $\delta = \tau(\omega - \omega_r)$, met $1/\tau$ de frequentie-breedte van een caviteit.

We merken dat de lineaire transmissie een kloof bezit tussen $\delta = -1$ en $\delta = 1$. In het niet-lineaire geval ontstaat er echter een extra transmissiepiek, die geen lineaire tegenhanger heeft. Deze modes hebben een gelijkaardig profiel als de hiervoor besproken gapsolitonen. Wanneer het vermogen verder opgedreven wordt zien we dat de anomalie-piek en de normale gapsoliton-piek naar elkaar toe neigen en elkaar uiteindelijk raken. Op een gegeven moment dalen de maximale transmissies zelfs onder één, zodat geen solitonen meer voorkomen.

Een derde en laatste type behelst modes die afkomstig zijn uit een lineaire piek, net zoals de normale gapsolitonen. Het verschil is echter dat het intensiteitsprofiel een *minimum* bezit in het centrum. In het niet-

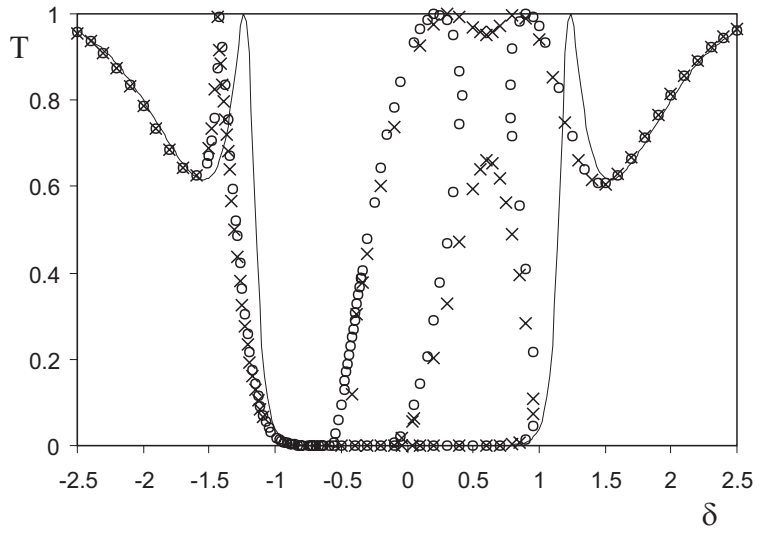

Figuur 16: Transmissie versus δ voor een zijwaartse rij met 5 resonatoren. In het lineaire geval (volle lijn) en bij twee vaste ingangsvermogens P_1 (bollen) en P_2 (kruisen) met $P_2 > P_1$.

lineaire geval zal er dus een energie-ophoping aan de randen van de structuur gebeuren. Dergelijke modes komen bij beide types van rijen voor, maar de uiteindelijke vorm van het profiel verschilt sterk.

Voor zijwaarts gekoppelde rijen bekomen we een vorm zoals weergegeven in figuur 17. Het (genormaliseerde) lineaire profiel wordt eveneens getoond. We merken dat het veld zich ophoopt aan de randen, zodat het minimum in het midden zich uitdiept.

Bij de resonante caviteiten is de vervorming aangetoond in figuur 18. We bekomen een donker soliton, waarbij de constante achtergrond groter wordt naarmate we verder afwijken van de frequentie van de lineaire piek.

We merken op dat dergelijke modes toepassingen hebben voor energielokalisatie aan de randen of in het midden van de structuur. Voorts vermelden we dat dergelijke rijen resonatoren reeds gefabriceerd werden voor filter-doeleinden. Niet-lineaire resultaten zijn echter nog niet vertoond. Indien een weinig van het licht in de caviteiten naar buiten koppelt, zouden we een interessante manier hebben om niet-lineaire lokalisatie direct waar te nemen.

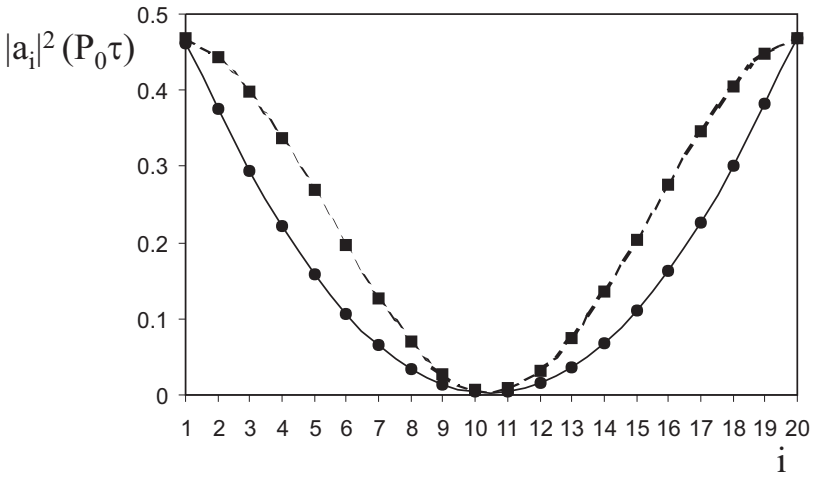

Figuur 17: Energieprofiel voor 20 zijwaartse caviteiten. Het (genormaliseerde) lineaire profiel is gestreept, de niet-lineaire mode wordt getoond met de volle lijn.

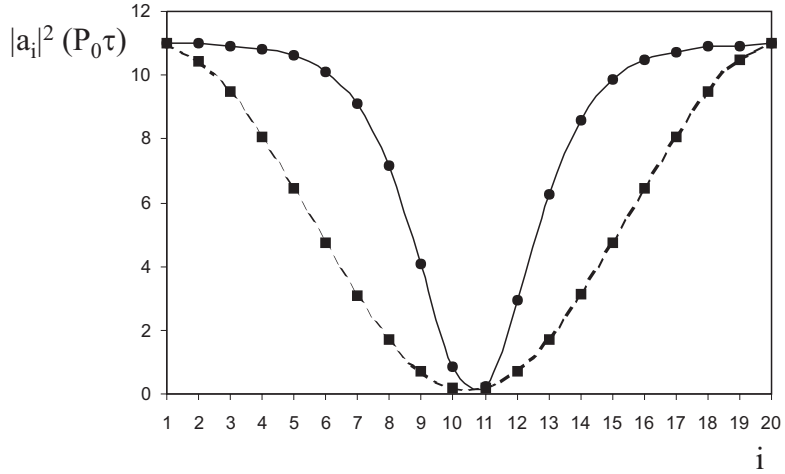

Figuur 18: Energieprofiel voor 20 resonant gekoppelde caviteiten. Niet-lineair profiel in volle lijn, genormaliseerde lineaire mode met gestreepte lijn.

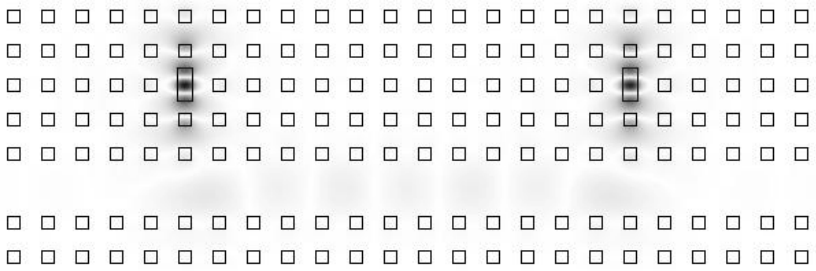

Figuur 19: Structuur van de schakelaar. Het veld op het transmissiemaximum wordt getoond. Door de hoge kwaliteit van de caviteiten is er slechts weinig veld zichtbaar in de golfgeleider.

3.3 Schakelen

De afstand tussen de resonatoren heeft een grote invloed op de spectra. We merkten op dat een rij van twee zijwaarts geplaatste caviteiten een heel smalle transmissiepiek kan vertonen, indien deze afstand juist wordt gekozen. In deze sectie stellen we een ontwerp voor dat gebruik maakt van deze piek om efficiënt te schakelen. We hanteren hiervoor zowel CMT als rigoureuze simulaties.

De structuur is voorgesteld in figuur 19. De twee caviteiten worden gevormd door twee grotere rechthoekige staafjes. Het transmissiespectrum voor één en twee resonatoren is getoond in figuur 20. Er is een goede overeenkomst tussen CMT en de simulaties.

Indien we de frequentie net links van de smalle piek kiezen, dan verwachten we een schakelfunctie als we een positieve niet-lineariteit veronderstellen. Het voorgaande wordt inderdaad bevestigd door de berekeningen, gepresenteerd in figuur 21. Door de smalheid van de piek kan er zeer efficiënt geschakeld worden. Het vermogen kan een factor 10^3 kleiner zijn dan bij één resonator.

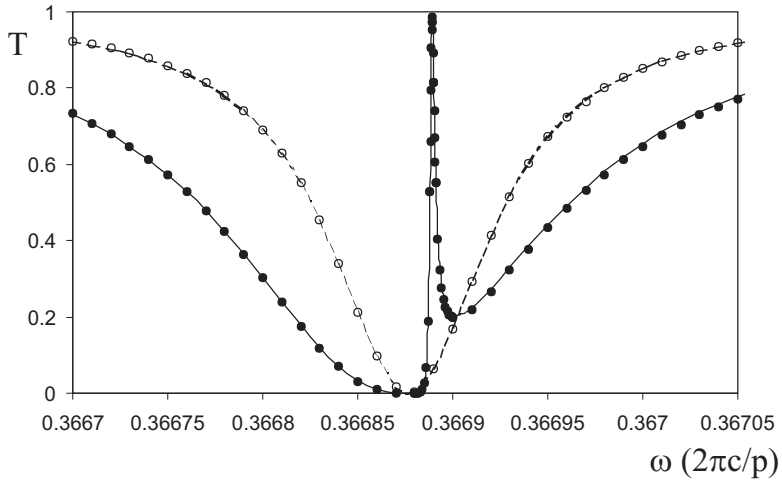

Figuur 20: Lineaire transmissie voor één en twee resonatoren. De gestreepte (volle) lijn stelt CMT voor, terwijl de bollen (stippen) de rigoureuze resultaten tonen voor één (twee) caviteit(en).

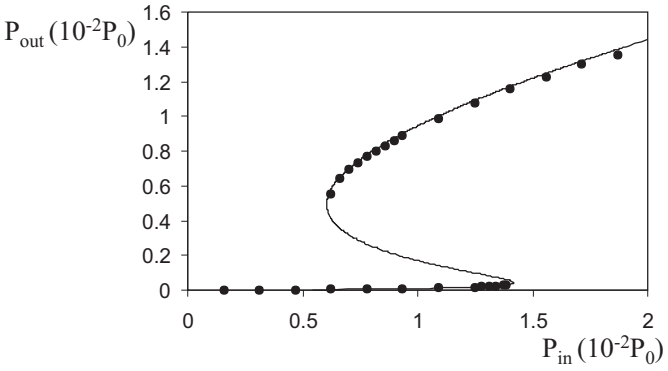

Figuur 21: Uitgangsvermogen versus ingangsvermogen voor de schakelaar. De volle lijn toont CMT resultaten, de simulaties worden met punten voorgesteld.

4. Zelf-gelokaliseerde golfgeleiders

Er bestaat een grote variëteit aan niet-lineair gelokaliseerde modes. Als we niet alleen homogene materialen beschouwen, maar ook periodische structuren dan breidt de familie sterk uit. We vermelden bv. het optreden van discrete en Bragg solitonen in structuren met parallelle golfgeleiders. Bij laag vermogen waaiert het licht uit, terwijl bij hoog vermogen een sterk gelokaliseerde entiteit tevoorschijn komt. Deze pakketten zijn natuurlijke kandidaten om aan gegevensverwerking te doen.

In deze sectie introduceren we een nieuw soort gap-solitonen in hoog-contrast fotonische kristallen. Het is bekend dat solitonen beschreven worden als de grondmode van hun zelf-geïnduceerde golfgeleider. We breiden dit idee uit naar Bloch modes. De gevonden solitonen komen in verschillende geometrieën voor en we hebben een semi-analytische theorie opgesteld om deze objecten te beschrijven.

4.1 Niet-lineair fotonische kristal

In fotonische kristallen weten we dat een verlaging van de index van een rij staafjes aanleiding kan geven tot een geleide Bloch mode. Wanneer we nu een fotonisch kristal zonder defecten maar met negatieve Kerr niet-lineariteit veronderstellen, dan moet het mogelijk zijn dat het veld voor zichzelf een geleider creëert. Lineair gezien bevinden we ons echter in een bandgap, zodat bij laag vermogen geen propagatie mogelijk is.

Met behulp van onze Kerr methode voor periodieke structuren vinden we inderdaad dergelijke zelf-gelokaliseerde golfgeleiders. Hiervoor moeten we de iteratie starten vanuit een berekening met een lagere index voor het centrale staafje. Met die resultaten bekomen we een schatting voor het benodigde vermogen en het veldprofiel. We vinden op deze manier twee types van modes, die we weergeven in figuren 22 en 23. De eerste soort heeft één centraal maximum, terwijl de andere twee gelijke maxima bezit net naast elkaar.

We bestudeerden de stabiliteit ten opzichte van kleine storingen. Hierbij moeten we een onderscheid maken tussen storingen die dezelfde symmetrie hebben als de mode en storingen die deze symmetrie niet bezitten. Voor de eerste soort perturbaties gebruiken we de halve rechthoek, zoals bv. in figuur 22. Voor de andere gebruiken we de volledige rechthoek.

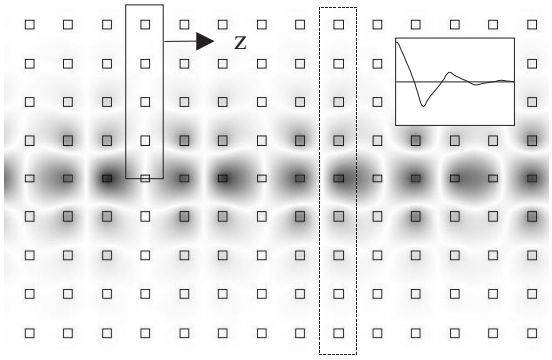

Figuur 22: Voorbeeld van een mode met één maximum. Het kader in volle lijn toont de simulatie-ruimte om de mode te vinden. Het gestreepte kader wordt gebruikt voor stabiliteitsberekeningen ten opzichte van asymmetrische perturbaties. De inzet toont het veldprofiel in een transversale doorsnede.

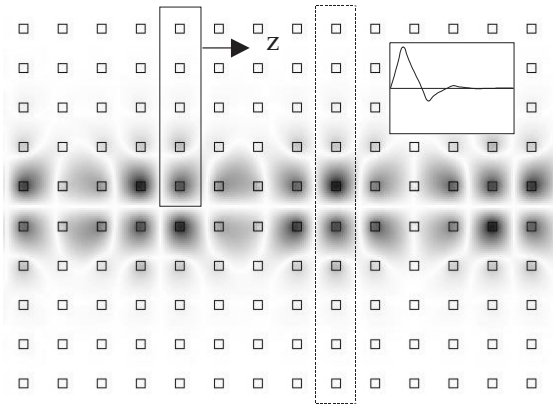

Figuur 23: Hetzelfde als in figuur 22 voor een mode met twee maxima.

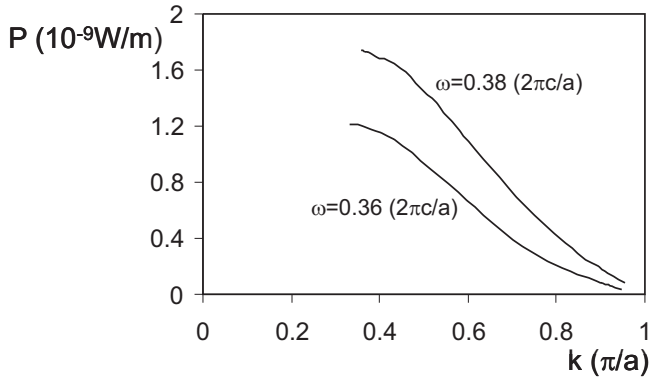

Figuur 24: Vermogen P versus Bloch propagatieconstante k voor dubbele maxima modes met frequenties $\omega = 0.36(2\pi c/a)$ en $\omega = 0.38(2\pi c/a)$.

Voor symmetrische storingen blijkt dat de modes stabiel zijn wanneer hun propagatieconstante groter is dan een bepaalde kritische k_{cr}. We vinden inderdaad met de rigoureuze methode (over de halve rechthoek) enkel modes in dit interval, zie figuur 24. We merken bovendien dat de stabiliteit verandert indien deze curves door een extremum passeren. Dit is analoog aan het Vakhitov-Kolokolov theorema uit de soliton theorie. We hebben hier dus numeriek bewijs dat dit criterium eveneens geldt in onze alternatieve situatie met 2D Bloch modes.

Wat betreft storingen die de symmetrie van de mode niet bezitten merken we op dat de enkele en dubbele maxima types een invloed hebben op elkaars stabiliteit. Hiervoor maken we gebruik van zogenaamde Peierls-Nabarro ideeën. In deze theorie worden de soorten gezien als twee voorstellingen van dezelfde entiteit. Het type met de laagste energie zal stabiel zijn. Dit betekent dat het type met de hoogste energie zich na verstoring spontaan zal omvormen tot de andere soort. Het verschil in energie definieert een potentiaal, de Peierls-Nabarro potentiaal, die de drempel voorstelt die moet overwonnen worden om van de ene site naar de andere te verplaatsen. Wanneer deze drempel klein wordt, dus als beide types dezelfde energie bezitten, dan verwacht men dat de mode gemakkelijk in de transversale richting beweegt. Deze stabiliteitsoverwegingen zijn dus belangrijk om eventuele schakeltoepassingen te bekomen.

De types met één maximum en twee maxima voldoen aan de basisvereiste van de theorie, ze hebben namelijk dezelfde topologie (het-

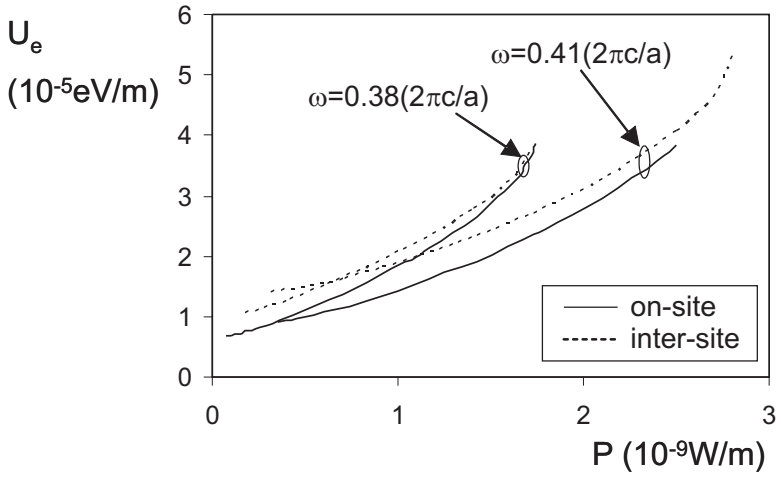

Figuur 25: Energie U_e versus vermogen P voor zelf-gelokaliseerde golfgeleiders bij verschillende frequenties.

zelfde afwisselende tekenpatroon). We hebben hun energie berekend in de bandgap en we presenteren de resultaten in figuur 25.

We merken dat de energie van het type met twee maxima groter is dan de energie van het andere type. Dit suggereert dat het dubbele maxima type onstabiel is en zich zal veranderen tot een mode met één piek.

Het vorige hebben we aangetoond door middel van numerieke experimenten. Hiervoor gebruikten we de grotere rechthoeken getoond in figuren 22 en 23. We starten van een bepaald type en injecteren een verstoring met modes van de andere symmetrie. Hierbij blijkt inderdaad dat in de bandgap het twee-maxima type zich vervormt tot het andere. Terwijl het enkele-maximum type heel robuust is tegen verstoringen.

4.2 Strip Green theorie

Om een meer theoretisch inzicht in de gelokaliseerde modes te bekomen hebben we een semi-analytische methode uitgewerkt. De filosofie is dat een formulering met Greense functies aangepast wordt voor de beschrijving van een Bloch mode. Hiervoor moet de Greense functie gecondenseerd worden tot één enkele periode in de longitudinale richting. Deze gecondenseerde vorm noemen we de strip Greense functie.

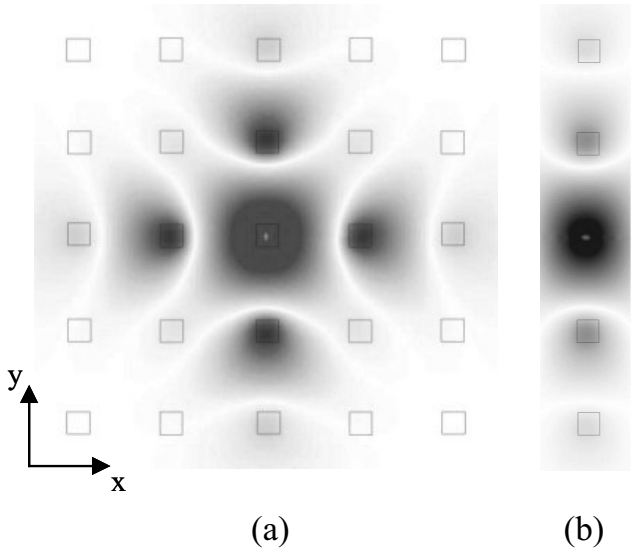

Figuur 26: Voorbeeld van een Greense en een strip Greense functie. (a) Greense functie met $\omega = 0.38(2\pi c/a)$ en bron in het centrum van een staafje, (b) corresponderende strip Green met $k_x = 0.7\pi/a$.

Een voorbeeld van de Greense en de strip Greense functie in een fotonisch kristal wordt getoond in figuur 26. De gewone Greense functie kan met behulp van een lineaire modelleringstool zoals CAMFR berekend worden. Bemerk dat de functie snel afzwakt naarmate de afstand tot het centrum toeneemt. Dit is een gevolg van de bandgap en zorgt er uiteindelijk voor dat de theorie leidt tot een beperkt aantal vergelijkingen.

Het verband tussen de strip Green g en de Green G wordt gegeven door de volgende vergelijking:

$$g(\mathbf{r}, \mathbf{u}|\omega, k_x) = \sum_{j \in \mathbb{Z}} G(\mathbf{r} + j\mathbf{a_x}, \mathbf{u}|\omega, k_x) e^{ijk_x a}. \tag{6}$$

We merken de fase-termen met k_x op, dit is de Bloch golfvector die we moeten vastleggen vooraleer we de strip Green berekenen.

Door middel van het Greense formalisme bekomen we een integraalvergelijking met de onbekende velden in het integrandum. Om deze moeilijkheid op te lossen voeren we de benadering in dat de velden constant zijn over de staafjes. Bij niet al te grote staafjes is dit een aanvaardbare benadering, zoals we zien in figuur 26. Op die manier

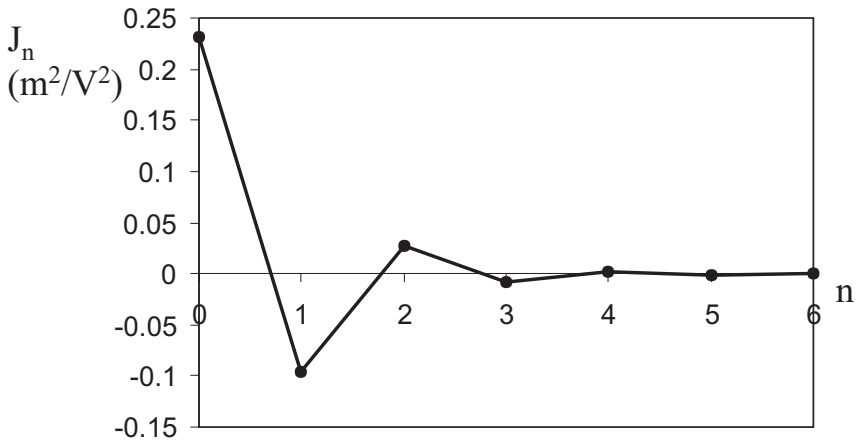

Figuur 27: De koppelcoëfficiënten J_n bij $\omega = 0.38(2\pi c/a)$ en $k_x = 0.7\pi/a$.

halen we de onbekende velden uit het integrandum en blijven er integralen over met het karakter van de niet-lineariteit en de strip Greense functie. Deze integralen leveren zogenaamde koppelcoëfficiënten J_n. Die constanten stellen de sterkte voor van de interactie tussen de staafjes, afhankelijk van hun onderlinge afstand na, met n een natuurlijk getal en a de periode. De exacte uitdrukking is:

$$J_n(\omega, k_x) = n_2 \left(\frac{\omega}{c}\right)^2 \int_{rod} \mathrm{d}^2\mathbf{u}\; g(\mathbf{r_0}, \mathbf{r_n} + \mathbf{u}|\omega, k_x). \tag{7}$$

Deze koppelconstanten nemen sterk af bij toenemende n, door het snelle verval van de Greense functie, zoals te zien in het voorbeeld in figuur 27.

Indien we het veld op staafje n voorstellen als E_n, dan bekomen we voor een mode met één maximum het volgende stelsel:

$$\begin{bmatrix} E_0 \\ E_1 \\ E_2 \\ E_3 \end{bmatrix} = \begin{bmatrix} J_0 & 2J_1 & 2J_2 & 2J_3 \\ J_1 & J_0 + J_2 & J_1 + J_3 & J_2 + J_4 \\ J_2 & J_1 + J_3 & J_0 + J_4 & J_1 + J_5 \\ J_3 & J_2 + J_4 & J_1 + J_5 & J_0 + J_6 \end{bmatrix} \cdot \begin{bmatrix} |E_0|^2 E_0 \\ |E_1|^2 E_1 \\ |E_2|^2 E_2 \\ |E_3|^2 E_3 \end{bmatrix}. \tag{8}$$

Een dergelijk niet-lineair algebraïsch stelsel met een beperkt aantal vergelijkingen is eenvoudig op te lossen met Newton-Raphson.

We vinden beide types modes terug. Een vergelijking tussen de rigoureuze berekeningen en de strip Greense theorie is getoond in figuur 28. We bemerken een kwalitatieve overeenkomst, daar de staafjes

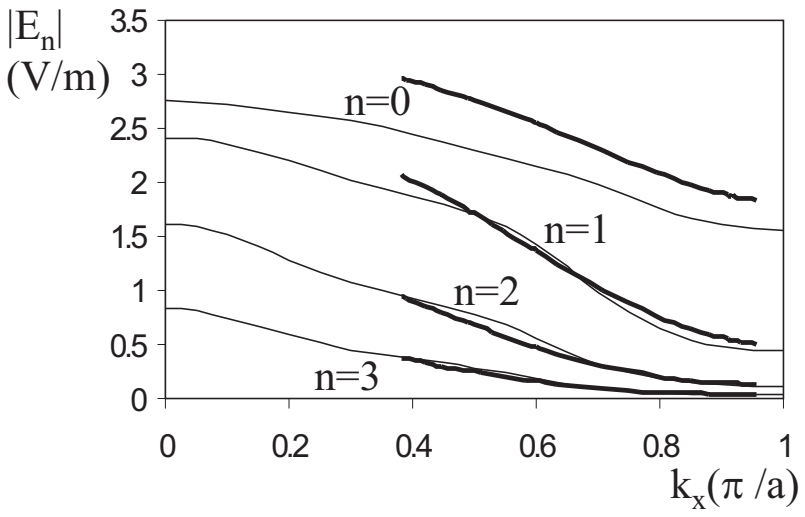

Figuur 28: Vergelijking van de veldwaarden in de individuele staafjes bekomen door strip Greense theorie (dunne lijn) en rigoureuze simulaties (dikke lijn).

in dit voorbeeld tamelijk groot zijn. Daarom behandelen we een alternatieve structuur in de volgende sectie.

4.3 Diatomisch fotonisch kristal

Een diatomisch fotonisch kristal bestaat uit twee roosters met verschillende staafjes. Een voorbeeld (met Greense en strip Greense functie) is getoond in figuur 29. We beschouwen hier staafjes met verschillende grootte. De grootste staafjes zijn lineair en zorgen voornamelijk voor de veldverstrooiing. De kleinere staafjes veronderstellen we niet-lineair met positief Kerr effect, zodat zij aanleiding geven tot niet-lineaire lokalisatie.

Het strip Green formalisme kan hierop toegepast worden. Door de kleinere afmeting van de niet-lineaire staafjes bekomen we een goede overeenkomst met de exacte simulaties, zoals voorgesteld in figuur 30. Hier is Q een maat voor de energie van de mode:

$$Q = \sum_n |E_n(\omega, k_x)|^2. \tag{9}$$

Een voorbeeld van deze bredere modes wordt getoond in figuur 31.

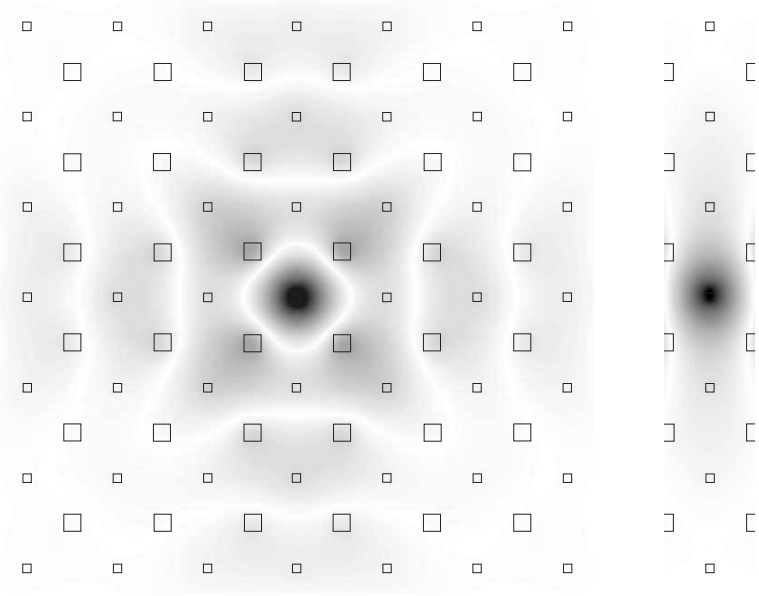

Figuur 29: (a) Diatomische geometrie met Greense functie bij $\omega = 0.4(2\pi c/a)$. (b) Strip Greense functie bij $\omega = 0.4(2\pi c/a)$ en $k_x = 0.85\pi/a$.

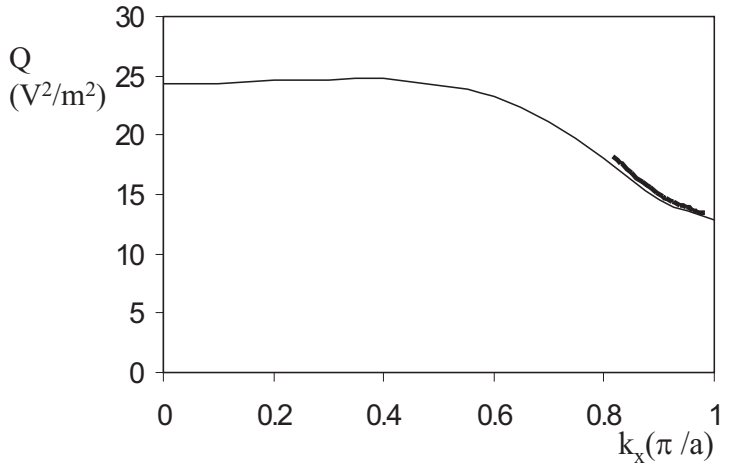

Figuur 30: Mode energie Q voor het diatomische PhC bij $\omega = 0.4(2\pi c/a)$, berekend met Stip Greense theorie (dunne lijn) en exacte berekeningen (dunne lijn), respectievelijk.

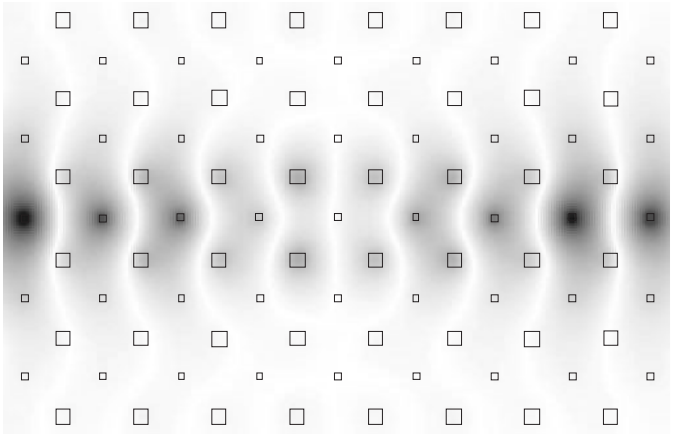

Figuur 31: Een propagerend diatomisch soliton bij $\omega = 0.4(2\pi c/a)$ en $k_x = 0.908\pi/a$.

We hebben bijgevolg de niet-gelokaliseerde golfgeleiders ontdekt in een nieuwe geometrie, en tegelijkertijd een goede overeenkomst met de strip Greense theorie vastgesteld. We merken tevens op dat ook in deze structuur modes voorkomen met één maximum en twee maxima. Dezelfde stabiliteitsoverwegingen als bij het gewone fotonisch kristal blijken hier eveneens te gelden.

5. Modelleren van tweede harmonische generatie

Bij het effect van tweede harmonische generatie (Second-Harmonic Generation of SHG) is het begrip fase-overeenkomst heel belangrijk. Indien deze overeenkomst er niet is, dan zal de tweede harmonische gegenereerd op een bepaalde plaats destructief interfereren met de generatie op een andere plaats. Op die manier bekomt men geen efficiënte omzetting.

Fase-overeenkomst is te bereiken door verschillende polarisaties te beschouwen in anisotrope media. Met deze methode bekomt men echter relatief grote structuren en is het mogelijk dat de fundamentele en tweede harmonische bundels in een verschillende richting propageren.

Een alternatieve techniek, genaamd quasi-fase overeenkomst (quasi-phase matching), maakt gebruik van roosters. Hiermee komen we meteen op het terrein van periodische structuren of fotonische kristallen. Een dergelijke structuur kan ervoor zorgen dat het verschil in golfvector tussen fundamentele en tweede harmonische gecompenseerd wordt door roosterreflecties, en dus door het kristalgolfgetal. Op die manier kan toch een goede omzetting gerealiseerd worden.

Verder is men voornamelijk geïnteresseerd in golfgeleiderstructuren, die dan in geïntegreerde circuits kunnen voorkomen. Golfgeleiders en periodieke structuren zijn zeer geschikt voor een beschrijving met mode expansie. Daardoor is een simulatiemethode voor SHG op basis van eigenmodes zeer veelbelovend.

5.1 Eigenmode methode

In dit gedeelte geven we een beknopt overzicht van de werking van de methode. Hier veronderstellen we dat de fundamentele golf slechts weinig invloed ondervindt van de tweede harmonische. Dit betekent dat er relatief weinig omzetting van de fundamentele gebeurt, hetgeen voor de meeste geïntegreerde structuren het geval is. Het schema van de methode is bijgevolg zoals in figuur 32. Hier is zichtbaar dat de berekening van de fundamentele onafhankelijk gebeurt. We gebruiken immers een lineaire berekening, die ons de nodige gegevens verschaft voor de bepaling van de tweede harmonische. Wanneer er veel omzetting gebeurt moeten we het algoritme aanpassen, dit wordt besproken in sectie 5.4.

De techniek is opgebouwd uit twee gedeelten. In eerste fase beschouwen we dat de modes in één richting propageren. Aan de hand

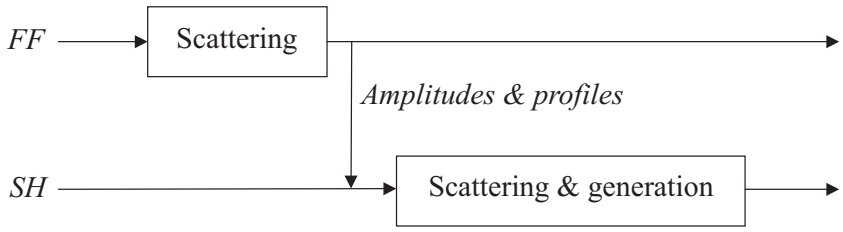

Figuur 32: Schema van de simulatiemethode. FF staat voor de fundamentele frequentie, SH betekent tweede harmonische.

van de sterktes van de fundamentele modes aan het begin kunnen we de sterktes van de tweede harmonische modes aan het einde afleiden. We veronderstellen geen niet-lineaire koppeling tussen modes die propageren in verschillende richtingen, daar ze geen fase-overeenkomst bezitten. In een tweede fase construeren we een formalisme waarbij modes in beide richtingen propageren en lineaire koppeling gebeurt aan de overgangen tussen verschillende secties.

Voor de niet-lineaire koppeling tussen copropagerende modes gebruiken we de volgende eigenmode superpositie in de Helmholtz vergelijking voor de tweede harmonische:

$$E_\omega = \sum_i A'_i e^{-j\beta_{\omega,i}z} E_{\omega,i}(x), \tag{10}$$

$$E_{2\omega} = \sum_i C'_i(z) e^{-j\beta_{2\omega,i}z} E_{2\omega,i}(x). \tag{11}$$

Met behulp van orthonormaliteit isoleren we een vergelijking voor één mode. Daar de omhullenden traag variëren bekomen we een eerste orde differentiaal vergelijking die analytisch oplosbaar is. Het uiteindelijke resultaat is:

$$\begin{aligned} C'_i(z) &= C'_i(0) - 2k_0^2 \sum_k A'^2_k \frac{e^{j\Delta\beta_{ki}z} - 1}{\beta_{2\omega,i}\Delta\beta_{ki}} O_{ki} \\ &\quad -4k_0^2 \sum_{l,m} A'_l A'_m \frac{e^{j\Delta\beta_{lmi}z} - 1}{\beta_{2\omega,i}\Delta\beta_{lmi}} O_{lmi}, \end{aligned} \tag{12}$$

met O_{ki} en O_{lmi} overlap-integralen tussen fundamentele en tweede harmonische mode profielen. De factoren met $\Delta\beta$ tonen de belangrijke invloed van fase-overeenkomst. Vergelijking 12 betekent dat we enkel

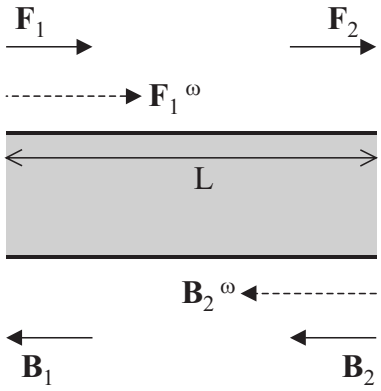

Figuur 33: Generatie in een invariante sectie. De nodige fundamentele vectoren worden getoond met gestreepte pijlen.

de fundamentele mode amplitudes en de overlapintegralen nodig hebben om ineens te berekenen hoe sterk de tweede harmonische modes gegenereerd worden na een afstand z.

Een volgende stap bestaat erin een formalisme af te leiden met modes die in beide richtingen propageren. De situatie in een invariante sectie is voorgesteld in figuur 33. Inspectie van vergelijking 12 leidt tot de conclusie dat er door de niet-lineariteit extra termen bijkomen. We gieten dit in een matrix-formalisme en bekomen:

$$\begin{bmatrix} \mathbf{F}_2 \\ \mathbf{B}_1 \end{bmatrix} = \begin{bmatrix} \mathbf{diag}(e^{-j\beta_{2\omega,i}L}) & \mathbf{0} \\ \mathbf{0} & \mathbf{diag}(e^{-j\beta_{2\omega,i}L}) \end{bmatrix} \cdot \begin{bmatrix} \mathbf{F}_1 \\ \mathbf{B}_2 \end{bmatrix} + \begin{bmatrix} \mathbf{N}_{fw} \\ \mathbf{N}_{bw} \end{bmatrix}. \tag{13}$$

De vermenigvuldiging met de diagonaalmatrices duidt op de gewone lineaire propagatie. De extra termen $\mathbf{N}_{fw}$ en $\mathbf{N}_{bw}$ staan voor de generatie van de tweede harmonische in voorwaartse en achterwaartse richting, respectievelijk. Zij vormen het enige verschil met het lineaire algoritme.

De overgangen tussen verschillende secties worden verwezenlijkt zoals in het lineaire geval. De invloed van niet-lineariteit is hier verwaarloosbaar. Dit leidt tot de gewone lineaire verstrooiing, beschreven door een verstrooiingsmatrix. Door deze matrices te combineren met de uitdrukkingen voor de secties bekomen we voor de volledige struc-

tuur een uitdrukking van de vorm:

$$\begin{bmatrix} \mathbf{F}_{out} \\ \mathbf{B}_{out} \end{bmatrix} = \mathbf{S} \cdot \begin{bmatrix} \mathbf{F}_{in} \\ \mathbf{B}_{in} \end{bmatrix} + \begin{bmatrix} \mathbf{N}_{fw}^{tot} \\ \mathbf{N}_{bw}^{tot} \end{bmatrix}, \tag{14}$$

met $\mathbf{S}$ de totale verstrooiingsmatrix. $\mathbf{N}_{fw}^{tot}$ en $\mathbf{N}_{bw}^{tot}$ zijn de totale voorwaarts en achterwaarts propagerende tweede harmonische eigenmode-amplitudes. We zijn enkel geïnteresseerd in deze vectoren als er geen rechtstreekse invoer van tweede harmonische is.

Het beschreven formalisme bezit verscheidene efficiënte kenmerken. Met behulp van vergelijking 12 bepalen we meteen de amplitudes op het einde van de sectie. We moeten bijgevolg geen discretisatie doorvoeren in de longitudinale richting, hetgeen een sterk voordeel is ten opzichte van methoden zoals FDTD of BPM. Voor de overlapintegralen gebruiken we een rooster in de transversale richting. Doordat het gedeelte niet-lineair materiaal vaak klein is, betekent dit echter dat het rooster niet over de volledig breedte nodig is.

Voor periodieke structuren is de methode uitermate geschikt. We kunnen immers effectief bepaalde data opnieuw gebruiken, zoals overlapintegralen en verstrooiingsmatrices.

Een ander kenmerk is dat we zelf kunnen bepalen welke modes lineair en welke niet-lineair koppelen. Voor accurate berekening is het vaak voldoende dat de laagste orde modes niet-lineair beïnvloed worden. De hogere modes kunnen we echter in de lineaire verstrooiing behouden om effecten zoals stralingsverliezen correct te modelleren. Deze beperktere koppelschema's verwezenlijken een sterke tijdwinst, zonder op accuraatheid in te boeten.

Tenslotte vermelden we dat de structuren vaak geïnterpreteerd worden aan de hand van hun mode-eigenschappen. In tegenstelling tot totale-veld aanpakken hebben wij direct gedetailleerde toegang tot deze data.

5.2 Diep-geëtste golfgeleider

We onderzoeken een structuur die reeds veel interesse opgewekt heeft, een golfgeleider met luchtspleten. De geometrie is getoond in figuur 34. Omwille van het hoog index contrast tussen de kern met index ~ 3 en de lucht met index 1, levert het rooster sterk dispersieve effecten. Deze kunnen gebruikt worden om fase-overeenkomst te bekomen bij tweede harmonische generatie. Het contrast zorgt er echter ook voor dat er sterke diffractieverliezen kunnen optreden. Vooral wanneer de

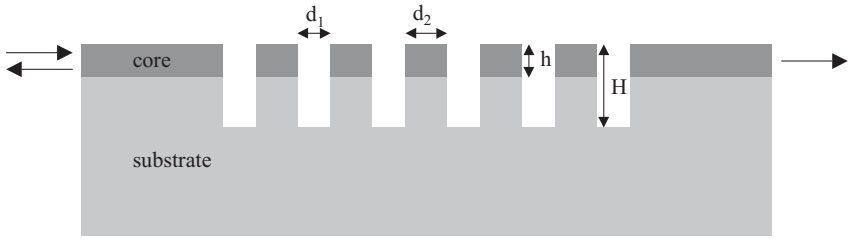

Figuur 34: Geometrie van een diep-geëtste golfgeleider.

modes boven de lichtlijn liggen, zoals meestal het geval is bij de tweede harmonische.

Er is aangetoond dat de mode expansie methode zeer geschikt is voor het lineair modelleren van deze structuur. Dit omdat de structuur periodisch is en omdat de verliezen efficiënt gemodelleerd worden met PML (Perfectly Matched Layer) randvoorwaarden. Hier tonen we aan dat de tweede harmonische generatie eveneens accuraat berekend wordt met onze niet-lineaire eigenmode extensie. We simuleren hiervoor een component die in de literatuur reeds met een FDTD methode beschreven is. Met deze methode is het echter niet praktisch om meer dan 20 perioden te behandelen, omwille van uit de hand lopende rekentijden. Wij zullen de bespreking uitbreiden tot 40 periodes, zodat we tevens meer data hebben om te vergelijken met een analytisch model.

Bij één-dimensionale lagenstructuren heeft men de voorwaarden aangetoond om de meeste generatie te bekomen. Hiervoor moet de fundamentele golf geplaatst worden op het transmissiemaximum met golflengte net boven de eerste bandgap. De tweede harmonische regelen we zodat omgezet wordt naar de tweede piek net naast de tweede bandgap. Op die manier is een optimaal evenwicht bereikt tussen modeoverlap, groepssnelheid en fase-overeenkomst. Met dit schema kan de omzetting toenemen met N^6, waarbij N het aantal perioden voorstelt.

Hetzelfde schema wordt nu toegepast op de twee-dimensionale componenten. Het verschil is echter dat de maximale transmissie niet meer één zal zijn omwille van stralingsverliezen. Bovendien ervaren de pieken aan de rand van de bandgap de grootste verliezen, zodat een evenwicht zich opdringt.

Een voorbeeld van een berekend generatiespectrum is getoond in figuur 35. We merken dat we inderdaad de optimale frequentie geregeld

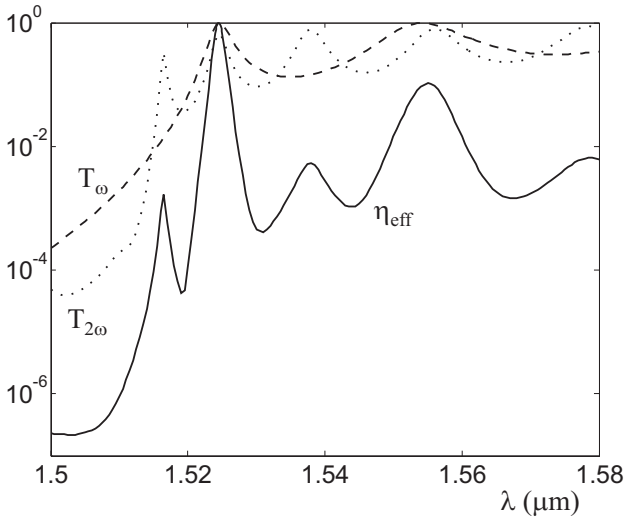

Figuur 35: Voorwaartse genormaliseerde SHG efficiëntie η_{eff} versus fundamentele golflengte (volle lijn) voor $h = 2\mu\mathrm{m}$ en $N = 20$. De streep- en puntlijn tonen de fundamentele en tweede harmonische transmissie ter referentie.

hebben respectievelijk op de eerste en de tweede piek naast de bandgap. Verder is zichtbaar dat de eerste piek van de tweede harmonische reeds veel verliezen ondervindt.

We onderzoeken nu de evolutie van de generatie als het aantal perioden toeneemt. Twee verschillende structuren met drastisch verschillend gedrag worden behandeld: De ene heeft $h = 1\mu m$ en de andere $h = 2\mu m$. Deze laatste heeft weinig verliezen ten opzichte van de eerste daar de mode veel breder is.

Een analytisch model uit de literatuur, waarbij de componenten als lekkende caviteiten beschouwd worden, leidt tot volgende efficiëntie:

$$\eta_{eff} \propto N^6 T_\omega^2 T_{2\omega} = N^6 \left(\frac{1}{1+N^3/a_\omega}\right)^2 \left(\frac{1}{1+N^3/a_{2\omega}}\right). \qquad (15)$$

T_ω en $T_{2\omega}$ stellen de respectievelijke maxima voor van de gebruikte transmissiepieken. De parameters a_ω en $a_{2\omega}$ modelleren de toenemende stralingsverliezen in functie van N en worden bepaald uit lineaire berekeningen. Intuïtief begrijpen we deze betrekking: Hoe meer verliezen, hoe kleiner de transmissies en bijgevolg hoe minder (nuttige) omzetting. T_ω is gekwadrateerd daar het fundamentele veld ook gekwadra-

teerd is in de niet-lineaire polarisatie. De voorfactor N^6 stelt het ideale gedrag voor, zoals besproken voor één-dimensionale lagenstructuren.

De resultaten zijn voorgesteld in figuur 36. We merken vooreerst op dat de berekende efficiënties overeenkomen met de FDTD-methode, die gekend zijn tot $N = 20$. De waarden voor $h = 1\mu m$ satureren en nemen af na een bepaalde N. Dit komt kwalitatief overeen met het model. De afname is in de exacte berekeningen echter sterker. We vermoeden dat in deze zone de verliezen zodanig groot worden, dat het niet langer correct is om het gedrag met caviteiten te behandelen. De overeenkomst bij $h = 2\mu m$ is beter. Hier zijn er slechts beperkte verliezen voor de tweede harmonische. Daarom loopt de lijn een weinig onder de ideale N^6-curve.

5.3 Fotonische kristal caviteit

In dit gedeelte bestuderen we een caviteit die aan weerszijden gekoppeld is met een golfgeleider, zie figuur 37. In combinatie met het Kerr-effect kan deze structuur een schakelaar verwezenlijken, zoals we reeds gezien hebben. Hier gebruiken we de opsluiting in de resonatoren om SHG te bekomen.

Efficiënte generatie vereist voldoening aan een aantal voorwaarden. Ten eerste moet er een bandgap aanwezig zijn voor fundamentele en tweede harmonische. Vervolgens is er nood aan een golfgeleidermode bij beide frequenties. Daarnaast moeten er twee resonanties zijn met bij voorkeur een goede overlap.

We hebben parameters gevonden die voldoen aan deze eisen. De transmissie-spectra voor fundamentele en tweede harmonische worden getoond in figuur 38. Beide pieken zijn Lorentziaans en we merken op dat de tweede harmonische mode veel smaller is dan de fundamentele.

Het spectrum van de tweede harmonische generatie wordt eveneens gepresenteerd in figuur 38. We veronderstellen hierbij dat enkel het centrale staafje niet-lineair is, omdat daar het grootste veld voorkomt. Slechts 30 modes zijn nodig. Hierbij moeten enkel de eerste 10 niet-lineair koppelen. Er is evenveel generatie in voorwaartse richting als in achterwaartse richting. Dit komt uiteraard omdat de resonatormode op eenzelfde wijze gekoppeld is met beide golfgeleiders. We merken op dat het verloop van $P_{2\omega}$ goed weergegeven is door $T_\omega^2 T_{2\omega}$. Dit correspondeert met het model van vorige paragraaf, zie vergelijking 15.

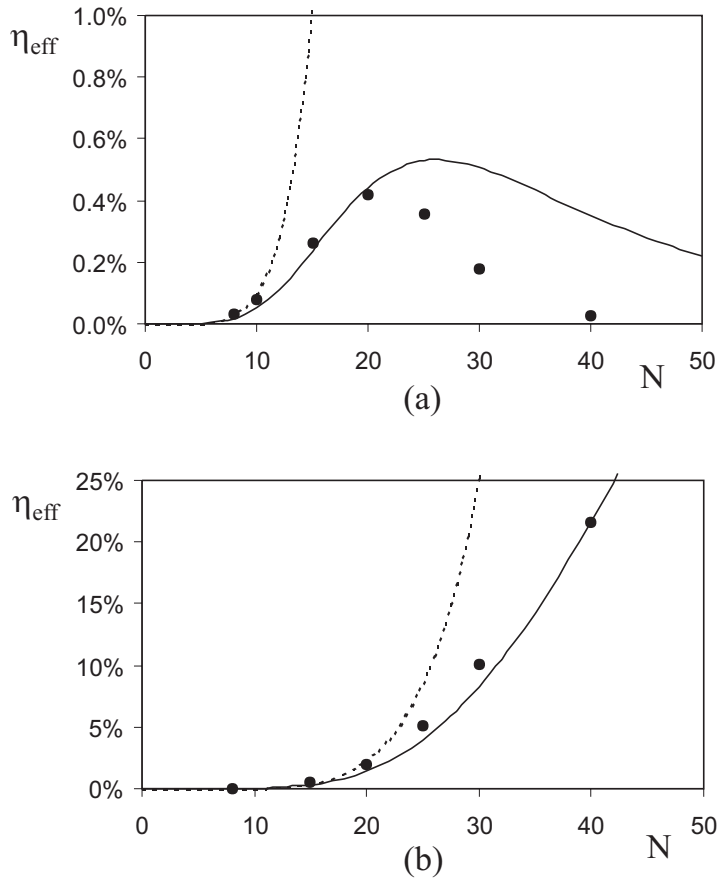

Figuur 36: SHG efficiëntie versus aantal perioden N. Vergelijking tussen het model (volle lijn) en de simulaties (punten) voor (a) $h = 1\mu\mathrm{m}$ en (b) $h = 2\mu\mathrm{m}$. De N^6 gestreepte lijn is toegevoegd ter referentie.

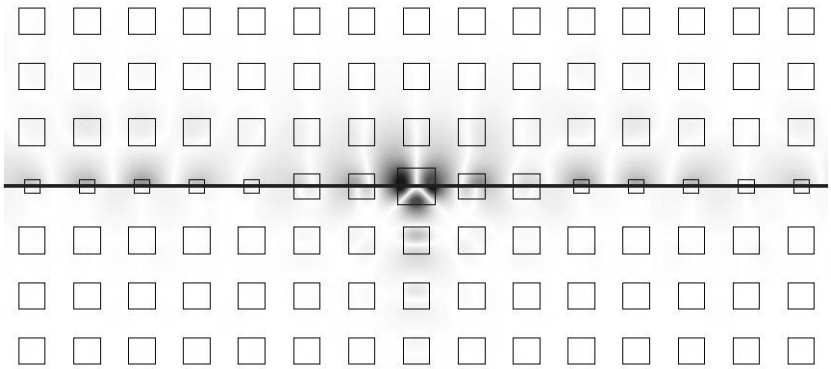

Figuur 37: Geometrie van de PhC component. De bovenste (onderste) helft toont het veld van de fundamentele (tweede harmonische) op resonantie. Dipool en kwadrupoolmodes zijn duidelijk. Door de hoge kwaliteit van de caviteit is het veld in de onderste golfgeleider nauwelijks zichtbaar.

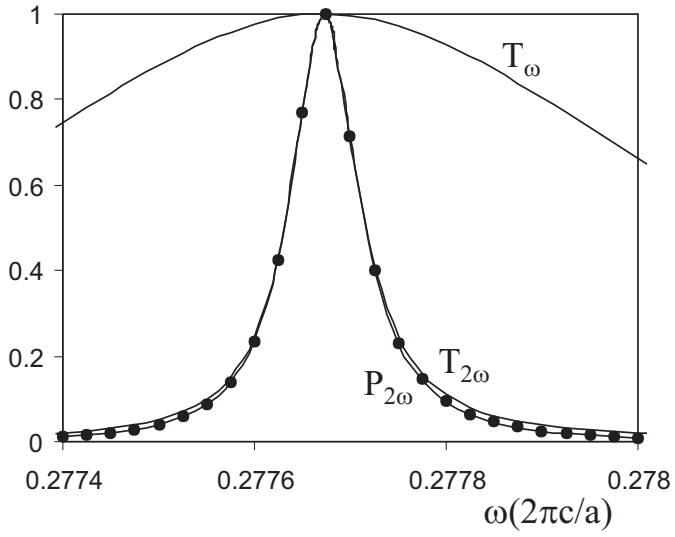

Figuur 38: PhC caviteit resultaten. De transmissie van de fundamentele T_ω en tweede harmonische $T_{2\omega}$ worden getoond, tezamen met tweede harmonische vermogen $P_{2\omega}$, met lijnen. $P_{2\omega}$ is genormaliseerd en alle curves zijn geplot versus de fundamentele frequentie. Waarden voor $T_\omega^2 T_{2\omega}$ zijn aangeduid met stippen.

Het voorgaande toont aan dat onze methode in staat is om op een efficiënte manier SHG in geavanceerde componenten te bestuderen.

5.4 Depletie methode

Indien de fundamentele sterk uitgeput wordt door de omzetting naar de tweede harmonische, dan moeten we het algoritme uitbreiden. Deze extensie is iteratief: We voeren een opeenvolging van gekoppelde fundamentele en tweede harmonische berekeningen uit. Met bepaalde benaderingen bekomen we opnieuw een analytische uitdrukking zoals vergelijking 12, maar dit keer voor de fundamentele amplitudes

$$\begin{aligned} A'_j(z) = A'_j(0) + \sum_{ni} \Gamma^j_{ni} \left(\frac{e^{-j\Delta\beta_{jni}z} - 1}{-j\Delta\beta_{jni}} \right) \\ + \sum_{nkl} \Gamma^j_{nkl} \left(\frac{e^{-j\Delta\beta'_{jnkl}z} - 1}{-j\Delta\beta'_{jnkl}} \right) + \sum_{nkl} \Gamma^j_{nkl} z. \end{aligned} \tag{16}$$

Met deze uitdrukking berekenen we de amplitudes op het einde van een invariante sectie, zonder dat we een rooster in de longitudinale richting moeten gebruiken. Hierdoor blijft de methode efficiënt.

Een voorbeeld van een berekening met deze uitgebreide methode wordt getoond in figuur 39. De structuur is de diep-geëtste golfgeleider van sectie 5.2. We zien duidelijk dat de SHG efficiëntie door depletie afneemt van 22% naar 8%. Dit bewijst dat het uitputtingseffect een grote invloed heeft bij dergelijke sterke omzettingen.

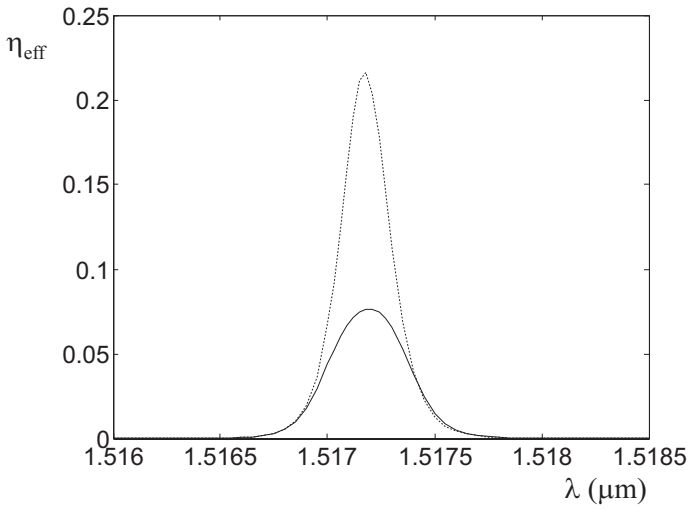

Figuur 39: SHG efficiëntie voor de diep-geëtste golfgeleider met $h = 2\mu m$ en $N = 40$ versus fundamentele golflengte. De berekeningen met en zonder depletie zijn getoond met volle en gestreepte lijnen, respectievelijk.

6. Conclusies

De combinatie van fotonische kristallen met niet-lineaire effecten biedt veel mogelijkheden, zowel voor fundamentele als voor toegepaste doeleinden. In dit werk hebben we modelleringsprogramma's ontwikkeld voor twee van de belangrijkste niet-lineariteiten, zijnde het Kerr effect en tweede harmonische generatie. Beide technieken breiden de eigenmode expansie methode uit en zijn uitermate geschikt voor periodieke structuren.

Het Kerr algoritme gebruikt een rooster voor de niet-lineaire gedeeltes en past de brekingsindex iteratief aan. Doordat de modes afhankelijk zijn van de exacte lokale index, is de methode accuraat zelfs in het geval van sterke niet-lineariteiten. De keerzijde is dat we veel modes moeten berekenen zodat de methode vooral bruikbaar is voor golflengteschaal componenten. Lineaire gedeelten moeten echter slechts één keer berekend worden.

We hebben de mogelijkheid zowel eindige als periodiek oneindige structuren te berekenen. In het laatste geval bekomen we een bandstructuur die verschuift in functie van het vermogen.

De methode voor SHG is een uitbreiding van het gekoppelde mode formalisme naar een situatie met meerdere modes. Wanneer het fundamentele signaal beperkt uitgeput wordt, kunnen we de berekeningen grotendeels onafhankelijk beschouwen. De tweede harmonische wordt in één berekening bekomen. Voor depletie moeten we een opeenvolging van gekoppelde fundamentele en tweede harmonische simulaties uitvoeren. In beide gevallen zijn de vergelijkingen analytisch oplosbaar en bekomen we dat een invariante sectie met één evaluatie behandeld wordt, zonder longitudinaal rooster. Het resulterende matrixformalisme is zeer efficiënt voor periodische structuren. We hebben dit aangetoond door berekeningen in de literatuur uit te breiden.

De ontwikkelde methodes zijn bidirectioneel en twee-dimensionaal. Het eerste betekent dat we reflecties volledig meerekenen, zodat effecten zoals interferentie en bistabiliteit optreden. Twee-dimensionaliteit duidt aan dat we transversale effecten beschouwen, zoals stralingsverliezen en (bandgap-)opsluiting.

Met deze tools hebben we een variëteit aan componenten onderzocht. De PhC caviteit in of naast een resonator bleek een zeer interessante bouwsteen. We beschouwden rijen van deze structuren en ontdekten een verscheidenheid aan intrinsiek gelokaliseerde modes. Wanneer we de afstand tussen twee resonatoren gepast kiezen, is het bovendien mogelijk om een efficiënte schakelwerking te verwezenlijken. Voor deze studies gebruikten we onze numerieke methode en CMT. Deze laatste blijkt een eenvoudige maar toch accurate theorie.

Verder beschreven we een nieuw soort gapsoliton in fotonische kristallen zonder lineaire defecten. Deze zelf-gelokaliseerde Blochmodes creëren hun eigen golfgeleider in de propagatierichting, maar blijven opgesloten door de bandgap in de transversale richting. Twee types treden op en we bestudeerden hun onderlinge stabiliteit. Voor de beschrijving van deze objecten ontwikkelden we bovendien een semi-analytische methode, die gebaseerd is op een opvouwprocedure voor de Greense functie.

Voor verder onderzoek kunnen we de bestaande methodes uitbreiden. Het formalisme voor SHG is bv. compatibel met som- en verschilfrequentie generatie en derde harmonische generatie. Verder kan SHG voor opsluitingseffecten zorgen wat aanleiding geeft tot de zogenaamde kwadratische solitonen. Dergelijke objecten in hoog-contrast twee-dimensionale structuren zijn nog grotendeels onbekend.

We besluiten dat de ontwikkelde technieken een grote klasse van componenten en fenomenen kunnen beschrijven. Verdere innovaties

en andere systemen zullen aanleiding geven tot nieuwe en onverwachte niet-lineaire concepten.

English Text

Chapter 1

Introduction

1.1 Context

In the last half of a century the understanding and manipulation of light has generated a revolution in physics and technology. This era was kickstarted with the first demonstration of a laser by Theodore Maiman in May 1960 [1]. First described by some as 'a solution looking for a problem', it became clear however that these intense bursts of coherent light had many important applications.

First of all the pumping schemes necessary to invert the electron population for lasing action, instigated the marriage of optics and electronics, which became known as optoelectronics. In addition, because the light power density was high enough it spurred the advent of nonlinear optics. The first experiment was conducted by Franken *et al.* who observed frequency doubling by propagating a ruby laser beam through a quartz crystal in 1961 [2]. Nonlinear electromagnetic effects had been known since Maxwell's time, with e.g. the saturation of magnetism in ferromagnets, but this was the first demonstration of coherent nonlinearities in the optical domain.

Another field that has experienced a breakthrough is communications technology. There it was realized that laser pulses could be guided with very low attenuation in ultra-pure silica fibres. Because signals with different wavelengths interfere weakly, the bandwidth is virtually unlimited. This gave rise to optical data networks that culminated into the backbones of the internet. In this regard the laser, together with the transistor, started today's information society.

The types of lasers and the number of applications are diverse and large. The medical world e.g. was quick to embrace the new technology.

Only sixteen months after Maiman's demonstration, a prototype ruby laser was used to destroy a retinal tumor in a patient [3]. Nowadays the beams are employed for high precision incisions, sometimes with the help of robotics [4].

Furthermore lasers are found in installations ranging from material cutters to bar code and optical disk readers. In the physical sciences they are necessary in experiments where high level accuracy or control is required. The precise wavelength properties make it possible to probe and manipulate individual quantum states in the burgeoning field of quantum technology. Alternatively the beams may act as traps for single particles.

As an example of a fundamental experiment made possible by laser technology, we mention the Laser Interferometer Gravitational-Wave Observatory or LIGO. The objective is to measure cosmic gravitational waves or ripples in space-time, produced by cataclysmic events such as colliding black holes. For this purpose two perpendicular ultrastable beams are bounced back and forth between test masses. The passing of a wave changes the lengths of the arms and induces a phase shift between the beams. With high precision is meant that distance changes of 10^{-18}m have to be measured [5].

Returning now to the field of photonics we have to mention the appearance of the field of nonlinear fiber optics. Already in the beginning of the seventies there were studies of nonlinear effects such as stimulated Raman and Brillouin scattering in single-mode fibers. The practical possibility of solitons in fibers was first demonstrated in 1980 [6]. In these nonlinear packets the broadening of pulses due to dispersion is countered by the Kerr nonlinearity. These solitons led to advances in the generation and control of ultrashort optical pulses [7].

Nowadays solitons are reported in a wide range of material systems and settings, with confinement in the temporal or the spatial domain [8, 9]. Various different nonlinear effects can be exploited. Interest in these topics is raised not only because of fundamental physics reasons, but also because of data processing opportunities.

Indeed, in today's networks the transportation of data is done in the optical regime via fibers, but the processing at nodes is achieved in electrical circuits. Therefore a time-consuming and expensive conversion between the optical and electrical domain is performed, as depicted in figure 1.1. After the necessary operations, the data is yet again converted and put into the next fiber. In order to increase the datarates over the network the number of conversions has to be minimized. Therefore

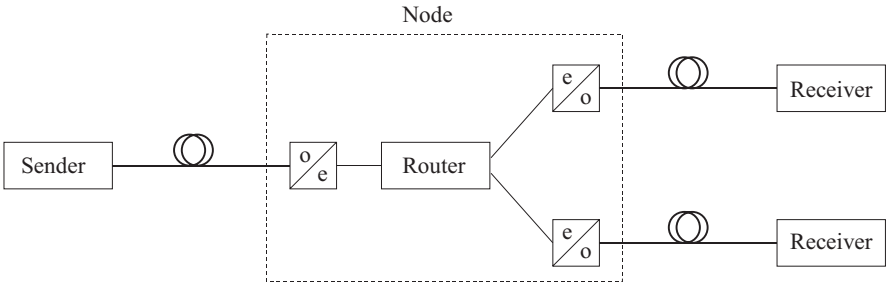

Figure 1.1: Schematic of a network with electro-optic conversions.

the challenge is to design an all-optical network, where the operations are conducted completely with optical signals.

Now, if we want these optical devices to be efficient and cheap, we need to make them as small as possible, preferably wavelength-scale. Furthermore, fabrication has to be done with integrated technology. In this way we create photonic integrated circuits or chips. In the last few years great progress is made and increasingly complex components are manufactured and measured [10]. Moreover these systems are also being used to probe new physical effects. Indeed, because of the tight control on the parameters these laboratories can measure phenomena, which appear in other branches of science, but are demonstrated first in the optical domain. An example here is the study of nonlinear localized modes [11].

However, to use these devices for all-optical information processing, we have to make light interact with light. To this end we can use the nonlinear effects of materials. As already mentioned these effects are rather weak and high power densities are necessary. A way to increase the power density is to confine the light tightly. This confinement is possible in photonic integrated circuits, with structures such as photonic wires, that are very narrow waveguides. Another promising technology is photonic crystals (PhCs), and this will be discussed in the next section.

In conclusion we can say that the revolution brought by the laser is still continuing today. The combination of photonic integrated components with nonlinearities delivers new concepts, both from the fundamental and applications point of view.

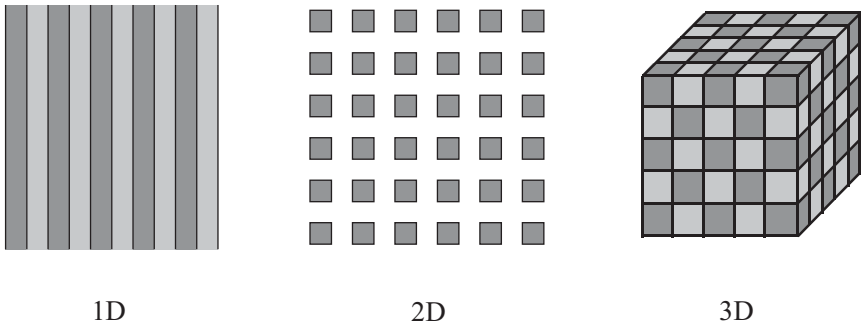

Figure 1.2: Examples of 1D, 2D and 3D photonic crystals.

1.2 Photonic crystals

Photonic crystals are periodic structures consisting of different materials, with a period on the order of the wavelength. They can be categorized according to their dimensionality and we depict a few examples in figure 1.2. Because of the periodic nature peculiar effects appear. Indeed, every interface between the materials gives rise to reflections that depend on the frequency, polarization and direction. The interplay between the many small contributions causes these metamaterials to obtain very selective features. The most important effect is the appearance of *bandgaps*. These gaps correspond to frequency intervals where no propagation is possible, in any direction. In this way the crystal can immediately act as a mirror. The bandgap concept is in complete analogy with electrons in semiconductors. There the potential of the nuclei generates forbidden energy regions for the electrons.

Although periodic structures have long been studied, the realization of omnidirectional bandgaps in 2D or 3D structures spurred a new line of research. In the late 1980s Eli Yablonovitch and his group began the first experiments on 3D structures in the microwave regime, where fabrication is easier [12]. Together with the advancement of manufacturing methods, photonic crystals are a possible road towards telecom wavelength devices [13].

Because of the mirror action it is possible to obtain new functionalities by incorporating defects into the structure. This intuitive picture is shown in figure 1.3, where a cavity and a waveguide are demonstrated. When a bend is introduced between two waveguides the light is not allowed to enter the regions next to the guides, because of the

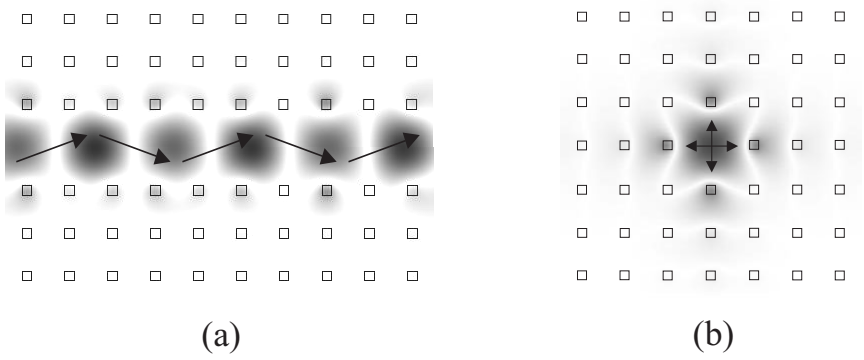

Figure 1.3: Photonic crystal defects: (a) waveguide and (b) resonator.

bandgap. For this reason it is possible to construct very sharp bends without radiation losses. This marks the difference with conventional waveguides, where sharp bends immediately induce losses. Because of these properties, truly molding the flow of light is achievable in photonic crystals [14].

The idea of the bandgap has also led to important developments in the fiber community. Indeed, instead of total internal reflection in conventional fibers, the gap reflection can be used for guiding purposes, as we already mentioned. Two possible designs are shown in figure 1.4, with respectively a one-dimensional and a two-dimensional transversal structure. The one-dimensional structures are called Bragg or omniguide fibers [15, 16], while the two-dimensional fibers are often named photonic crystal or holey fibers.

Remark that both bandgap and index guidance can be used in these components. Together with the freedom to design the layers and holes, it is clear that many structures are possible. If the core is hollow e.g. one can achieve low losses or nonlinearities, as the material experiences a very weak evanescent field [17]. On the other hand a fiber with a very small solid core can induce strong nonlinear effects, dramatically illustrated by the phenomenon of supercontinuum generation [18]. Therefore new wavelength regimes and applications are expected from these devices.

Returning now to the topic of integrated PhC circuits, new functions arise if we combine the previously introduced building blocks. An example of such a structure, that can perform a nonlinear switching function, is shown in figure 1.5 [19]. It is a combination of a resonator

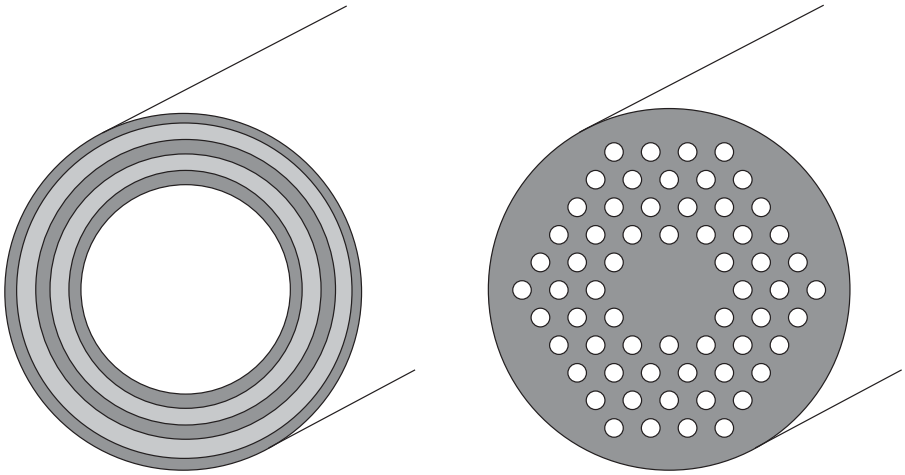

Figure 1.4: Examples of microstructured fibers.

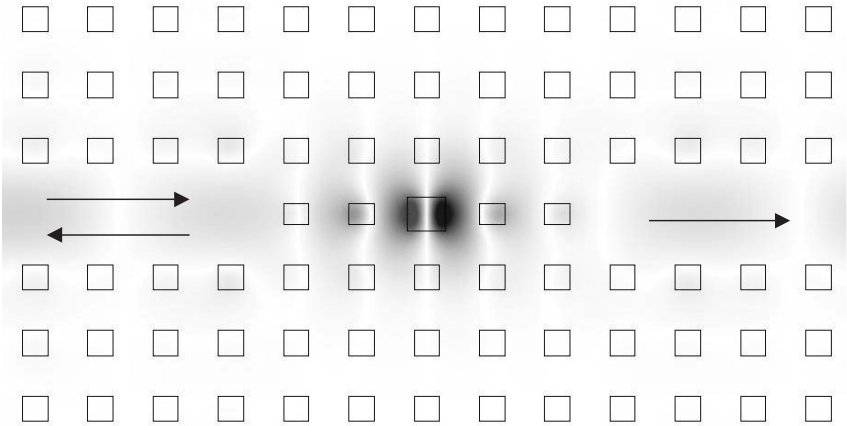

Figure 1.5: A PhC switching device.

with waveguides on the left and the right. A possible operation of this device is called switching: At low power transmission is negligible, at high power the light is transmitted to the output waveguide on the right.

Because the field is enhanced in such a very small cavity, PhCs offer a real advantage for compact and efficient nonlinear circuits. A multitude of possible designs provides us with a rich set of possibilities and applications [20].

1.3 Optical modeling

The fabrication and measurement of components is a time-consuming and expensive process. Therefore one has to resort to computer simulations in order to design and optimize the structures. Because of the complexity and precision of the fabricated features the demands on these numerical tools continue to increase. Consequently the challenge is to develop accurate and efficient computational methods.

In an industrial or rapidly evolving scientific context it is clear that the speed and ease of simulations in the design-cycle become important. In addition, because the calculations try to approximate the physical problems as close as feasible, it is possible to give numerical proof-of-principle of new devices and phenomena. An important step is then to gain (analytical) insight into the processes. Later on, these concepts often lead to practical applications.

The development of numerical schemes for electromagnetic problems in general, and optical structures in particular, has grown into a scientific discipline. As a result there exists an abundance of calculation approaches. In this introduction we can only highlight some of the more popular methods. For a more in depth discussion we refer e.g. to the textbook [21].

We can make a first distinction between time-domain and frequency-domain techniques. The former calculate the evolution of the pulses through the structure as time steps forward. Therefore one gets a highly detailed account of what can happen in actual experiments, as many components are excited with pulses. Furthermore if the input is a narrow pulse, the frequency response of the structure is deduced from one calculation run using the Fourier transform.

On the other hand frequency-domain methods calculate the steady-state behaviour at one particular frequency. So in order to obtain the full spectrum several simulations have to be performed. However, if a

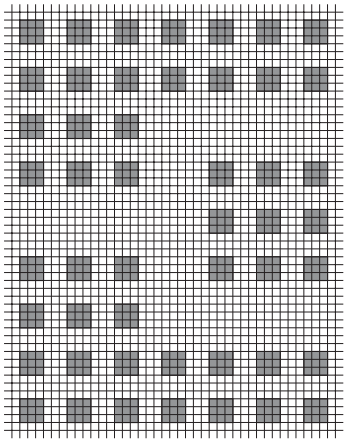

Figure 1.6: Example of a PhC splitter with a grid.

good frequency resolution is needed, e.g. with high-quality resonators, time-domain methods have to model longer pulses, which decreases efficiency. Furthermore, for nonlinear situations precautions need to be taken in the time-domain, so that different frequency components do not interfere with each other, for example in the case of material dispersion [22].

Additionally, we can distinguish between techniques that discretize the computational domain, and those that use a more analytical approach. Two of the most popular algorithms belong to the first category: They are the Finite-Difference Time-Domain method (FDTD) [23] and the Beam Propagation Method (BPM) [24]. In FDTD Maxwell's differential equations are rewritten as differences, with the fields defined on the points of a mesh. An example of such a grid is schematically shown in figure 1.6. If the grid is fine enough, the results are exact. Furthermore, the difference equations are easy to implement. However, as with most methods that use a grid, if the structure becomes large, the number of parameters increases dramatically, and calculation times and memory requirements become excessive.

In BPM the assumption is made that the field propagates mostly along one direction. Advanced versions incorporate larger deviations from this axis. Here special care is needed for reflections and high index contrasts.

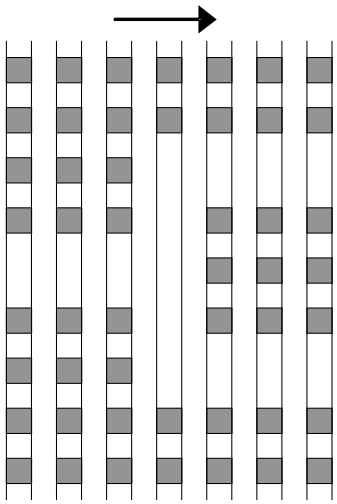

Figure 1.7: The splitter in the modal scheme: only four different sections. The arrow indicates the main propagation direction.

Both BPM and FDTD have been expanded for nonlinearities such as the Kerr effect and SHG [25, 26]. These extensions naturally inherit the same problems and advantages as their linear formulations.

In this work we are interested in the eigenmode expansion method, that belongs to the class of more analytical approaches. Here the structure is sliced into piecewise constant sections along a certain direction, as in figure 1.7. If we consider such a section, one can prove that these slabs have a set of field profiles that can propagate indefinitely without changing their shape. Therefore these modes form a natural basis for the description of the fields, just as the harmonic functions present the basis in Fourier analysis.

If we know the modes, we only have to keep track of their weight coefficients, which greatly reduces the number of parameters. By combining the different sections, we obtain an efficient scheme for an entire, more complicated structure. In addition, the method is exact if enough modes are employed. Eigenmode expansion is especially suitable for periodic structures (and thus PhCs) because data can effectively be reused. The technique has been applied successfully to model a variety of complex devices [27].

1.4 Objectives and overview of this work

At the onset of this work 2D simulation tools for nonlinear effects were scarce. However because of the advancements in fabrication there was an increasing interest in all-optical devices. This interest was also fueled by the peculiarities and potential of PhCs. Nowadays actual measurements are starting to appear, and novel designs are reported via numerical tools.

We made a contribution by studying the potential of the eigenmode method for the simulation of nonlinear structures. For this purpose we extended the formalism as implemented in the CAMFR framework [28].

We focused on two of the most common nonlinearities: the Kerr effect and second-harmonic generation (SHG). The objective is to strike a balance between rigorousness and efficiency. The calculations must be sufficiently accurate, while the execution times have to remain short. For this latter feature we need to preserve the efficient characteristics of the linear method as much as possible.

In addition, we applied these tools to explore innovative concepts and phenomena in PhC components. We will offer several examples of Kerr switching and SHG in PhC cavities and related periodic structures. Furthermore we examined different types of solitons in sequences of nonlinear resonators and two-dimensional Kerr PhCs.

This work is structured as follows. In the next chapter we describe the background concepts and calculation methods such as PhCs, nonlinear optics, mode expansion and coupled mode theory.

Then in chapter 3 we describe our technique to model the Kerr effect. Both finite and infinite periodic structures are simulated. After validation of the algorithm, we demonstrate more advanced devices, such as a PhC cavity exhibiting a Fano line shape, and a PhC waveguide with a bistable dispersion curve.

In chapter 4 we examine finite series of nonlinear PhC switches using coupled mode theory and our Kerr simulation method. It is proven that a variety of soliton-like modes exist in these structures. By properly selecting the parameters of the system dark solitons arise. In addition an actual design with two cavities is rigorously calculated that provides an efficient switching opportunity.

We examine a novel variety of gap-solitons in chapter 5. These Bloch modes induce their own waveguide through a nonlinear crystal without linear defects. A related on-site and inter-site kind is demon-

strated and their stability is studied. Furthermore a semi-analytical tool to describe these modes is developed.

The extension for second-harmonic generation is described in chapter 6. We elaborate the algorithm with and without pump depletion. The particular efficiency of the method for 2D periodic structures is proven by calculating extensive high-contrast devices with radiation losses. In addition, SHG in a PhC cavity is examined.

Finally, chapter 7 offers conclusions and directions for future research.

1.5 Publications

The work performed in this thesis contributed to a number of publications in international refereed journals:

- B. Maes, P. Bienstman, R. Baets, 'Modeling of Kerr nonlinear photonic components with mode expansion', Optical and Quantum Electronics 36 (1-3): 15-24 Jan-Feb (2004).
- G. Priem, I. Notebaert, B. Maes, P. Bienstman, G. Morthier, R. Baets, 'Design of all-optical nonlinear functionalities based on resonators', IEEE Journal of Selected Topics in Quantum Electronics 10 (5): 1070-1078 Sept-Oct (2004).
- B. Maes, P. Bienstman, R. Baets, 'Bloch modes and self-localized waveguides in nonlinear photonic crystals', Journal of the Optical Society of America B 22 (3): 613-619 Mar (2005). (Also appeared as invited paper in Virtual Journal of Nanoscale Science & Technology, March 28, 2005.)
- G. Van der Sande, B. Maes, P. Bienstman, J. Danckaert, R. Baets, I. Veretennicoff, 'Nonlinear lattice model for spatially guided solitons in nonlinear photonic crystals', Optics Express 13 (5): 1544-1554 Mar (2005).
- B. Maes, P. Bienstman, R. Baets, 'Switching in coupled nonlinear photonic crystal resonators', accepted in Journal of the Optical Society of America B.
- B. Maes, P. Bienstman, R. Baets, 'Modeling second-harmonic generation with mode expansion', accepted in Journal of the Optical Society of America B.

We presented our results at several international conferences:

- B. Maes, P. Bienstman, R. Baets, 'Modelling of nonlinear effects in a mode expansion context', Workshop 2D photonic crystals, Switzerland, p.I-05 (2002).
- B. Maes, P. Bienstman, R. Baets, 'Rigorous modelling of nonlinear wave-length-scale structures with mode expansion and spatial index discretisation', OWTNM (Optical Waveguide Theory and Numerical Modelling), Czech Republic, p.98 (2003).
- B. Maes, P. Bienstman, R. Baets, 'Rigorous modelling of non-linear photonic components with mode expansion and spatial index discretisation', IPR (Integrated Photonics Research), United States, p.105-107 (2003).
- B. Maes, P. Bienstman, R. Baets, 'Bloch modes and self-localized waveguides in non-linear photonic crystals', IEEE Leos Benelux Annual Symposium, The Netherlands, p.303-306 (2004).
- B. Maes, P. Bienstman, R. Baets, 'A novel photonic crystal flip-flop device', NLGW (Nonlinear Guided Waves and Their Applications), Canada, TuC45 (2004).
- B. Maes, P. Bienstman, R. Baets, 'Modeling second harmonic generation with mode expansion', OWTNM, Belgium, p.36 (2004).
- G. Van der Sande, B. Maes, P. Bienstman, J. Danckaert, R. Baets, I. Veretennicoff, 'Semi-analytical model for spatial solitons in nonlinear photonic crystals', IEEE Leos Benelux Annual Symposium, Belgium, p.303-306 (2004).
- B. Maes, G. Van der Sande, P. Bienstman, J. Danckaert, R. Baets, I. Veretennicoff, 'Self-localized Waveguides in Nonlinear Photonic Crystals', IPRA (Integrated Photonics Research and Applications), United States, p.ITuB2 (2005).
- G. Van der Sande, B. Maes, P. Bienstman, J. Danckaert, R. Baets, I. Veretennicoff, 'Nonlinear lattice model for self-localized waveguides in nonlinear photonic crystals', accepted for SPIE Optics and Optoelectronics, Poland (2005).
- B. Maes, P. Bienstman, R. Baets, 'Efficient and rigorous modeling of second-harmonic generation including moderate pump-depletion', submitted to NLGW, Germany (2005).

- S.-P. Gorza, C. Cambournac, P. Emplit, M. Haelterman, D. Taillaert, B. Maes, R. Baets, 'Identification of gap soliton through phase measurement', submitted to NLGW, Germany (2005).

Chapter 2

Overview of the main concepts

2.1 Introduction

In this chapter we provide an overview of the main concepts utilized throughout this book. The aim of our work is the combination of photonic crystals and nonlinear optics, therefore we introduce these separate fields. Because these subjects are extensive, we restrict the discussion and refer to the literature for more information.

One of our objectives is the development of numerical tools to study nonlinear wavelength scale structures. For this purpose we extend the eigenmode expansion method, as implemented in the CAMFR framework [27, 28]. By building upon this flexible and efficient tool, we inherit attractive features such as rigorousness, fully vectorial solutions, advanced (PML) boundary conditions, etc. Therefore it is suitable to explain the workings of linear eigenmode expansion, which we do in section 2.4.

Finally, a very intuitive analytic technique to study systems with waveguides and resonators is Coupled Mode Theory (CMT). We will encounter such structures in various forms and settings. More specifically, we examine series of coupled cavities in chapter 4. Therefore, we introduce CMT here in section 2.5. We show which restrictions apply to the parameters, and how the theory is extended for nonlinear resonators.

Readers already familiar with these concepts may wish to proceed directly to the next chapter.

2.2 Photonic crystals

Photonic crystals are usually defined as periodic structures with a period on the order of the wavelength of the light and a high refractive index contrast. The term crystal refers to the strong analogy with electrons in crystalline materials. There the periodic potential of the nuclei can lead to electronic bandgaps, regions of energy where no allowed electron level exists. This brings us to the main property of PhCs, the possibility of obtaining a photonic bandgap, frequency bands where the light cannot propagate through the structure.

The appearance of bandgaps necessitates translational symmetry and high index contrast. However, by breaking this symmetry, molding the flow of light is truly possible. If we combine these defects, we can create waveguides and cavities with highly tunable features. How these features originate and how we describe them is the subject of this section. For a more in depth review we refer to the introductory textbook [14].

2.2.1 Photonic crystals without defects

The nuclei and electrons in solid-state crystal lattices correspond with macroscopic dielectric materials and electromagnetic waves in photonic crystals, respectively. Consequently their behaviour is modeled with the macroscopic Maxwell equations. Assuming harmonically varying fields with $e^{j\omega t}$, these equations in the complex representation are:

$$\nabla \times \mathbf{E} = -j\omega\mathbf{B}, \tag{2.1}$$
$$\nabla \times \mathbf{H} = \mathbf{J} + j\omega\mathbf{D}, \tag{2.2}$$
$$\nabla \cdot \mathbf{D} = \rho, \tag{2.3}$$
$$\nabla \cdot \mathbf{B} = 0. \tag{2.4}$$

Here, ρ and $\mathbf{J}$ represent the free charge and current, respectively. In this work we will use the concept of *modes*. These are solutions of the Maxwell equations that propagate, even without internal sources of light, so we can set $\rho = 0$ and $\mathbf{J} = 0$.

In addition to the Maxwell system we need the constitutive equations, that describe the response of the material to the electromagnetic fields. In linear media the following equations hold:

$$\mathbf{D} = \varepsilon\mathbf{E}, \tag{2.5}$$
$$\mathbf{B} = \mu\mathbf{H}. \tag{2.6}$$

Nonlinearity of the material is introduced by changing equation 2.5. We postpone the discussion of the nonlinear model to section 2.3. Furthermore, we focus here on the isotropic lossless case, so ε and μ are real scalars. For *anisotropic* materials these quantities are tensors, whereas loss is modeled by an imaginary part of the coefficients. In this work we assume $\mu = \mu_r \mu_0 = \mu_0$.

Using the constitutive and the curl equations we can derive

$$\nabla \times \nabla \times \mathbf{E} = \varepsilon \mu \omega^2 \mathbf{E}, \tag{2.7}$$

or

$$\nabla(\nabla \cdot \mathbf{E}) - \nabla^2 \mathbf{E} = \varepsilon \mu \omega^2 \mathbf{E}. \tag{2.8}$$

In media where ε is piecewise constant, equation 2.3 gives us $\nabla \cdot \mathbf{E} = 0$, and the previous formula becomes the Helmholtz equation:

$$\nabla^2 \mathbf{E} + \varepsilon \mu \omega^2 \mathbf{E} = 0, \tag{2.9}$$

provided the boundary conditions at the interfaces are implemented.

In *homogeneous* media, where ε is a constant, the solutions (or modes) are plane waves:

$$\mathbf{E} = \mathbf{E}_0 e^{-j\mathbf{k}\cdot\mathbf{r}}, \tag{2.10}$$

where $\mathbf{k}$ is called the wavevector, and the field is transversal $\mathbf{E}_0 \cdot \mathbf{k} = 0$. The direction of $\mathbf{k}$ indicates the direction of propagation, whereas the amplitude k is defined by

$$k = \sqrt{\varepsilon \mu}\omega = \frac{\sqrt{\varepsilon_r \mu_r}}{c}\omega = \frac{n}{c}\omega. \tag{2.11}$$

Here the refractive index is $n = \sqrt{\varepsilon_r}$. This connection between ω and k is generally called the *dispersion relation*. In homogeneous media this relation is a straight line.

Now we can categorize the solutions, in the sense that for every ω there is a corresponding wavevector k, determined by equation 2.11. The wave propagating in the opposite direction is characterized by $-k$.

Note that material dispersion will be neglected, meaning that we simply fix the material index in the frequency region of interest. In the frequency domain this does not constitute a restriction.

If we alternate the indices the dispersion relation adjusts profoundly, this is called geometric dispersion. Many features and applications of

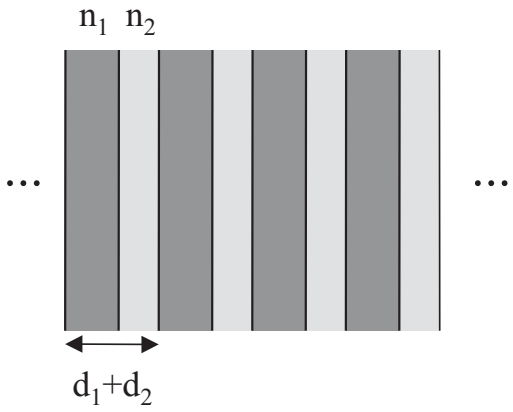

Figure 2.1: An infinite multilayer structure.

PhCs arise solely from these geometric properties.

Now we specify the structure to be periodic. If we consider a 1D PhC along direction z this means

$$\varepsilon(z) = \varepsilon(z + a), \tag{2.12}$$

with a the period. Using this symmetry only, it is possible to show that the modes have the following structure [14]:

$$\mathbf{E}(z) = \mathbf{u}_k(z)e^{-jk_z(\omega)z}, \tag{2.13}$$

with $\mathbf{u}_k(z)$ having the same lattice periodicity, thus

$$\mathbf{u}_k(z + a) = \mathbf{u}_k(z). \tag{2.14}$$

These modes are called *Bloch modes*, and k_z is the Bloch propagation constant. This is the main result from Floquet-Bloch theory.

The dispersion relation $k_z(\omega)$ is no longer the simple straight line as in equation 2.11. We illustrate this by the traditional example of the multilayer stack, see figure 2.1. From this example many general characteristics become apparent.

The results in figure 2.2 are obtained with parameters $n_1 = 1.0$ and $n_2 = 3.0$, with respective widths $d_1 = 0.625a$ and $d_2 = 0.375a$. We notice the appearance of bandgaps. For a frequency in the gap, there is no k_z and thus no available mode. For a frequency outside the gap, and

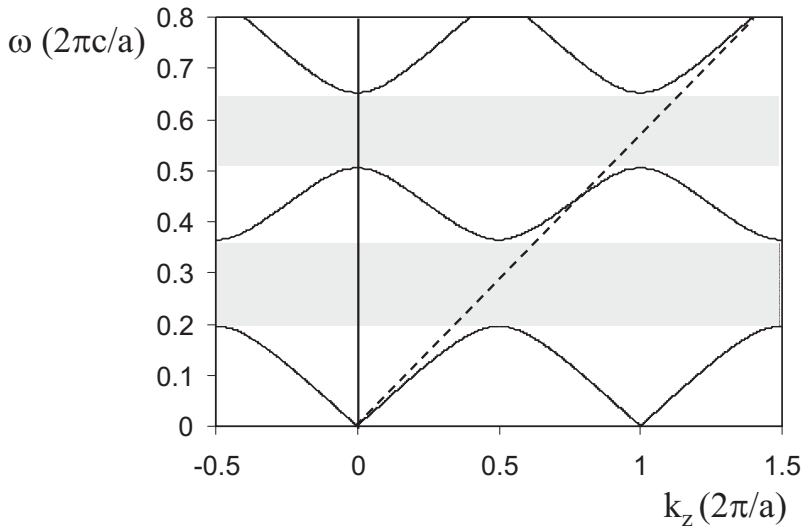

Figure 2.2: Dispersion relation for the multilayer structure. The shaded regions indicate the bandgaps. The dashed line shows the dispersion of a homogeneous medium with index $(d_1 n_1 + d_2 n_2)/a = 1.75$.

thus in a *band*, there is an infinite number of k_z's available. However, because we notice the periodicity of the dispersion relation, and the solutions are equivalent, we can get all necessary information from the interval $k_z = [-\pi/a, \pi/a]$. This is called the first Brillouin zone in the reciprocal or k-space. Furthermore, because of the symmetry between $-k_z$ and k_z, we only have to consider $k_z = [0, \pi/a]$, which is the reduced Brillouin zone. The (ω, k)-depictions are called band diagrams or band structures.

From a physical point of view the origin of the bandgap can be interpreted as a result of constructive interference of Fresnel reflections on the individual interfaces. On the other hand, we can consider the different character of the fields. The mode just below a bandgap has its field concentrated more in the high-n regions of the structure, whereas the mode just above has more energy in the low-n parts. Localizing energy in high index regions tends to lower the frequency. This leads to different frequencies of the two modes and opening of a bandgap.

The gaps become larger as the index contrast increases. Furthermore, from the moment $n_1 \neq n_2$ and there is normal incidence, a gap appears in 1D. This is in contrast with 2D or 3D, where more require-

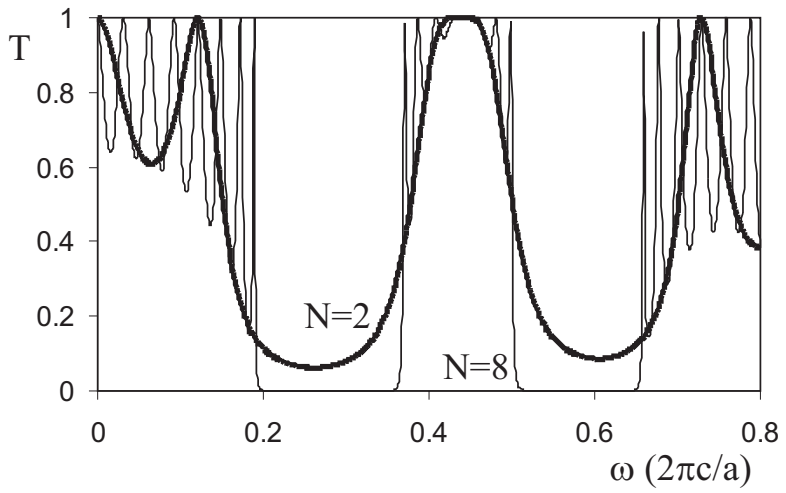

Figure 2.3: Transmission versus frequency for a finite periodic multilayer stack. The number of periods N is indicated in the figure.

ments are needed. In the gap itself, k_z has an imaginary component. It means that the modes are exponentially dampened or evanescent. Because they are not translationally invariant, there is no way to excite them in a perfect infinite crystal. However, they do show up around defects, where they can localize the field, e.g. in resonators.

The connection between finite periodic structures and the infinite Bloch modes is visible if we consider the transmission spectrum of a finite multilayer device. We calculate structures with increasing numbers of periods, the results are shown in figure 2.3. The same parameters as the previous stack are used. We see, already with two periods, a strong reflection in the gap regions. With eight periods the bandgaps are clear, and more peaks appear in the transmission bands.

Next, we turn our attention to 2D PhCs. The geometry we will often encounter is depicted in figure 2.4(a). It consists of a square lattice of squares. We usually take the system of high index rods in air. This is an ideal test-case for many linear and nonlinear systems. It possesses a bandgap (as we will see shortly), and it is very well suited for our simulation methods, both linear and nonlinear. This last statement will

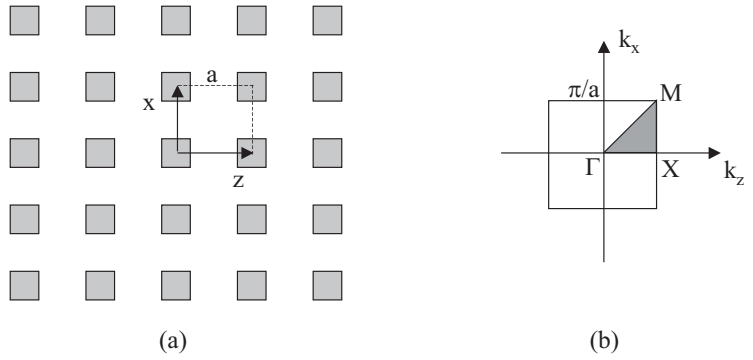

Figure 2.4: (a) Square lattice PhC structure. (b) Corresponding first and reduced (shaded) Brillouin zones.

become more concrete when we describe the mode expansion method in section 2.4.

We consider propagation in the plane of the PhC, so the fields are independent of the perpendicular direction y. In that case Maxwell's equations reduce to two sets, (E_y, H_x, H_z) and (H_y, E_x, E_z), respectively, corresponding to the separate TM- and TE-polarizations. This name convention is used most often in the literature, and we will adopt it here. However, note that in some articles TM and TE are interchanged, because of the difference with fields in conventional and PhC slabs.

In 2D the Bloch modes are described by

$$\mathbf{E}(x,z) = \mathbf{u}_k(x,z)e^{-jk_x(\omega)x}e^{-jk_z(\omega)z} = \mathbf{u}_k(\mathbf{r})e^{-j\mathbf{k}\cdot\mathbf{r}}. \tag{2.15}$$

The structure now includes two independent lattice vectors that describe the periodicity, therefore there are two wavevector components k_x and k_z.

To find the complete band diagram we know that only the reduced Brillouin zone has to be taken into account. The first and reduced Brillouin zones are shown in figure 2.4(b). To depict the possible (ω, k_x, k_z)-combinations, we would have to plot surfaces. To ease interpretation and because the surfaces are monotonic (except in rare cases), we can restrict the band diagram to the edges of the reduced Brillouin zone. The resulting diagram is shown in figure 2.5. We observe the opening of a bandgap between $\omega = 0.348(2\pi c/a)$ and $0.478(2\pi c/a)$, which means no propagation for all directions in the plane. Apparently, the

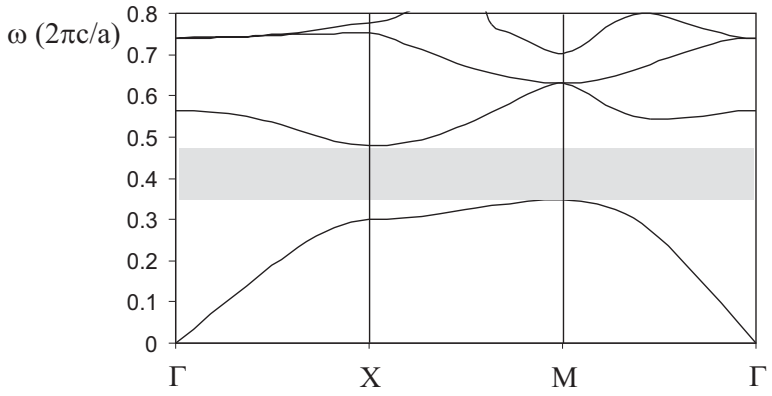

Figure 2.5: Band diagram for TM-polarization of the square lattice PhC structure. The squares have index 3.4 in an air background, and diameter $d = 0.25a$.

gaps for the different directions overlap, because of the high symmetry and index contrast.

The square lattice of rods has a bandgap for TM-polarization only, and not for TE-polarization. In contrast a triangular structure may exhibit a bandgap for both polarizations [14]. For the triangular geometry with airholes it is possible that the gaps overlap, which represents a *complete* or *absolute* bandgap. Many practical applications focus on this structure [10]. A lot of concepts are equivalent however, regardless of the exact geometry.

2.2.2 Photonic crystals with defects

Up until now we have considered the PhC to be infinite and perfect in every direction. However, the number of applications dramatically increases if we include symmetry breaking defects. Moreover, real world structures necessarily exhibit boundaries. The simplest cases are categorized according to their dimensionality. A 1D defect in a 2D or 3D PhC, e.g. removing or changing a row of rods, can create a waveguide. Adjusting one rod, which brings about a point or 0D defect, can lead to a resonator or cavity.

Because the defect disturbs the symmetry, the k-formulation is not always exact anymore, strictly speaking. However, the band diagram still provides a physical interpretation. If the frequency is in the gap, the behaviour of the field a few wavelengths away from the defect will

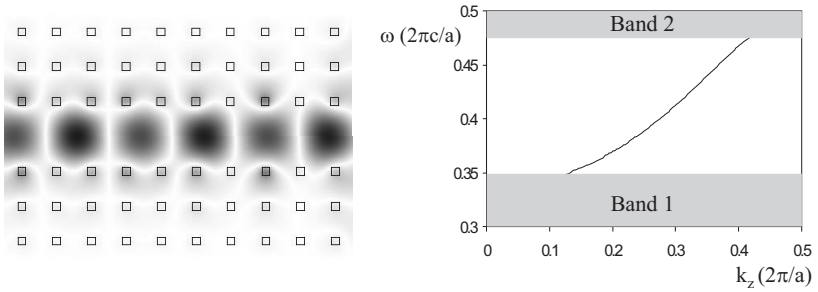

(a) (b)

Figure 2.6: (a) PhC waveguide formed by removing a row of rods. The (real part of the) electric field at $\omega = 0.4(2\pi c/a)$ is superimposed. The same parameters as in fig. 2.5 are used. (b) Diagram of the waveguide band.

exhibit the previous behaviour of only accepting evanescent modes. In this way the field is localized in the direction away from the disruption. Consequently, the surrounding PhC acts as an omnidirectional mirror.

The concrete example of a waveguide is shown in figure 2.6. The structure remains periodic in the z-direction, so we can still plot the k_z band diagram. The line defect creates a mode in the bandgap, as the PhC planes above and below reflect the light.

We remark that this photonic bandgap guiding principle is one of the most striking differences with conventional waveguides. In ordinary guides the field is confined to the core, because it has a higher index than the cladding. This scheme is called guiding by total internal reflection. In contrast, the surrounding medium in the bandgap structure has a higher effective index than the core, highlighting the fundamental distinction.

Point, or 0D defects create highly localized modes. In fact, these are very promising structures in PhCs, compared to other systems, as they combine very small volumes with very strong confinement (to be explained later). Intuitively, such modes are restricted in space, therefore their k-vector is undetermined. Alternatively, in the time picture, because of the high quality PhC mirrors surrounding them, the modes can sustain themselves for a long time, indicating their frequency is well defined. From the previous we conclude that the defect introduces a horizontal line in the band diagram, as illustrated in figure 2.7. Note however, that the symmetry is broken in both directions, so the band di-

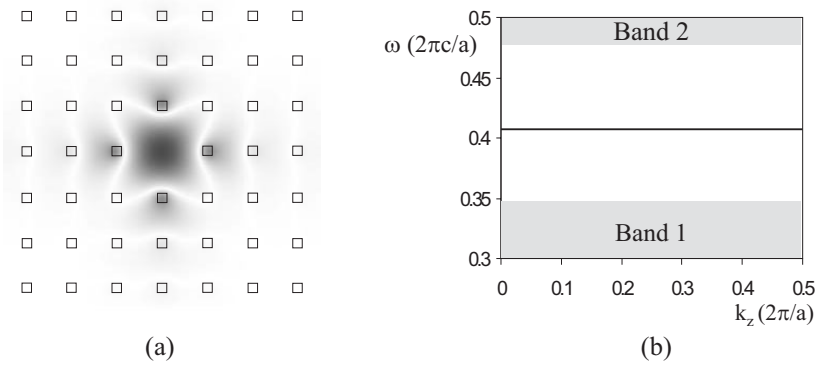

Figure 2.7: (a) PhC monopole defect at $\omega = 0.407(2\pi c/a)$, formed by removing one rod. The same PhC parameters as in fig. 2.5 are used. (b) Defect level in the band diagram.

agram concept is not rigorous anymore. The precise doping frequency is highly tunable throughout the bandgap.

The previous two devices can be used as building blocks for more complex structures, such as bends, splitters, filters, add-drop devices etc. Remark that light can only escape via interfacing waveguides, if the system is surrounded by PhC regions. Indeed, a bend e.g. cannot exhibit radiation losses, they are not allowed in the PhC! The field can only reflect or transmit in the guides. This is in sharp contrast with conventional waveguides. Of course, it is only strictly valid in 3D PhCs. In 2D PhCs out-of-plane losses have to be managed [29].

We will describe a system combining a waveguide and a cavity in section 2.5. There, Coupled Mode Theory, as the name suggests, provides more insight in the coupling between defects.

In conclusion, we have provided a short introduction to periodic structures, their Bloch modes, dispersion and band diagrams. Furthermore, we investigated 2D bandgap PhCs. These form our preferred laboratory. Finally, we added defects to enhance their functionality.

2.3 Nonlinear optics

There is a multitude of possible nonlinear effects in materials, with strongly varying power scales. Nonetheless, many phenomena are described with a straightforward extension to Maxwell's equations, which is the nonlinear polarization $\mathbf{P}_{nl}$. This approach is mainly valid for nonresonant interactions, meaning that absorption and emission are neglected. We will restrict ourselves to this case. For the resonant or dynamical interactions other theories are more appropriate, such as density matrix formalism or rate equations.

A main difference between resonant and nonresonant effects lies in the speed and strength of the response. The nonresonant phenomena are nearly instantaneous, ideal for high-speed information processing, but very weak. The resonant effects are stronger, but prove relatively slow, e.g. because of carrier relaxation times.

First, we review a simple classical picture showing the origin and character of nonlinearity. Then we provide the general form of the nonlinear polarization. Using this expression the second and third order processes are highlighted, with particular attention to second-harmonic generation and the Kerr effect.

As nonlinear optics is an extensive subject, we only give a concise description suited for our purposes. We refer to the literature for more information [30].

2.3.1 Classical picture and general description

In many cases the response of a material to an electromagnetic field is dictated by the movement of the electrons. In dielectric media this means the bound valence electrons will have the most reaction. Under influence of the electric field force $F_{el} = -eE$, the electron is displaced from the equilibrium position. This displacement x induces an electric dipole, so the resulting polarization is

$$P = -Nex, \tag{2.16}$$

with N the number of electrons per unit volume.

The bound electron can be described by a particle in a potential well $V(x)$, so the reaction force to a displacement is $F_r = -\mathrm{d}V/\mathrm{d}x$. The resulting displacement is reached if the forces balance each other

$$F_{el} + F_r = 0. \tag{2.17}$$

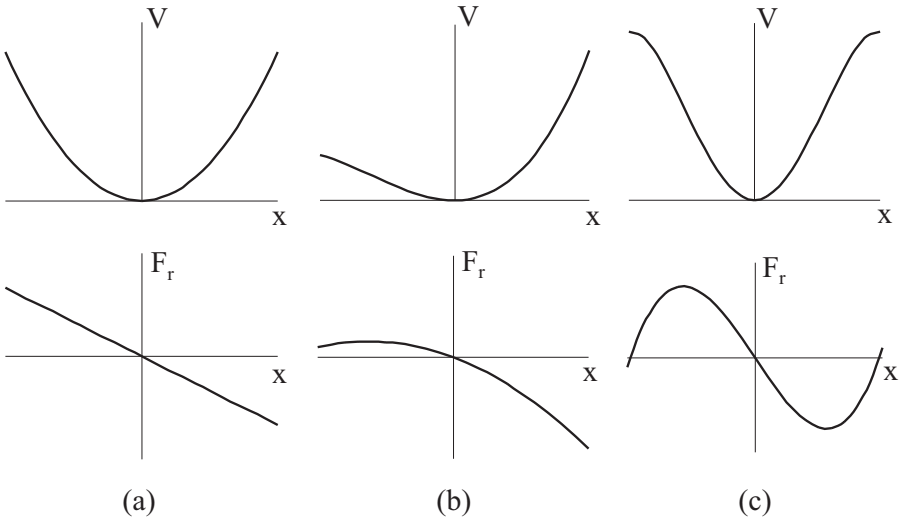

Figure 2.8: Depiction of the potential well V and the reaction force F_r in three cases: (a) Linear, (b) second order and (c) third order.

This means that the form of the potential determines the polarization. In what follows, we examine the dependence of P on the field E, using the shape of the well.

In the lowest order approximation the reaction force is simply proportional to the displacement $F_r = -\alpha x$, which means a parabolic potential $V = \alpha x^2/2$. The situation is depicted in figure 2.8(a). With eq. 2.17 we obtain

$$x = -eE/\alpha. \tag{2.18}$$

Finally, using eq. 2.16 the result is

$$P = \frac{Ne^2}{\alpha} E \equiv \varepsilon_0 \chi^{(1)} E. \tag{2.19}$$

This corresponds to the linear case, already encountered with the constitutive equation 2.5 and $\mathbf{D} = \varepsilon_0 \mathbf{E} + \mathbf{P}$.

If the displacement becomes stronger, the linear approximation is not valid anymore. The adjustment to the potential can be modeled by a higher order term:

$$V = \frac{\alpha x^2}{2} + \frac{\beta x^3}{3}. \tag{2.20}$$

This leads to a force $F_r = -\alpha x - \beta x^2$, so for the displacement

$$-eE - \alpha x - \beta x^2 = 0. \tag{2.21}$$

The potential and force are shown in figure 2.8(b). Remark that this is the simplest model for an asymmetric potential, so that $|F_r(-x)| \neq |F_r(x)|$. Therefore the extra term in V is only possible in noncentrosymmetric crystals, where $V(-x) \neq V(x)$. Instead of solving this nonlinear relation, we use eq. 2.18 as an approximation for x^2. In this way we get

$$x \approx -eE/\alpha - \beta e^2 E^2/\alpha^3. \tag{2.22}$$

For the polarization this means

$$P = \frac{Ne^2}{\alpha}E + \frac{N\beta e^3}{\alpha^3}E^2 \equiv \varepsilon_0\chi^{(1)}E + \varepsilon_0\chi^{(2)}E^2. \tag{2.23}$$

From this simple picture we are led to a nonlinear polarization term, dependent on the square of the electric field. It is responsible for the so-called second order processes.

In centrosymmetric crystals, or with higher powers, the potential obtains a quartic contribution:

$$V = \frac{\alpha x^2}{2} + \frac{\gamma x^4}{4}. \tag{2.24}$$

For this case the curves are presented in figure 2.8(c). If $\gamma < 0$ this is the simplest way to express a saturation of the potential and a dissociation energy. Following the same procedure we obtain

$$P = \frac{Ne^2}{\alpha}E - \frac{N\gamma e^4}{\alpha^4}E^3 \equiv \varepsilon_0\chi^{(1)}E + \varepsilon_0\chi^{(3)}E^3. \tag{2.25}$$

This third power term is the origin of the third order processes. The physical view of the non-parabolic potential well is thus able to provide the character of the nonlinearities.

Now we explain how the Maxwell equations are adjusted in general. From the previous it is clear that the polarization consists of a linear and a nonlinear contribution:

$$\mathbf{P} = \mathbf{P}_{lin} + \mathbf{P}_{nl}, \tag{2.26}$$

so the constitutive equation (see eq. 2.5) changes to:

$$\mathbf{D} = \varepsilon_0 \mathbf{E} + \mathbf{P} = \varepsilon \mathbf{E} + \mathbf{P}_{nl}. \tag{2.27}$$

Consequently, equation 2.8 obtains an extra term:

$$\nabla(\nabla \cdot \mathbf{E}) - \nabla^2 \mathbf{E} = \varepsilon \mu_0 \omega^2 \mathbf{E} + \omega^2 \mu_0 \mathbf{P}_{nl}. \tag{2.28}$$

To use this equation we need an expression for the nonlinear polarization. Its general form in the frequency domain is written as:

$$\mathbf{P}_{nl}(\mathbf{r}, \omega) = \varepsilon_0 \sum_{i=2}^{\infty} \chi^{(i)}(\mathbf{r}, \omega; \omega_1, \ldots, \omega_i) : \mathbf{E}(\mathbf{r}, \omega_1) \ldots \mathbf{E}(\mathbf{r}, \omega_i), \tag{2.29}$$

where

$$\omega = \sum_{k=1}^{i} \omega_k. \tag{2.30}$$

Indeed, because of the products, fields at different frequencies can couple, and new frequencies are generated. Note that ω_k is also allowed to be zero or negative. In the latter case we use $\mathbf{E}(-\omega) = \mathbf{E}^*(\omega)$, as $\mathbf{E}(t)$ is real. In general $\chi^{(i)}$ is a tensor of rank $i + 1$. However, because of (crystal) symmetry many elements will be equal or zero. Moreover, in many cases only one element is exploited or dominant.

Finally, although we assume media with isotropic *linear* properties, this does not imply that the *nonlinear* characteristics are isotropic. Therefore we start from the general expression 2.29. It is clear that this equation comprises many different vectorial interactions. In the next sections we turn our attention to specific effects.

2.3.2 Second order processes

The second order effects are described in scalar notation with:

$$P_{nl,m}(\omega) = \varepsilon_0 \sum_{k,l} \sum_{a,b} \chi^{(2)}_{mkl}(\omega; \omega_a, \omega_b) E_k(\omega_a) E_l(\omega_b), \tag{2.31}$$

where $m, k, l = x, y, z$, and $\omega = \omega_a + \omega_b$. If we specify that the input consists of ω_1 and ω_2 ($\omega_2 > \omega_1$), they can generate contributions to P_{nl}

at the following frequencies:

$$\begin{aligned} 0 &= \omega_1 - \omega_1 = \omega_2 - \omega_2, && (2.32)\\ 2\omega_1 &= \omega_1 + \omega_1, && (2.33)\\ 2\omega_2 &= \omega_2 + \omega_2, && (2.34)\\ &\omega_1 + \omega_2, && (2.35)\\ &\omega_2 - \omega_1. && (2.36) \end{aligned}$$

The first is associated with optical rectification. The others are obviously called second-harmonic, sum and difference frequency generation.

We are mainly concerned with second-harmonic generation. In that case the fundamental frequency ω gives rise to the second harmonic 2ω. The products appearing in equation 2.31 are conveniently ordered in a matrix:

$$\begin{bmatrix} P_{nl,x}(2\omega) \\ P_{nl,y}(2\omega) \\ P_{nl,z}(2\omega) \end{bmatrix} = \varepsilon_0 \begin{bmatrix} d_{11} & \cdots & d_{16} \\ d_{21} & \cdots & d_{26} \\ d_{31} & \cdots & d_{36} \end{bmatrix} \begin{bmatrix} E_x^2(\omega) \\ E_y^2(\omega) \\ E_z^2(\omega) \\ 2E_z(\omega)E_y(\omega) \\ 2E_z(\omega)E_x(\omega) \\ 2E_x(\omega)E_y(\omega) \end{bmatrix}. \qquad (2.37)$$

Because of the aforementioned symmetry, most applications retain one or two product terms. Therefore, we can clarify specific SHG aspects by studying the scalar plane-wave case. Consider the fundamental and second harmonic fields as waves propagating in the z-direction, with one component along x.

$$\begin{aligned} E_\omega &= A_\omega e^{-jk_\omega z}, && (2.38)\\ E_{2\omega} &= A_{2\omega}(z)e^{-jk_{2\omega}z}. && (2.39) \end{aligned}$$

The amplitude of the fundamental is supposed to be constant. This is the undepleted pump approximation, where the contribution $P_{nl}(\omega)$ is ignored. This is more or less valid up until about 10% conversion. To model SHG the amplitude of the second harmonic is z-dependent. Equation 2.28 simplifies to a perturbed Helmholtz equation

$$\frac{\mathrm{d}^2 E_{2\omega}}{\mathrm{d}z^2} + k_{2\omega}^2 E_{2\omega} = -(2\omega)^2 \mu_0 P_{nl}, \qquad (2.40)$$

where we assume

$$P_{nl} = \varepsilon_0 d_{nl} E_\omega^2, \tag{2.41}$$

with d_{nl} the nonlinear coefficient. Input of equations 2.38 and 2.39 in 2.40 leads to a second order differential equation. We ignore $\frac{\mathrm{d}^2 A_{2\omega}}{\mathrm{d}z^2}$, which is called the slowly varying envelope approximation, and obtain:

$$\frac{\mathrm{d}A_{2\omega}}{\mathrm{d}z} = -\frac{2jk_0^2}{k_{2\omega}} d_{nl} A_\omega^2 e^{j\Delta k z}, \tag{2.42}$$

with $k_0 = \omega/c$ and

$$\Delta k = k_{2\omega} - 2k_\omega. \tag{2.43}$$

We can analytically solve this equation. After a length L, and starting with $A_{2\omega}(0) = 0$, we get

$$A_{2\omega}(L) = -\frac{2jk_0^2}{k_{2\omega}} d_{nl} A_\omega^2 e^{j\Delta k L/2} \frac{\sin(\Delta k L/2)}{\Delta k/2}. \tag{2.44}$$

Finally, for the intensity we arrive at

$$|A_{2\omega}(L)|^2 = \frac{4k_0^4}{k_{2\omega}^2} d_{nl}^2 |A_\omega|^4 \left[\frac{\sin(\Delta k L/2)}{\Delta k/2}\right]^2. \tag{2.45}$$

Here, the important factor is the one with Δk, which indicates SHG is a coherent process. If $\Delta k = 0$, which means

$$k_{2\omega} = 2k_\omega \quad \text{and} \quad n_{2\omega} = n_\omega, \tag{2.46}$$

the interaction is phase-matched. Then, the conversion is optimal and the efficiency scales as L^2, see figure 2.9(a). Excluding, of course, corrections because of pump depletion.

On the other hand, if $\Delta k \neq 0$, the second harmonic intensity oscillates in function of L. It reaches a maximum after a coherence length

$$L_c = \frac{\pi}{|\Delta k|} = \frac{\lambda_0}{4|n_{2\omega} - n_\omega|}. \tag{2.47}$$

An example is shown in figure 2.9(c). Intuitively, the decline is the result of destructive interference between second harmonic fields generated at $z = 0$ and $z = L_c$, respectively.

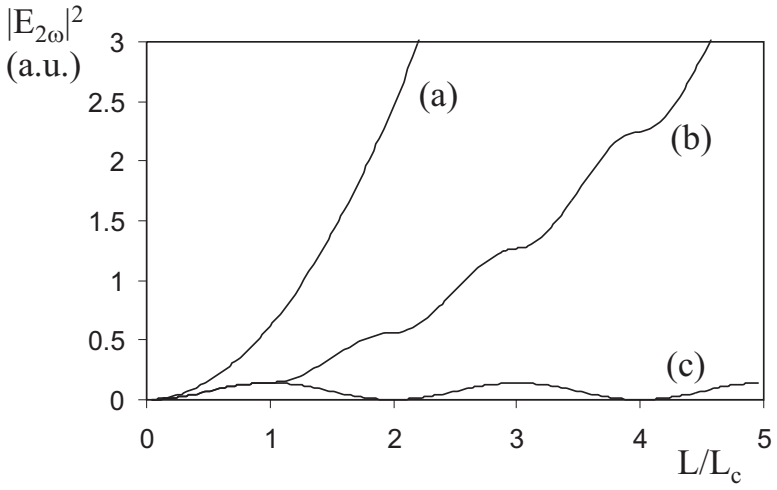

Figure 2.9: SHG efficiency in the case of (a) perfect matching, (b) quasi phase matching and (c) mismatch.

In general, because of chromatic dispersion, materials are not phase-matched. There are different ways to compensate for this mismatch. The classical approach is to use birefringent crystals and different polarizations. Where the index ellipsoids of fundamental and second harmonic cross, they are matched. However, because the directions of power flow can differ for both beams, the efficiency diminishes after a certain length, this is called the spatial walk-off effect. Furthermore, only a small set of materials and directions fit into this scheme.

Another method is called quasi-phase matching. Here the linear index or the nonlinear coefficient is modulated. We can understand both approaches. From the section on PhCs we know that fields in periodic media are described as Bloch modes, and their propagation constants differ from the homogeneous waves. Therefore, one can tailor the dispersion relation, so that the fundamental and the second harmonic have the same Bloch propagation constant.

On the other hand, if the nonlinear coefficient d_{nl} is periodically modulated, we can present it as a Fourier series in equation 2.42. If there is a term that compensates Δk, we obtain more efficient conversion. This is e.g. achieved if the sign of d_{nl} is changed after every L_c. An example of such a generation curve is shown in figure 2.9(b).

In chapter 6 we will develop a modeling tool for SHG in 2D structures. We have seen in section 2.2 that the field in 2D has TM- or TE-polarization. For TM-polarization the first term in equation 2.28 ($\nabla(\nabla\cdot\mathbf{E})$) vanishes identically, as there is one y-invariant $\mathbf{E}$-component along the out-of-plane y-direction, so $\nabla\cdot\mathbf{E}=0$.

For TE-polarization this term does not vanish always, although in many cases it is small, especially when the slowly varying envelope approximation is valid [31]. Therefore, we will ignore this term, and start in chapter 6 from the perturbed Helmholtz equation:

$$\nabla^2\mathbf{E}+\varepsilon\mu_0\omega^2\mathbf{E}=-\omega^2\mu_0\mathbf{P}_{nl}. \tag{2.48}$$

2.3.3 Third order processes

The potential well picture showed us that the polarization depends on the cube of the field, for third order effects. In general this means

$$P_{nl,n}(\omega)=\varepsilon_0\sum_{k,l,m}\sum_{a,b,c}\chi^{(3)}_{nklm}(\omega;\omega_a,\omega_b,\omega_c)E_k(\omega_a)E_l(\omega_b)E_m(\omega_c), \tag{2.49}$$

where $n,k,l,m=x,y,z$, and $\omega=\omega_a+\omega_b+\omega_c$. Multiple frequencies can interact, leading to e.g. third harmonic generation or four-wave mixing. However, we concern ourselves with the Kerr effect, where the nonlinear influence of a frequency ω upon itself is examined. Furthermore, we assume that there is no mixing between different polarizations. In that case, the contributions have the form $\chi^{(3)}(\omega;\omega,-\omega,\omega)$, and globally

$$\mathbf{P}_{nl}(\omega)=\varepsilon_0\chi^{(3)}|\mathbf{E}(\omega)|^2\mathbf{E}(\omega). \tag{2.50}$$

For TM-polarization we already mentioned at the end of the previous subsection that we can use the Helmholtz equation, as $\nabla\cdot\mathbf{E}=0$. For TE-polarization we have to make a preliminary remark about the Kerr modeling method of chapter 3. There we will use a grid with small sections of constant (nonlinearly adjusted) ε_{nl}. So in the limit of very small sections we have from equation 2.3 that $\nabla\cdot\varepsilon_{nl}\mathbf{E}=\varepsilon_{nl}\nabla\cdot\mathbf{E}\rightarrow 0$.

Thus for both polarizations we can use the Helmholtz equation with

$$\nabla^2\mathbf{E}+\frac{\omega^2}{c^2}(\varepsilon_r+\chi^{(3)}|\mathbf{E}|^2)\mathbf{E}=0. \tag{2.51}$$

This means the permittivity obtains an intensity dependent term, or equivalently, for the refractive index:

$$n=\sqrt{\varepsilon_{nl}}=\sqrt{n_{lin}^2+\chi^{(3)}|\mathbf{E}|^2}\approx n_{lin}+n_2|\mathbf{E}|^2, \tag{2.52}$$

with $n_2 = \chi^{(3)}/(2n_{lin})$. Because of the appearance of the modulus, the process is regarded as non-coherent, in contrast with SHG. The Kerr effect, which is the most studied, generates phenomena such as self-phase modulation, self-focusing, temporal and spatial solitons etc. We will employ it in PhC cavities and for soliton formation in the bandgap.

2.3.4 Conclusions

The previous section contains a short summary of the nonlinear polarization formalism. We restricted ourselves mainly to SHG and the Kerr effect. For SHG the importance of phase matching was proven with a plane-wave example. Note that we will extend this single-mode analysis in chapter 6, therefore we went into some detail. The Kerr effect is described with an intensity dependent refractive index. This view will guide our modeling method.

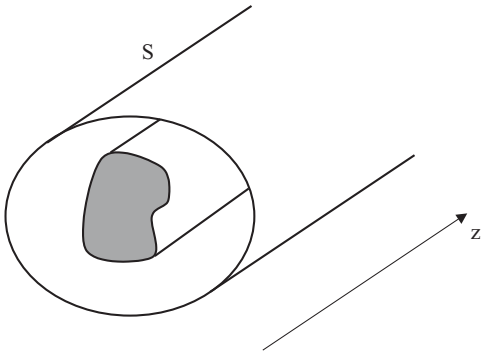

Figure 2.10: Invariant structure along z. The surface S indicates the boundary of the computational domain.

2.4 Eigenmode expansion method

In this section we provide an overview of the linear mode expansion framework. We build upon this knowledge for the Kerr and the second harmonic nonlinear extensions, developed in chapters 3 and 6, respectively. The global eigenmode picture provides insight in the kinds of structures that are especially suited for the method. The more detailed expressions outline the concrete algorithms.

The basis of mode expansion is the consideration of a structure that is invariant along a certain direction z, as in figure 2.10. In this case ε and μ are independent of z. In theory, the structure may be infinite in the perpendicular direction(s). In practice, however, a boundary surface will always be introduced. In a general invariant structure the sourceless Maxwell equations have solutions of the form [32]:

$$\mathbf{E}(\mathbf{r}) = \mathbf{E}(\mathbf{r}_t)e^{-j\beta z}, \tag{2.53}$$

$$\mathbf{H}(\mathbf{r}) = \mathbf{H}(\mathbf{r}_t)e^{-j\beta z}, \tag{2.54}$$

with $\mathbf{r}_t$ the tangential component of $\mathbf{r}$, and β the mode propagation constant. Note the difference with *Bloch* modes, see equation 2.13. Here the only z-dependence is the exponential factor, whereas the Bloch modes possess an extra periodic modulation.

By inserting eq. 2.53 in the Helmholtz equation 2.9, which is valid for (transversally) piecewise constant geometries, we obtain an eigenvalue problem:

$$\left(\nabla_t^2 + \omega^2\mu\varepsilon\right)\mathbf{E} = \beta^2\mathbf{E}, \tag{2.55}$$

hence the term *eigenmode* expansion. ∇_t^2 is the transverse Laplacian operator. The expression for the $\mathbf{H}$-field is analogous.

If β has a real component the mode is propagative. If β has an imaginary part the mode amplitude is exponentially decaying (evanescent) or increasing. In analogy with Bloch modes in perfect PhCs, the modes with real β can persist in the absence of any sources, while maintaining their general shape. On the other hand, the evanescent modes are excited at discontinuities between different structures, and are negligible a few (effective) wavelengths away from the interface. This is reminiscent of the bandgap modes around PhC defects.

Using adequate boundary conditions we obtain a set of eigenmodes with the interesting property of *completeness* [32]. This means the forward propagating field in the structure, in response to an arbitrary excitation, can be written as a superposition of the modes:

$$\mathbf{E}(\mathbf{r}) = \sum_i A_i \mathbf{E}_i(\mathbf{r}_t) e^{-j\beta_i z}, \tag{2.56}$$

$$\mathbf{H}(\mathbf{r}) = \sum_i A_i \mathbf{H}_i(\mathbf{r}_t) e^{-j\beta_i z}, \tag{2.57}$$

with A_i complex mode amplitudes. In this way, with the knowledge of the modal field profiles and propagation constants, the field throughout the invariant structure is reduced to a vector of mode amplitudes:

$$(\mathbf{E}(\mathbf{r}), \mathbf{H}(\mathbf{r})) \leftrightarrow \mathbf{A} = [A_i]. \tag{2.58}$$

The number of modes is infinite. However, for calculations the series has to be truncated to a finite number N. The results are still relevant, because the method converges as N increases. Indeed, the contributions of strongly evanescent modes become negligible.

From the Lorentz reciprocity theorem one can show that the modes are orthogonal. Furthermore, we can always normalize the profiles, and in our formalism the important orthonormality relation is expressed as:

$$\int_t (\mathbf{E}_i \times \mathbf{H}_j) \cdot \mathbf{u}_z \mathrm{d}l = \delta_{ij}, \tag{2.59}$$

with $\mathbf{u}_z$ the unit vector along z, δ_{ij} the Kronecker delta and integration along the transverse direction. We note this integral as $\langle E_i | H_j \rangle$, where we understand that only the transverse component is needed.

If an interface between two structures occurs, as in figure 2.11(a), an incident mode can scatter. On the reflection side there are fields prop-

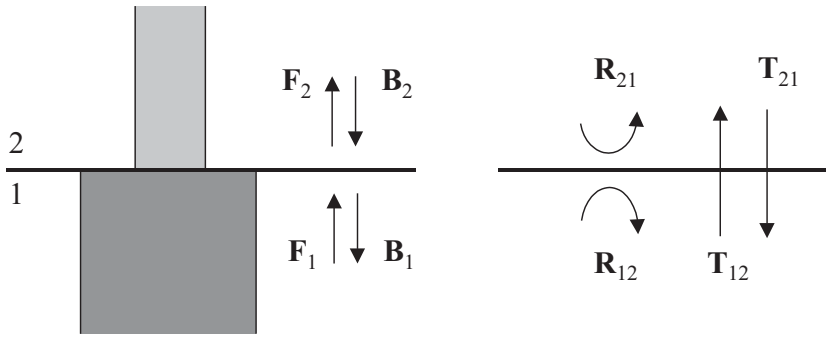

Figure 2.11: (a) Scattering from an interface, the amplitude vectors are shown. (b) Corresponding reflection and transmission matrices.

agating in both directions. These bidirectional situations are also modeled by mode expansion, if we include backward propagating modes in equations 2.56 and 2.57. By splitting Maxwell's equations in transverse and longitudinal components, it is possible to show that a mode with components

$$(\mathbf{E}_{i,t}, \mathbf{E}_{i,z}, \mathbf{H}_{i,t}, \mathbf{H}_{i,z}, \beta_i) \tag{2.60}$$

has a corresponding counterpropagating mode with

$$(\mathbf{E}_{i,t}, -\mathbf{E}_{i,z}, -\mathbf{H}_{i,t}, \mathbf{H}_{i,z}, -\beta_i)\,. \tag{2.61}$$

To describe scattering from an interface between two sections the well-known mode-matching technique is used. This technique imposes continuity of the tangential total field components to deduce reflection and transmission matrices, see figure 2.11(b). The matrix elements depend on overlap integrals of the modes in the different sections. The final result is

$$\begin{bmatrix} \mathbf{F}_2 \\ \mathbf{B}_1 \end{bmatrix} = \begin{bmatrix} \mathbf{T}_{12} & \mathbf{R}_{21} \\ \mathbf{R}_{12} & \mathbf{T}_{21} \end{bmatrix} \cdot \begin{bmatrix} \mathbf{F}_1 \\ \mathbf{B}_2 \end{bmatrix}, \tag{2.62}$$

with forward and backward vectors indicated in figure 2.11(a).

The propagation in a single layer without interfaces is simply handled via the propagation constants, see figure 2.12:

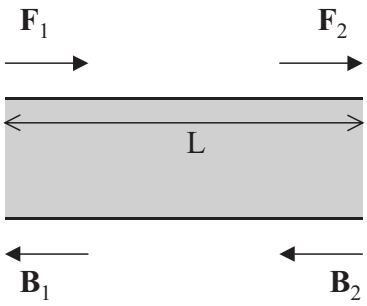

Figure 2.12: Propagation through a layer.

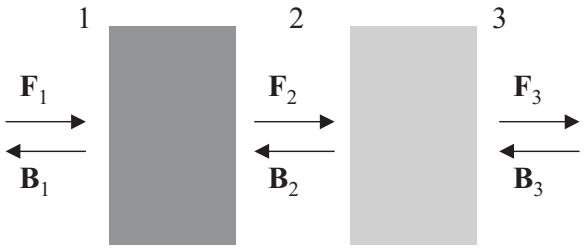

Figure 2.13: Combining two scatterers.

$$\begin{bmatrix} \mathbf{F}_2 \\ \mathbf{B}_1 \end{bmatrix} = \begin{bmatrix} \mathbf{diag}(e^{-j\beta_i L}) & 0 \\ 0 & \mathbf{diag}(e^{-j\beta_i L}) \end{bmatrix} \cdot \begin{bmatrix} \mathbf{F}_1 \\ \mathbf{B}_2 \end{bmatrix}, \tag{2.63}$$

where **diag** indicates a diagonal matrix and L is the layer length.

The objective is to model structures consisting of many different layers and interfaces. Therefore we have to combine the interface and propagation matrices, eqns. 2.62 and 2.63. There are many ways to do this, but the so-called S-scheme, based on scattering operators, is numerically the most stable for our purposes. We note that both interface and propagation relations are scattering matrices. Therefore, if we can combine two scattering matrices, we can construct the matrix for an arbitrary structure.

The reference points are indicated in figure 2.13. Both the left and the right part are described by scatter matrices, so:

$$\begin{bmatrix} \mathbf{F}_2 \\ \mathbf{B}_1 \end{bmatrix} = \begin{bmatrix} \mathbf{T}_{12} & \mathbf{R}_{21} \\ \mathbf{R}_{12} & \mathbf{T}_{21} \end{bmatrix} \cdot \begin{bmatrix} \mathbf{F}_1 \\ \mathbf{B}_2 \end{bmatrix}, \tag{2.64}$$

$$\begin{bmatrix} \mathbf{F}_3 \\ \mathbf{B}_2 \end{bmatrix} = \begin{bmatrix} \mathbf{T}_{23} & \mathbf{R}_{32} \\ \mathbf{R}_{23} & \mathbf{T}_{32} \end{bmatrix} \cdot \begin{bmatrix} \mathbf{F}_2 \\ \mathbf{B}_3 \end{bmatrix}. \tag{2.65}$$

We eliminate $\mathbf{F}_2$ and $\mathbf{B}_2$ from the above equations and, after some algebra, we obtain

$$\begin{bmatrix} \mathbf{F}_3 \\ \mathbf{B}_1 \end{bmatrix} = \begin{bmatrix} \mathbf{T}_{13} & \mathbf{R}_{31} \\ \mathbf{R}_{13} & \mathbf{T}_{31} \end{bmatrix} \cdot \begin{bmatrix} \mathbf{F}_1 \\ \mathbf{B}_3 \end{bmatrix}, \tag{2.66}$$

where:

$$\begin{aligned} \mathbf{T}_{13} &= \mathbf{T}_{23} \cdot (\mathbf{I} - \mathbf{R}_{21} \cdot \mathbf{R}_{23})^{-1} \cdot \mathbf{T}_{12}, \\ \mathbf{R}_{31} &= \mathbf{T}_{23} \cdot (\mathbf{I} - \mathbf{R}_{21} \cdot \mathbf{R}_{23})^{-1} \cdot \mathbf{R}_{21} \cdot \mathbf{T}_{32} + \mathbf{R}_{32}, \\ \mathbf{R}_{13} &= \mathbf{T}_{21} \cdot (\mathbf{I} - \mathbf{R}_{23} \cdot \mathbf{R}_{21})^{-1} \cdot \mathbf{R}_{23} \cdot \mathbf{T}_{12} + \mathbf{R}_{12}, \\ \mathbf{T}_{31} &= \mathbf{T}_{21} \cdot (\mathbf{I} - \mathbf{R}_{23} \cdot \mathbf{R}_{21})^{-1} \cdot \mathbf{T}_{32}, \end{aligned} \tag{2.67}$$

with $\mathbf{I}$ the identity matrix.

Another scheme, that is popular in single-mode methods, is the transfer matrix scheme. However, in that scheme transfer matrices have to be inverted. Intuitively, it is clear that the transmission coefficients of evanescent modes will tend to zero. Therefore, the transmission matrix can become close to singular. For this reason the scattering scheme is more stable, as it evades these particular inversions. However, the price of robustness is that more matrix manipulations have to be performed [32].

We remark that because of all the matrix calculations involved, the simulation times of eigenmode methods scales as N^3, with N the number of modes used. Therefore, it is obvious that every method to limit the number of modes is welcome. The exploitation of symmetry e.g. may lead to a reduction of N. A symmetric structure excited with an even source, can completely be described by even modes. In this case, only these modes are necessary, which speeds up the calculations. Another method is the use of perfectly matched layer (PML) boundary conditions [32]. If modes are calculated with PML, the parasitic reflections on the transverse boundaries are reduced. In this way, the edges can be placed closer to the structure, so less modes are needed to accurately describe the fields.

The mode expansion method is especially suited for longitudinally periodic structures. Indeed, a lot of data can be reused in repeating sections, such as propagation constants, mode profiles and scattering matrices. Because of this, calculation times scale logarithmically with the number of periods, instead of linearly. This is one of the reasons that

prompted us to consider nonlinear extensions, suitable for 2D photonic crystals.

The matrix formalism we explained here is independent of the exact nature of the transverse geometry. Possibilities are e.g. cylindrical structures or 2D planar devices. The procedure of calculating the modes is determined by the geometry. We will not describe these techniques here, but refer to [27] as they do not change in our nonlinear extensions. In this work we restrict ourselves to planar 2D devices. However, it is clear that we may also apply the algorithms to other kinds of structures.

In this section we provided an outline of the linear eigenmode expansion method. We are now aware how the method works, and why it is especially suited for periodic devices. In the Kerr extension of chapter 3 we adopt a more passive use of eigenmode expansion, as we perform a series of linear calculations. In contrast, the extension for second-harmonic generation in chapter 6 adjusts the matrix formalism, therefore we went into some detail.

2.5 Coupled Mode Theory

We introduce Coupled Mode Theory or CMT in this section, because we will encounter devices that are very well described by this framework. It is especially suited for the interaction between sharp resonant structures and waveguide modes. We remark that the approach is strictly valid when the width of the resonance is much smaller than the resonance frequency. In that case waveguide dispersion can safely be ignored [33].

Linear CMT has been applied to many problems, such as add-drop filters [33], Fano resonances [34] and demultiplexers [35]. We shall introduce the equations and the constraints that the coefficients have to satisfy.

Furthermore, the theory has been extended to incorporate Kerr nonlinear resonators [19]. The nonlinear theory has been applied to a resonator in the waveguide [19] and next to the waveguide [36], an add-drop system [37] and a cross-waveguide transistor [38]. We will apply CMT to series of resonators in chapter 4, in addition to a variety of examples.

2.5.1 Linear theory

We restrict ourselves to a system of one resonator, coupled with n ports, as in figure 2.14, and closely follow the treatment in [34]. In our case the ports represent waveguides, and both the resonator and the guides are single-mode. Multiple resonators or resonator modes can also be modeled, by incorporating their interaction [33, 38], or by simply connecting them with waveguides, as in chapter 4.

The equations of temporal CMT are written as:

$$\frac{\mathrm{d}a}{\mathrm{d}t} = \left(j\omega_r - \frac{1}{\tau}\right) a + \left(\langle\kappa|^*\right) |s_+\rangle, \tag{2.68}$$

$$|s_-\rangle = C|s_+\rangle + a|d\rangle. \tag{2.69}$$

Here a is the complex resonance mode amplitude, with ω_r the center resonance frequency and τ the lifetime of the resonance. $|s_+\rangle$ and $|s_-\rangle$ represent the incoming and outgoing waves, respectively. The coupling between the input and the resonator is determined by $|\kappa\rangle$, the coupling from resonator to output by $|d\rangle$.

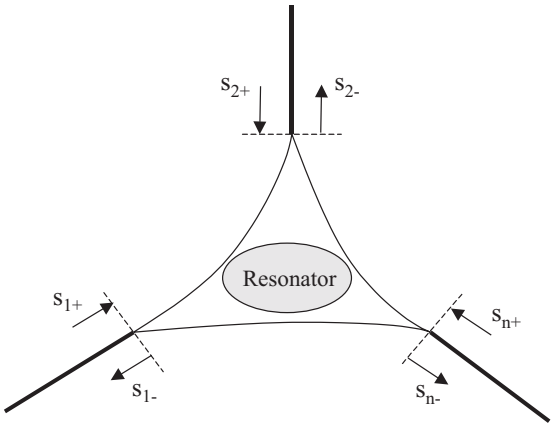

Figure 2.14: Schematic of coupling between a resonator and multiple ports. The dashed lines indicate reference planes, the thin lines indicate direct pathways.

Note the use of Dirac's bracket notation, so a ket $|v\rangle$ can be represented by the column vector

$$|v\rangle = \begin{bmatrix} v_1 \\ \vdots \\ v_n \end{bmatrix}, \tag{2.70}$$

and a bra $\langle v|$ with the row vector

$$\langle v| = \begin{bmatrix} v_1^* & \cdots & v_n^* \end{bmatrix}, \tag{2.71}$$

with * indicating complex conjugate. The matrix C is an arbitrary scattering matrix, that describes the direct coupling between input and output ports, without intervention of the resonance.

The quantities are normalized, so that $|a|^2$ is equal to the energy in the resonator mode. Furthermore, the forward (backward) propagating power in port i corresponds to $|s_{i+}|^2$ ($|s_{i-}|^2$). Therefore, energy conservation in the lossless case means

$$\frac{\mathrm{d}|a|^2}{\mathrm{d}t} = \langle s_+|s_+\rangle - \langle s_-|s_-\rangle. \tag{2.72}$$

We mainly work in the frequency domain. In that case the quantities oscillate with $e^{j\omega t}$, so equation 2.68 becomes

$$a = \frac{(\langle \kappa|^*)|s_+\rangle}{j(\omega - \omega_r) + 1/\tau}. \tag{2.73}$$

This highlights the Lorentzian, single pole character of the resonator. The 'confinement' or 'narrowness' of such a resonance is quantified by the quality factor Q

$$Q = \frac{\omega_r \tau}{2}. \tag{2.74}$$

In the frequency domain it is proportional to the resonance frequency divided by the bandwidth. In analogy, in the time domain it relates to the lifetime divided by the resonance period. Note that in the frequency picture energy conservation simplifies to

$$\langle s_+|s_+\rangle = \langle s_-|s_-\rangle. \tag{2.75}$$

The parameters $|d\rangle$ and $|\kappa\rangle$ are not independent or arbitrary. Using energy conservation and time reversal symmetry one can show that the following conditions hold [34]:

$$|\kappa\rangle = |d\rangle, \tag{2.76}$$
$$\langle d|d\rangle = 2/\tau, \tag{2.77}$$
$$C|d\rangle^* = -|d\rangle. \tag{2.78}$$

Equation 2.76 indicates the symmetry between input and output coupling. Equation 2.77 shows that the total decay rate is determined by the sum of the partial decays, as expected. The third condition means that the coupling constants are related to the direct scattering matrix C. Using eq. 2.76 the global process can be written with a scatter matrix S:

$$|s_-\rangle = S|s_+\rangle = \left[C + \frac{|d\rangle\langle d|^*}{j(\omega - \omega_r) + 1/\tau}\right]|s_+\rangle. \tag{2.79}$$

For lossless and reciprocal structures the scattering matrices will be unitary and symmetric, respectively.

We apply the previous theory to a concrete PhC example, shown in figure 2.15. This is a 2-port structure with the resonator evanescently coupled to the waveguide that connects the ports. Note that we choose two reference planes where the input and output amplitudes are defined. Their positions are the left and right boundary of figure 2.15. The direct scattering matrix is simple here:

$$C = \begin{bmatrix} e^{-j\beta L} & 0 \\ 0 & e^{-j\beta L} \end{bmatrix}, \tag{2.80}$$

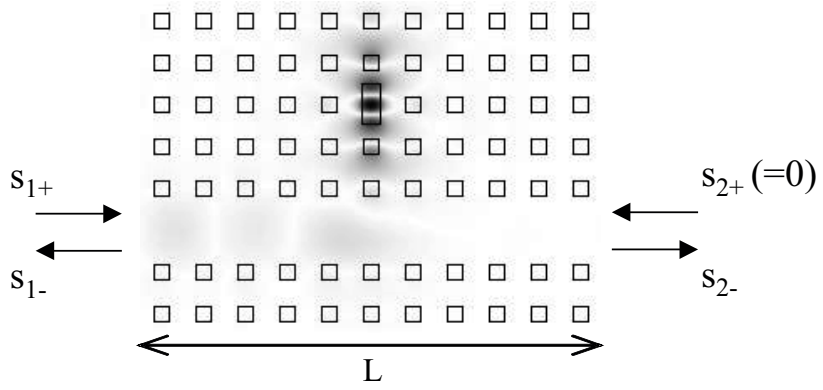

Figure 2.15: PhC 2-port resonator structure. The field on resonance is superimposed.

with β the propagation constant and L the length of the waveguide between the reference planes. Because the structure has a transversal symmetry plane through the center of the resonator, the diagonal elements of the scattering matrices S and C (individually) have to be equal. With equation 2.79 this leads to $d_1^2 = d_2^2$. Combining the previous with equation 2.77 we obtain

$$|d_1| = |d_2| = 1/\sqrt{\tau}. \tag{2.81}$$

The phases are found using equation 2.78. We obtain two possibilities:

$$\pm j\frac{e^{-j\beta L/2}}{\sqrt{\tau}}. \tag{2.82}$$

If the mode has a central nodal plane, we have to choose $d_1 = -d_2$. Otherwise, if the mode is symmetric around the mirror plane, we take $d_1 = d_2$.

The simulated transmission $T = |s_{2-}|^2/|s_{1+}|^2$, with input from one side, is shown in figure 2.16 and agrees well with the CMT-curve. The PhC consists of rods with diameter $0.4a$ and index 3.5 in air. The resonator is formed by a larger rectangular defect with sides $0.5a$ and $0.24a$. A single line of missing rods creates the waveguide, with $\beta = 0.266(2\pi/a)$ around $\omega_r = 0.36688(2\pi c/a)$. We use TM-polarization. The resonance frequency ω_r and the lifetime τ are fitted, with $\tau = 19476a/(2\pi c)$, resulting in a quality factor $Q = 3573$.

The operation of the device is as follows. Far from resonance transmission is unity, as the waveguide propagates all the light from left

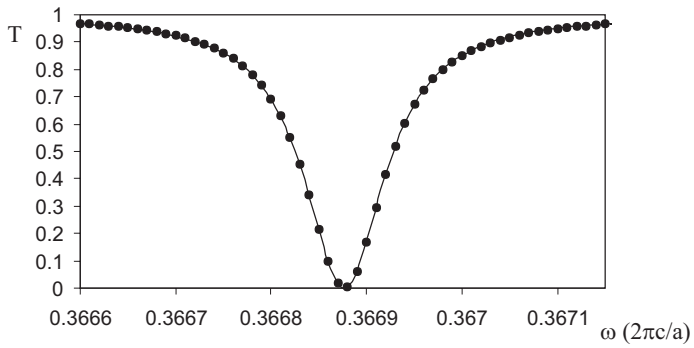

Figure 2.16: Transmission of the PhC structure with CMT (solid line) and rigorous simulations (dots).

to right. On resonance the resonator is strongly excited. The field propagating to the right interferes destructively with the field leaking from the resonator. Therefore, the field is reflected to the input, see figure 2.15.

2.5.2 Nonlinear theory

Here we describe how CMT accommodates Kerr nonlinear resonators. This theory is presented in [19]. Many nonlinear phenomena are in first order modeled by a tuning of parameters such as propagation constants, coupling constants or resonance frequencies. In that case the mode profiles themselves remain relatively undisturbed. This corresponds to the weak nature of (instantaneous) nonlinear effects.

In the resonator case the nonlinear effect is accurately represented by a resonance frequency shift $\delta\omega$. With first order perturbation theory one proves that [19]

$$\delta\omega = -\frac{|a|^2}{\tau^2 P_0}. \tag{2.83}$$

Here P_0 is a 'characteristic nonlinear power' and is determined by

$$P_0 = \frac{1}{\kappa Q^2 n_2 (\omega_r/c)^{d-1}}. \tag{2.84}$$

d is the dimensionality of the system, so in our case $d = 2$. The Kerr coefficient is n_2, defined so $n_2'|E|^2 = nc\varepsilon_0 n_2|E|^2$ is the nonlinear index change of the medium with index n. The parameter κ is called

a 'nonlinear feedback parameter'. It quantifies the degree of spatial confinement of the mode in the nonlinear material. Because of the robustness of the mode profile, it is a weak function of all the other parameters, such as power or operating frequency. The value of κ (and of other coupling constants such as τ) can be obtained via a surface integral [19]. However, it is much easier to obtain the exact P_0 (and thus κ) via a fitting to the transfer function. When this parameter is determined, the entire nonlinear behaviour can be calculated. Moreover, circuits of resonators and waveguides are easily managed, as we will show in chapter 4.

We notice that P_0 is defined by two (independent) parameters: Q and κ. This illustrates the importance of low loss and strong confinement, respectively. Indeed, this combination is achievable in PhC resonators, hence their strong potential for all-optical switching.

Equation 2.83 indicates a resonance frequency shift from ω_r to $\omega_r + \delta\omega$. For positive nonlinearities $n_2 > 0$ the resonance frequency decreases. For negative n_2 the resonance shifts to higher frequencies. If we excite with a fixed frequency ω, the operation of the nonlinear resonator is interpreted as a shift of the spectrum, which is sampled at ω.

This is demonstrated with the example of the previous resonator structure. We consider the larger resonator rod to be nonlinear, with $n_2' = 2 \times 10^{-19}\mathrm{m}^2/\mathrm{V}^2$. We operate at $\omega = 0.36673(2\pi c/a)$, thus with detuning $\delta \equiv \tau(\omega - \omega_r) = -2.857$. The nonlinearity is positive and ω is smaller than ω_r, so we expect that the resonance frequency sweeps through the operating frequency, if we increase the power. This is indeed shown by the input/output power curve in figure 2.17. How the rigorous nonlinear simulations are carried out, is the subject of chapter 3. The CMT curve in this figure is deduced by the modification of equation 2.68 and the first equation from set 2.69:

$$a = \frac{d_1 s_{1+}}{j(\omega - \omega_r - \delta\omega) + 1/\tau}, \tag{2.85}$$

$$s_{1-} = a d_1. \tag{2.86}$$

Together with equation 2.81 and energy conservation the transmission becomes [36]:

$$T = \frac{P_{trans}}{P_{in}} = \frac{(P_{ref}/P_0 + \delta)^2}{1 + (P_{ref}/P_0 + \delta)^2}, \tag{2.87}$$

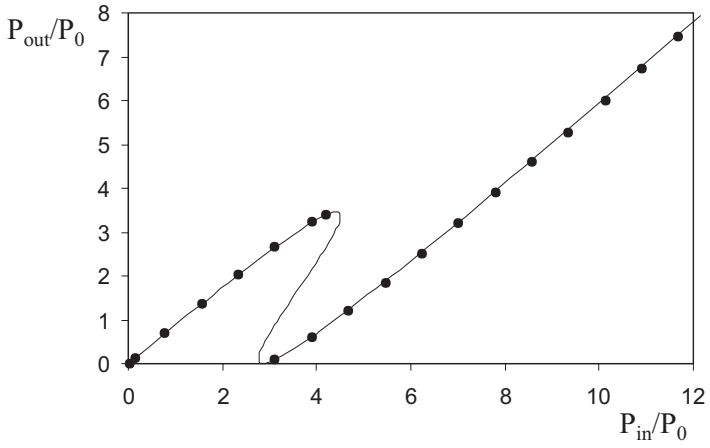

Figure 2.17: Output power versus input power of the nonlinear PhC structure with CMT (solid line) and rigorous simulations (dots).

where

$$P_{ref} = |s_{1-}|^2 = P_{in} - P_{trans} = |s_{1+}|^2 - |s_{2-}|^2 \tag{2.88}$$

is the reflected power.

At low input powers the transmission is high, as we would expect from the linear characteristic. At high input power the system can switch to a nonlinear state with lower transmission: the linear characteristic has shifted. We note the existence of a region where one input power corresponds to multiple output powers. The folded part of the curve, without rigorous simulation points, is unstable, which means that the system will evolve into the lower or upper branch. Therefore, two possible stable outputs are possible. This is called *bistability*, and it generally occurs in systems with nonlinearity and feedback, such as resonators [39]. It is a kind of hysteresis phenomenon, where the system remembers its previous state. From equation 2.87 we may deduce that bistability appears if $\delta < -\sqrt{3}$. Because of the contrast between the two states, these devices are interesting for all-optical switching.

In conclusion we note that the nonlinear CMT curve of eq. 2.87 with $P_0 = 0.3209 \times 10^4 \mathrm{W/m}$ fully agrees with the rigorous simulations. Therefore it is an efficient analytical tool to study resonator systems.

2.6 Conclusions

In this chapter we presented an overview of the major fields and methods used in the following work. We started with periodic structures, and noted how their dispersion gives rise to Bloch modes and band diagrams. Integrated functionality is achieved with line and point defects.

Then, we moved on to nonlinear optics. Our modeling methods focus on SHG and the Kerr effect, so we gave some insight into the physics and the appropriate formalism.

Next, we developed the eigenmode expansion method. Here, we describe the fields as a superposition of modes that fit the transversal index profile. With a matrix approach we model the propagation through invariant layers, and the scattering on interfaces. The efficiency for periodic structures and the need for a limited set of modes are important points.

Finally, the linear and nonlinear Coupled Mode Theory is explained. The procedure for obtaining its parameters is outlined, and an example of a PhC resonator system is provided.

Chapter 3

Modeling the Kerr effect

3.1 Introduction

In this chapter we explain how we combined the Kerr nonlinearity with mode expansion. Different approaches are possible, but we opted for a straightforward iterative scheme, using a grid for the nonlinear sections. In this way a lot of the functionality of the linear method is inherited or portable. We mention e.g. the possibility to model finite as well as periodic structures. Furthermore, the formalism allows the modeling of strongly nonlinear modes, which we will encounter in chapter 5. Together with the choice of positioning the nonlinear materials in the arbitrary 1D or 2D structure, a large class of devices is available.

The chapter is structured as follows. In section 3.2 the basic algorithm is presented. Then we highlight the specifics of simulating finite and periodic structures in section 3.3. The method uses a grid and we discuss its fineness in section 3.4 by a waveguide example. Then we compare our results in section 3.5 with a bistable grating structure from the literature. After that a review of characteristics and a comparison with other methods is given in section 3.6. More challenging devices consisting of a photonic crystal cavity with a Fano-like response are discussed in section 3.7. Finally, in section 3.8 some examples of calculations in periodic structures are reviewed. Amongst others we examine the bistable dispersion curve of a PhC waveguide.

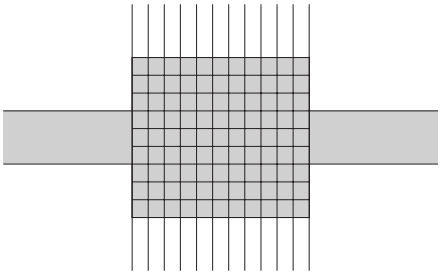

Figure 3.1: An example of spatial discretization, the middle section is nonlinear.

3.2 Method

If we want to simulate the Kerr effect, we have to take into account an intensity dependent refractive index:

$$n(\mathbf{r}) = n_0 + n_2 I(\mathbf{r}), \tag{3.1}$$

with n_0 the linear index, n_2 the Kerr coefficient and I the intensity. Because the intensity is spatially dependent, the refractive index is too, so we try to model this by dividing the nonlinear section(s) in small rectangles, as in figure 3.1. Each rectangle is assigned its refractive index during each iteration.

Because the intensity or index distribution is not known a priori, the method is iterative and proceeds as follows. We start from a certain index distribution, this is e.g. the linear index or a previously calculated approximate solution. Using this index grid we perform a *linear* eigenmode calculation (with CAMFR), yielding the fields in the structure. With the intensities in the center of each rectangle we update the refractive index distribution employing equation 3.1. If the new index distribution is equal to the old index distribution, within a certain tolerance, we have converged to a solution of the full nonlinear problem. If not, we repeat the described procedure. This algorithm is shown schematically in figure 3.2.

3.3 Finite and periodic structures

Here we discuss the differences in using the previous iterative method for finite and periodic structures. In both cases a certain constant is necessary to keep the calculation self-consistent.

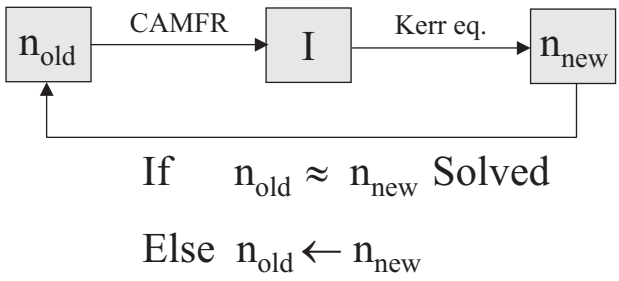

Figure 3.2: Schematic of the Kerr algorithm.

For finite devices the procedure is simple: The input mode amplitude vector is kept constant during the iterations. In this way we follow the evolution of the total scattering matrix, each time imposing the same input boundary condition.

For infinite periodic structures we describe the scattering behavior of a unit cell with reflection and transmission matrices in the following way (see section 2.4):

$$\begin{aligned} \mathbf{F}_2 &= \mathbf{T}_{12} \cdot \mathbf{F}_1 + \mathbf{R}_{21} \cdot \mathbf{B}_2, \\ \mathbf{B}_1 &= \mathbf{R}_{12} \cdot \mathbf{F}_1 + \mathbf{T}_{21} \cdot \mathbf{B}_2, \end{aligned} \tag{3.2}$$

with $\mathbf{F}$ and $\mathbf{B}$ denoting mode amplitude vectors of forward and backward propagating fields, respectively. The indices 1 or 2 indicate the left or right boundary. Then we impose Bloch boundary conditions, meaning:

$$\begin{bmatrix} \mathbf{F}_2 \\ \mathbf{B}_2 \end{bmatrix} = e^{ik_B p} \begin{bmatrix} \mathbf{F}_1 \\ \mathbf{B}_1 \end{bmatrix}, \tag{3.3}$$

with k_B the Bloch propagation constant and p the period. Together with eq. 3.2 this leads to a generalized eigenvalue problem:

$$\begin{bmatrix} \mathbf{T}_{12} & \mathbf{R}_{21} \\ 0 & \mathbf{I} \end{bmatrix} \begin{bmatrix} \mathbf{F}_1 \\ q\mathbf{B}_1 \end{bmatrix} = q \begin{bmatrix} \mathbf{I} & 0 \\ \mathbf{R}_{12} & \mathbf{T}_{21} \end{bmatrix} \begin{bmatrix} \mathbf{F}_1 \\ q\mathbf{B}_1 \end{bmatrix}, \tag{3.4}$$

where $\mathbf{I}$ is the unity matrix and $q = e^{ik_B p}$ [40]. Other formulations are possible, but the previous is numerically more robust.

From the set of resulting eigenvalues we select the mode of interest. This is normally the lowest order value, as we are interested in lossless Bloch modes most of the time. The previous process of solving

the eigenvalue problem is done at each iteration. However, because the unit cell is often small, the calculations are rapid. In contrast, simulating a finite structure with tens of periods can be time consuming.

In contrast with the finite case there is no input vector that we can keep constant during iteration. Another normalization parameter is needed to keep the calculations consistent. To this end we use an excitation strength of the Bloch mode. After fixing this strength at the start, we rescale the linear Bloch modes of the subsequent calculations.

There are different possibilities to define this excitation strength. We can use the flux of the Poynting vector through a boundary:

$$P = \frac{1}{2}\mathrm{Re}\int (\mathbf{E}\times\mathbf{H}^*)\cdot \mathrm{d}\mathbf{S}, \tag{3.5}$$

which we apply e.g. in chapter 5 for waveguide modes, as P immediately delivers a parameter of interest for waveguides. On the other hand, if one tries to calculate band edge modes, the previous definition is not effective, because the flux approaches zero. Therefore, in these cases, it is better to keep the electrical energy in a period constant:

$$U_e = \frac{\varepsilon_0}{2}\int n^2 I \,\mathrm{d}V. \tag{3.6}$$

A drawback here is the need to calculate an integral over the spatial period. We employ this normalization in section 3.8.

In conclusion, for finite structures the input wave vector is chosen and constant during iteration. For periodic structures the power flux or the energy is fixed, and we inspect the guided Bloch waves e.g. to investigate the nonlinear tuning of the band structure.

3.4 Grid size

One intuitively assumes that the results should converge, as the grid becomes finer. Here, we illustrate this by an example, a waveguide with a nonlinear section, shown in figure 3.3. This multimode waveguide has a width λ_0 and index 3.0, the cladding has index 1.0. A waveguide section of length $2\lambda_0$ is considered with $n_2 = 3\times 10^{-18}\mathrm{m}^2/\mathrm{V}^2$. For this test we use a strong excitation with the fundamental TM mode of $10^{20}\mathrm{W/m}$, so that the maximum nonlinear index change is about 0.2.

We varied the number of divisions in the longitudinal and transversal waveguide direction, N_{long} and N_{trans} respectively, and calculated the reflection coefficient of the fundamental TM mode.

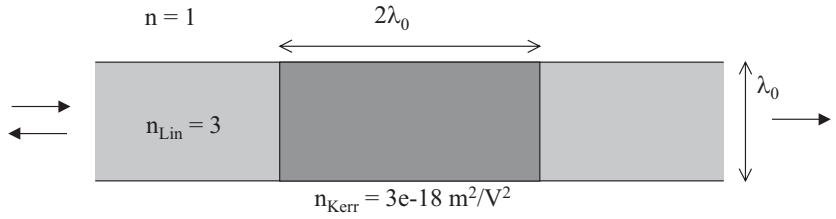

Figure 3.3: Waveguide with a nonlinear section in a darker shade.

As can be seen in figure 3.4, above a certain threshold the results converge. More than 50 longitudinal and 8 transversal divisions give good results in this case. Of course the finer the grid, the longer the calculations take. A disadvantage of the method is that the simulation times scale unfavorably with the number of grid points. Indeed, each division introduces new modes and scattering matrices that have to be calculated. Therefore, depending on the situation, the calculation times scale between n^2 and n^3, with n the number of grid points.

The nature of the convergence is clear from figure 3.5. Here we can extrapolate parabolically to a limit value of $R = 0.046$, so in this example the results converge as $1/N_{trans}^2$. With constant N_{trans}, the same behaviour according to $1/N_{long}^2$ can be deduced.

For these calculations we included 20 eigenmodes, consisting of 3 guided, 2 propagating radiative and 15 evanescent radiative modes in the linear waveguide. Because of the symmetry of the problem, we only considered modes symmetric to the waveguide axis. Therefore the number of transversal divisions N_{trans} relates to one half of the waveguide width.

Note that the spike in figure 3.4 at $N_{long} = 25$, independent of N_{trans} and the number of used modes, is the result of a Bragg resonance between the rough sampling grid and the fundamental waveguide mode. The forward and backward propagating fundamental mode interfere, and induce a standing-wave refractive index pattern that oscillates with $k_{induced} = 2\beta$, where β is the propagation constant of the fundamental mode. If we use a sampling grid with a certain $dz = 2\lambda_0/N_{long}$, that agrees more or less with the nonlinearly induced index pattern, then the rough sampling gives rise to a rectangular grating with $k_{sampling} = 2\pi/(2dz)$. If $N_{long} = 25$ we find that $k_{sampling} = 39.27\mu\mathrm{m}^{-1}$, and using the average of β over the different sections, thus including nonlinear

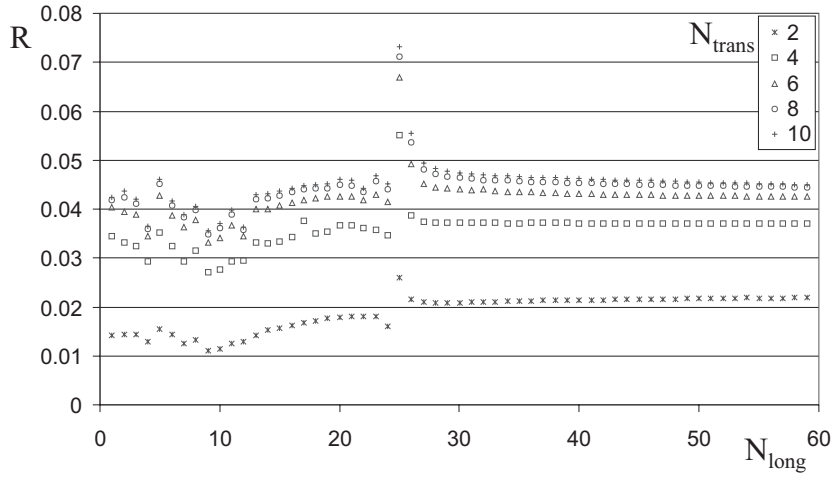

Figure 3.4: Magnitude of reflection coefficient of fundamental mode versus the number of longitudinal divisions N_{long}, for different numbers of transversal divisions N_{trans} (inset).

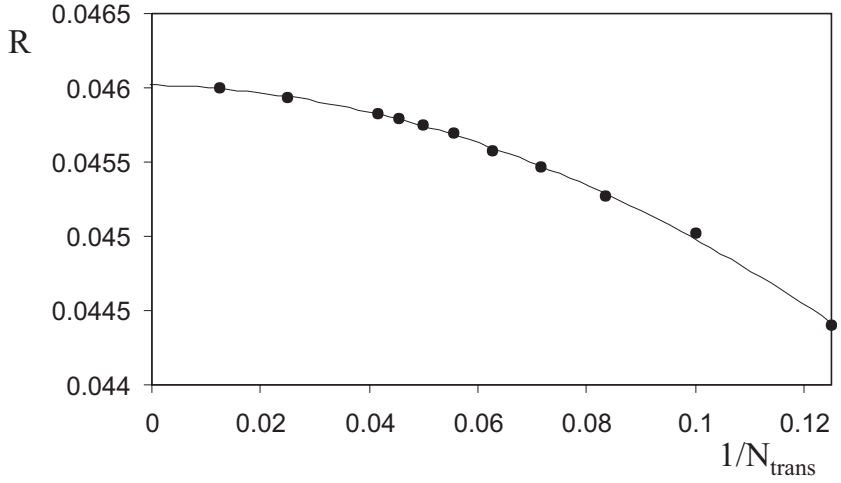

Figure 3.5: Magnitude of reflection coefficient of fundamental mode versus the inverse of the number of transversal divisions N_{trans}, for $N_{long} = 60$. The extrapolation parabola is also shown.

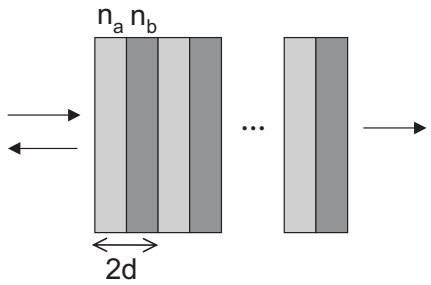

Figure 3.6: Grating with the nonlinear sections in a darker shade.

effects, we obtain $k_{induced} = 38.76 \pm 0.26\mu\mathrm{m}^{-1}$. With other N_{long} this agreement between $k_{sampling}$ and $k_{induced}$ is not as good, and the sharp peak then disappears.

As the required grid size is dependent on the unknown field structure, there is no simple relation of fineness versus desired accuracy. A solution is thus to study different grids for one input power, choose an accuracy threshold and then use this division to determine other related solutions. One can also determine the character of the convergence and extrapolate towards the limit of an infinitely fine grid. Another method is to use an adaptive grid, which we will discuss briefly in section 3.6.

3.5 Quantitative comparison

In order to validate the algorithm we have to compare our results with the literature. We present one example, a grating that exhibits bistability. This phenomenon, arising from feedback in combination with nonlinearity, lies at the basis of many proposed all-optical components.

The grating structure, depicted in figure 3.6, consists of 20 unit cells, each comprising two films with equal width $d = 0.125\lambda_0$ and indexes respectively $n_a = 1.5$ and $n_b = 2.12$. The first material is linear, while the second has a negative Kerr coefficient $n_2 = -1\ \mathrm{m}^2/\mathrm{V}^2$. Note that for this example $n = n_b\sqrt{1 + n_2 I}$. The used frequency ($\lambda_0 = 1\mu\mathrm{m}$) lies in the stopgap just above the bottom edge. For the nonlinear sections we employ a one-dimensional grid with $dz = 0.0125\mu\mathrm{m}$. The input is a plane wave with amplitude E_0 and normal incidence.

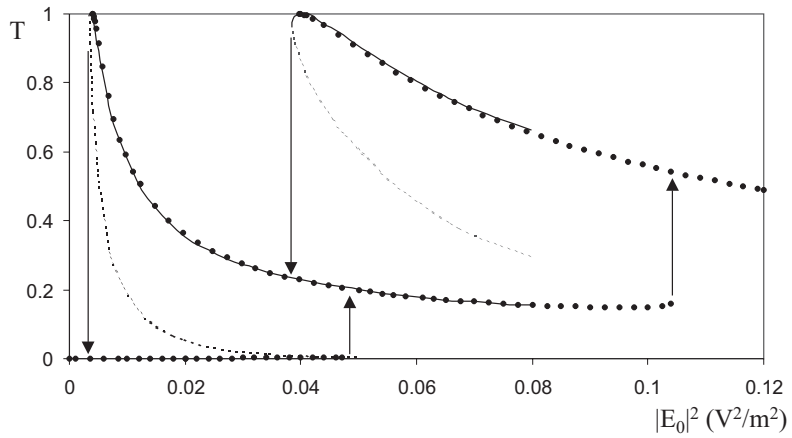

Figure 3.7: Transmission versus input power $|E_0|^2$ of the nonlinear grating. Our data is presented by dots, data from the literature by lines. Continuous lines show stable solutions, dotted lines are unstable states. The arrows indicate the two hysteresis cycles.

As in this example we will often use values of n_2 that are normalized or theoretically high. Because the refractive index change is the product $n_2 I$, the obtained results can be rescaled for realistic n_2 values. If we use physical n_2's they will be in the range of 10^{-18}–$10^{-19}\mathrm{m}^2/\mathrm{V}^2$.

In figure 3.7 we plot the simulated transmission of the grating, together with data from figure 3 in [41]. There is a good agreement with the literature. The dotted lines present unstable solutions, which means that a small deviation causes the system to switch to the upper or lower stable state. Our method does not calculate these solutions as the iteration can only converge to stable branches.

At low input power there is very low transmission, as we are working in the gap. Because of the nonlinearity, at higher powers the system can switch to higher transmission states. There are even fields with unity transmission, that represent gap solitons. One can see two hysteresis loops that coincide for a part, which gives rise to a region of tristability.

With our method one starts with the linear index distribution and low input power. Gradually increasing the input power yields the low transmission curve. After the folding point of this curve, there is no longer a low transmission state and the solution switches to a higher nonlinear solution. After finding one solution on an upper branch,

we can then increase or decrease the power in steps to map the entire higher branch. If one would want to model these solutions with FDTD, the long input pulse would have to be preceded by a sufficiently strong short one, in order to reach the upper branch, which complicates matters [19].

The data from [41] stops at $|E_0|^2 = 0.08\mathrm{V}^2/\mathrm{m}^2$. However in fig. 3.7 we plot until $0.12\mathrm{V}^2/\mathrm{m}^2$ to show that we need to pass the second folding point in order to reach the upper branch of the second hysteresis loop.

3.6 Characteristics

This section brings together some characteristics and a comparison with other calculation methods.

An important issue is the number of iterations needed for convergence. Of course this is dependent on the desired accuracy and the deviation from a previous solution, but, as in the examples, with reasonable parameters convergence is mostly reached in about ten or twenty iterations.

Some more difficult points however require another update equation, instead of equation 3.1. These are e.g. points close to a folding bifurcation, the first solution on an upper branch or highly nonlinear states, such as gap solitons. In these cases we use:

$$n'_{new} = \left(n_{new} + \alpha n_{old}\right) / \left(1 + \alpha\right), \qquad \alpha \geq 0 \tag{3.7}$$

with n_{new} the index if we used the normal Kerr relation, equation 3.1. With this weighted average we hold on longer to the previous index distribution n_{old}, the iterations are thus less abrupt. This prevents the solution from dropping back to more linear branches. Values of α up to about thirty are sometimes necessary.

Another trait of our algorithm is that other types of Kerr-like nonlinearities can easily be implemented. By adjusting equation 3.1 we can e.g. model a saturable Kerr effect:

$$n = n_0 + \frac{n_2 I}{1 + I/I_s}. \tag{3.8}$$

Absorption has also been applied.

We note that the method is rigorous. There is no approximation in Maxwell's equations, so in the limit of an infinite number of modes and a very fine grid, the solutions are exact.

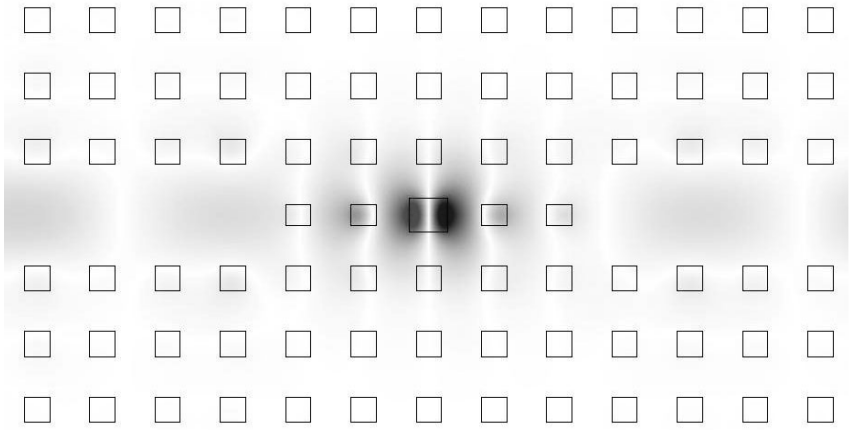

Figure 3.8: Structure of the photonic crystal device. The electric field of a completely transmitting resonant state is superimposed.

The bidirectional character of the mode expansion technique gives us an advantage over unidirectional standard BPM programs. Concerning efficiency we mention that linear sections need only one calculation and that we immediately obtain continuous-wave solutions, in contrast with FDTD [42]. Moreover an adaptive grid can be implemented, which means we merge sections, if their nonlinear index contrast is too small, or we refine them otherwise. In this way the calculation should find its optimal grid. Although adaptive gridding is very straightforward in our method, this is not the case with FDTD, as the latter requires special treatments on the boundaries between different grids.

3.7 Advanced finite examples

3.7.1 Photonic crystal switch

Now we present calculation results on a bistable photonic crystal device, shown in figure 3.8. This device has been described in [19] and is particularly suited for our method. First of all it is obvious that the smaller the nonlinear sections are, the more efficient our simulations become. In these calculations only the central rod is considered nonlinear, a good approximation as it experiences the strongest fields. Related

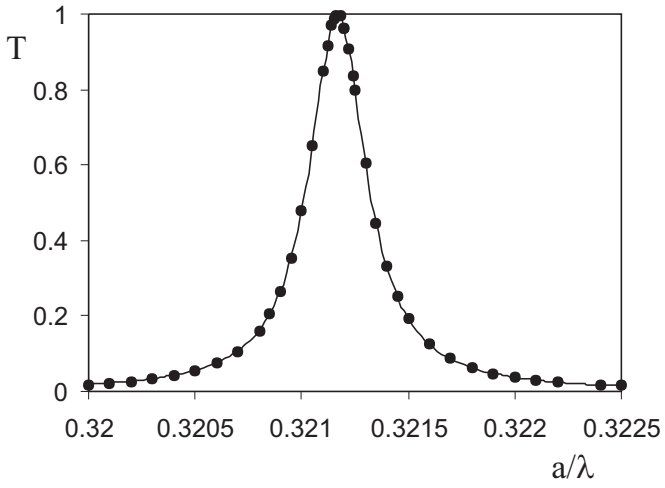

Figure 3.9: Linear transmission of the photonic crystal device. Dots show the numerical values, the solid line is the Lorentz curve.

to this, efficiency is improved because the linear sections before and after the nonlinear rods have to be calculated only once, as they consist of linear materials, and therefore their scattering matrix is power independent. In addition, because the structure and excitation are symmetric with respect to the waveguide axis, we can halve the simulation area by using a perfect magnetic wall as boundary condition along this axis. In the longitudinal direction Fabry-Pérot effects are avoided by using non-reflecting semi-infinite repetitions of the photonic crystal waveguide period [27].

Let us briefly review the operation of the switch, which is dual to the CMT example in section 2.5. The larger defect rod in the center forms a dipole-type cavity mode, that is coupled to input and output photonic crystal waveguides by tunneling effects through two normal-sized rods on either side. The linear transmission with the Lorentzian profile is shown in figure 3.9. We operate on a frequency slightly below the linear resonance frequency of the cavity. So at low input almost all power reflects to the input waveguide. Increasing the input power changes the index of the Kerr rod and the resonance frequency adjusts and shifts through the operating frequency. This means a stronger excitation of the cavity mode and leads to transmission of power to the

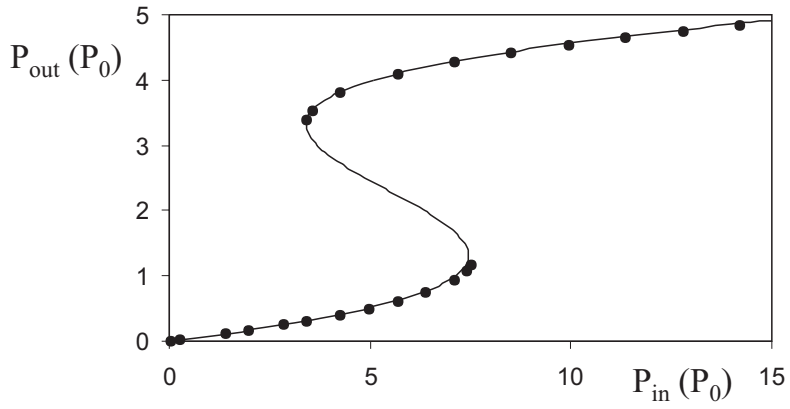

Figure 3.10: Output power P_{out} versus input power P_{in} for the photonic crystal switch. The dots present calculation results. The line is the third-order curve from equation 3.9.

output waveguide. Buildup in the high Q cavity makes the device even bistable.

This operation is clearly presented in the calculation results in figure 3.10. Our simulations follow the third-order curve derived with CMT in [19]:

$$\frac{P_{out}}{P_{in}} = \frac{1}{1 + (P_{out}/P_0 - \delta)^2}, \tag{3.9}$$

with $\delta = 3.475$ and $P_0 = 3.52\mathrm{MW/m}$. Here P_{in} and P_{out} are defined by the flux of the longitudinal component of the Poynting vector at the end of the output waveguide without and with the five center rods, respectively.

For these simulations we used a square lattice, with period $0.6\mu\mathrm{m}$, of square rods with index 3.5 and side length $0.4\mu\mathrm{m}$ in air. The frequency is $0.320606(2\pi c/a)$, which lies in the bandgap and close to the resonance frequency $0.32117(2\pi c/a)$, formed by the defect rod with side length $0.6a$. The nonlinear material has a realistic nonlinear coefficient $n_2 = 2 \times 10^{-19}\mathrm{m}^2/\mathrm{V}^2$. The large central nonlinear rod has a grid with $dx = 0.0225\mu\mathrm{m}$ and $dz = 0.03\mu\mathrm{m}$. Only sixty eigenmodes were used in these calculations.

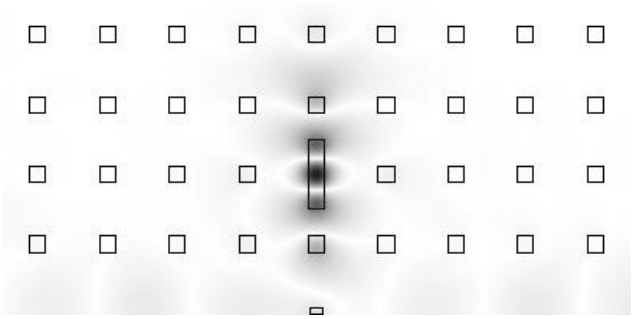

Figure 3.11: Geometry of the PhC device showing a Fano resonance. The field with transmission unity is superimposed. Only one half of the simulation domain is shown because of symmetry.

3.7.2 Fano resonance

A related structure concerns a cavity next to the waveguide [36], that we already encountered in detail in section 2.5. This device has a dual behaviour as opposed to the cavity in the waveguide of the previous paragraph. Thus at resonance power is reflected, whereas off resonance power is transmitted freely through the guide.

Here we study a slightly modified geometry, exposing a very different response, see figure 3.11. The obstacle in the waveguide creates an asymmetric Fano-type transmission spectrum, shown in figure 3.12. This line shape is created by the interference between the direct channel (the waveguide with obstacle) with slowly varying phase, and the indirect channel (the cavity) with a rapid phase change around the resonance frequency.

Other physical systems have analogous characteristics. They are called Fano resonances because of Fano's work on atomic systems with the interaction between discrete energy levels and a radiation continuum [43]. In photonic crystals it has mostly been studied in the optical transfer through free-standing membranes or films [34, 44].

In the nonlinear regime the asymmetric transmission gives rise to alternative power diagrams [44, 45]. We study these curves here, because they prove our tool can handle many kinds of solutions, and because numerical calculations on concrete waveguide structures are lacking. Furthermore, the obstacle is placed right next to the cavity, instead of somewhere further along the waveguide [45], thus reducing

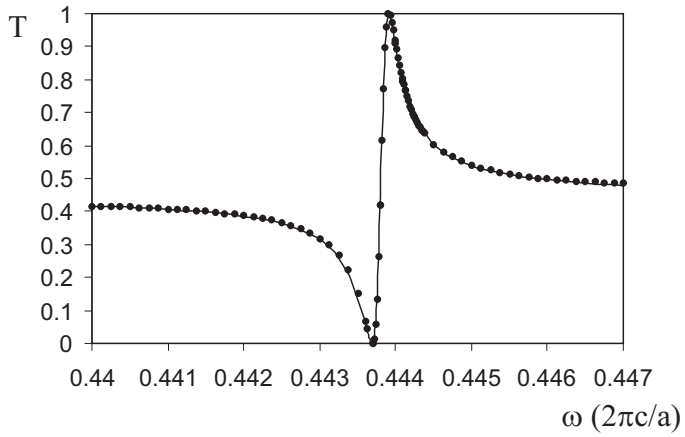

Figure 3.12: Linear transmission spectrum showing an asymmetric Fano resonance. Dots show simulation results, the line is the CMT curve.

the footprint of the device. We show that the simulations agree with (nonlinear) CMT.

The structure has the following parameters: The index of the rods is 3.4 in an air background, and they have a diameter of $0.25a$. The cavity rectangle has the same width as the rods, but has a length a. The obstacle square is slightly smaller and measures $0.2a$. The linear transmission of figure 3.12 agrees with the CMT curve obtained using the principles of section 2.5 [36]:

$$T = \frac{(t\tau(\omega - \omega_r) + r)^2}{\tau^2(\omega - \omega_r)^2 + 1} \tag{3.10}$$

with parameters $\omega_r = 0.44381(2\pi c/a)$, $\tau = 9096/(2\pi c/a)$ and $t = 0.6675$ (thus $r = \sqrt{1 - t^2} = 0.7446$). The cavity rectangle is considered nonlinear with $dx = 0.02\mu\mathrm{m}$ and $dz = 0.06\mu\mathrm{m}$. Because of the field profile, see figure 3.12, we can choose a larger dz compared to dx, and still get quite accurate results.

To study the nonlinear characteristics we choose two frequencies: One smaller than the resonance frequency at $0.422(2\pi c/a)$, where we use a positive Kerr $n_2 = 2 \times 10^{-19}\mathrm{m}^2/\mathrm{V}^2$, and the other one larger than ω_r at $0.4455(2\pi c/a)$ with a negative Kerr coefficient $-n_2$. The two responses are shown in figures 3.13 and 3.14, respectively. Remark the difference with the previous paragraph, and the peculiar possibility of crossing curves. These crossings with the same amplitudes are different

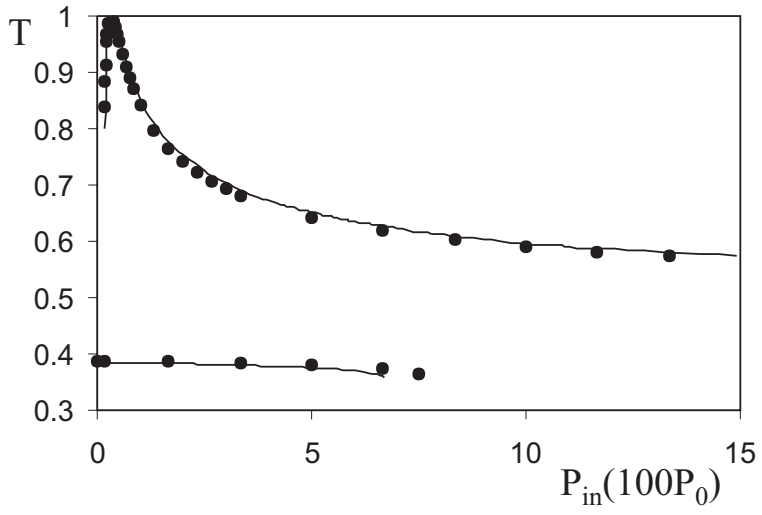

Figure 3.13: Transmission versus input power at $\omega = 0.442(2\pi c/a)$ with positive Kerr nonlinearity. The dots and line present simulation and CMT results, respectively.

solutions however, because they are not degenerate in phase. For both nonlinear CMT curves we use the same $P_0 = 60\mathrm{MW/m}$, and there is a good agreement.

The previous examples show that the method is able to model finite photonic crystal cavity devices rigorously and efficiently.

3.8 Periodic devices

We already mentioned how the algorithm applies to both finite and infinite periodic devices. Up until now we showed examples of the former. So in this section we provide a few examples of the latter. We demonstrate how the Kerr effect modifies their band structure.

3.8.1 Nonlinear photonic crystal

Figure 3.15 shows the geometry of a square lattice of square rods along the ΓX-direction. The simulations in this section suppose TM polarization, with the electric field parallel to the rods. The rods have index 3.4 and are considered nonlinear with $n_2 = 10^{-5}\mathrm{m}^2/\mathrm{V}^2$. The background is

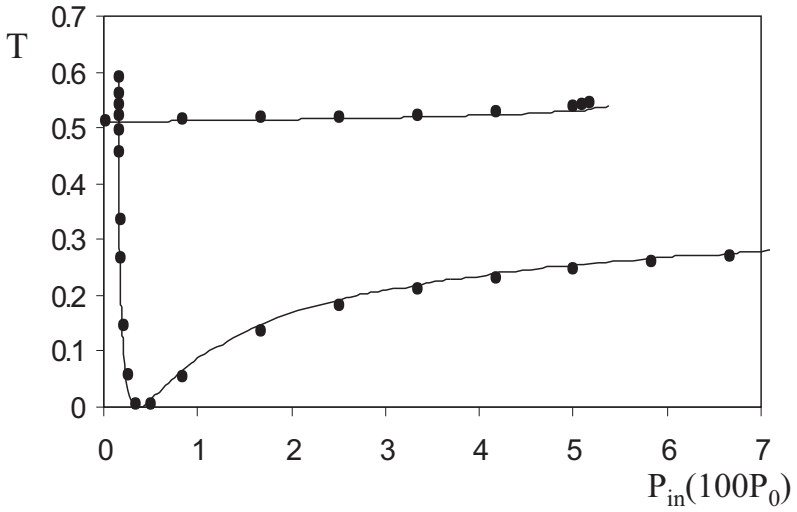

Figure 3.14: Transmission versus input power at $\omega = 0.4455(2\pi c/a)$ with negative Kerr nonlinearity. The dots and line present simulation and CMT results, respectively.

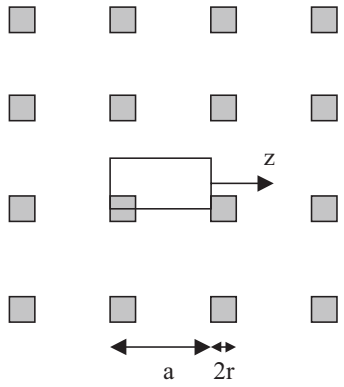

Figure 3.15: Nonlinear photonic crystal geometry. The box shows the used unit cell, exploiting symmetry.

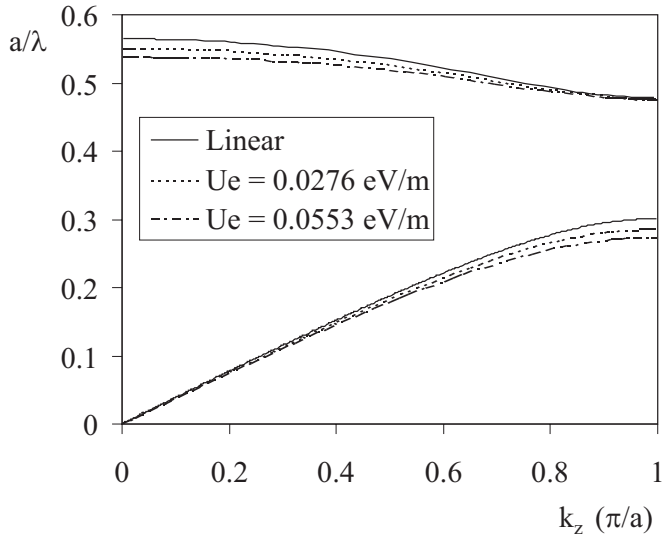

Figure 3.16: Nonlinear photonic crystal band structure. Solid lines show linear bands, dashed lines present nonlinearly adjusted bands.

air. The ratio of the side of the rods to the crystal period is $2r/a = 0.25$. Note that, because of symmetry, only the small box in figure 3.15 has to be modeled, which speeds up calculations significantly.

The linear photonic crystal has a TM-gap from $a/\lambda = 0.347$ to 0.477. This gap is tunable and the results are shown in figure 3.16. Here, the typical down-shifting of the bands for positive n_2 with increasing energy U_e is apparent. Similar calculations have been performed [46, 47, 48]. Applications of these band shifts are reported e.g. in [48] and for the superprism effect in [49].

3.8.2 Coupled cavity waveguide

In this section we calculate the dispersion relation of coupled cavity waveguides or CCWs in nonlinear photonic crystals [50]. These waveguides are formed by evanescent coupling between neighbouring resonator modes. In our case, the monopole modes are formed by lowering the diameter of a rod to $0.1a$, see figure 3.17. The resonator spacing is $3a$ and the same crystal lattice and polarization as previously is used. We consider only the defect rod to be nonlinear, with $n_2 = 10^{-5}\mathrm{m}^2/\mathrm{V}^2$.

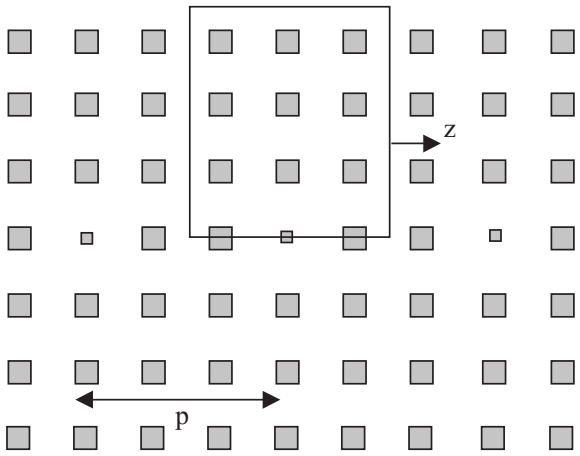

Figure 3.17: CCW Geometry. The box shows the used unit cell. The period $p = 3a$.

The dispersion relationship for a linear CCW has a cosine form [50]:

$$\omega = \omega_0 + \Delta\omega \cos(k_z p), \tag{3.11}$$

with p the period, here $p = 3a$. ω_0 and $\Delta\omega$ are determined by the resonance frequency of the mode and nearest neighbour overlap integrals. We retrieve this cosine form, as shown in figure 3.18. For the nonlinear bands there is again a downward shift. As a reference we also plot linear bands, determined with the mean nonlinear index of the central rod for a fixed U_e. Indeed the nonlinear calculations should overlap with these linear results.

3.8.3 Limiter device

Many periodic nonlinear devices are based on shifting modes in and out of the bandgap for varying intensities. To gain insight in these devices studying the infinite structure can rapidly provide information on geometry, operational frequencies or intensities, without the need for time consuming simulations on a finite long structure.

We illustrate this by modeling a PhC waveguide limiter [51]. Geometry and results are shown in figures 3.19 and 3.20. The same lattice as above is used, but with a defect waveguide and larger nonlinear rods ($D = 0.4a$, $n_2 = 10^{-5}\mathrm{m}^2/\mathrm{V}^2$) alongside every two subperiods.

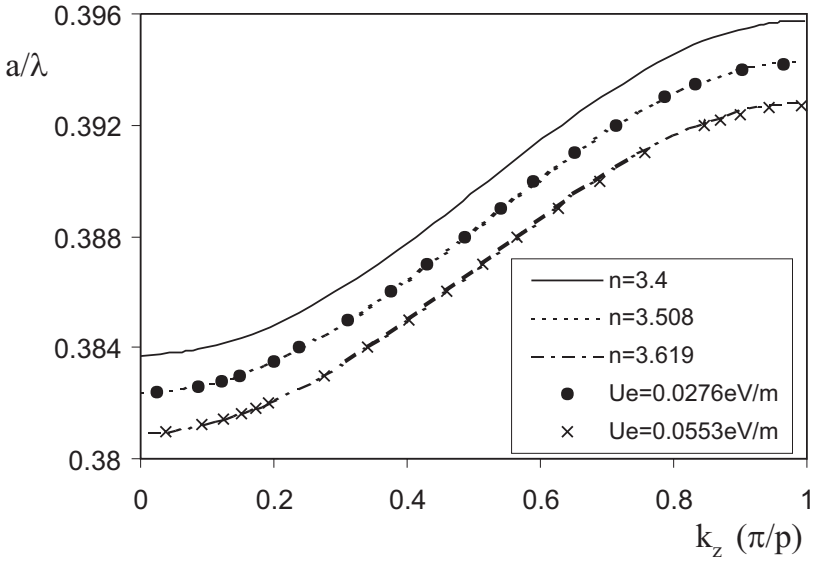

Figure 3.18: CCW band structure. Lines show the linear bands with defect rod index n, dots and crosses present nonlinearly shifted bands.

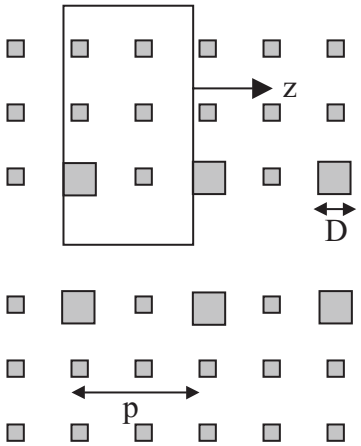

Figure 3.19: Photonic crystal limiter geometry: defect waveguide with larger nonlinear rods alongside. The box shows the used unit cell.

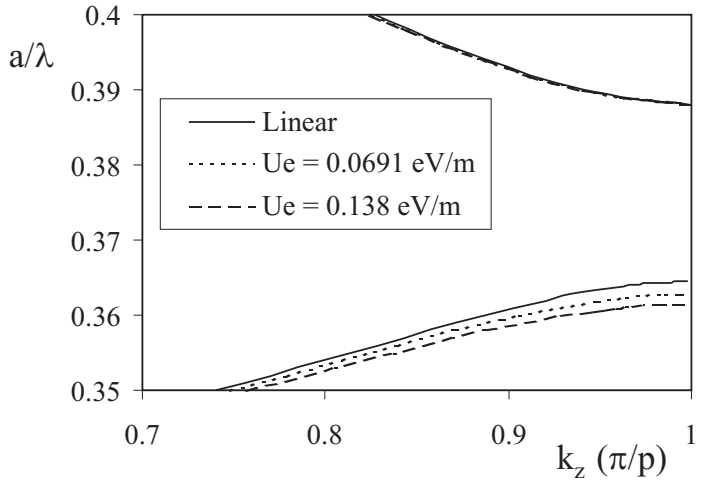

Figure 3.20: Photonic crystal limiter waveguide bands. Solid lines present linear bands, dashed lines show nonlinearly adjusted bands. The upper bands overlap. The period $p = 2a$.

The band structure shows two waveguide bands within the gap. Increasing the intensity shifts the lowest defect band downwards. The upper defect band is very insensitive to the nonlinearity. Field plots show indeed that the fields in this band are concentrated in the smaller linear rods along the waveguide, whereas in the lower band fields are strongest in the large nonlinear rods. Thus, if we operate on top of the lowest waveguide band, low amplitudes will give a high transmission. But as we increase the amplitude our simulations indicate the guided Bloch mode disappears below the working frequency, so we get limiting action.

3.8.4 Photonic crystal waveguide

Certain phenomena that appear in conventional waveguides have their counterpart in PhC waveguides. However because of the different guiding mechanisms, there will be distinguishing features. In this section we provide an example, that to our knowledge has not been reported yet in the PhC version.

It has been established that novel effects arise if a conventional waveguide with a Kerr layer is examined. More specifically, the dispersion curve (flux S versus effective index n_{eff}) can be highly distorted,

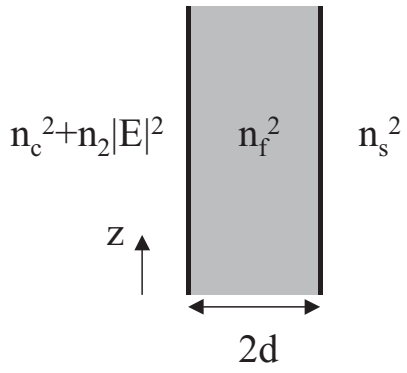

Figure 3.21: Structure of the waveguide with a nonlinear cladding.

with the possibility of bistability [52]. We illustrate this with a waveguide structure containing a nonlinear cladding, see figure 3.21. The film and substrate have index $n_f = 1.57$ and $n_s = 1.55$, respectively. The cladding has permittivity $n_c^2 + n_2|E|^2$, with $n_c = 1.55$ and $n_2 = 0.01\mathrm{m}^2/\mathrm{V}^2$. We use TM-polarization and $d = 4\lambda_0/\pi$.

We can model this problem using a one-dimensional simplification of the proposed simulation method. Only one mode has to be iterated, while keeping the flux constant. The results are presented in figure 3.22. There are two separate curves: The left one is the 'linear' branch, with modes mainly guided by the film. The other branch indicates 'nonlinear' solutions, where the modes are located in the nonlinearly adjusted cladding. Above a certain critical power, the mode confined in the film no longer exists, and switches to the substrate mode. Remark the region of bistability. These features have suggested applications e.g. in optical limiting.

The nonlinear branch is much more sensitive to the flux, which is understandable as these modes are located in the nonlinear region, see the insets in figure 3.22. Furthermore, the nonlinear modes are associated with spatial soliton emission in the cladding, as proven by propagation studies [53]. Indeed, if the power is high enough a localized entity may form and propagate away from the core in the cladding.

Now we consider the PhC analogy. The situation is shown in figure 3.23(a). We examine a PhC waveguide, with one adjacent row having a negative Kerr nonlinearity, but with the same linear index as the rest of the crystal. With increasing power the index of the nonlinear

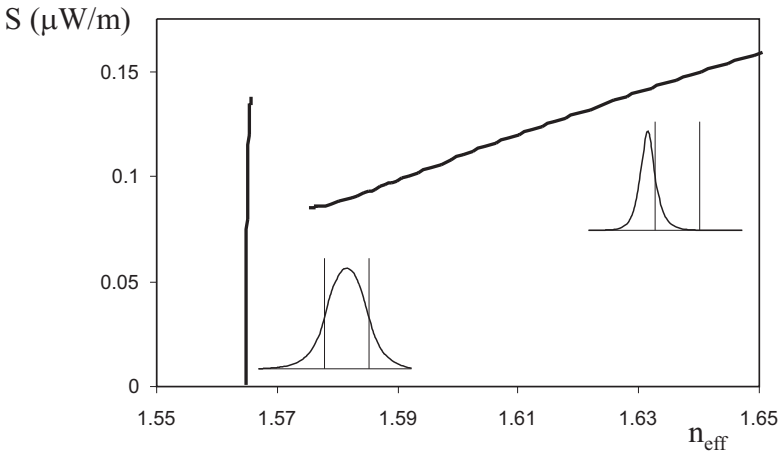

Figure 3.22: Mode flux versus effective index for the waveguide with nonlinear cladding. The insets show representative mode profiles (field strength in arbitrary units) for the linear and nonlinear branch.

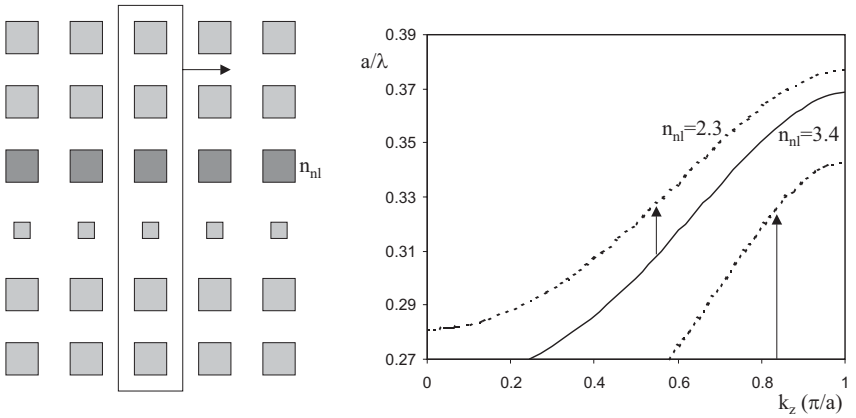

Figure 3.23: (a) Geometry of the PhC waveguide. The darker rods are considered nonlinear. The arrow indicates the z-axis which is the propagation direction. (b) Band structure. The solid and dotted lines correspond with an index of 3.4 and 2.3, respectively, for the nonlinear rod. The arrows indicate the band movement for decreasing index.

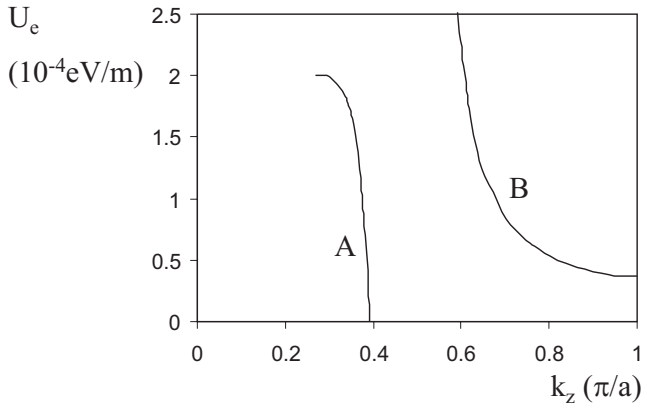

Figure 3.24: Energy versus Bloch wavevector for the PhC waveguide. The 'linear' ('nonlinear') branch is indicated with A (B).

rod decreases, so we expect another Bloch mode to appear, with the field located on the nonlinear row.

The previous is clearly understood from the band structure, shown in figure 3.23(b). Here the first bandgap region is presented. The crystal has a row with a smaller rod, which induces a waveguide mode. If we decrease the index of the nonlinear rod, this band shifts upward. When this index is low enough, another guided mode appears, and the first band detaches from the lower bandgap edge. Thus, if we operate at a frequency above this lower edge, we can expect the same behaviour as with the conventional waveguides we have already described.

We check these statements with nonlinear calculations. We choose the following parameters: The crystal consists of rods with diameter $0.4a$ and index 3.4, creating a gap between 0.27 and $0.387(2\pi c/a)$. The smaller waveguide rods have diameter $0.2a$, and the nonlinear rods have Kerr coefficient $-1\mathrm{m}^2/\mathrm{V}^2$. We operate at $\omega = 0.285(2\pi c/a)$. The simulation results are presented in figure 3.24. Remark that the flux used with conventional waveguides corresponds to energy here. There is again a threshold above which the 'linear' mode no longer exists, and the system switches to another branch. This is in agreement with the linear band structure analysis. The character of the two branches is illustrated with the field profiles in figure 3.25. On the nonlinear branch the center of the profile is shifted towards the nonlinear rod.

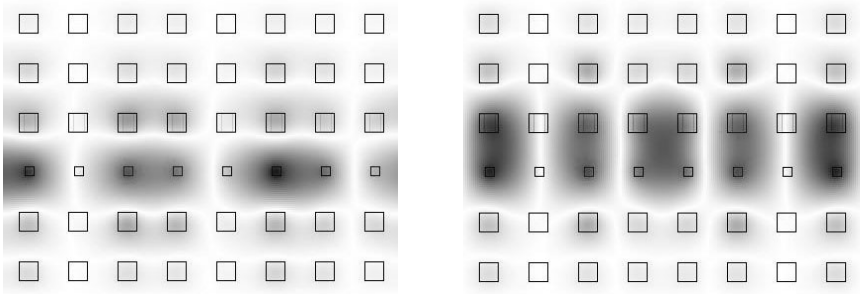

Figure 3.25: Representative depiction of the fields for the branches A and B, respectively (see figure 3.24). Calculated by linearly propagating the Bloch mode, using the index profile from the nonlinear calculation.

The difference with the limiter device in section 3.8.3 lies in the fact that we switch here to a new mode, whereas in the limiter no other mode is available. Remark that the alternative Bloch wave is induced in the PhC guide by a negative nonlinearity. This is impossible for conventional waveguides, where a lowering of the cladding index merely increases the confinement in the center film. We note that the index changes are theoretically high, so the scheme is not immediately adaptable for experiments. Finally, we could also consider a guide with nonlinear rows at *both* sides. In analogy with ordinary waveguides, symmetry breaking effects are expected [52].

3.9 Conclusions

We presented an extension to the eigenmode method which allows the modeling of 2D structures with Kerr materials. The basic idea is to divide the nonlinear sections in a grid and to iterate consistently towards a solution. Both finite and periodic structures are possible. For periodic devices Bloch boundary conditions and a constant excitation strength, such as energy, are used.

After an examination of the grid fineness and a quantitative validation with the literature, a few examples are demonstrated. PhC devices with cavities are especially suited for the method. The necessary number of modes is limited and the linear sections have to be calculated only once. These calculations clearly demonstrate the bidirectionality of the method via e.g. bistability. In this context a structure exhibiting Fano line shapes is proposed. Finally, a number of periodic devices is shown, such as a coupled cavity waveguide, a limiter and a waveguide with a nonlinear cladding. More complex Bloch modes are the subject of chapter 5.

Chapter 4

Coupled photonic crystal resonators

4.1 Introduction

Systems with waveguides and resonators are nowadays widely studied because of their ability to tune coupling strengths and resonance frequencies for many purposes. If chains of these devices are examined new effects and switching opportunities arise [50, 54, 55]. This has been examined for many types of structures, including distributed-feedback mirrors, ring-resonators and photonic crystal defects [56, 57].

The PhC structures have the potential to provide ultra-compact photonic integrated structures of only a few μm. Some examples have already been studied in the previous chapters. Because of the bandgap, all the light in two-dimensional PhC components remains confined in the waveguides. Therefore, analysis of the devices becomes easier and radiation losses can be ignored. Moreover, the strong confinement in cavities makes it possible to use weak nonlinear effects.

In this chapter we study the linear and nonlinear continuous-wave behaviour of chains of PhC resonator devices using Coupled Mode Theory (CMT) and rigorous simulations. We introduced CMT in section 2.5 and employed it for systems with coupling between a cavity and a waveguide. Here we use these equations in a transfer-matrix scheme to calculate sequences consisting of two kinds of cavities: The resonant coupling and the side coupling case, as shown in figure 4.1(a) and (b), respectively.

In the resonant coupling structure the resonator blocks the waveguides, therefore light is only transmitted on resonance. In contrast, in

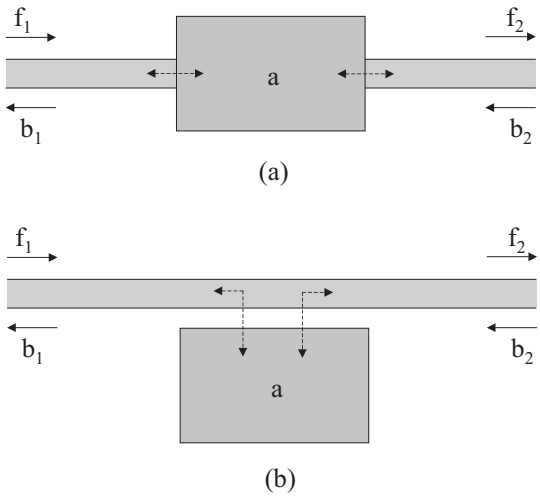

Figure 4.1: Two geometries with resonator and waveguide amplitudes: (a) Resonant coupled structure. (b) Side coupled structure.

the side coupling case there is a high reflection on resonance. We encountered these devices in sections 3.7 and 2.5, respectively. We focus on finite sequences with identical resonators. However, the formalism can also be used for chains with nonuniform parameters, e.g. apodized structures.

If finite periodic structures are examined, the relation with Bloch modes in infinite structures can be considered. We introduced these modes in the PhC theory of section 2.2. Where light is strongly reflected, gaps appear. The resonant coupled case gives rise to a transmission band, whereas the side coupled cavities can amount to a resonator gap. However, due to nonlinearity a finite system can switch from a highly reflective state in the gap to a state with unity transmission, or vice versa. The nonlinear transmission state is called the gap soliton [41, 58, 59, 60, 61]. We already calculated these special modes in the multilayer example of section 3.5. They also appear in infinite periodic structures as stationary or moving nonlinear entities.

These gap solitons are an example of *intrinsic localized modes* or *discrete breathers* [11]. The former term stems from the fact that the linear structure itself is invariant, in contrast with e.g. photonic crystals with defects. Indeed, a defect in a PhC can create an *extrinsic* localized mode. The discrete part of discrete breathers follows of course from the nature

of the problem with distinct sites or resonators. On the other hand, a breather is a localized time-periodic solution. Because we work in the time-harmonic domain, if we obtain a nonlinearly localized solution, we trivially have a breather.

There are multiple ways to interpret the gap solitons in finite settings. On the one hand they correspond to a kind of tunneling phenomenon. The incident field is completely transmitted through the structure, with the aid of the nonlinear mode. On the other hand, they are analogous to scattering resonances in atomic physics. In that setting resonances appear when a slight modification of the Hamiltonian leads to a bound state. In our case the slight modification is the difference between the finite and infinite devices. More specifically, the gap soliton exists in the infinite structure as a bound state. Cutting of its low-amplitude tails may lead to a resonance or localized mode in the finite setting [62].

These nonlinear states have consequences for energy localization and appear in various physical settings. Experiments are already performed in solid-state transition metal complexes, arrays of Josephson junctions, micromechanical oscillators and in photonic systems [11]. We will discuss some optical realizations in the next chapter. There we also theoretically examine another kind of solitary wave in 2D PhCs, the self-localized waveguide. Note that there is an interest in localized modes for biological systems. The buckling and folding of biopolymer chains e.g. can be explained through the action of intrinsic nonlinear modes [63].

In this chapter we study a variety of nonlinear modes in both the resonant and side coupled geometry. The normal gap soliton, originating from the adjustment of a linear transmission peak, appears in both geometries. In contrast, nonlinear transmission anomalies have been examined in [62]. These are transmission maxima that only appear because of the nonlinearity, and as such present 'purer' intrinsic localized modes. Finally, we show a new kind of nonlinear resonances with an alternative energy profile. For these modes the energy is localized at the boundaries of the finite series, instead of in the center. The three types of modes appear in both cavity configurations.

An important parameter for these coherently interacting cavities is the length of the intermediate waveguide, which can be tuned to change the phase and interference characteristics. If we carefully choose this length, the linear spectrum of two side coupled resonators can exhibit a very narrow transmission peak [56]. We shall exploit this peak

in an actual design, to demonstrate efficient switching both with CMT and more exact simulations.

In section 4.2 we describe the CMT calculation methods. We use these for a description of the linear spectra for both geometries in section 4.3. Studies of different types of nonlinear resonances and gap solitons are performed in section 4.4. Finally, in section 4.5 we present the concrete PhC device consisting of two side coupled resonators.

4.2 Calculation method

4.2.1 Resonant coupling

We assume that the waveguides and resonators are single mode in the frequency region of interest. Furthermore, the resonators are placed sufficiently far from each other so that interaction only occurs via the intermediate waveguides. Then, with CMT, the fields in a single cell of the resonant coupling geometry (see figure 4.2(a)) are described by

$$\frac{\mathrm{d}a_1}{\mathrm{d}t} = \left[j\left(\omega_r + \delta\omega\right) - \frac{1}{\tau}\right] a_1 + df_1 + db_2, \tag{4.1}$$

$$b_1 = \exp(j\phi) f_1 + da_1, \tag{4.2}$$

$$f_2 = \exp(j\phi) b_2 + da_1. \tag{4.3}$$

Here a_1 denotes the complex cavity mode amplitude, whereas f_1 and f_2 (b_1 and b_2) denote the forward (backward) waveguide Bloch mode amplitudes. The cavity lifetime is τ and the resonance frequency is ω_r, with $Q = \tau\omega_r/2$. In the previous $d = j\exp(j\phi/2)/\sqrt{\tau}$, where the phase ϕ depends on the waveguide and the PhC reflection properties. $\delta\omega$ indicates the nonlinear resonance frequency shift [19, 37]:

$$\delta\omega = -\frac{|a_1|^2}{P_0\tau^2}, \tag{4.4}$$

with P_0 the 'characteristic nonlinear power' of the cavity, see section 2.5. The amplitudes are normalized so that $|a_1|^2$ is equal to the energy in the resonator and $|f_i|^2$ ($|b_i|^2$) indicates the power in the forward (backward) mode of waveguide i.

The previous equations are valid for resonator modes with a vertical mirror plane through the center, e.g. monopoles. They are adjusted for modes with a vertical nodal plane, e.g. horizontal dipoles, by changing the sign of the last term in equation 4.1 and equation 4.3. Here we will

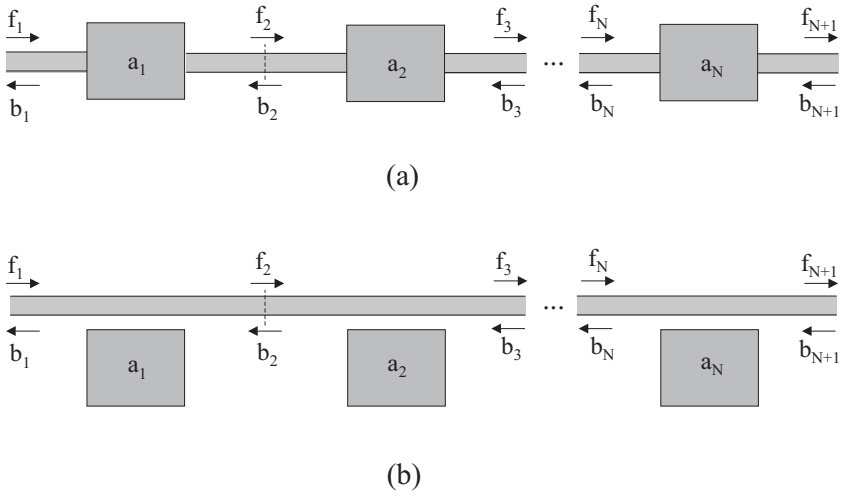

Figure 4.2: Presentation of the two types of series: (a) Resonant coupled structure. (b) Side coupled structure.

work in the continuous wave regime, so $\mathrm{d}/\mathrm{d}t$ is simply replaced by $j\omega$ in equation 4.1. In this regime we can analyze the possible states of the system. Specific excitations to reach or avoid the states need to be examined in the time domain [36].

In the resonant coupled geometry it is easy to concatenate cells with a transfer-matrix approach. We work from right to left, after fixing the output power. An input from the right is optional, but in the work here we assume $b_{N+1} = 0$. With equation 4.3 we determine a_N, which we then use in equation 4.1 to obtain f_N. Finally, with equation 4.2 we get b_N. In this way we calculate non-iteratively through a chain of nonlinear resonators. Note that both the stable and unstable states can be determined.

4.2.2 Side coupling

In the side coupling geometry, see figure 4.2(b), an analogous set of equations is derived:

$$\frac{\mathrm{d}a_1}{\mathrm{d}t} = \left[j\left(\omega_r + \delta\omega\right) - \frac{1}{\tau}\right] a_1 + df_1 + db_2, \tag{4.5}$$

$$f_2 = \exp(j\phi) f_1 + da_1, \tag{4.6}$$

$$b_1 = \exp(j\phi) b_2 + da_1. \tag{4.7}$$

Again $d = j\exp(j\phi/2)/\sqrt{\tau}$, but here $\phi = -k_z np$ with k_z the waveguide mode propagation constant, n the number of periods and p the PhC period. Note that these equations are equivalent to a model of a ring resonator adjacent to two waveguides [64]. Therefore the conclusions we reach are immediately portable to this system.

A direct transfer-matrix approach is only possible here for linear resonators. Calculating a nonlinear series has to be done differently. With equations 4.5 and 4.6 we obtain a nonlinear equation with f_2, b_2 and a_1. With the fixed f_2 and b_2, and starting from a guess resonator amplitude a_1 we can solve this equation with e.g. Newton-Raphson. Finally, using equations 4.6 and 4.7 we obtain the fields f_1 and b_1 on the left side of the cell. As in the previous system we find both the stable and unstable states. However the calculations are more difficult here, because Newton-Raphson is an iterative method which needs an initial guess. The guesses have to be good enough, in order to find all the states.

4.3 Linear transmission

In this section we give an overview of the linear transmission spectra for both geometries, as depicted in figure 4.2. Here, the two main parameters are the number of resonators N and the phase ϕ. We can fix this phase to a desired value, by adjusting the intermediate waveguide length. In PhC systems this means changing the number of periods. Remark that the spectra are 2π-periodic in ϕ, so that even with the discreteness of PhC waveguides, we can reach any phase. Of course, only if the structure is sufficiently short, will the continuous wave calculations accurately represent short pulse excitations. Furthermore, because of fabrication and loss issues, actual designs need to have a minimum of periods.

The spectra in this section ignore dispersion. For real PhC structures the main effect is waveguide dispersion. However, this k_z-dependence on ω can be included. Moreover, with high-Q resonators it is sufficient to use a constant k_z or a linear $k_z(\omega)$ function. Without dispersion the spectra are only symmetric around ω_r, if $\phi = m\pi$ or $\phi = \pi/2 + m\pi$ (with m an integer). These values represent the special cases. Spectra calculated in this section are plotted versus the dimensionless detuning $\delta = \tau(\omega - \omega_r)$.

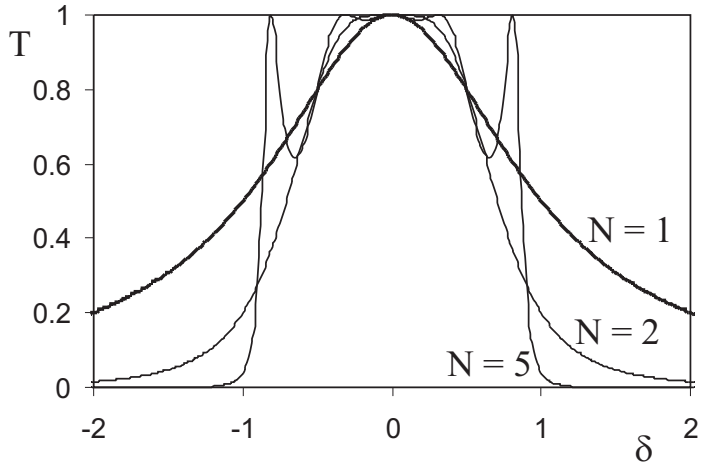

Figure 4.3: Transmission spectra for resonant coupled geometry with $\phi = \pi/2$ and $N = 1, 2$ and 5.

4.3.1 Resonant coupling

Now we discuss the resonant coupling case in more detail. In general the transmission spectrum consists of N peaks that shift in function of ϕ. Only the central peak at ω_r remains stationary. If $\phi = \pi/2$ these peaks are closest together, as shown in figure 4.3. For even values of N the central two peaks coalesce into one broader peak. As ϕ approaches 0 the $N-1$ non-stationary peaks move (infinitely) far away from ω_r. In the case of $N = 2$ e.g. one can calculate that the position of the moving peak varies as $\delta_{peak} = -\cot\,\phi$. When $\phi = 0$ all resonators have the same magnitude and the same (or opposite) phase, they behave as one cavity. For this case the $N = 2$ example is shown in figure 4.4. These spectra are simply proportional to the spectrum of one resonator, and have a width $1/(N\tau)$.

When N increases the situation becomes comparable to infinite structures, and we can use Bloch modes. These are studied via

$$\begin{bmatrix} f_2 \\ b_2 \end{bmatrix} = \exp(j\beta\Lambda) \begin{bmatrix} f_1 \\ b_1 \end{bmatrix} = \mathbf{T} \cdot \begin{bmatrix} f_1 \\ b_1 \end{bmatrix} \tag{4.8}$$

with β the Bloch mode propagation constant and Λ the length of a unit cell, see section 2.2. The transfer matrix $\mathbf{T}$ is obtained from equations 4.1-4.3. In a bandgap, the amplitudes of its eigenvalues are smaller

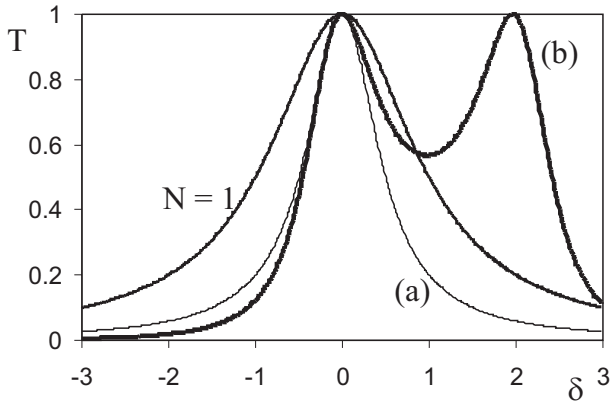

Figure 4.4: Transmission for resonant coupling. $N = 1$ is indicated, whereas curves (a) and (b) correspond to $N = 2$ but with $\phi = 0$ and $\phi = -0.15\pi$, respectively.

than 1, or equivalently, β has a non-zero imaginary part. The resulting diagram with the resonator transmission regions is shown in figure 4.5, and agrees with the finite results of e.g. $N = 5$ in figure 4.3. The center separating curve in figure 4.5 corresponds to $\tan(\phi/2)$. The case $\phi = 0$ is again highlighted as a special value.

4.3.2 Side coupling

There are many similarities between the side and resonant coupling structures [56]. Indeed, for a single resonator reflection and transmission are exchanged, immediately exposing the duality. Thus, the resonator transmission band of the previous section becomes a resonator reflection band or resonator gap. However, specific features will become apparent.

Here, the transmission spectrum of N resonators has $N - 1$ peaks with unity transmission, see figure 4.6. For $\phi = \pi/2$ these peaks are evenly distributed, one half on the lower edge, the other half on the upper edge. For odd numbers of maxima one peak moves to infinity at this phase. If ϕ decreases from $\pi/2$ to 0 the maximum peaks first shift to one side of ω_r, then they gradually disappear at ω_r. Before dissolving these peaks become extremely small, as shown in figures 4.7 and 4.8. At $\phi = 0$ the spectra are proportional to the dip for $N = 1$, with width N/τ. We will exploit the narrow resonances with small ϕ for nonlin-

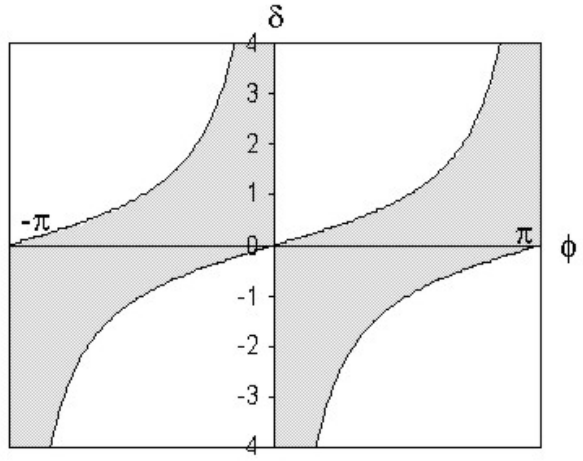

Figure 4.5: Bloch mode results. For the resonant coupled structure the shaded region indicates the transmission band, for the side coupled geometry it represents the resonator gap.

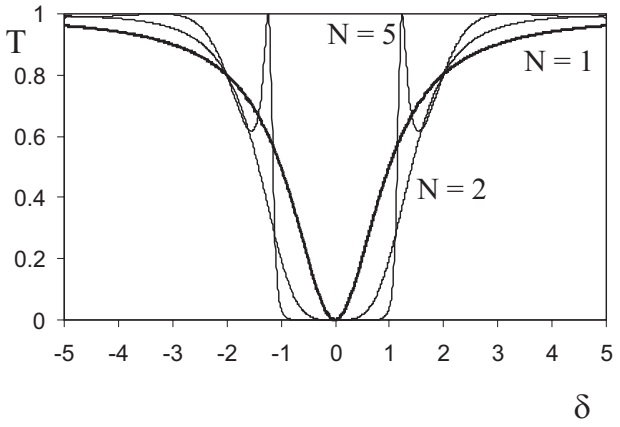

Figure 4.6: Transmission spectra for side coupled geometry with $\phi = \pi/2$ and $N = 1, 2$ and 5.

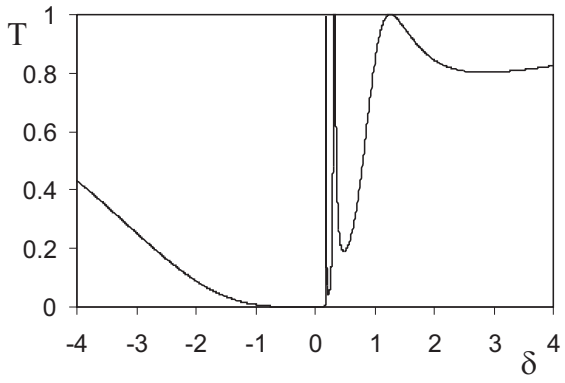

Figure 4.7: Transmission for side coupling with $\phi = 0.1\pi$ and $N = 4$.

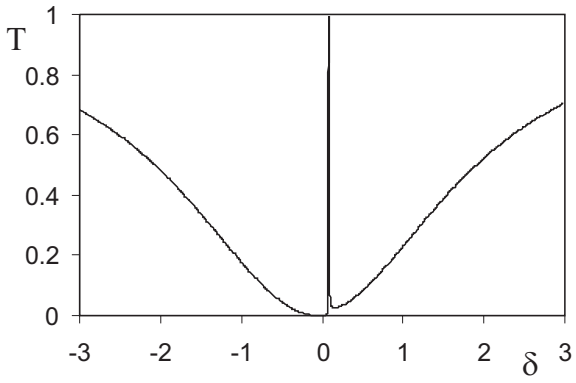

Figure 4.8: Transmission for side coupling with $\phi = 0.025\pi$ and $N = 2$.

ear switching in section 4.5. Here, we give a simple description of this peak for two resonators. The transmission is calculated for $N = 2$ from equations 4.5-4.7:

$$T = \frac{\frac{\delta^4}{4\cos^2\phi}}{\frac{\delta^4}{4\cos^2\phi} + (\delta - \tan\phi)^2} \tag{4.9}$$

For small $\delta \ll 1$ and $\phi \ll 1$ this describes a Lorentzian peak around $\tan\phi$ with width proportional to δ^4. These maxima are Fabry-Pérot resonances, which also appear in nonuniform grating structures [65].

Using the Bloch relation (see equation 4.8) but with the transfer matrix from equations 4.5-4.7 we can determine the resonator gaps in function of ϕ. The transmission band of the previous section directly corresponds to the resonator gap here, so we can use the same diagram of figure 4.5. Compare e.g. the curves for $N = 5$ in figures 4.3 and 4.6.

4.4 Nonlinear resonances

In this section we examine the special nonlinear modes that appear in these finite resonator systems. The linear properties we described provide insight in their origin. We present three types of resonances, which are possible in both the resonant and side coupled structures.

First, we show that the well-known gap solitons can be excited in the resonator geometries. Second, in systems with a few resonators, transmission maxima of a purely nonlinear origin are reported. These modes have been studied in resonantly coupled systems [62], but not yet in side coupled devices. Finally, starting from linear transmission peaks with a field minimum in the center of the series, we obtain new nonlinear modes with the energy localized on the boundaries of the system. With higher powers, the center field minimum deepens and broadens in the resonant coupled case. In contrast, in the side coupled case, the mode evolves into a dark soliton.

4.4.1 Gap solitons

Generally speaking, when there is a frequency gap of some origin, light is exponentially dampened in the structure. However, in nonlinear media when the field has the required strength and shape, it is able to propagate through the gap with complete transmission. Such field excitations are called gap solitons, and they appear in both finite and infinite settings. Chen and Mills were the first to theoretically report gap

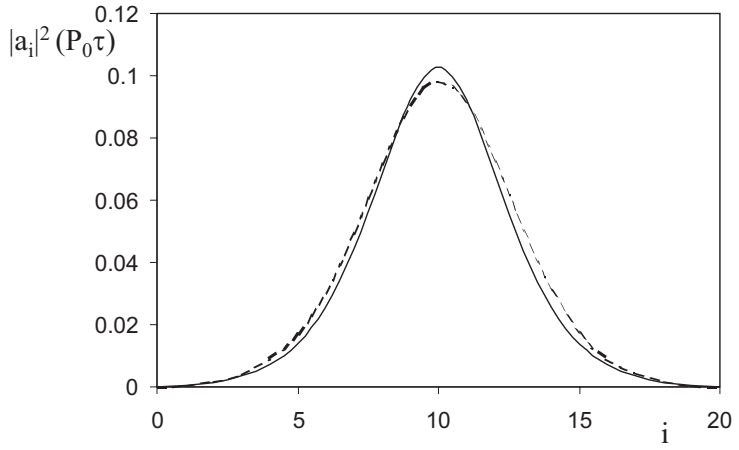

Figure 4.9: Fundamental gap solitons for resonant (solid line) and side coupling (dashed line) geometry, with necessary input powers respectively $0.94 \times 10^{-4} P_0$ and $1.08 \times 10^{-4} P_0$. a_i is the amplitude of resonator number i. The energy profiles follow a sech^2-curve.

solitons in finite distributed Bragg reflectors [41], but they appear in numerous other systems [58, 59, 60, 61]. In section 3.5 we presented calculations on a DBR structure, with formation of gap solitons.

Here, we find the same type of fundamental gap solitons in both cavity geometries. In figure 4.9 we show the sech-profiles of the resonator amplitudes for $N = 21$. For the calculations in this section we use $Q = 1000$, $P_0 = 0.5 \times 10^5 \mathrm{W/m}$, $\omega_r = 0.4 \times (2\pi c/p)$, and $p = 0.6\mu\mathrm{m}$. We choose $\delta = -1.05$ for the resonant coupled case and $\delta = 0.95$ for the side coupled case. These frequencies are near the upper frequency edge of the gap with $\phi = \pi/2$, so in combination with positive nonlinearity, gap soliton switching is possible. Note that the higher-order multiple-hump modes can also be observed in these systems.

The previous modes develop from linear transmission maxima. A small detuning from the linear peak gives a profile of the nonlinear mode similar to the linear profile. By increasing the detuning the nonlinear mode evolves into the sech-shape, because the center maximum acts as a nonlinear energy trap for the field.

We can comprehend the existence of gap solitons for resonantly coupled systems in the following way. If $\sin\phi \neq 0$, we can eliminate the waveguide amplitudes from equations 4.1-4.3. The relations are rewrit-

ten as a chain of equations with the resonator amplitude a_n coupling to the nearest neighbours a_{n-1} and a_{n+1}. We obtain:

$$j\frac{\mathrm{d}a_n}{\mathrm{d}t} = \left(-\omega_r + \frac{\cot\phi}{\tau}\right) a_n + \frac{1}{P_0\tau^2}|a_n|^2 a_n + \frac{1}{2\tau\sin\phi}(a_{n-1} + a_{n+1}). \tag{4.10}$$

This is the *discrete nonlinear Schrödinger* (DNLS) equation. When the intensity varies slowly over adjacent resonators, this discrete set of equations can be converted to a single continuous *nonlinear Schrödinger* (NLS) equation [9]. This is the case if the chain consists of many resonators and the excitation is broad enough. The NLS equation for the infinite system has soliton solutions. Therefore, we expect these solutions to appear in our finite series. Indeed, truncation of the soliton tails can present a relatively small perturbation.

Remark that one cannot simply cast the equations of the side coupled system in the DNLS form. This reflects the distributed feedback character of the geometry, in contrast with the localized feedback in the resonant coupled case [66].

4.4.2 Transmission anomalies

In contrast to the previous, where the modes originate from linear transmission peaks, resonances from a purely nonlinear origin are also possible [62]. If the input power becomes strong enough, a branch with solutions in the gap appears. The new branch does not have a linear source.

This principle is explained in figure 4.10, where we show the transmission versus δ for a fixed input power. The graph corresponds to a resonantly coupled system of five resonators. The number of resonators is limited in this section, in order to be able to keep track of the possible states. The branch with maximum transmission near (a) actually consists of two nearby curves, and the one with highest transmission is stable. The inset in the figure shows the energy profile of the gap soliton state indicated by (a).

Note that by increasing the input power, the maximum (a) moves to the right, in contrast with the 'normal' gap soliton of 'linear' origin. Eventually they connect and interact with each other. Transmission then drops below one, so these soliton states no longer exist above this power threshold. It was shown in [62] that the new finite gap solitons are very similar to the solitons of the infinite structure. These modes are therefore more 'intrinsic' than the conventional gap solitons.

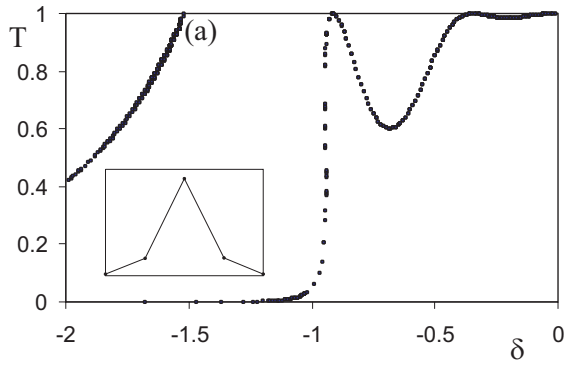

Figure 4.10: Transmission versus δ for a resonant coupled system with $N = 5$ at fixed input power $0.02P_0$. The gap soliton originating from a nonlinear resonance is indicated by (a), and the energy profile $|a_i|^2$ is shown in the inset.

The previous modes are reported in resonant coupled series. However, we found that they also appear in side coupled systems, with similar characteristics. In figure 4.11 we show transmission versus δ for the linear case and for two different input powers. The nonlinear branch is clearly separated from the 'linear' branch with the smallest power P_1. The branches connect at power P_2. Thus, the curves illustrate the same movement and interaction of the two types of solitons, as in the resonant coupled case.

4.4.3 Dark solitons and boundary states

We established that the conventional gap solitons evolve from a linear transmission peak with maximum intensity in the center. Here, we apply this idea to find other types of nonlinear modes. Indeed, for certain ϕ-values peaks appear with a *minimum* in the center, and maxima on the boundaries. These profiles are present both in side coupled and resonantly coupled systems. However, the form of the nonlinear mode is different for both geometries.

First, we turn our attention to side coupled resonators and the peaks in their spectrum near $\phi = 0$, see figure 4.7. The rightmost peak in this spectrum has a profile with a minimum in the center and two maxima on the input and output boundaries. This is different from the gap solitons, and indeed allows for energy localization near the interfaces.

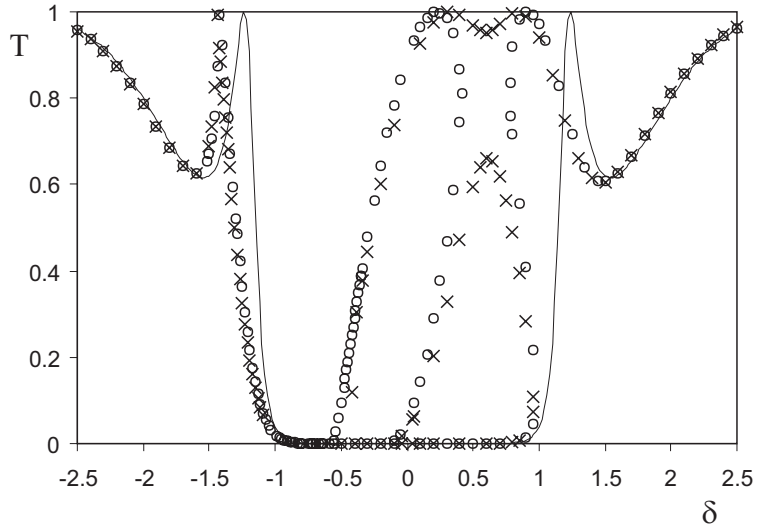

Figure 4.11: Transmission versus δ for a side coupled system with $N = 5$ at fixed input powers $P_1 = 0.08P_0$ (circles) and $P_2 = 0.09P_0$ (crosses). The linear transmission is also shown with a solid line.

In order to have reasonable contrast switching we choose ϕ so that the peak is located near the left side of ω_r. This is possible as it is the last peak to disappear as ϕ approaches zero from the negative side. With $\phi = -0.005\pi$ and $N = 20$ a linear maximum is located at $\delta = -1.3$. We switch from $\delta = -1.6$ with transmission $T = 0.34$ towards this state. The nonlinear mode profile, together with the normalized original linear profile, is shown in figure 4.12. Clearly the nonlinearity adjusts the mode, creating a different profile with energy near the edges. If the detuning increases, the field becomes more localized along the boundaries, with strong decay towards the center.

Now we examine the resonantly coupled devices. If $\phi = 0$ there is only one maximum at $\delta = 0$. When we increase ϕ slightly, new peaks appear and approach $\delta = 0$ from the negative side. The first one, which is thus closest to $\delta = 0$, has a minimum in the center. For $\phi = 0.005\pi$ and $N = 20$ there is such a resonance at $\delta = -0.775$. With positive nonlinearity we have to detune to the left side of this peak. The linear profile and the corresponding nonlinearly adjusted mode are shown in figure 4.13. In contrast to the side coupled case, the mode evolves into a dark soliton! If we increase the detuning, the power of the con-

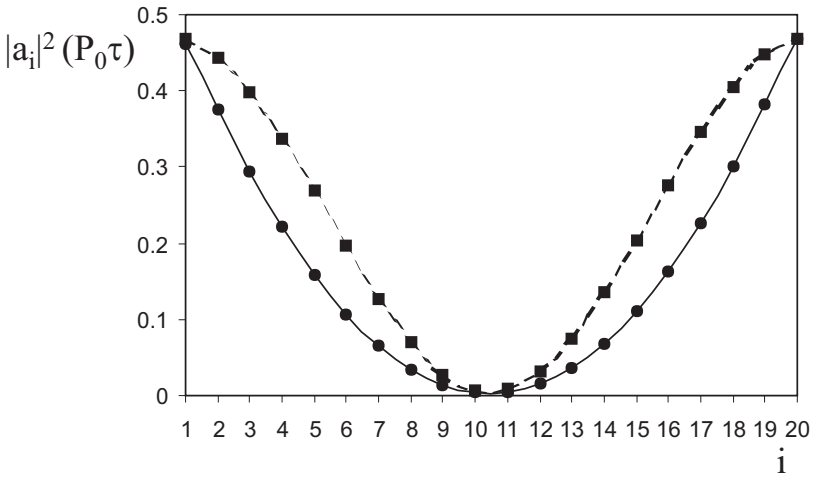

Figure 4.12: Resonator energy profile of the nonlinear switching mode for 20 side coupled cavities. The dashed line shows the corresponding linear resonance profile at $\delta = -1.3$, normalized according to the maximum nonlinear value. The solid line shows the nonlinearly adjusted resonance with $\delta = -1.6$ and input power $0.6P_0$.

stant background increases and the dip becomes narrower. Again, we intuitively understand the existence of this dark soliton via the NLS equation, which contains dark soliton solutions.

On the experimental side much progress has been made in the fabrication of ring resonators [67]. However, nonlinear reports remain scarce [68, 69]. On the other hand, multiple consecutive side coupled resonators in photonic crystals have already been made [70]. But, again, a nonlinear PhC resonator has not been shown yet. If one allows the cavities to couple a bit of their light out-of-plane, it would provide a very direct channel to observe the nonlinear modes.

In this section we gave an overview of possible nonlinear states in both systems. We will now turn our attention to a more concrete switching example, as multiple resonators promise lower power requirements.

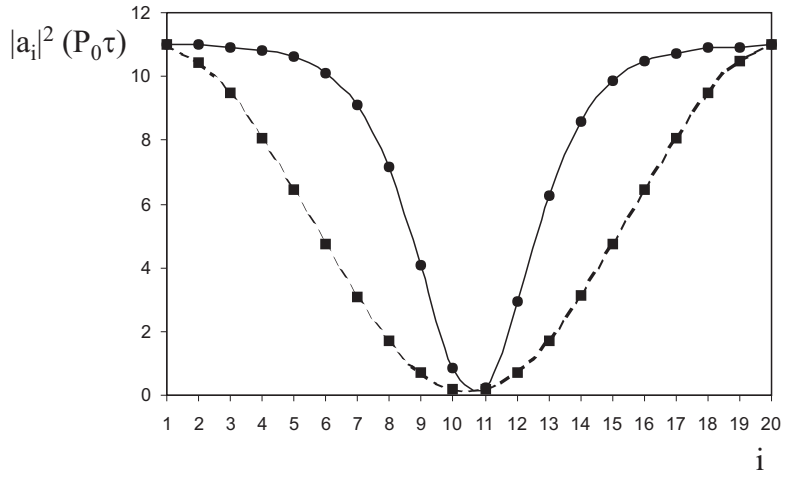

Figure 4.13: Resonator energy profile of the nonlinear switching mode for 20 resonantly coupled cavities. The dashed line shows the linear resonance profile at $\delta = -0.775$, normalized according to the maximum nonlinear value. The solid line shows the nonlinearly adjusted resonance with $\delta = -11$ and input power $10.97P_0$.

4.5 Switching

Here we focus on two side coupled resonators, and look at the switching opportunity of the narrow peak appearing with small ϕ, see figure 4.8. We design a PhC structure and calculate the linear and nonlinear characteristics with rigorous simulations. For this purpose we use the method explained in chapter 3. These calculations are compared with CMT.

The structure is shown in figure 4.14. The PhC is a square lattice with period $p = 0.6\mu\mathrm{m}$ of square rods with diameter $d = 0.4p$. The rods have index 3.5 in an air background. A waveguide is formed by removing a row of rods. The two larger rectangles create the resonators and have sides p and $0.48p$. We use TM-polarization, thus with one electric field component parallel to the rods.

The linear transmission for one and two resonators is plotted in figure 4.15, both with CMT and mode expansion. From the single resonator transmission we get a resonance frequency $\omega_r = 0.3668767 \times (2\pi c/p)$ and $\tau = 19475.8/(2\pi c/p)$. Thus the resonator has $Q = \omega_r\tau/2 = 3573$. In the region around ω_r the waveguide phase is $-k_z p = -1.6731$.

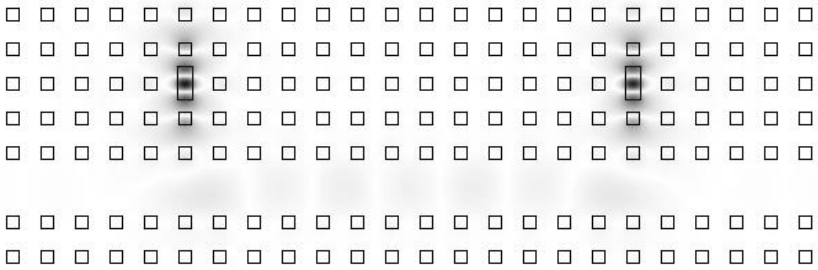

Figure 4.14: Structure of the PhC switching device. The electric field at the transmission maximum is superimposed. Because of high Q the waveguide field is very small compared to the resonator fields.

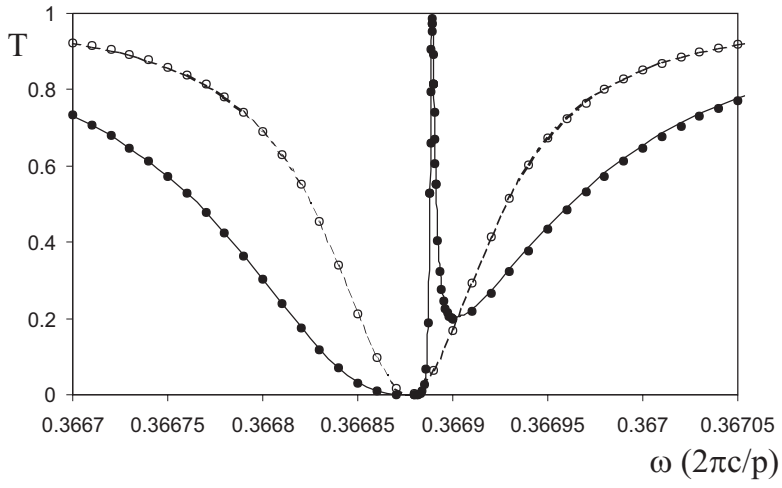

Figure 4.15: Linear transmission for one and two resonators. The dashed (solid) line represents the CMT calculations, whereas the circles (dots) show the rigorous simulations for one (two) resonator(s), respectively.

With a cell of thirteen periods, and thus twelve periods between the resonators, the phase equals $\phi = 0.2408$. The CMT curve with these parameters agrees well with the exact simulations.

For the nonlinear CMT calculations we need the characteristic power P_0 of the resonator. This power can be determined from an integral or a fitting to a nonlinear input/output-curve of one resonator from rigorous simulations [36]. We used the latter approach and obtained $P_0 = 0.32086 \times 10^4 \mathrm{W/m}$. Here the resonator rectangle is considered nonlinear with Kerr coefficient $n_2 = 2 \times 10^{-19} \mathrm{m}^2/\mathrm{V}^2$. The nonlinear index change is $n_2|\mathbf{E}|^2$ with $\mathbf{E}$ the electric field.

Then we performed nonlinear exact simulations on the system with two resonators separated by twelve periods. We choose $\omega = 0.366883 \times (2\pi c/p)$ which is next to the transmission maximum. The bistable transmission curve is shown in figure 4.16, and agrees with the CMT calculations. It is clear from the scale in the figure that lower powers are required for switching, than with one resonator. Of course, two resonators have twice the amount of nonlinear material, but the main reason is the narrow maximum. Although this peak is only approximately Lorentzian, its fitted Q is about 40 times larger than the Q of one resonator. As P_0 is proportional to the inverse square of Q, we can estimate the characteristic power of our device to be three orders of magnitude smaller, and thus more power efficient.

The previous argument is more concrete, if we compare the input power at the bistability threshold of one and two resonators, respectively. However, this comparison is not strict, because the systems have a different nonlinear behaviour. For one resonator bistability appears if $\delta < -\sqrt{3}$, so we choose $\delta = -\sqrt{3}$ and obtain at the switching point (where the transmission decreases rapidly) $P_{in} = 1.347 P_0$. For the device with two resonators the bistability threshold is $\omega = 0.3668863(2\pi c/p)$ and at the switching point (where transmission increases rapidly) $P_{in} = 2.52 \times 10^{-3} P_0$. This corresponds indeed with a factor 10^3.

4.6 Conclusions

In this chapter we showed that CMT is a fast and flexible tool to study series of resonators. Here, we examined cavities inside and adjacent to the waveguide. For the former the calculations are direct. For the latter we have to implement the iterative Newton-Raphson method to solve the nonlinear equation.

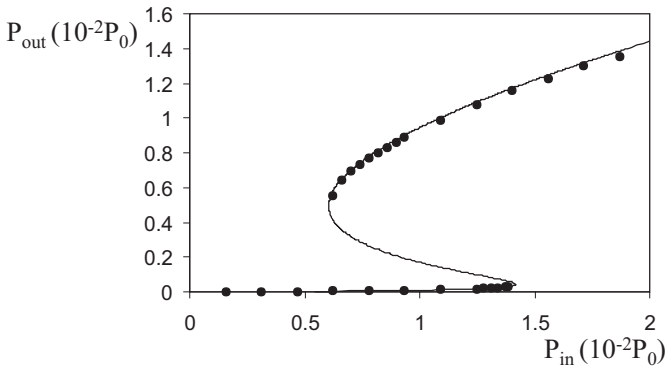

Figure 4.16: Output power versus input power for the two resonator device at $\omega = 0.366883 \times (2\pi c/p)$. The CMT calculation is shown with a solid line, the dots represent rigorous simulations.

An overview of the linear properties demonstrates the similarities and differencies between the geometries. The important parameters are the phase ϕ and the number of resonators. These determine the number, location and width of the transmission peaks.

In both systems we examined three types of nonlinear modes for finite series: (conventional) gap solitons, anomalous resonances and boundary states. In fact, the first two can be termed gap solitons, as their frequency lies in a gap. They have an intensity profile with a maximum in the center. The anomalous resonance has no linear peak as origin, therefore it is a new kind of intrinsic localized mode. In side coupled systems these had not been reported yet.

On the other hand, the boundary states correspond with a linear peak, but with an intensity minimum in the center. In the side coupled case the field on the boundaries becomes large, with immediate decay towards the center. However, in the resonant coupled case they obtain a dark soliton shape.

Finally, with a correctly chosen inter-resonator distance (and thus ϕ), a narrow linear transmission peak appears in the spectrum of two side coupled resonators. We designed a PhC device to exploit the nonlinear switching near this peak, and demonstrated its efficient operation with both CMT and rigorous calculations. The agreement between the methods proves their usefulness and validity.

Chapter 5

Self-localized waveguides

5.1 Introduction

Solitons have proven to be key to an understanding of nonlinear systems. They are widespread and form because of some sort of balance between linear broadening and nonlinear influences. In optical systems their appearance is varied and in many cases accessible for experiments. Note that we use the term 'soliton' here broadly as a 'solitary wave', meaning a distinct entity created by such an interplay. In contrast, in the strict mathematical sense a soliton is a solution to a system that is integrable, which is rarely the case. Because of their particle-like behaviour (hence the '-on' in soliton) they are natural candidates for representing and processing data.

A division is made between temporal and spatial solitons. For temporal solitons the linear effect of dispersion is balanced, whereas for spatial solitons the effect of diffraction is countered. The previous distinction is not conclusive, of course. A lot of analytical machinery e.g. is applicable in both settings. However it is clear that the spatial kind offers a broader set of possibilities, e.g. because of the number of transverse dimensions. Note that both types can arise from different kinds of nonlinearities. For spatial Kerr solitons the self-focusing effect because of a central refractive index increase is clear. However, quadratic solitons exist also, where fundamental and second harmonic are locked with each other. Here we will mainly restrict ourselves to spatial solitons with the Kerr nonlinearity.

Combining nonlinearities with periodic structures offers an abundance of soliton types. A short overview of some interesting structures is given in section 5.2. In this chapter we make an addition to the fam-

ily of gap or Bragg solitons. In the linear regime a wave with frequency in the gap is exponentially dampened. With nonlinearity a localized structure (propagating or nonpropagating) can be obtained. These entities are also called intrinsic localized modes or discrete breathers.

The solitons we propose are guided Bloch modes in high-contrast 2D photonic crystals without defects. They are confined in the transverse direction because of the gap, but propagate longitudinally as they carve their own guide. With the tool of chapter 3, they can be analyzed efficiently. Two related varieties are presented, and we discuss the important issue of stability. Furthermore we develop a semi-analytical theory, to further understand these solitons. This theory employs the Green's function in a setting with Bloch boundary conditions. From this function effective discrete equations are derived.

We apply the previous methods (numerical and semi-analytic) to diatomic PhCs. These are 2D structures with two superimposed lattices of rods with different dimensions. We consider the larger rods to be linear, so they are responsible for most of the scattering. On the other hand the smaller rods are nonlinear, in order to induce self-localization. Gap solitons appear in these systems too, with numerical and semi-analytical methods showing good agreement.

This chapter begins in section 5.2 with an overview of interesting types of solitons in PhCs. The self-localized waveguide is discussed in section 5.3. Then, in section 5.4 the Green approach is studied. Finally, nonlinear modes in diatomic PhCs are shown in section 5.5.

5.2 Spatial solitons in photonic crystals

A first possible categorization we can make is the disctinction between 1D and 2D PhCs. If we focus first on 1D or planar structures, we can further separate between a periodicity parallel with or perpendicular to the propagation direction, respectively, see figure 5.1. In the former case (fig. 5.1(a)), the appearance of gap solitons is possible, which was first discussed by Chen and Mills [41]. We already encountered these objects in chapter 4, so we move on to structures with periodicity perpendicular to the propagation.

This last case is exemplified by a waveguide array, see fig. 5.1(b). The behaviour of light in such an array can be described in different ways, leading to different types of solitons. If the light is strongly confined in each individual waveguide, coupling between adjacent guides occurs because of overlap of evanescent mode tails. If the array is bet-

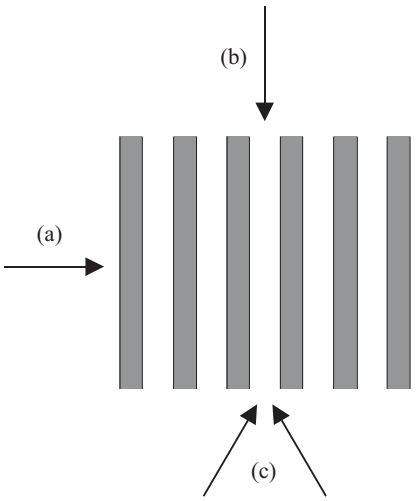

Figure 5.1: Schematic of the 1D PhC geometries. The arrows indicate the main propagation direction for: (a) parallel periodicity and (b) perpendicular periodicity. The two arrows near (c) show the excitation scheme for spatial Bragg solitons.

ter described as a broad waveguide with a periodic perturbation on top, the interaction is more distributed. We now discuss the first case.

If the waveguides are sufficiently separated, the discrete nature of the structure is apparent. When light is injected in only one waveguide, the light will spread via coupling to the other waveguides, which is called discrete diffraction. Here the diffraction strength and character is controllable by the grating parameters [71], as opposed to continuous diffraction. If the intensity increases, the nonlinear phase modulation can overcome this diffraction and discrete solitons are formed. Nonlinear waveguide arrays are easily accessible structures and several experimental studies have been reported [72, 73]. Because of the strong confinement, only nearest-neighbour interaction is needed, and the solitons are solutions of a discrete nonlinear Schrödinger equation (DNLSE). Both wide and narrow waves, consisting of only a few waveguides, are possible, but the latter offer interesting highly compact steering and switching opportunities [74].

By inspecting the DNLSE a rich zoology of solutions has been found. Here we mention that the fundamental ones are the on-site and intersite variety, with respectively one maximum on a center waveguide (see fig. 5.2), and two maxima of equal strength on adjacent waveguides.

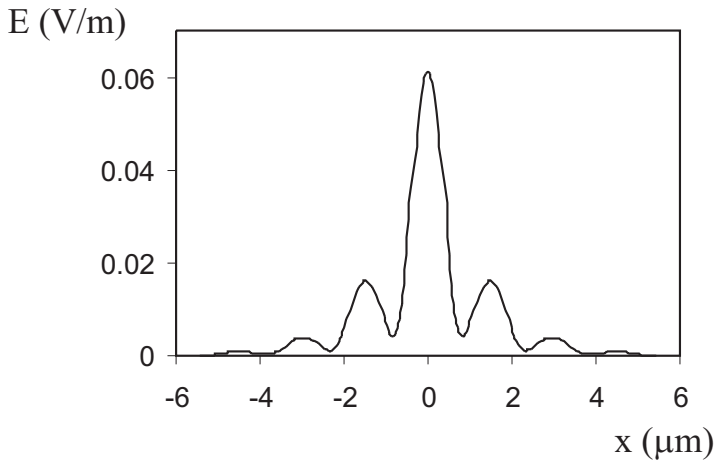

Figure 5.2: Profile of a discrete soliton.

The interplay between these modes affects their stability and mobility, as will become clear in section 5.3.

The discrete solitons of the previous paragraph can also be studied with the iterative nonlinear tool of chapter 3. The profile in figure 5.2 is reached by following the evolution of only one eigenmode, starting from the waveguide array with a slightly higher (or lower, depending on the sign of the nonlinearity) index for the center waveguide. For the figure we operated at $\lambda = 1\mu\mathrm{m}$ with $n_2 = 1\mathrm{m}^2/\mathrm{V}^2$. The waveguides have index 1.5 and width $1\mu\mathrm{m}$, with air layers of $0.5\mu\mathrm{m}$ in between.

Now we turn to the situation with a broad waveguide and a periodic perturbation on top. In this geometry the light reflected from the different interfaces can give rise to Bragg effects. The system is in fact regarded as the gap soliton in a multilayer, with an extra spatial dimension. The localized gap soliton is propagated in this extra direction [75]. When two beams, with frequency around the Bragg resonance, are incident upon the array (as in fig. 5.1(c)), their transversal wavevector components generate strong reflections. If the center amplitude is strong enough, the nonlinearity can create a linear region where the Bragg condition is disturbed, the beam tunes itself outside of the gap. The low amplitude edges are still reflected. We know, e.g. from chapter 2, that a linear defect can create a waveguide mode, hence the creation of this soliton, which is also called a Bragg soliton. This alternative localized mode, which is mostly associated with broad excitations, has

recently been observed experimentally [76, 77], and opens a new road towards applications. Finally, we note that the distinction between the discrete and the Bragg soliton is not conclusive, therefore mixed modes are possible.

The situation in 2D PhCs is less explored. Finite energy gap solitons have been shown to exist and propagate in these structures [78, 79]. Here, different directions correspond to different Brillouin zone points, and give rise to new varieties of solitary waves. The solutions correspond to short, high intensity pulses that propagate with a group velocity between zero and the average speed of light in the medium. However, the previous study is performed in the weak modulation limit, using coupled-mode theory[1]. In this approximation the gap becomes infinitely thin. Therefore, other effects are expected and new approaches are needed for high index contrast structures, beyond the continuous medium approximation.

The long-range interaction in a high-contrast 2D waveguide was shown to exhibit *stationary* localized modes [58]. These solitons correspond with nonlinearly created *point* defects, whereas the self-localized waveguides we propose relate to *line* defects. We adapt their Green's function approach leading to effective discrete equations in section 5.4. The fundamental modes are the same as the previous discrete solitons, meaning on-site and inter-site varieties. Here too, in most cases the on-site mode is stable, whereas the inter-site mode is unstable. We remark that, because of the long-range character of the Green's function, interaction between sites that are multiple periods apart has to be taken into account. Thus, because of the nonlocal effective influence the nearest neighbour approximation is no longer sufficient.

An important system was recently introduced in photorefractive crystals [80]. In these materials an optical pattern can induce a 2D waveguide array. If a probe beam is launched along a waveguide it can couple to neighbouring waveguides in two transverse directions because of 2D discrete diffraction. However, with high nonlinearity the beam may remain in one waveguide. These 2D discrete solitons have been observed experimentally [81, 82].

We gave a short overview of spatial solitons in Kerr nonlinear PhCs. It is clear that every system has its unique characteristics. However,

[1] Not to be confused with the different CMT of section 2.5.

the physics and equations have a lot in common. Therefore, the ideas offered here, will reappear in the next sections.

5.3 Self-localized waveguides

Spatial solitons can be interpreted from a more linear point of view. Indeed, they appear to be the linear guided modes of their self-induced waveguides [83]. This also means e.g. that every linear guided mode is the soliton of a certain nonlinearity, provided that the amplitudes and the nonlinearity relation are consistent with each other. This idea is very fruitful in a mode expansion context, as the soliton is described with only one mode. We used this already for the discrete soliton in the previous section. Here we extend the modal description of solitons towards Bloch modes in 2D PhCs. In this way, the spatial 2D soliton is the linear guided Bloch mode of the self-induced 2D waveguide.

With the waveguide idea we are also led to an analogous way to understand the self-localized waves. In a perfect PhC excitations with frequency within the bandgap are exponentially dampened. If a linear defect is introduced, a waveguide mode can be created. Now, in a nonlinear PhC without defects the field itself can change the index locally, and create its own waveguide, hence the creation of gap solitons.

From these ideas we set out to find self-localized waveguides in a nonlinear photonic crystal, starting from a linear waveguide mode. Figures 5.3 and 5.4 illustrate the waveguide modes. They are confined in one direction by bandgap effects, and propagate in the other direction because the beam itself creates a defect waveguide. The lattice consists of rods with diameter $0.25a$ and index 3.4 in air. The rods have a negative Kerr nonlinearity $n_2 = -1\ \mathrm{m}^2/\mathrm{V}^2$. Note that we applied $\varepsilon(\mathbf{r}) = \varepsilon_0 + n_2 I(\mathbf{r})$ instead of $n(\mathbf{r}) = n_0 + n_2' I(\mathbf{r})$, in order to correspond with the semi-analytical method of section 5.4. If the nonlinear index change is small compared to the linear index, both are equivalent, with $n_2 = 2n_0 n_2'$.

To model these modes we use the technique of chapter 3, but start with a 'seed'. We lower the index of a center rod to create a linear defect waveguide. The linear guided Bloch mode with this index gives an estimate of the needed flux and a starting index distribution. If we iterate from this distribution, with constant flux, and converge to a guided mode, we have reached a self-localized waveguide. After finding one mode we can slightly change the frequency or the flux to iterate to new modes quickly and map their properties.

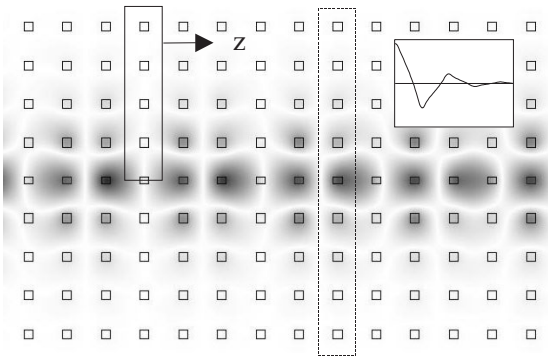

Figure 5.3: Example of the electric field of an on-site staggered self-localized waveguide. The solid box shows the used unit cell to find the mode. The dashed box is used for the study of stability versus asymmetric perturbations. For the figure the mode is linearly propagated through a crystal with refractive index distribution derived from the box calculation. The inset shows the electric field profiles in a transversal cut through the rod centers. Parameters are $a/\lambda = 0.38$ and $P = 8 \times 10^{-10}\mathrm{W/m}$.

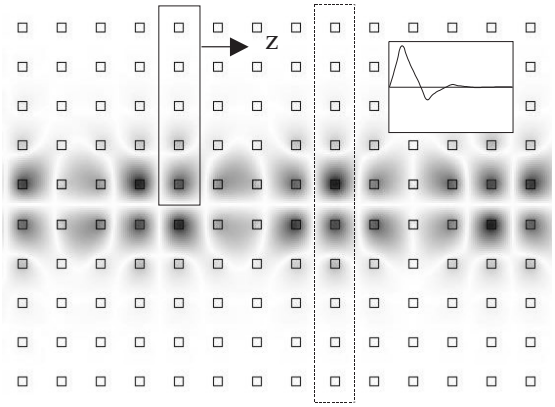

Figure 5.4: Same as fig. 5.3 but for an inter-site mode and with $a/\lambda = 0.41$ and $P = 9 \times 10^{-10}\mathrm{W/m}$.

We found two types of modes. The on-site variety is depicted in figure 5.3, the inter-site type is shown in figure 5.4. The insets show a typical field profile. These profiles are reminiscent of the types of localized modes reported in the previous section. This suggests the possible existence of similar modes in other propagation directions or geometries, e.g. air holes in material.

Stability

The issue of stability is very important for spatial solitons. Only stable waves may be observed easily in experimental situations. On the other hand, we can exploit the onset of instabilities for steering or switching the packets in future networks.

In this section we examine the stability of the self-localized waveguides, in the sense that we explore their robustness against small perturbations. Because the waves are two-dimensional Bloch modes, we will have to adapt the known analytical criteria of soliton theory.

We can study stability with our rigorous modeling method, as the iterative character means the calculations only converge onto stable solutions.

First of all we have to distinguish between perturbations that have the same symmetry as the mode and perturbations that do not include this symmetry. The former are studied with the solid boxes in figures 5.3 and 5.4. Indeed, the boundary condition along the lower edge of this unit cell determines the symmetry of the solutions and of the perturbations. We examine the other perturbations using the dotted larger boxes shown in figures 5.3 and 5.4.

From the half-box simulations we conclude that the on-site modes are stable against same-symmetry perturbations for propagation constants k ranging from a critical value k_{cr} up to π/a. This is shown in figure 5.5, where we see e.g. that $k_{cr} \approx 0.33\pi/a$ for $\omega = 0.36(2\pi c/a)$. The same conclusions apply to the inter-site modes. Furthermore, we notice that the curve of the power P versus k shows an extremum at the critical value k_{cr}. This means that the stability of the mode changes if

$$\frac{\mathrm{d}P}{\mathrm{d}k} = 0. \tag{5.1}$$

This is very analogous to the well-known Vakhitov-Kolokolov theorem of soliton theory [9]. For certain models, such as the generalized nonlinear Schrödinger equation, it has been shown that stability depends

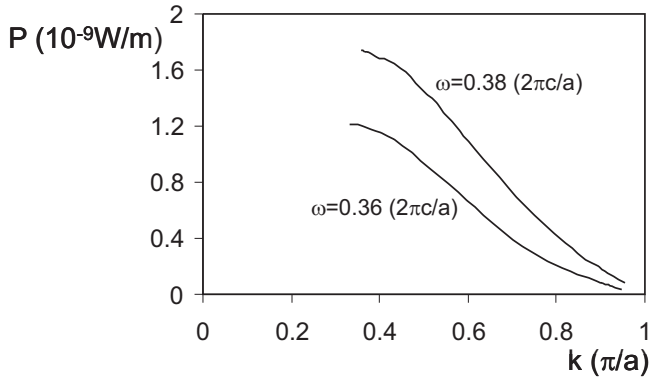

Figure 5.5: Power P versus Bloch propagation constant k for on-site modes of frequencies $\omega = 0.36(2\pi c/a)$ and $\omega = 0.38(2\pi c/a)$.

on the sign of $\mathrm{d}P/\mathrm{d}k$, where P stands for the relevant 'power' of the system, and k indicates the propagation constant. When the stability changes, this of course implies equation 5.1. In our system the solitons are Bloch modes of a high-contrast two-dimensional PhC, so k is a *Bloch* propagation constant. Thus we presented numerical proof that the Vakhitov-Kolokolov criterium still applies in this situation. We will show more evidence in section 5.5, where another geometry is examined.

Notice that the data in figure 5.5 stops close to $k = \pi/a$. This does not mean the mode is unstable at the edge of the Brillouin zone, but it is a consequence of the power normalization choice. We mentioned in chapter 3 that in order to reach the edges, it is better to normalize using energy instead of power, because the power tends to zero as the mode becomes a standing wave. However, even with power normalization it is possible to come close to the edge, but it involves careful iterations with large values of α, see equation 3.7. We try to avoid energy normalization as it is much slower.

Now we discuss stability against perturbations that lack the symmetry of the mode. For this purpose we perform calculations on the complete modes, using the dashed boxes in figures 5.3 and 5.4. In this box we can slightly perturb the indices of a rod and start the iteration. This procedure injects the soliton with eigenmodes of the symmetry which are not present in the half-box simulations.

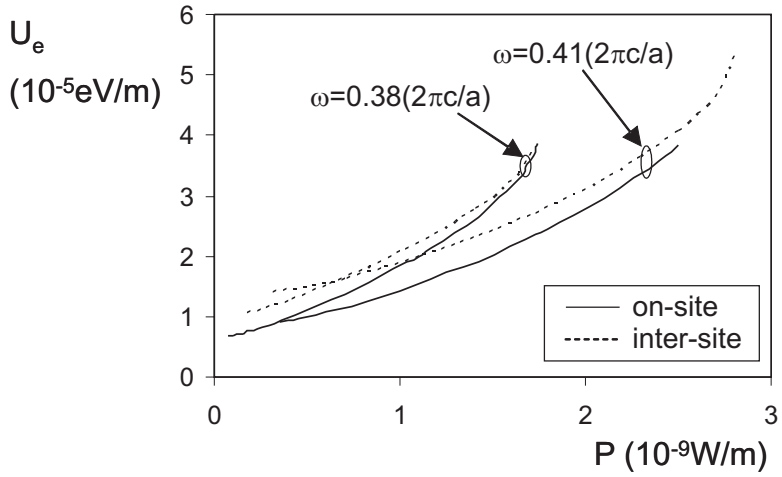

Figure 5.6: Energy U_e versus power P for self-localized waveguides of different wavelengths.

The results can be understood by applying Peierls-Nabarro potential ideas [84]. According to this concept, inter- and on-site modes with the same topology can be seen as constituents of the same soliton. Assuming equal intensity (or power), the component with the highest energy will be unstable and evolve into the stable one with lowest energy. This qualitative picture gives insight not only into stability, but also into mobility and switching opportunities. If the soliton wants to move in the transversal direction, it has to change between the on-site and the inter-site modes. The difference in energy determines the Peierls-Nabarro barrier that has to be overcome to change from one stable mode to the next via the unstable intermediate mode. Thus, if the energies are the same the modes are expected to be mobile in the transverse direction. Note that there is always propagation in the longitudinal direction.

We have calculated the energy of both types of self-localized waveguides for frequencies in the gap. Remark that the two types have the same topology, both are staggered, and thus the previous ideas can be applied. Results are shown in figure 5.6. Assuming a constant power P, the on-site modes have the lowest energy, so this suggests they are stable, whereas we expect the inter-site component to be unstable.

This statement is confirmed by numerical calculations. Even a small change of 0.1% in the indices of an inter-site center rod is enough to

push the iteration towards convergence on an on-site mode. On the other hand, the on-site modes are very robust.

The previous is in agreement with the analysis of discrete solitons and stationary gap solitons in 2D PhCs. There too the inter-site modes are unstable and transform into the corresponding on-site counterpart. For discrete solitons this has been confirmed experimentally and used for beam steering [73].

Confinement

Next, we study the transverse width of the modes, by calculating the following simple 'deviation':

$$\sigma = \sqrt{\sum_i d_i^2 E_i^{max} / \sum_j E_j^{max}}, \tag{5.2}$$

with d_i the distance from the center and E_i^{max} the maximum electric field absolute value of rod i. This deviation versus maximum refractive index change for the on-site modes is shown in figure 5.7. For the inter-site waveguides the curves are parallel. At the low frequency gap edge we notice a strong broadening of the modes as we decrease the power. Although the nonlinear index change is lowest here, below 0.05, these modes lose the strong discrete localization and instead get a more continuous character. In the gap decreasing the wavelength or the refractive index change (or power P) leads to narrower waveguides. However, these trends no longer apply on the upper frequency edge of the gap. Remark that the modes in the gap have a deviation smaller than 1.6, so these are indeed strongly localized modes. If σ is below 1 the waveguides appear very tightly bound on one center rod. This is illustrated by the insets in figure 5.7.

The broad modes at the low bandgap edge are analogous to the fundamental solitons in bulk nonlinear materials [85]. However, there are important differences. First, the bandgap structure makes it possible to support waveguides with a low refractive index core. Solitons in bulk material are guided in a self-induced high refractive index core, by total internal reflection. Next, because of the anisotropic and discrete lattice the stability and dynamical behaviour will be different from the continuous counterpart, especially for the modes localized around a few periods. We provided some insight in the stability, however a full analysis and dynamical treatment is beyond the current scope of the modeling method.

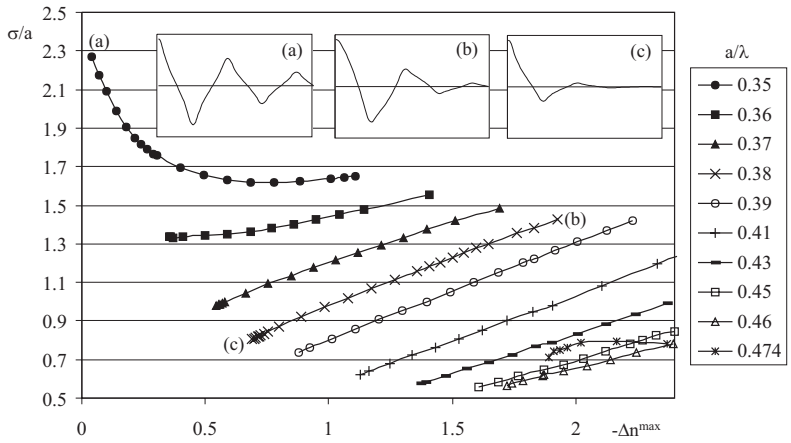

Figure 5.7: Width σ versus maximum refractive index change Δn_{max} for on-site modes of various wavelengths (see legend). The insets show the electric field profile for the three indicated points.

We note that the minimum nonlinear index change for strongly localized solutions in the gap is very high, around 0.3. However, it is clear that there are possibilities for optimization. On the other hand, a possible route towards experiments might be the inclusion of liquid crystals in the holes of a PhC [86, 87]. The slow but giant nonlinearities of these materials can reach the needed values for self-localized waveguides.

In recent theoretical studies related waveguide modes have been examined [88, 89, 90]. However, in these papers a coupled mode approach is used, with a system of equations that does not contain a true bandgap. Because the bandgap confinement is crucial for our modes, we developed another method, that we explain in the next section.

5.4 Strip Green theory

In this section we provide a theoretical framework to better understand the self-localized waveguides. The theory originated from a collaboration with Guy Van der Sande at the VUB in the context of the IAP Photon project. The analysis models the fields in the PhC as an interaction between the rods, that is dependent on the distance between the sites. Furthermore, because we obtain a set of algebraic equations, instead of differential equations, it can provide information on modes that are un-

stable. In contrast the rigorous method is unable to converge to these modes.

The idea is to combine two concepts. First, the Green's function is an efficient tool to describe PhC structures [58]. Moreover, the Bloch character of a waveguide mode can be exploited to restrict the function to a narrow strip, the strip Green's function [91]. Second, starting from the Green's function effective discrete equations can be derived to model nonlinear interactions [58]. The previous concepts are now explained and linked to each other.

Note that until the end of this chapter the axes are oriented as shown in figure 5.8. We assume that the gap solitons propagate along the horizontal x-direction.

5.4.1 Green formulation

We consider TM-polarization so we can start from the scalar Helmholtz equation:

$$\left[\nabla^2 + \varepsilon(\mathbf{r})\left(\frac{\omega}{c}\right)^2\right] E(\mathbf{r}|\omega) = 0. \tag{5.3}$$

We note $E(\mathbf{r}|\omega)$ to emphasize ω is a chosen constant parameter. In the following ε will consist of two contributions:

$$\varepsilon(\mathbf{r}) = \varepsilon_{pc}(\mathbf{r}) + \varepsilon_d(\mathbf{r}). \tag{5.4}$$

Here, ε_{pc} is the linear PhC background, and ε_d is a defect permittivity change. In our case ε_d will represent the nonlinearity. The PhC periodicity means:

$$\varepsilon_{pc}(\mathbf{r} + r\mathbf{a_x} + s\mathbf{a_y}) = \varepsilon_{pc}(\mathbf{r}), \tag{5.5}$$

with r, s arbitrary integers, and $\mathbf{a_x}, \mathbf{a_y}$ the lattice vectors of a unit cell of the PhC. With eq. 5.4 in eq. 5.3 we obtain:

$$\left[\nabla^2 + \varepsilon_{pc}(\mathbf{r})\left(\frac{\omega}{c}\right)^2\right] E(\mathbf{r}|\omega) = -\varepsilon_d(\mathbf{r})\left(\frac{\omega}{c}\right)^2 E(\mathbf{r}|\omega). \tag{5.6}$$

This equation can be solved via the Green's formalism, where the Green's function G is defined as:

$$\left[\nabla^2 + \varepsilon_{pc}(\mathbf{r})\left(\frac{\omega}{c}\right)^2\right] G(\mathbf{r}, \mathbf{u}|\omega) = -\delta(\mathbf{r} - \mathbf{u}). \tag{5.7}$$

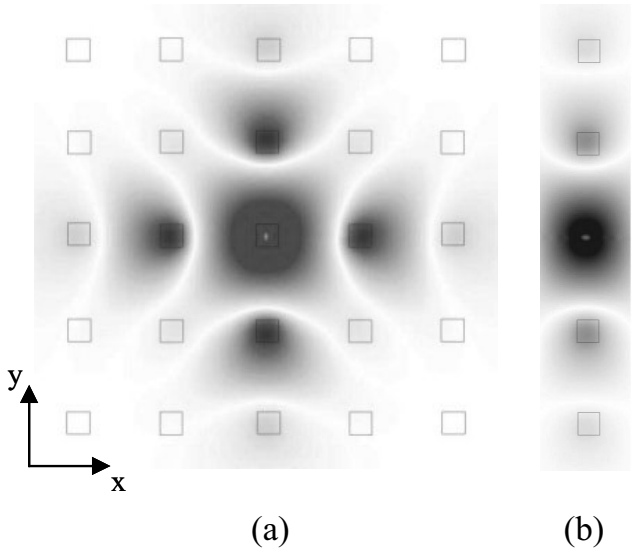

Figure 5.8: Example of the Green's and strip Green's function. (a) Green's function with $\omega = 0.38(2\pi c/a)$ and source in the center of a rod, (b) corresponding strip Green's with $k_x = 0.7\pi/a$.

The following symmetries hold for G:

$$G(\mathbf{r} + r\mathbf{a_x} + s\mathbf{a_y}, \mathbf{u} + r\mathbf{a_x} + s\mathbf{a_y}|\omega) = G(\mathbf{r}, \mathbf{u}|\omega), \tag{5.8}$$

$$G(\mathbf{r}, \mathbf{u}|\omega) = G(\mathbf{u}, \mathbf{r}|\omega). \tag{5.9}$$

The solution of equation 5.6 can then be written in an integral form:

$$E(\mathbf{r}|\omega) = \left(\frac{\omega}{c}\right)^2 \int \mathrm{d}^2\mathbf{u}\, G(\mathbf{r}, \mathbf{u}|\omega)\, \varepsilon_d(\mathbf{u}) E(\mathbf{u}|\omega). \tag{5.10}$$

An example of a Green's function in the perfect linear PhC is shown in figure 5.8(a), with the lattice parameters of the previous section. Because we choose a frequency in the bandgap, the function is exponentially decaying, as only evanescent modes are excited.

Instead of searching for a way to solve the integral equation in the whole 2D space, we exploit the Bloch nature of the problem. Let $\mathbf{r} = (x, y)$ and the period is a. If the self-localized waveguides propagate along x, the system will remain translationally invariant along this direction. In contrast, the periodicity in the y-direction is lost. Therefore, according to Floquet-Bloch theory the mode is characterized by the reciprocal wavevector k_x. In this way, we restrict the model to a strip

$(x, y) = [-\frac{a}{2}, \frac{a}{2}] \times \mathbb{R}$, so the equation becomes

$$\left[\nabla^2 + \varepsilon_{pc}(\mathbf{r}) \left(\frac{\omega}{c}\right)^2\right] E(\mathbf{r}|\omega, k_x) = -\varepsilon_d(\mathbf{r}) \left(\frac{\omega}{c}\right)^2 E(\mathbf{r}|\omega, k_x), \qquad (5.11)$$

with the boundary condition

$$E(x + a, y|\omega, k_x) = E(x, y|\omega, k_x) e^{ik_x a}. \qquad (5.12)$$

Using the partial Floquet transform the corresponding strip Green's function g can be constructed and satisfies [91]:

$$\left[\nabla^2 + \varepsilon_{pc}(\mathbf{r}) \left(\frac{\omega}{c}\right)^2\right] g(\mathbf{r}, \mathbf{u}|\omega, k_x) = -\sum_{j\in\mathbb{Z}} \delta(\mathbf{r} + j\mathbf{a_x} - \mathbf{u}) e^{ijk_x a}, \qquad (5.13)$$

$$g(\mathbf{r} + \mathbf{a_x}, \mathbf{u}|\omega, k_x) = g(\mathbf{r}, \mathbf{u}|\omega, k_x) e^{ik_x a}. \qquad (5.14)$$

The strip Green's function is related to the whole space Green's function via:

$$g(\mathbf{r}, \mathbf{u}|\omega, k_x) = \sum_{j\in\mathbb{Z}} G(\mathbf{r} + j\mathbf{a_x}, \mathbf{u}|\omega) e^{ijk_x a}. \qquad (5.15)$$

So equation 5.8 is also valid here:

$$g(\mathbf{r} + r\mathbf{a_x} + s\mathbf{a_y}, \mathbf{u} + r\mathbf{a_x} + s\mathbf{a_y}|\omega, k_x) = g(\mathbf{r}, \mathbf{u}|\omega, k_x). \qquad (5.16)$$

By folding the whole space Green's function on itself, we reduce the study to modes which are Bloch modes with propagation constant k_x. An example of the strip Green's function is shown in figure 5.8(b).

5.4.2 Effective discrete equations

With the strip Green's function the differential equation 5.11 is transformed into

$$E(\mathbf{r}|\omega, k_x) = \left(\frac{\omega}{c}\right)^2 \int_{strip} \mathrm{d}^2\mathbf{u}\; g(\mathbf{r}, \mathbf{u}|\omega, k_x)\; \varepsilon_d(\mathbf{u}) E(\mathbf{u}|\omega, k_x), \qquad (5.17)$$

with integration restricted to the strip region. We consider the rods nonlinear, so

$$\varepsilon_d(\mathbf{r}) = \delta_{rods}(\mathbf{r})\; n_2 |E(\mathbf{r}|\omega, k_x)|^2, \qquad (5.18)$$

where $\delta_{rods} = 1$ inside the rods and zero outside. Then we use the approximation that the field in a rod is constant. Considering e.g. the profiles in figure 5.8, this is an acceptable assumption. We label the fields with an integer. The center rod is 0. The other rods in the positive (negative) y-direction are positive (negative). With the constant rod field values, noted as $E_n(\omega, k_x)$, the integral in eq. 5.17 is replaced by a discrete sum over the rods:

$$E_n(\omega, k_x) = \sum_{m \in \mathbb{Z}} J_{n,m}(\omega, k_x) |E_m(\omega, k_x)|^2 E_m(\omega, k_x), \tag{5.19}$$

with the coupling coefficients

$$J_{n,m}(\omega, k_x) = n_2 \left(\frac{\omega}{c}\right)^2 \int_{rod} \mathrm{d}^2\mathbf{u}\, g(\mathbf{r_n}, \mathbf{r_m} + \mathbf{u}|\omega, k_x). \tag{5.20}$$

Here $\mathbf{r_n}$ denotes the center of rod n. In our system the number of coefficients is reduced by symmetry. Because of equation 5.16 we immediately obtain $J_{n,m} = J_{0,m-n}$. Furthermore, because we choose as basis points the centers of the rectangles, and these points are on a horizontal symmetry axis of ε_{pc}, it follows that

$$G(\mathbf{r_0}, \mathbf{r_n}|\omega, k_x) = G(\mathbf{r_0}, \mathbf{r_{-n}}|\omega, k_x). \tag{5.21}$$

This implies $J_{0,n} = J_{0,-n}$. Finally, we obtain that the coefficient is only dependent on the distance between the rods, thus $J_{n,m} = J_{|n-m|}$, so we have:

$$J_n(\omega, k_x) = n_2 \left(\frac{\omega}{c}\right)^2 \int_{rod} \mathrm{d}^2\mathbf{u}\, g(\mathbf{r_0}, \mathbf{r_n} + \mathbf{u}|\omega, k_x). \tag{5.22}$$

Now, we can summarize the procedure. First the Green's function is determined for a chosen frequency in the bandgap, so the function is exponentially decaying. This can be done with e.g. CAMFR. Then, the wavevector k_x is fixed and the strip Green's function is calculated with equation 5.15. Averaging of this function, as in equation 5.22, one obtains the long-range coupling coefficients J_n. Because the nonlinear mode excites a limited number of rods, we can truncate the set of coefficients and the effective discrete equations in equation 5.19. The resulting system is nonlinear and can be solved with e.g. the standard Newton-Raphson method [92], already encountered in chapter 4.

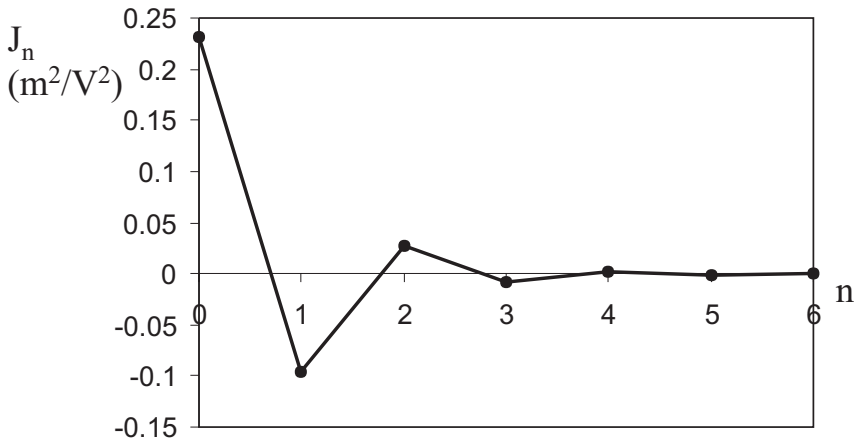

Figure 5.9: The coupling coefficients J_n at $\omega = 0.38(2\pi c/a)$ and $k_x = 0.7\pi/a$.

5.4.3 Comparison

With the strip Green method it is possible to compare the rigorous simulations with semi-analytical results. First of all, we show an example of the coupling coefficients. In figure 5.9 J_n is presented for $\omega = 0.38(2\pi c/a)$ and $k_x = 0.7\pi/a$. The same lattice parameters are used, so index 3.4 in air and square rods with diameter $d = 0.25a$. The exponential and staggered (changing sign) behaviour, originating from the Green's function, is evident. It is clear that a truncation at J_6 is acceptable. This is in agreement with the numerical simulations, where four nonlinear rods (including symmetry) are enough for convergence. Indeed, the set of equations for an on-site self-localized waveguide, centered on $\mathbf{r_0}$, is given by:

$$\begin{bmatrix} E_0 \\ E_1 \\ E_2 \\ E_3 \end{bmatrix} = \begin{bmatrix} J_0 & 2J_1 & 2J_2 & 2J_3 \\ J_1 & J_0+J_2 & J_1+J_3 & J_2+J_4 \\ J_2 & J_1+J_3 & J_0+J_4 & J_1+J_5 \\ J_3 & J_2+J_4 & J_1+J_5 & J_0+J_6 \end{bmatrix} \cdot \begin{bmatrix} |E_0|^2 E_0 \\ |E_1|^2 E_1 \\ |E_2|^2 E_2 \\ |E_3|^2 E_3 \end{bmatrix}. \quad (5.23)$$

An analogous set for the inter-site variety can be derived.

From these systems solutions of both types are found, complying with the existence in the full simulations. With the discrete field values

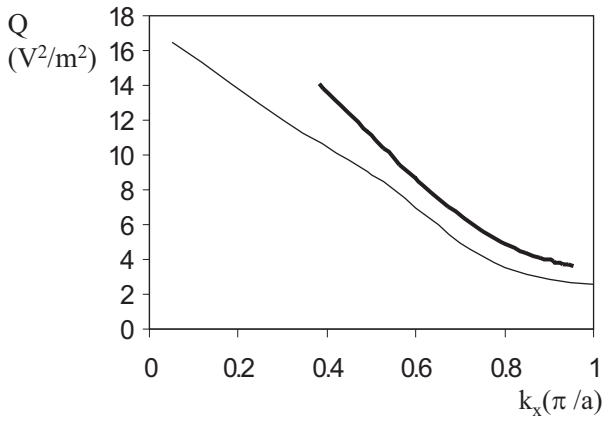

Figure 5.10: Modal energy comparison between strip Green (thin line) and rigorous simulations (thick line).

the modal energy can be described by:

$$Q = \sum_n |E_n(\omega, k_x)|^2, \tag{5.24}$$

which is related, but not equal, to the energy of the electric field, equation 3.6. For the modal energy of the rigorous calculations we average over the rods. In figure 5.10 we show a comparison of this energy Q for on-site modes at $\omega = 0.38(2\pi c/a)$ with varying k_x. The agreement is qualitative, but the strip Green's method is able to cover a larger k_x-range. If we look at the individual rod amplitudes, shown in figure 5.11, it is clear that the discrepancy stems from the center rod.

In conclusion, the long-range interaction inherent in the strip Green method gives a theoretical understanding for the existence and qualitative behaviour of the self-localized waveguides. The quantitative difference is a consequence of the main approximation of the method, the assumption that the field is constant in a rod. This is understandable, as in the used geometry the diameter is a quarter of the period. To improve the accuracy, it is not straightforward to reduce the diameter, because the bandgap then narrows and the modes become less stable. Therefore, we proceed instead with an alternative geometry.

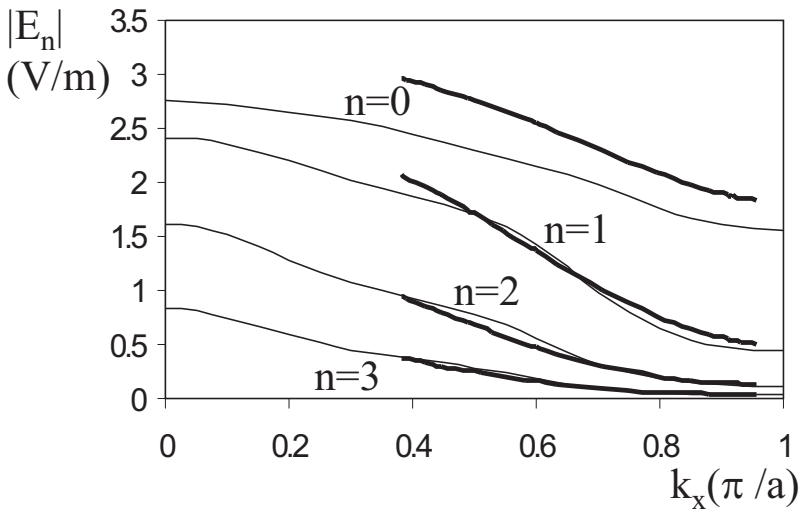

Figure 5.11: Individual rod amplitude comparison between strip Green (thin line) and rigorous simulations (thick line).

5.5 Diatomic lattice

Here we consider an alternative PhC geometry, depicted in figure 5.12. This PhC consists of two offset square lattices with rods of different size, therefore it is also called a diatomic crystal. The structure is able to exhibit larger absolute bandgaps (overlapping gap for both polarizations), compared to the normal square lattice [93]. This is because the reduction of symmetry can lead to the cancelling of degeneracies at band edges, thereby opening the way towards larger gaps. We do not use this characteristic. Instead, we will consider the larger rods to be linear, so they impart most of the linear scattering. On the other hand, we assume the small rods have a positive nonlinearity, so they may be able to induce nonlinear localization.

Because the nonlinear sections are smaller than in the previous section, we expect a better agreement between the strip Green method and the rigorous calculations. All rods in the PhC have index $\sqrt{12}$ in an air background. The diameters are, respectively, $0.2a$ and $0.1a$. This crystal has a TM bandgap between $\omega = 0.389$ and $0.436(2\pi c/a)$. An example of the Green's and strip Green's function is shown in figure 5.12.

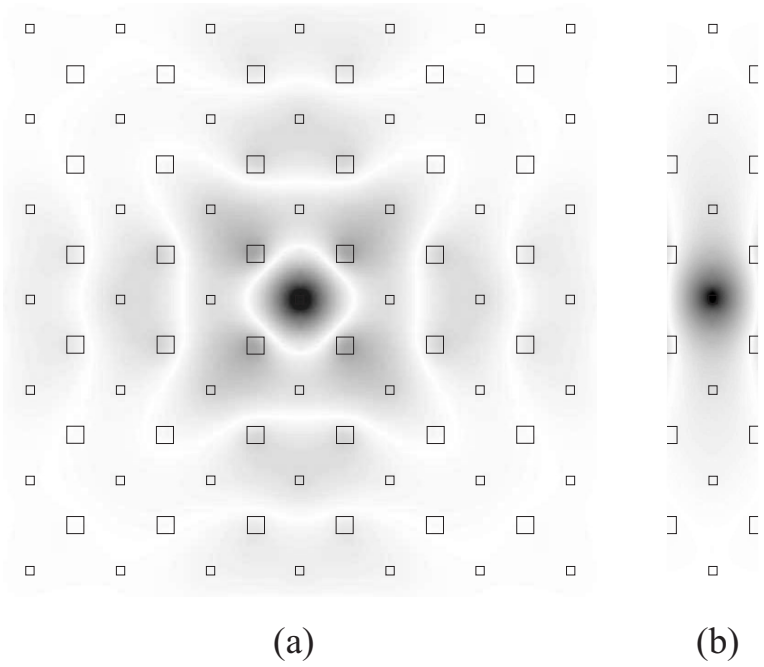

Figure 5.12: (a) Diatomic PhC geometry with Green's function at $\omega = 0.4(2\pi c/a)$ superimposed. (b) Strip Green's function at $\omega = 0.4(2\pi c/a)$ and $k_x = 0.85\pi/a$.

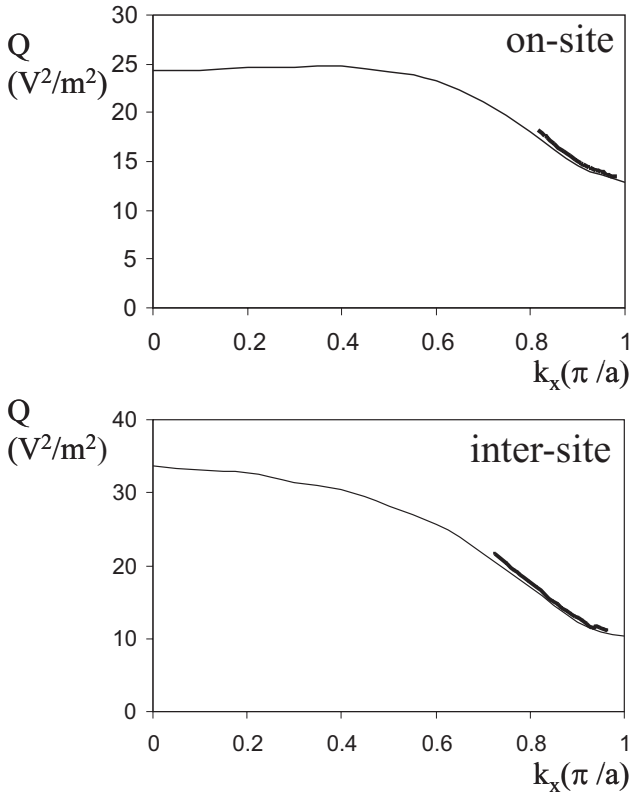

Figure 5.13: Modal energy Q versus propagation constant k_x for the on-site and inter-site solitons of a diatomic PhC at $\omega = 0.4(2\pi c/a)$, calculated with strip Green theory (thin line) and exact simulations (thick line), respectively.

With both the strip Green method and the exact simulations we find self-localized waveguides in the diatomic PhC. Here too we uncovered two varieties: an on-site and an inter-site wave. A comparison of the modal energy in both cases is shown in figure 5.13. We see a good agreement between the two methods, as expected. However, with the semi-analytic method we can cover the entire k_x-range. This is because the modes are unstable if the propagation constant is smaller than a certain critical k_{cr}. If $k_x < k_{cr}$ the wave is unstable against perturbations having the same symmetry as the mode itself, therefore the iterative method does not converge. The onset of this instability is again characterized by an extremum in the curve of power versus propagation constant, which is clearly shown in figure 5.14. This presents further

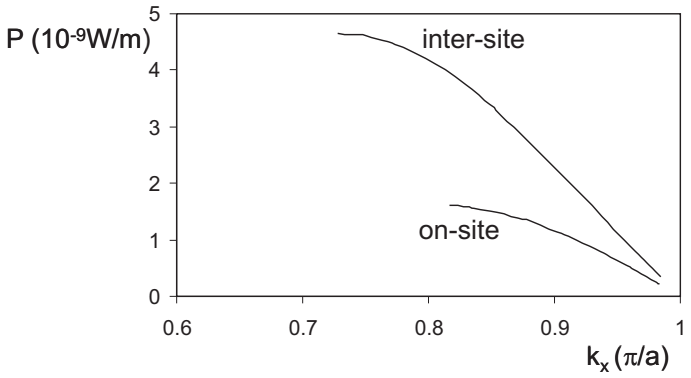

Figure 5.14: Power P versus propagation constant k_x for the on-site and inter-site solitons of a diatomic PhC at $\omega = 0.4(2\pi c/a)$, calculated with the rigorous simulation method.

numerical proof of the generalization of the Vakhitov-Kolokolov criterium for 2D Bloch modes.

The rigorous calculations with the entire modes explore the robustness against perturbations that do not include the symmetry of the solitons. Here again iterations starting from an inter-site mode deviate from this solution and converge onto an on-site mode. Therefore the inter-site modes are unstable and the on-site modes are stable (if $k_x > k_{cr}$). This is consistent with a larger energy U_e for the inter-site modes, and thus with Peierls-Nabarro ideas.

Examples of propagating self-localized waveguides in diatomic crystals are depicted in figures 5.15 and 5.16. Notice how in this case the staggered Green's function gives rise to an unstaggered mode, which is also shown by the unstaggered strip Green's function in figure 5.12(b). Indeed, if the rods aside from the central column have a larger field than the center rod, and if they are multiplied by the appropriate phase factor (see equation 5.15), the sign can change.

The *stationary* localized 2D PhC modes described in the introductory section 5.2 (that create their own *point* defect) appear also in the diatomic PhC [58], which further strengthens the analogy. However, because these nonpropagating solitons are zero-dimensional point defect modes, their description needs one degree of freedom less. There, one frequency leads to one mode. This is in contrast with our self-localized waveguides, where one frequency leads to a one-parameter family of modes, characterized by the Bloch constant k_x.

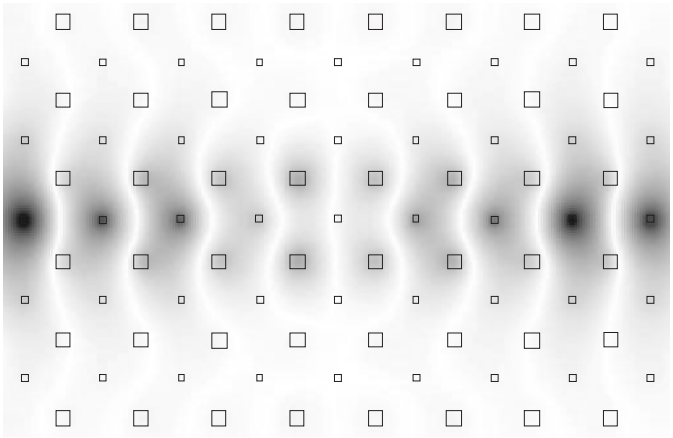

Figure 5.15: A propagating on-site soliton in a diatomic PhC with $\omega = 0.4(2\pi c/a)$ and $k_x = 0.908\pi/a$.

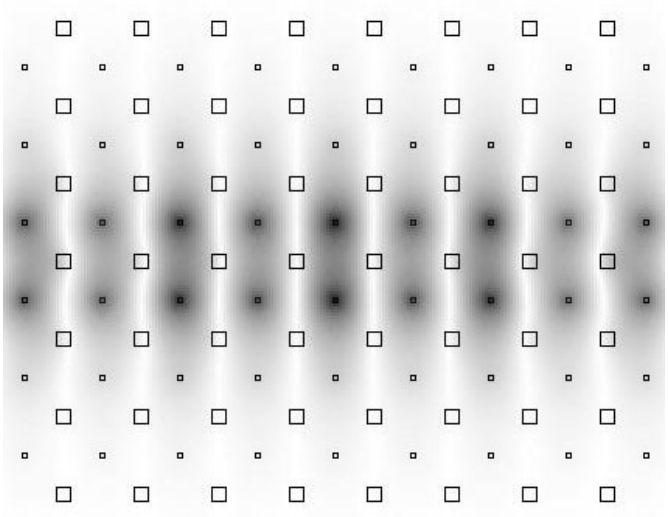

Figure 5.16: A propagating inter-site soliton in a diatomic PhC with $\omega = 0.4(2\pi c/a)$ and $k_x = 0.936\pi/a$.

5.6 Conclusions

In this chapter we proposed and studied a new variety of spatial gap solitons in high contrast 2D PhCs. These are modes with frequency in the bandgap, but they propagate by creating their own waveguide channel. In the square lattice PhC we examined two types of self-localized waveguides: the on-site and inter-site soliton.

In analogy with discrete solitons and localized PhC modes, we applied Vakhitov-Kolokolov and Peierls-Nabarro ideas for stability analysis. The solitons are stable against perturbations having the same symmetry for propagation constants between a certain critical k_{cr} and the edge of the Brillouin zone π/a. At the onset of instability the curve of power versus propagation constant reaches a maximum. For frequencies in the bandgap the on-site variety has the lowest energy, therefore the inter-site is unstable (versus perturbations without symmetry) and will evolve into an on-site mode. These stability issues were confirmed by numerical simulations.

The Bloch mode tool of chapter 3 is well suited for the rigorous analysis of spatial solitons. To gain insight, we also developed a semi-analytical theory. The analysis uses a strip Green's function, which is the Green's function restricted and folded to a period. If we employ this procedure the PhC system is described by a finite set of discrete nonlinear equations, that models the effective long-range interaction between rod sites. A qualitative agreement between the theory and simulations was established.

However, a better agreement was found in diatomic PhCs, consisting of two offset lattices with large linear and small nonlinear rods. Moreover, this also shows the existence of self-localized waveguides in these systems. Finally, because there are on-site and inter-site varieties in the diatomic PhC as well, we presented further proof of the stability issues.

Chapter 6

Modeling second-harmonic generation

6.1 Introduction

In chapter 2 we outlined how the second order nonlinearity leads to the generation of a second harmonic. Apart from the Kerr nonlinearity, second-harmonic generation (SHG) is one of the most studied nonlinear effects.

In order to obtain efficient processes, phase-matching is crucial. For this purpose, one can use the anisotropy of bulk crystals and different polarizations. However, these lead to large structures, with complications such as walk-off, where the beams carry energy in different directions. Another principle is quasi-phase matching, where a grating provides a modulation of the linear or nonlinear parameters, generating a k-vector to compensate the Δk mismatch. In this way, we immediately enter the realm of periodic structures or photonic crystals.

On the other hand, diffraction and walk-off is overcome by using waveguide structures. Propagation in these guides, that are preferably integrated or wavelength-scale, is efficiently modeled by a limited number of eigenmodes. Therefore, we conclude that a simulation method for SHG using eigenmodes, if possible suited for periodic structures, is highly desirable.

There are many possible applications of second-order processes in all-optical integrated networks [94]. We note e.g. the creation of sources at frequencies where direct lasers are lacking. In WDM networks these effects can be used for switching, amplification or channel conversion.

We mentioned the existence of quadratic solitons in chapter 5, where the envelopes of the fundamental and second harmonic are locked with each other. As is often the case, both spatial and temporal varieties exist. The first experimental observations of these entities are fairly recent, dating from the mid-nineties [8]. But, as is happening for the Kerr spatial solitons, research is quickly moving towards interaction and switching for applications.

Many studies of SHG examine the plane-wave situation in one-dimensional layered structures. This is the single-mode case, where one wave bounces back and forth between the interfaces. The description of these structures is handled with transfer matrices [95]. In this approximation analytical insight is gained in the intricate interplay of phase, group velocity, density of modes etc. [96, 97]

Two-dimensional devices are a lot less explored. Here, the transverse effects or, equivalently, multiple modes have to be taken into account. We mention e.g. that the radiation losses in high contrast waveguides with air slits have to be controlled [98]. Parallel or multi-mode waveguides offer different phase-matching possibilities [99]. The dispersion of PhC waveguides can be engineered to obtain equal effective indices at both frequencies [25]. Defects in bulk PhCs have also been considered [100].

The used modeling methods often incorporate discretization in both dimensions, with e.g. FDTD [25] and BPM [101]. In this chapter we develop an eigenmode expansion extension, so the longitudinal grid is no longer necessary. In the transversal direction we need to calculate overlap integrals, so in this sense there is a transversal grid. However, because of the limited number of modes, the method remains efficient. Furthermore, using the undepleted pump approximation we construct a linear matrix algorithm. With this formalism the second harmonic is calculated in one run. The method is especially efficient for periodic structures, because data can be reused.

In addition, we develop an extension to incorporate pump depletion in the formalism. This method is iterative as it involves a sequence of coupled fundamental and second-harmonic calculations. Because of approximations the approach is valid for weak to moderate depletions. However, the use of a grid in the longitudinal direction is avoided, so efficiency is preserved.

We describe the undepleted simulation method in section 6.2. Validation of the algorithm is provided by a plane-wave and a waveguide example in sections 6.3 and 6.4. Transversally and longitudinally pe-

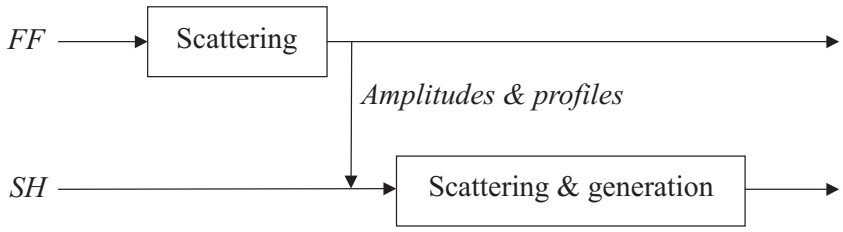

Figure 6.1: Diagram of the simulation method.

riodic structures are studied in sections 6.5 and 6.6, respectively. We prove that the method is capable of simulating long structures, by expanding upon the literature. In addition, a more advanced photonic crystal cavity device is discussed in section 6.7. Finally, we present the method that includes depletion in section 6.8.

6.2 Undepleted eigenmode method

We introduce the method in two steps. First, we examine how a combination of fundamental modes, propagating in one direction, generates a vector of second harmonic modes. Modal overlap integrals and propagation constants are important here. In the second step, we compose a scattering matrix formalism, where propagation in both directions and reflections are taken into account. We will notice that the scheme of the linear method is adjusted because of the generation.

In essence, the algorithm is a combination of a plane-wave formalism and the eigenmode method [95]. A schematic of the complete procedure is depicted in figure 6.1. Because of the undepleted pump approximation, which is explained below, there is a one-way interaction between the fundamental frequency (FF) and the second harmonic (SH).

6.2.1 Generation in a layer

We start from the Helmholtz equations in the case of SHG, see equation 2.48 [102, 103]:

$$\nabla^2 E_\omega + k_\omega^2 E_\omega = -\omega^2 \mu_0 \varepsilon_0 2 d_{nl} E_{2\omega} E_\omega^*, \tag{6.1}$$

$$\nabla^2 E_{2\omega} + k_{2\omega}^2 E_{2\omega} = -(2\omega)^2 \mu_0 \varepsilon_0 d_{nl} E_\omega^2, \tag{6.2}$$

with E_ω and $E_{2\omega}$ the complex fields of the fundamental and second harmonic, respectively. ∇^2 is the total Laplacian, k_ω and $k_{2\omega}$ denote the appropriate wavenumbers.

In the undepleted pump approximation we ignore the right side of equation 6.1. This means the conversion efficiency is low, so the effect from the nonlinear process on the fundamental frequency is negligible. With this approximation we recover the linear Helmholtz equation for the fundamental, that we can solve with the methods of chapter 2. We note that a high pump depletion is seldom reached in wavelength-scale integrated structures. For weak and moderate depletions we devise a scheme in section 6.8 that expands on the method described in this section.

The formalism is presented here for generation from TM to TM (one E-component which is out-of-plane), with a single nonlinear polarization component along the out-of-plane direction y. However, the adaptation to other polarizations is straightforward. Indeed, from the vectorial Helmholtz equation (see section 2.3)

$$\nabla^2 \mathbf{E}_{2\omega} + k_{2\omega}^2 \mathbf{E}_{2\omega} = -\omega^2 \mu_0 \mathbf{P}_{nl} \tag{6.3}$$

we conclude that $P_{nl,x}$ and $P_{nl,z}$ couple to TE polarization, whereas $P_{nl,y}$ couples to TM polarization. This means we only have to consider scalar Helmholtz equations for the electric fields, as in equation 6.2. The polarizations remain independent. The exact expression for the right hand side of equation 6.2 depends on the polarization of the fundamental and the nonlinearity tensor, see equation 2.37. Changing these terms only results in different components being used for the mode overlap integrals, which will become clear below. We employ only one term on the right side of equation 6.2 because extra terms are managed via superposition of the individual contributions.

To solve equation 6.2 in an invariant section we write the fields as a sum of eigenmodes:

$$E_\omega = \sum_i A_i' e^{-j\beta_{\omega,i} z} E_{\omega,i}(x), \tag{6.4}$$

$$E_{2\omega} = \sum_i C_i'(z) e^{-j\beta_{2\omega,i} z} E_{2\omega,i}(x) = \sum_i C_i(z) E_{2\omega,i}(x). \tag{6.5}$$

We assume that only copropagating modes interact nonlinearly, because of phase mismatch, therefore we can ignore the modes propagating in the other direction for the moment. Note the z-dependence of

the mode amplitudes C_i', that indicates the possibility of generation. In the linear case these amplitudes are constant in a section. The constant amplitudes A_i' are provided by the first linear calculation. Substituting equation 6.5 in 6.2 we get a second-order differential equation:

$$\sum_i e^{-j\beta_{2\omega,i}z}\left[E_{2\omega,i}\left(\frac{\mathrm{d}^2C_i'}{\mathrm{d}z^2}-2j\beta_{2\omega,i}\frac{\mathrm{d}C_i'}{\mathrm{d}z}\right)\right.$$
$$\left.+C_i'\left(\frac{\mathrm{d}^2}{\mathrm{d}x^2}+k_{2\omega}^2-\beta_{2\omega,i}^2\right)E_{2\omega,i}\right]=-(2\omega)^2\mu_0\varepsilon_0 d_{nl}E_\omega^2. \quad (6.6)$$

The terms with mode profile derivatives are eliminated using equation 2.55. We ignore the second-order derivatives of the envelopes $C_i'(z)$. The resulting relation combined with equation 6.4 contains sums over modes:

$$\sum_i -2j\beta_{2\omega,i}e^{-j\beta_{2\omega,i}z}\frac{\mathrm{d}C_i'}{\mathrm{d}z}E_{2\omega,i}=$$
$$-(2\omega)^2\mu_0\varepsilon_0 d_{nl}\left(\sum_k A_k'e^{-j\beta_{\omega,k}z}E_{\omega,k}\right)^2. \quad (6.7)$$

We can select one second harmonic mode by using orthonormality, see equation 2.59. Performing the operation $\int(.\times\mathbf{H}_{2\omega,i})\cdot\mathbf{u}_z\mathrm{d}S\equiv\langle .|H_{2\omega,i}\rangle$ results in the first order differential equation:

$$\begin{aligned}\frac{\mathrm{d}C_i'}{\mathrm{d}z} &= -2jk_0^2\sum_k A_k'^2\frac{e^{j\Delta\beta_{ki}z}}{\beta_{2\omega,i}}\left\langle d_{nl}E_{\omega,k}^2|H_{2\omega,i}\right\rangle \\ &\quad -4jk_0^2\sum_{lm}A_l'A_m'\frac{e^{j\Delta\beta_{lmi}z}}{\beta_{2\omega,i}}\left\langle d_{nl}E_{\omega,l}E_{\omega,m}|H_{2\omega,i}\right\rangle, \quad (6.8)\end{aligned}$$

with $\Delta\beta_{ki}=\beta_{2\omega,i}-2\beta_{\omega,k}$, $\Delta\beta_{lmi}=\beta_{2\omega,i}-\beta_{\omega,l}-\beta_{\omega,m}$ and $k_0=\omega/c$. With $\sum_{lm}$ we indicate $\sum_{l=1}^{N-1}\sum_{m=l+1}^{N}$, so it represents a sum concerning two different fundamental modes.

We write the overlap integrals as

$$O_{ki} = \left\langle d_{nl}E_{\omega,k}^2|H_{2\omega,i}\right\rangle, \quad (6.9)$$
$$O_{lmi} = \left\langle d_{nl}E_{\omega,l}E_{\omega,m}|H_{2\omega,i}\right\rangle, \quad (6.10)$$

where we note that the nonlinear coefficient d_{nl} may depend on the transversal coordinate. Finally, equation 6.8 can be integrated to:

$$\begin{aligned} C'_i(z) &= C'_i(0) - 2k_0^2 \sum_k A'^2_k \frac{e^{j\Delta\beta_{ki}z} - 1}{\beta_{2\omega,i}\Delta\beta_{ki}} O_{ki} \\ &\quad -4k_0^2 \sum_{lm} A'_l A'_m \frac{e^{j\Delta\beta_{lmi}z} - 1}{\beta_{2\omega,i}\Delta\beta_{lmi}} O_{lmi}. \end{aligned} \tag{6.11}$$

The terms on the right side of this equation are physically clear. The first term represents the linear propagation. The second and third terms describe SHG from one fundamental mode to one second-harmonic mode, and from two fundamental modes to a single second-harmonic mode, respectively. The integrals weigh the overlap of the mode profiles, whereas the factors with $\Delta\beta$ incorporate the modal phase matching.

Note that in the case of perfect phase matching, or $\Delta\beta = 0$, equation 6.8 can still be solved. However, these expressions are not necessary in practice. If one includes dispersion, exact phase matching is seldom encountered.

With the final equation we obtain the second harmonic mode vector at an arbitrary propagation length z, using only the modal info (β's and profiles) and the fundamental mode amplitudes at the beginning.

6.2.2 Combining layers

The previous analysis allows us to construct a matrix formalism, with the inclusion of reflections and modes propagating in both directions. Note that we work here with the unprimed mode amplitudes, see equation 6.5. For this convention equation 6.11 is easily adapted with $C'_i(z) = C_i(z)e^{j\beta_{2\omega,i}z}$.

By inspecting equation 6.11 we write the bidirectional propagation of modes in an invariant section as follows:

$$\begin{bmatrix} \mathbf{F}_2 \\ \mathbf{B}_1 \end{bmatrix} = \begin{bmatrix} \mathbf{diag}(e^{-j\beta_{2\omega,i}L}) & \mathbf{0} \\ \mathbf{0} & \mathbf{diag}(e^{-j\beta_{2\omega,i}L}) \end{bmatrix} \cdot \begin{bmatrix} \mathbf{F}_1 \\ \mathbf{B}_2 \end{bmatrix} + \begin{bmatrix} \mathbf{N}_{fw} \\ \mathbf{N}_{bw} \end{bmatrix}, \tag{6.12}$$

with **diag** a diagonal matrix and L the length of the section. Positions of the vectors are shown in figure 6.2. The difference with the linear situation, see equation 2.66, is the presence of the extra generation vectors $\mathbf{N}_{fw}$ and $\mathbf{N}_{bw}$. These are calculated by equation 6.11 with

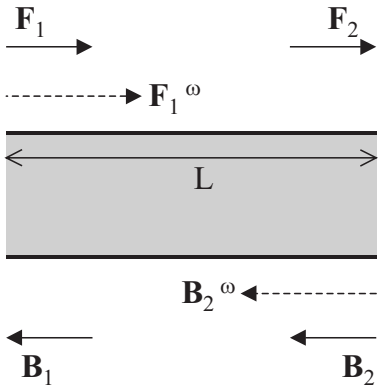

Figure 6.2: Generation in an invariant section. The needed fundamental vectors are shown with dashed arrows.

input from the forward and backward fundamental mode amplitudes, respectively.

We now have to implement interfaces in the algorithm. For this purpose we use the same mode-matching procedure as in the linear case. We note that the adjustment of the boundary condition by the nonlinearity has been examined in [101]. However, the simulations in this study with and without the nonlinear change showed no difference, so the linear method is a very good approximation. Reflection on and transmission through an interface is thus described by a scattering matrix, as in equation 2.62.

The interface formalism has the same structure as a section without generation, see equation 6.12. Therefore, if we can combine two general scatterers, we can construct the matrix for an entire structure composed of multiple interfaces and sections. Because of stability reasons, we employ the (modified) S-scheme. To be specific, we combine

$$\begin{bmatrix} \mathbf{F}_2 \\ \mathbf{B}_1 \end{bmatrix} = \begin{bmatrix} \mathbf{T}_{12} & \mathbf{R}_{21} \\ \mathbf{R}_{12} & \mathbf{T}_{21} \end{bmatrix} \cdot \begin{bmatrix} \mathbf{F}_1 \\ \mathbf{B}_2 \end{bmatrix} + \begin{bmatrix} \mathbf{N}_{12} \\ \mathbf{N}_{21} \end{bmatrix}, \tag{6.13}$$

and

$$\begin{bmatrix} \mathbf{F}_3 \\ \mathbf{B}_2 \end{bmatrix} = \begin{bmatrix} \mathbf{T}_{23} & \mathbf{R}_{32} \\ \mathbf{R}_{23} & \mathbf{T}_{32} \end{bmatrix} \cdot \begin{bmatrix} \mathbf{F}_2 \\ \mathbf{B}_3 \end{bmatrix} + \begin{bmatrix} \mathbf{N}_{23} \\ \mathbf{N}_{32} \end{bmatrix}, \tag{6.14}$$

into

$$\begin{bmatrix} \mathbf{F}_3 \\ \mathbf{B}_1 \end{bmatrix} = \begin{bmatrix} \mathbf{T}_{13} & \mathbf{R}_{31} \\ \mathbf{R}_{13} & \mathbf{T}_{31} \end{bmatrix} \cdot \begin{bmatrix} \mathbf{F}_1 \\ \mathbf{B}_3 \end{bmatrix} + \begin{bmatrix} \mathbf{N}_{13} \\ \mathbf{N}_{31} \end{bmatrix}. \tag{6.15}$$

The algebra leads to

$$\mathbf{N}_{13} = \mathbf{T}_{23} \cdot (\mathbf{I} - \mathbf{R}_{21} \cdot \mathbf{R}_{23})^{-1} \cdot (\mathbf{R}_{21} \cdot \mathbf{N}_{32} + \mathbf{N}_{12}) + \mathbf{N}_{23}, \tag{6.16}$$

$$\mathbf{N}_{31} = \mathbf{T}_{21} \cdot (\mathbf{I} - \mathbf{R}_{23} \cdot \mathbf{R}_{21})^{-1} \cdot (\mathbf{R}_{23} \cdot \mathbf{N}_{12} + \mathbf{N}_{32}) + \mathbf{N}_{21}. \tag{6.17}$$

The other elements are exactly the same as in the linear case, see equations 2.67. Note that the generated second harmonic is scattered via the interfaces. The total $\mathbf{N}$-vectors immediately give the generated output if there is no external second harmonic input.

6.2.3 Discussion

The proposed algorithm has several efficient characteristics. First of all, one evaluation of the analytical equation 6.11 is enough to calculate the generation in an invariant section of arbitrary length. There is no need to discretize in the propagation direction, as opposed to Finite-Difference Time-Domain or Beam Propagation methods. One of the main advantages of the linear mode expansion method is thus conserved.

Furthermore, for the overlap integrals only the nonlinear sections have to be included. Often, this means integration has to be done over a limited transversal part.

Nowadays periodic structures are heavily examined, and our technique is especially suited for these devices. Data such as mode profiles, propagation constants, scattering matrices and overlap integrals can effectively be reused.

Another characteristic is the flexibility of the coupling scheme. It is possible to choose the subsets of fundamental and second harmonic modes, respectively, that couple nonlinearly. This simply happens by neglecting the nonlinear terms in equation 6.11 for the excluded modes. Because of phase-mismatch, small overlap or the excitation specifics many structures can be modeled with only the lower modes contributing nonlinearly. However, higher order modes are still included in the linear scattering to rigorously simulate effects such as radiation losses. As already noted, we can drastically reduce the total number of modes included in the eigenmode expansion by employing symmetry and PML (Perfectly-Matched Layer) boundary conditions.

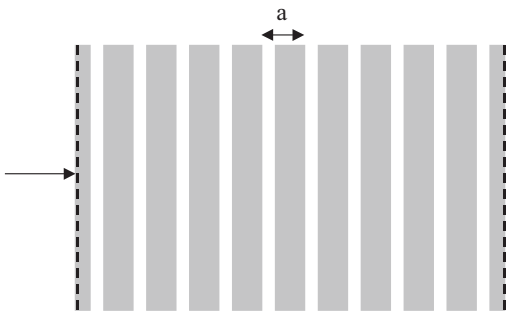

Figure 6.3: Geometry of the multilayer example.

Finally, many devices can be understood via their underlying modal behaviour. Because the proposed method has immediate access to this data, it is very suitable for interpretation of the structures. This is in contrast to other methods that only manipulate the total fields.

6.3 Multilayer

We validate the algorithm for plane-waves in a multilayer example reported in [104]. The structure is depicted in figure 6.3. It consists of eleven AlGaAs-layers with $d_{nl} = 300\mathrm{pm/V}$, separated by air. The period is $a = 234.59\mathrm{nm}$, with air layer thickness $91.55\mathrm{nm}$. The first and last material layers are half as thick as an internal layer. The AlGaAs has index 3.3426 for the fundamental, and 3.6342 for the second harmonic.

The stack is engineered so the fundamental vacuum wavelength $\lambda = 1.55\mu\mathrm{m}$ presents a first transmission maximum near the low frequency band edge, and $\lambda/2$ is on a second transmission resonance. It has been shown that such a doubly resonant configuration results in high conversion efficiencies [96], because of a high density of modes, a strong field enhancement and exact phase-matching. The structure is excited with a fundamental forward propagating field of $10^7\mathrm{V/m}$. Note that the input and output fields are considered in AlGaAs, so the stack has linear material layers on both sides.

The SHG results are shown in figure 6.4. We clearly see that the fundamental and the second harmonic are matched on a first and second resonance, respectively. So, we indeed obtain a maximum SHG

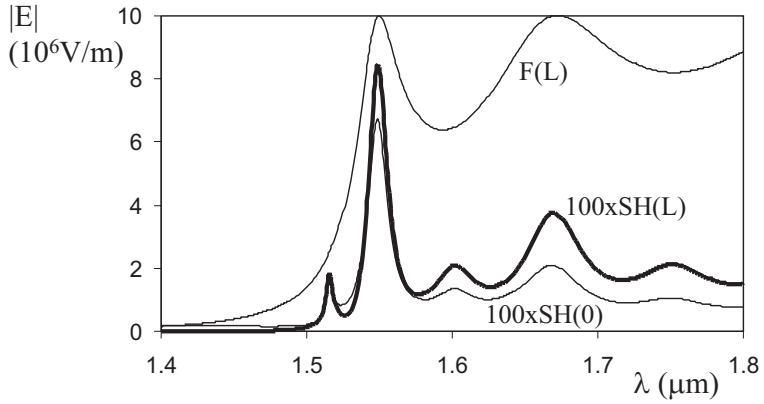

Figure 6.4: Multilayer SHG results. F(L) is the transmitted fundamental field, whereas SH(0) and SH(L) represent the backward and forward generated second harmonic, respectively.

at $\lambda = 1.55\mu\mathrm{m}$. The results agree with figure 4 in [104]. Thus, in this single-mode example our method correctly models the strong and multiple reflections.

6.4 Waveguide

As our method is an extension of a plane wave method, we focus on a structure that shows the necessity of a multi-mode approach in order to get more exact results. The proposed example is a waveguide, see figure 6.5. The core indices are 3.0 and 3.1 for fundamental and second harmonic, respectively, whereas the background is air. The waveguide has length $1\mu\mathrm{m}$ and we operate at $\lambda = 1.55\mu\mathrm{m}$. We assume nonlinear generation from TM to TM with coefficient $d_{nl} = 400\mathrm{pm/V}$. The structure is excited with the fundamental lowest-order mode, such that the electric field in the center is $10^5\mathrm{V/m}$.

We now vary the waveguide width and examine the second harmonic field at the center of the output position. The calculations are done for one second harmonic mode and for multiple modes, respectively. A maximum of 40 modes was used. Because of the short length the contributions of some radiation modes are needed. Results are shown in figure 6.6. Up until a width of $0.132\mu\mathrm{m}$ both curves agree, and this is precisely where the waveguide becomes multi-modal for

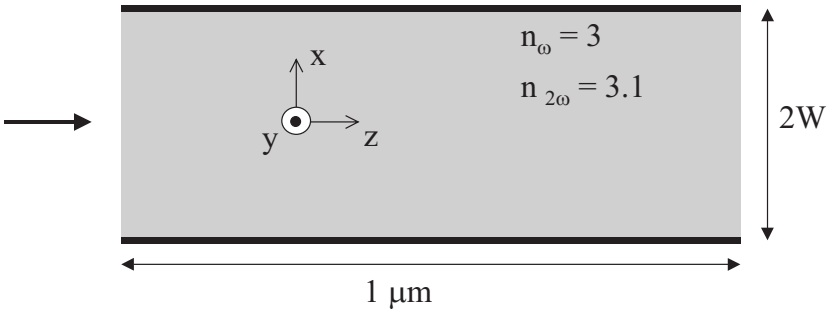

Figure 6.5: Geometry of the waveguide example.

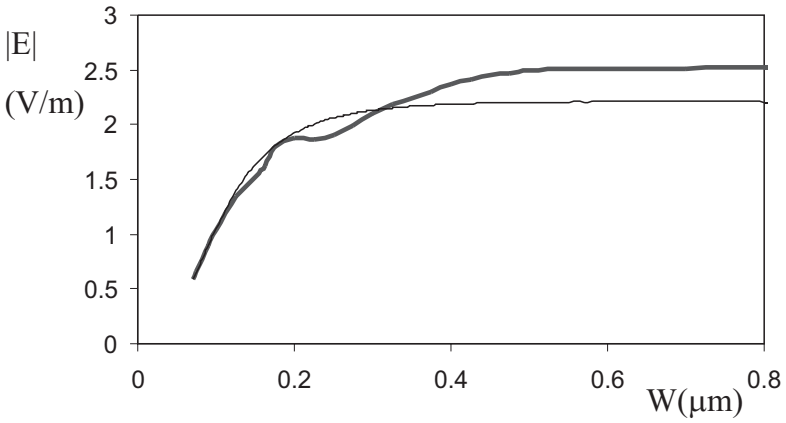

Figure 6.6: Generated electric field in the center at the end of the waveguide section, versus half of the waveguide width. The thin line is the result with one mode, the thick line with multiple modes.

the second harmonic. At $0.8\mu\mathrm{m}$ there are already seven guided modes, and the field with multiple modes converges towards the plane-wave value of $2.54\mathrm{V/m}$.

One might expect that the single-mode calculation also converges to the plane-wave case, in the limit of broad waveguides. However, in this limit all the modes become plane-wave like in the center, and their contributions are governed by the overlap integral with the (square of the) fundamental lowest-order mode.

We prove this with an analysis using modes of a waveguide with hard walls (zero field on the boundaries). In this case the electric field profile of the modes is a cosine:

$$E_i(x) = A_i \cos(k_i x), \tag{6.18}$$

with $k_i = (2i+1)\frac{\pi}{2W}$ and A_i the normalization factor. Note that we only need even modes here. Using Maxwell's $\nabla \times \mathbf{E} = -j\omega\mu_0 \mathbf{H}$ we get

$$\frac{\partial E_y}{\partial z} = j\omega\mu_0 H_x. \tag{6.19}$$

With $E_y = E_i(x)e^{-j\beta_i z}$ and $H_x = H_i(x)e^{-j\beta_i z}$ we obtain

$$H_i(x) = -A_i \frac{\beta_i}{\omega\mu_0} \cos(k_i x). \tag{6.20}$$

The normalization factor is determined from

$$-\int_{-W}^{W} E_i H_i dx = 1, \tag{6.21}$$

and leads to

$$A_i = \sqrt{\frac{\omega\mu_0}{\beta_i W}}. \tag{6.22}$$

Now, in the limit of large widths W, we have

$$\beta_i = \sqrt{k_{med}^2 - k_i^2} \approx k_{med}, \tag{6.23}$$

with k_{med} the wave vector of the medium. This means the phase-matching factors for SHG of the different second harmonic modes have the same magnitude. The only other factor is the overlap integral. Because the coefficients A_i are approximately the same for all the modes,

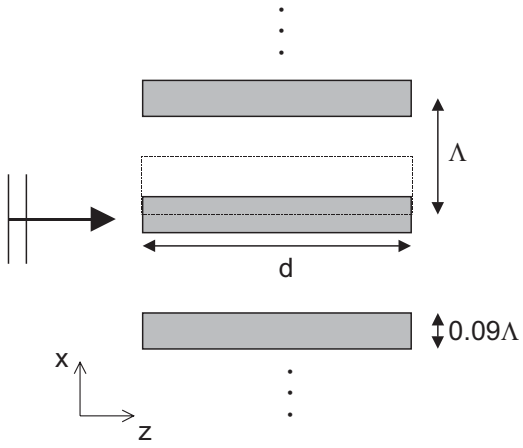

Figure 6.7: Transverse grating structure. Only the dashed section is needed in the simulation because of symmetry.

the differences stem from the following overlaps with the fundamental mode:

$$\int_{-W}^{W} \cos^2(k_0 x) cos(k_i x) dx. \tag{6.24}$$

Evaluation shows that the overlap integrals of the consecutive modes behave as: $O_{00}, O_{00}/5, -O_{00}/35, \ldots$ Thus about five modes are enough for accurate results.

Clearly, this example proves that the interference of the many generated modes has to be taken into account.

6.5 Transverse grating

The structure in this section combines the previous two examples. Here, we need to use multiple modes, and include reflections. Furthermore, we can compare it with another modeling method.

The geometry was proposed in [99] and we show it in figure 6.7. It consists of a transversely periodic array of waveguides with length d in air, excited by a TM plane wave. Because of the finite length d reflections and modes propagating in both directions have to be taken into account. The grating has a period $\Lambda = 0.65\lambda$ and the waveguides have a width $w = 0.09\Lambda$ with indices $n_\omega = 3.346$ and $n_{2\omega} = 3.539$.

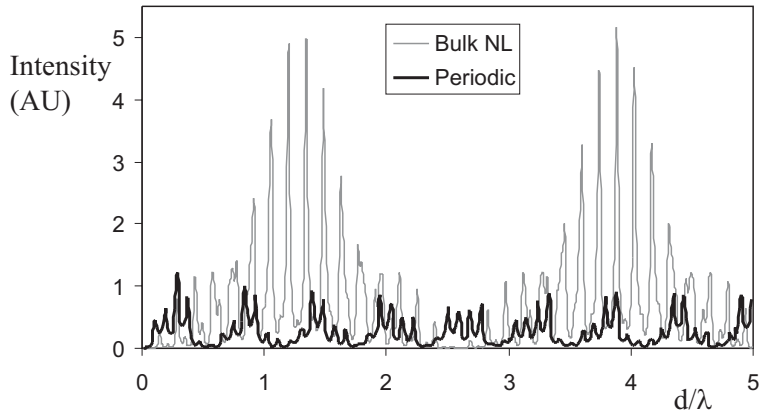

Figure 6.8: Grating SHG intensity in the forward direction versus length d, normalized with the fundamental wavelength λ.

We compare the forward SHG of this device with the case of bulk nonlinear material of the same thickness d in figure 6.8. These results are comparable with figure 2 of [99] where another method was used. The SHG curve is a result of the interplay between Fabry-Pérot reflections, phase matching and modal field profiles. As already mentioned, we have immediate access to this modal data. Moreover, because there are respectively one and two guided modes for fundamental and second harmonic, the use of twenty modes already provides accurate results.

In addition, we can fully exploit the symmetry of the system, as the calculation area is limited to the box in figure 6.7. Indeed, because of the TM excitation and the symmetry of the structure we can use perfect magnetic walls ($\partial E/\partial x = 0$) for the upper and lower boundaries. Furthermore, because the areas to the left and right of the box are invariant along z, we may end the calculations just outside the interfaces. Finally, we note that for the sweep over the length d we only have to calculate the overlap integrals once.

6.6 Longitudinal grating

In this and the next section we study more complex devices. Here we consider deeply etched waveguides [26, 98], an example of which is

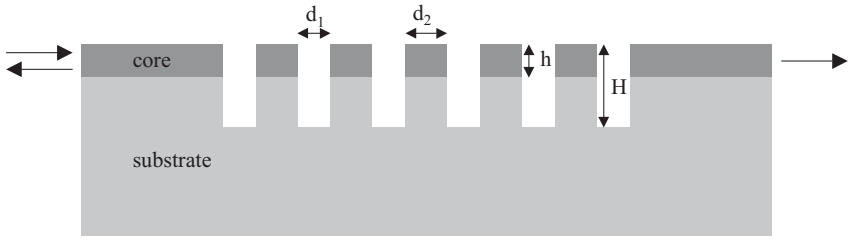

Figure 6.9: Geometry of a deeply etched waveguide.

shown in figure 6.9. This is a longitudinally periodic structure, like the 1D multilayer of section 6.3. It is known for multilayers that the SHG can increase with N^6, where N is the number of periods, if the right phase matching is achieved [97]. Note that N periods corresponds to $N+1$ air slits. However, in integrated devices we prefer waveguide structures. The guidance leads to a number of advantages. With transverse confinement there is a field enhancement. Moreover, there are no spatial walk-off effects. Finally, one can sometimes use larger elements of the nonlinear tensor, in contrast to polarization-type phase-matching. A major drawback is the appearance of diffraction losses [29, 105]. Indeed, if we want a short structure with strong dispersion effects, we need a high index contrast, such as air slits in a waveguide. In many cases, the high frequency second harmonic mode lies above the light line, so that strong coupling with radiation modes is possible.

The linear properties of these kinds of structures are extremely well suited for eigenmode expansion with PML boundary conditions. Indeed, the geometry is highly periodic and the losses towards the boundaries have to be absorbed. A comparison between different modeling methods on such a Bragg grating has been performed in the COST 268 program [106]. Now, the COST P11 project has started and one of the topics is SHG in deeply etched waveguides. As there is clearly a strong interest in this geometry, we compare our method with the devices in [98].

There, an FDTD-extension for SHG is employed. They state that their method is unsuitable for more than 20 periods because of time consumption. With our algorithm we can extend the calculation to more periods, still needing only seconds or minutes. Furthermore, an analytical model was introduced in [98] to describe the evolution of the SHG efficiency in function of the number of periods. Now we can

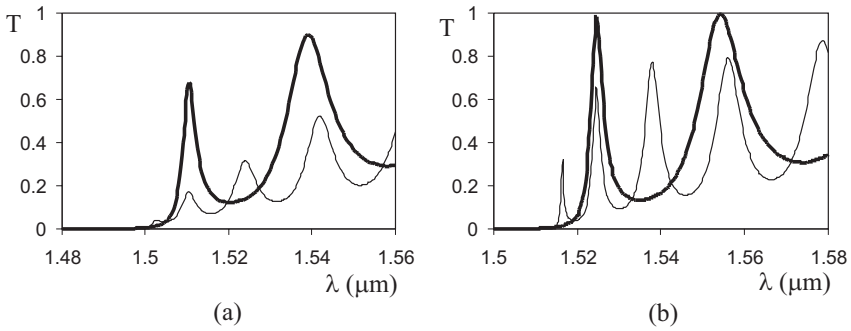

Figure 6.10: Transmission spectra with $N = 20$ of fundamental (thick line) and second harmonic (thin line) for: (a) $h = 1\mu\mathrm{m}$ and (b) $h = 2\mu\mathrm{m}$. The wavelength for the second harmonic on the horizontal scale is doubled.

broaden the comparison with rigorous simulations, and check the validity of the model.

We use the following parameters: The index of the core at the fundamental is 3.2311, whereas the index of the substrate is 3.137 and 3.324 at fundamental and second harmonic, respectively. The second harmonic core index is tuned for phase-matching, in the same way as for the multilayer structure. This means the index is chosen so the first transmission peak on the lower frequency edge of the first bandgap for the fundamental, coincides with the second peak on the lower edge of the second gap for the second harmonic. The resulting index depends on the number of periods. The surrounding medium is air. The widths are $d_1 = 0.15\mu\mathrm{m}$ and $d_2 = 0.095\mu\mathrm{m}$. The core is considered nonlinear with $d_{nl} = 120\mathrm{pm/V}$. For fundamental and second harmonic we use TM- and TE-polarization, respectively, with the nonlinear polarization vector along the transversal direction. We use as input the fundamental lowest-order mode with power $120\mathrm{W}/\mu\mathrm{m}$.

Two combinations of core thickness h and etching depth H are considered, with different loss and SHG behaviour. The first one has $h = 1\mu\mathrm{m}$ and $H = 1.8\mu\mathrm{m}$, whereas the second measures $h = 2\mu\mathrm{m}$ and $H = 3\mu\mathrm{m}$. Because the latter has a larger mode size, its losses are smaller, and the maximum values of the transmission peaks will be larger. This is evident from the spectra in figure 6.10, where transmission is measured from lowest-order mode to lowest-order mode. The peaks near the gap experience the most losses, as they have the lowest group velocity. However an increased density of modes, associ-

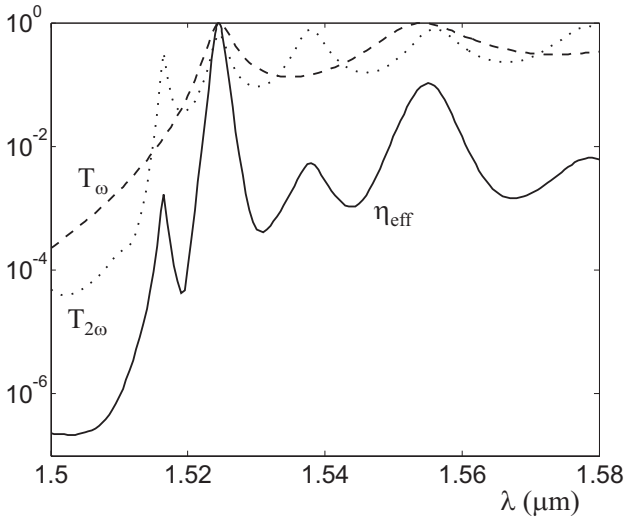

Figure 6.11: Forward SHG normalized efficiency η_{eff} versus fundamental wavelength (solid line) for $h = 2\mu\mathrm{m}$ and $N = 20$. The dashed and dotted lines show the fundamental and second harmonic transmission for reference.

ated with a lower group velocity, is beneficial for nonlinear interactions. Clearly, a trade-off is necessary.

We plot the (normalized) efficiency η_{eff} of the forward generated second harmonic in figure 6.11. Efficiency is defined as the second harmonic flux in the core of the output waveguide, divided by the input fundamental flux. Clearly, the positions of the SHG maxima are determined by the fundamental and second-harmonic transmission peaks. Where the structure is matched, the global maximum appears. We recall that we immediately obtain continuous-wave values, whereas the spectra obtained with FDTD often correspond to the pulsed regime. The obtained efficiency values with the two methods are comparable.

The influence of the number of periods N on the maximum efficiency is analytically described in [98] with an equivalent-cavity model. We apply this theory to our calculations. In this model the transmission resonances behave as cavities. The analysis leads to

$$\eta_{eff} \propto N^6 T_\omega^2 T_{2\omega} = N^6 \left(\frac{1}{1+N^3/a_\omega}\right)^2 \left(\frac{1}{1+N^3/a_{2\omega}}\right), \qquad (6.25)$$

where T_ω and $T_{2\omega}$ represent the maximum transmissions. The parameters a_ω and $a_{2\omega}$ model the diffraction losses via the decline of T_ω and

$T_{2\omega}$ in function of N. They are found by fitting to linear transmission data. The structure of equation 6.25 is intuitively clear. The factor N^6 presents the maximally efficient plane-wave case. The other factors model the decrease of efficiency via diffraction losses. The quadratic interaction involves the square of the fundamental fields, therefore T_ω^2 appears. Finally, only the field that is captured to the output contributes to the efficiency, hence $T_{2\omega}$. The exact amplitude of η_{eff} is determined by fitting.

We applied the equivalent-cavity model to the two structures. These results are shown in figure 6.12. The profoundly different behaviour is a consequence of the losses. For the $h = 1\mu\mathrm{m}$ waveguide, both the fundamental and second harmonic exhibit losses, so eventually the efficiency decreases. For the other $h = 2\mu\mathrm{m}$ guide, the model is close to the N^6-slope. This corresponds to negligible fundamental and modest second harmonic losses. The analysis agrees with [98]. Here, however we have extended the simulations beyond $N = 20$. For the $h = 1\mu\mathrm{m}$ structure we notice a sharper drop in efficiency than the theory predicts. For these large N-values, the losses are abundant. Consequently, the resonances are barely visible. In that case, it is dubious to model the structures as doubly-resonant cavities. Therefore the equivalent-cavity model is no longer strictly valid. We believe this causes the difference for $N > 20$.

We remark that both the model and the calculation method use the non-depleted pump approximation. So we expect differences with pump depletion from an efficiency of about 10%. An example of this is provided in section 6.8 where pump depletion is included. As a final note, we used 30 modes for the fundamental, and 50 for the second harmonic. A coupling from 10 to 10 modes proved accurate, resulting in short calculation times.

6.7 Photonic crystal cavity

Now we study a photonic crystal cavity device depicted in figure 6.13. In combination with the third order Kerr nonlinearity this structure gives rise to bistable switching [19], which we have already encountered in previous chapters. Here we exploit the cavity effects for SHG.

The device consists of a resonator mode in the center, formed by a larger rod, evanescently coupled to two waveguides. The left waveguide is used for input of the fundamental power. On resonance the cavity is strongly excited and all the power is transmitted to the wave-

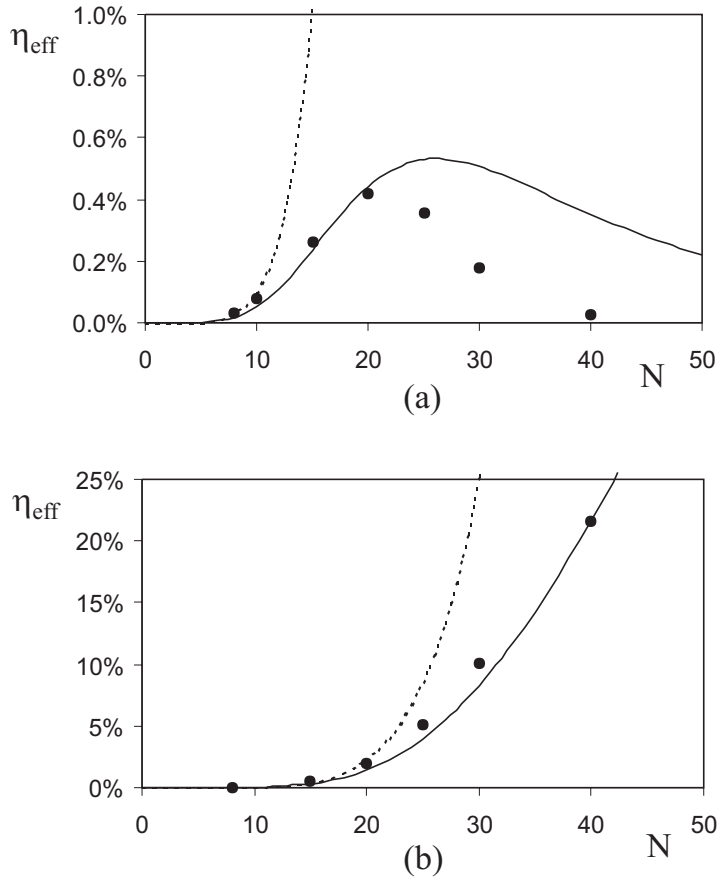

Figure 6.12: SHG efficiency versus number of periods N. Comparison between the model (solid line) and the simulations (dots) for (a) $h = 1\mu\mathrm{m}$ and (b) $h = 2\mu\mathrm{m}$. The N^6 dashed line is added as a reference.

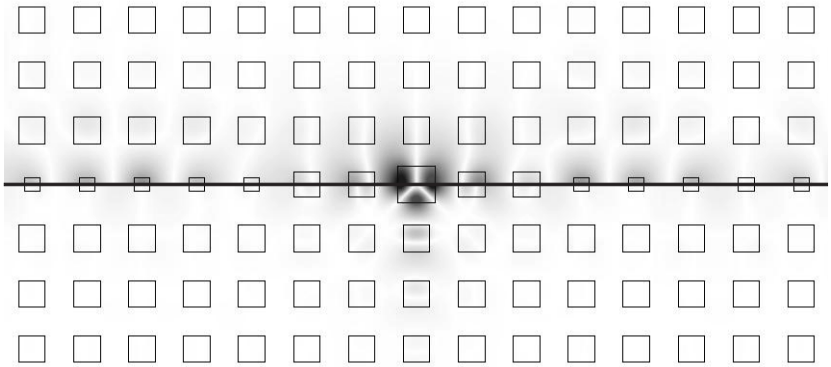

Figure 6.13: Photonic crystal device geometry. The upper (lower) half shows the electric field of the fundamental (second harmonic) at resonance. Dipole and quadrupole modes are clear. Because of high Q the field in the lower waveguide is barely visible.

guide on the right. Off resonance the power is reflected back to the left, with negligible excitation of the defect mode. In figure 6.13 the upper half shows the fundamental resonance, whereas the lower half shows the second harmonic field on resonance.

For this device to work in a SHG setting, there are conditions that have to be fulfilled for both the fundamental and second harmonic: First of all a bandgap and a (preferably single mode) waveguide are necessary. Second, if we demand efficient cavity SHG, there have to be resonator modes at both frequencies, preferably with good mode profile overlap. We designed such a structure, although it will prove difficult to find parameters in a real material system.

The used photonic crystal is a square lattice of square rods in air with period a and diameter $d = 0.5a$. With indices $n_\omega = 3.5$ and $n_{2\omega} = 2.95$ we can work in the first gap for the fundamental, between $\omega = 0.235$ and $0.314(2\pi c/a)$, and the second gap for the second harmonic, between $\omega = 0.497$ and $0.569(2\pi c/a)$ [107]. By decreasing the diameter of a line of rods to $0.3a$ a single mode waveguide is created for both frequencies, with normalized fundamental frequency in $[0.265, 0.283]$. A second harmonic resonance mode at $\omega_{sh}^{res} = 0.55535(2\pi c/a)$ is produced by a larger central rod of diameter $0.7a$. We tune a (broader) fundamental resonance to $0.5\omega_{sh}^{res}$ with a central rod index of 3.5743. Both Lorentzian transmission profiles T_ω and $T_{2\omega}$ are shown in figure 6.14,

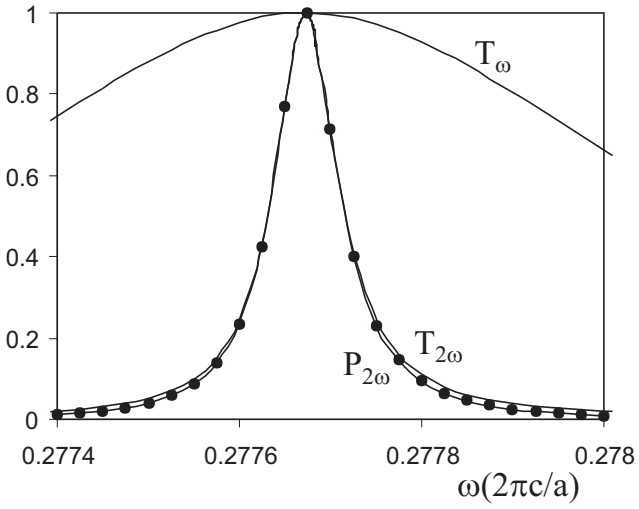

Figure 6.14: Photonic crystal device results. The transmission of fundamental T_ω and second harmonic $T_{2\omega}$ are shown, together with the generated second harmonic power $P_{2\omega}$, with lines. $P_{2\omega}$ is normalized and all curves are plotted versus the fundamental ω. Values for $T_\omega^2 T_{2\omega}$ are indicated with dots.

with

$$T(\omega) = \frac{\gamma^2}{(\omega - \omega^{res})^2 + \gamma^2}. \tag{6.26}$$

They correspond to Q-values of respectively $Q_\omega = 301$ and $Q_{2\omega} = 3239$, with $Q = \omega^{res}/(2\gamma)$.

For the SHG calculations we assume that only the larger central rod is nonlinear, a good approximation as the field is strongest there. Because the second harmonic defect mode is excited by the fundamental and this mode is equally coupled to both waveguides, the generated outgoing power to the left and the right is the same. This power is plotted in figure 6.14. Because the outgoing power is proportional to the energy of the second harmonic mode and the second harmonic is excited by the square of the fundamental field, it results that the generation at resonance is proportional to $Q_\omega^2 Q_{2\omega}$ and the normalized SHG power profile follows $T_\omega^2 T_{2\omega}$, see figure 6.14. This directly corresponds with the equivalent-cavity model of deeply etched waveguides, see equation 6.25 of the previous paragraph. For these calculations only 30 modes were used for both frequencies. Moreover, if we allow the

lowest 10 of these modes to couple nonlinearly, we already obtain accurate results.

This structure, using a 2D PhC, is a combination of the previous examples with transversal and longitudinal periodicity, respectively. Obtaining the steady state response with time domain approaches in these high-Q cavities, necessitates a very fine resolution. The low number of modes, together with the exploitation of the periodic character, proves we can efficiently handle complex 2D geometries.

6.8 Pump depletion

In this section we explain how we extend the SHG formalism to include pump depletion. In order to keep the calculations efficient and tractable we have to use some approximations. This means that calculations with strong depletions, such as tens of percents, will not be exact. However, for weak to moderate depletions (or proportions between the second harmonic and fundamental amplitudes) we can now simulate the interplay between both frequencies. This means it is possible to witness effects such as the weakening of the fundamental wave, and the decrease of the SHG efficiency. In addition, the SHG process may impart a phase change upon the fundamental. In the weak depletion regime this useful effect is termed the *cascading limit* [8]. It presents an alternative for the Kerr phase shift, because the Kerr shift is often weaker.

6.8.1 Algorithm

The main changes to the undepleted method of section 6.2 are the following: First of all the technique becomes iterative. A sequence is performed of fundamental and second harmonic calculations. Secondly, the propagation in a layer of the fundamental is adjusted, in an analogous way as for the second harmonic. This means we obtain a matrix formalism for the fundamental amplitudes of the known form:

$$\begin{bmatrix} \mathbf{F}_{out} \\ \mathbf{B}_{out} \end{bmatrix} = \mathbf{S} \cdot \begin{bmatrix} \mathbf{F}_{in} \\ \mathbf{B}_{in} \end{bmatrix} + \begin{bmatrix} \mathbf{N}_{fw}^{tot} \\ \mathbf{N}_{bw}^{tot} \end{bmatrix}, \tag{6.27}$$

with $\mathbf{S}$ the linear scattering matrix, and $\mathbf{N}_{fw}^{tot}, \mathbf{N}_{bw}^{tot}$ the nonlinear adjustments. The interfaces are handled in the linear way, with the mode-matching method. Because the same form is retained, the combination

of layers is done in the same way as for the harmonic. Therefore, the matrix manipulations in 6.2.2 are the same for the fundamental amplitudes, and we do not repeat them here.

Now we deduce how the propagation in a layer is adjusted by the nonlinearity. The procedure is analogous to the undepleted case in section 6.2.1. We start from the previously neglected Helmholtz equation for the fundamental, equation 6.1, that we repeat for convenience:

$$\nabla^2 E_\omega + k_\omega^2 E_\omega = -2k_0^2 d_{nl} E_\omega^* E_{2\omega}. \tag{6.28}$$

For mode expansion we use the decompositions:

$$E_\omega = \sum_i A_i'(z) e^{-j\beta_{\omega,i} z} E_{\omega,i}(x) \ = \sum_i A_i(z) E_{\omega,i}(x), \tag{6.29}$$

$$E_{2\omega} = \sum_i C_i'(z) e^{-j\beta_{2\omega,i} z} E_{2\omega,i}(x) = \sum_i C_i(z) E_{2\omega,i}(x). \tag{6.30}$$

Note the difference with the undepleted case: Now $A_i'(z)$ depends on the propagation distance. We import equations 6.29 and 6.30 in equation 6.28. With the slowly varying envelope approximation and the mode property of equation 2.55 we obtain

$$\sum_j \beta_{\omega,j} e^{-j\beta_{\omega,j} z} E_{\omega,j} \frac{\mathrm{d}A_j'}{\mathrm{d}z} = \\ -jk_0^2 d_{nl} \left(\sum_n A'^*_n e^{j\beta_{\omega,n} z} E_{\omega,n}^* \right) \left(\sum_i C_i' e^{-j\beta_{2\omega,i} z} E_{2\omega,i} \right). \tag{6.31}$$

Again we select one mode on the left hand side by using orthonormality. After performing this integral we get

$$\frac{\mathrm{d}A_j'}{\mathrm{d}z} = \frac{-jk_0^2}{\beta_{\omega,j}} \sum_{ni} O_{nij}^{depl} A'^*_n C_i' e^{j(\beta_{\omega,j} + \beta_{\omega,n} - \beta_{2\omega,i}) z}, \tag{6.32}$$

with the new depletion overlap integrals

$$O_{nij}^{depl} = \left\langle d_{nl} E_{\omega,n}^* E_{2\omega,i} | H_{\omega,j} \right\rangle. \tag{6.33}$$

We solve equation 6.32 using a perturbation approach. To integrate we need to determine the z-dependence of the amplitudes A'_n and C_i' on the right hand side.

For the fundamental amplitudes we suppose

$$A'_n(z) = A'_n(0). \tag{6.34}$$

This estimate is refined during the iterations, which will become clear later. In contrast, for the second harmonic we use the previously deduced z-dependence of equation 6.11. In a more condensed form with one summation we write this equation as

$$C'_i(z) = C'_i(0) - \frac{2k_0^2}{\beta_{2\omega,i}} \sum_{kl} O^{gen}_{kli} A'_k(0) A'_l(0) \frac{e^{j\Delta\beta_{kli}z} - 1}{\Delta\beta_{kli}}, \tag{6.35}$$

where $\Delta\beta_{kli} = \beta_{2\omega,i} - \beta_{\omega,k} - \beta_{\omega,l}$ and the overlap integral is denoted with gen for 'generation' as opposed to the 'depletion' overlaps.

We insert equations 6.34 and 6.35 in 6.32. The resulting right hand side has terms with three different z-dependencies:

$$e^{j(\beta_{\omega,j}+\beta_{\omega,n}-\beta_{2\omega,i})z} \equiv e^{-j\Delta\beta_{jni}z}, \tag{6.36}$$

$$e^{j(\beta_{\omega,j}+\beta_{\omega,n}-\beta_{\omega,k}-\beta_{\omega,l})z} \equiv e^{-j\Delta\beta'_{jnkl}z}, \tag{6.37}$$

$$\text{constants.} \tag{6.38}$$

The constants arise if $\Delta\beta'_{jnkl}z = 0$. We assume that $\Delta\beta_{jni} \neq 0$ because of material dispersion.

These three terms are integrable, so the solution of the differential equation reads:

$$\begin{aligned} A'_j(z) = A'_j(0) &+ \sum_{ni} \Gamma^j_{ni} \left(\frac{e^{-j\Delta\beta_{jni}z} - 1}{-j\Delta\beta_{jni}} \right) \\ &+ \sum_{nkl} \Gamma^j_{nkl} \left(\frac{e^{-j\Delta\beta'_{jnkl}z} - 1}{-j\Delta\beta'_{jnkl}} \right) + \sum_{nkl} \Gamma^j_{nkl} z, \end{aligned} \tag{6.39}$$

with coefficients

$$\Gamma^j_{ni} = -\frac{jk_0^2}{\beta_{\omega,j}} O^{depl}_{nij} A'^*_n(0) \left(C'_i(0) + \frac{2k_0^2}{\beta_{2\omega,i}} \sum_{kl} \frac{O^{gen}_{kli} A'_k(0) A'_l(0)}{\Delta\beta_{kli}} \right), \tag{6.40}$$

$$\Gamma^j_{nkl} = \frac{2jk_0^4}{\beta_{\omega,j}} A'^*_n(0) A'_k(0) A'_l(0) \sum_i \frac{O^{depl}_{nij} O^{gen}_{kli}}{\Delta\beta_{kli}}. \tag{6.41}$$

The first term on the right side of equation 6.39 represents linear propagation. The other terms stem from nonlinear coupling effects. We indeed obtain the same structure as required for the matrix formalism in equation 6.27. With equation 6.39 we can propagate the fundamental amplitudes in one run to the end of an invariant layer.

Note the appearance of factors $A'^{*}_{n} A'_{k} A'_{l}$ that may lead to $|A'|^2 A'$. These represent Kerr-like effects, such as incoherent nonlinear phase shifts, that we previously mentioned.

6.8.2 Discussion

The iterative character of the method originates because the fundamental amplitudes are influenced by the second harmonic amplitudes, and vice versa. Indeed, the algorithm proceeds as follows: We calculate the scattering of the fundamental input field in a completely *linear* way. From these amplitudes we determine the second harmonic, as in section 6.2. Here the undepleted method ends. For depletion we evaluate equation 6.39 with the obtained second harmonic and the old fundamental amplitudes in every invariant section. With these results we construct the total scattering, as in equation 6.27, and obtain new fundamental amplitudes throughout the structure. If the difference between the old and new amplitudes is negligible, we have converged. If this is not the case, we perform another iteration: We recalculate the second harmonic. With these amplitudes we then determine the new fundamental fields. These steps are repeated until convergence is reached.

Remark that we could use the new z-dependence of the fundamental amplitudes in equation 6.39 to derive extra terms for the second harmonic, and extend equation 6.35. Then, these terms lead to new fundamental contributions, and so on. This would lead to better approximations, as more perturbation terms are included. However, the number of different terms increases dramatically, so the expressions become impractical and inefficient. Therefore we stop at equations 6.35 and 6.39.

To describe the interaction between fundamental and second harmonic exactly, even in the case of deep depletion, we would have to integrate the differential equations in a stepwise manner, with e.g. Runge-Kutta methods. However this introduces a grid in the propagation direction, which we try to avoid in eigenmode methods as it decreases efficiency. Therefore we stick to the single evaluation formalism of equations 6.35 and 6.39, that are applicable for weak or moderate depletion.

We make the following notes on the approximations. In the situation of one fundamental and one second harmonic mode we inspected power conservation with and without the linear term in equation 6.39. If the propagation distance is smaller than the coherence length L_c, see equation 2.47, and the depletion is weak, the linear term is negligible. However if the depletion is moderate, the linear term provides better power conservation, for distances shorter than L_c. If we want to model propagation over a length much larger than L_c the contribution of the linear term diverges. The exact solution is periodic however [102], so a better approximation is reached if the linear term is neglected. In any case, if the magnitudes of the fundamental and second harmonic become comparable the method has to be extended.

Finally, we remark that care must be taken in the transition from the primed to the unprimed amplitudes, see equations 6.29 and 6.30. Because of the exponentials numerical instabilities may occur, but they can be avoided. Indeed, equation 6.39 includes expressions of the form $e^{j(\beta_{\omega,j}+\beta_{\omega,n})z}$. An evanescent mode has a propagation constant β with a negative imaginary part, so the relations increase exponentially.

The first factor is neutralized by the transition

$$A_j(z) = A'_j(z)e^{-j\beta_{\omega,j}z}, \tag{6.42}$$

just as in the undepleted algorithm. The second factor is balanced by using the (previously obtained) values of $A'^*_n(z)$ at the end of the section instead of $A'^*_n(0)$ in the expressions for Γ^j_{ni} and Γ^j_{nkl}. Indeed, the compensating transition reads

$$A'^*_n(z) = A^*_n(z)e^{-j\beta_{\omega,n}z}. \tag{6.43}$$

This corresponds to another choice of the approximation, needed for integration. Note that we keep $A'_k(0)A'_l(0) = A_k(0)A_l(0)$. Otherwise we would inject exponentials with the wrong sign in the calculations, with unstable consequences.

6.8.3 Simulation example

We have compared the depletion method with the plane-wave examples in [95] and obtained good agreement. Therefore we provide a more complex depletion calculation with the deeply etched waveguide structure of section 6.6.

We consider the structure with core width $h = 2\mu m$ and 40 periods. The results with and without depletion are shown in figure 6.15. In

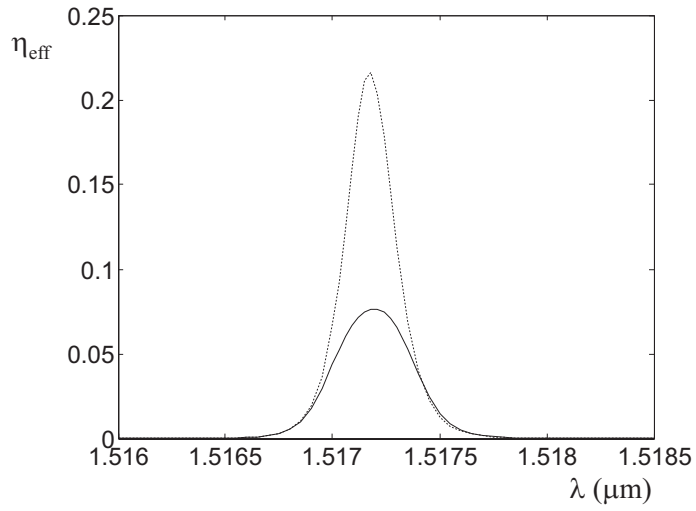

Figure 6.15: SHG efficiency for the deeply etched waveguide with $h = 2\mu m$ and $N = 40$ versus fundamental wavelength. The calculations with and without depletion are presented with solid and dashed lines, respectively.

the undepleted approximation an efficiency of 22% is reached, whereas with depletion only 8% is converted. Remark that the depletion calculations may still be valid, even if the undepleted calculations give high conversions. Indeed, as in this example, the inclusion of depletion dramatically decreases the efficiency. Note that the effect of the linear term is negligible for this structure, because of the relatively short nonlinear sections.

The effect of depletion on the fundamental is readily seen in figure 6.16. The transmitted power decreases with a factor 1.72, which corresponds approximately with the drop in SHG efficiency with a factor $2.82 \approx 1.72^2 = 2.96$.

6.9 Conclusions

In this chapter we extended the eigenmode expansion method for rigorous and efficient calculation of vectorial SHG in two-dimensional structures. Specific and related algorithms are presented for both the undepleted and depleted cases.

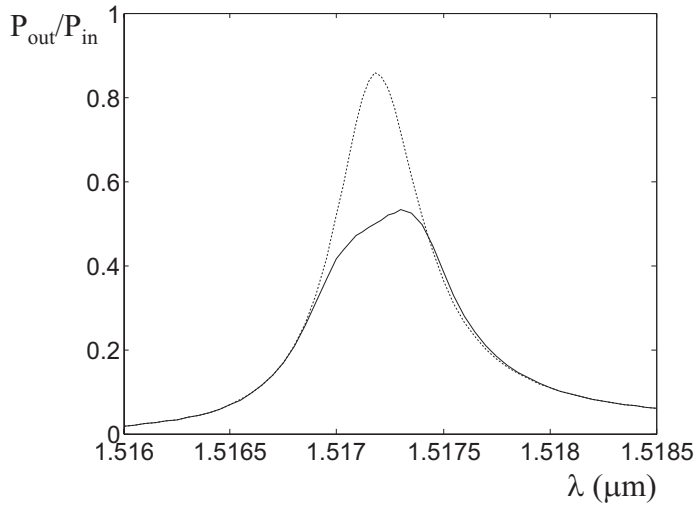

Figure 6.16: Transmitted fundamental power versus wavelength. The calculations with and without depletion are shown with solid and dashed lines, respectively.

By applying the undepleted pump and slowly varying envelope approximation the differential equation for the amplitudes is solved analytically. Therefore no grid is required in the propagation direction. The formalism of the eigenmode method is adjusted by an extra generation vector, thereby remaining a linear matrix operation. Because of immediate knowledge of modal phase-matching factors and overlap integrals, more insight is gained compared to full-field approaches. A flexible coupling scheme, advanced boundary conditions and reuse of data in periodic structures further enhance the efficiency.

For situations with weak or moderate pump depletion an iterative scheme is devised that models the interplay between fundamental and second harmonic. Because no grid is introduced in the longitudinal direction, the calculations remain efficient.

The method was validated with a plane-wave multilayer, a waveguide example and a structure with transversal periodicity. In the next sections, more advanced devices were studied, namely a deeply etched waveguide and a photonic crystal cavity device. Both structures are analytically described via their linear transmissions. We proved how the nonlinear eigenmode method is able to efficiently handle long periodic

structures exhibiting losses. The strong influence of pump depletion in such a long device is presented.

Chapter 7

Conclusions and outlook

7.1 Conclusions

The combination of photonic crystals and nonlinear effects offers a lot of possibilities, both from the physics and applications point of view. In this work we developed modeling tools to simulate two of the most important nonlinearities: the Kerr effect and second-harmonic generation. Both methods extend upon eigenmode expansion and are especially suited for periodic structures.

The Kerr algorithm uses a grid and adjusts the refractive index iteratively. Because the modes depend on the exact local value of the index, the method is accurate even in the case of strong nonlinearities. However, because of this the tool is mainly used for wavelength scale structures. On the other hand, linear sections are handled in one calculation. Both finite and infinite periodic structures can be simulated. In the latter case, we obtain Bloch band structures that shift with increasing power.

The method for SHG is an extension of the coupled-mode equations to multiple modes. Algorithms for the undepleted and moderately depleted situations have been developed. In the undepleted pump approximation the fundamental and second harmonic simulations are largely independent. The second harmonic is calculated in one run. For pump depletion a sequence of coupled fundamental and second harmonic simulations is performed. In both cases the equations become analytically solvable. Therefore, an invariant nonlinear section is handled in one calculation. The resulting matrix formalism is especially efficient for periodic structures. We proved this by expanding upon simulations from the literature to longer devices.

The time and memory requirements of both tools are small, compared to methods such as FDTD. All the calculations presented here took seconds or minutes, instead of hours or days.

We note that the algorithms are bidirectional and two-dimensional. The former means we take reflections fully into account, so that effects such as bistability emerge. The latter indicates we can examine transverse effects such as radiation losses and (bandgap) confinement.

Armed with these tools we studied a variety of devices. An interesting component is the PhC waveguide with a resonator in or adjacent to the waveguide, that we calculated in different settings. When these components are put in series, we uncovered a rich set of intrinsic localized modes. Here, CMT-theory proved a simple and accurate calculation method. Apart from the well-known finite gap-solitons, nonlinear resonances emerged without a linear counterpart. Furthermore, tuning of the distance between the resonators allowed the appearance of transmission peaks, that deform in nonlinear boundary modes. If the resonators are placed in the waveguide, these modes obtain dark soliton profiles. Finally, with two cavities judiciously located next to the waveguide, we indicated a narrow transmission peak that allows efficient switching.

In a regular PhC we discovered a new type of intrinsic localized mode, related to the previously mentioned gap solitons. We considered a Kerr nonlinear PhC without defects. In this system we demonstrated self-localized waveguides. They are bandgap confined in the transverse direction, but they propagate longitudinally because of a self-induced index change. Both an on-site and an inter-site variety is possible. We gave numerical evidence of the extension of Vakhitov-Kolokolov and Peierls-Nabarro stability ideas in this 2D Bloch setting. We concluded that the on-site soliton is stable above a certain propagation constant. The inter-site soliton proved unstable, and consequently evolves into the on-site type, if the latter is stable.

For these modes we developed a semi-analytical description. This theory employs a folding of the Green function, to incorporate the Bloch character. Using approximations a simple algebraic set of nonlinear equations is derived. A qualitative agreement with the simulations is found. However, for a diatomic PhC, with smaller nonlinear rods, a better correspondence is established. Simultaneously, the existence of self-localized waveguides in these diatomic lattices is proven.

7.2 Future work

Two directions of further research are immediately clear. On the one hand, we can optimize and expand the current algorithms. On the other hand, they can be applied to other devices.

To optimize the Kerr tool, it would be beneficial to reuse modes during iteration. In the case of weak nonlinearities e.g. the profiles remain largely invariant, whereas the propagation constants change slightly.

For expansion it is notable that the method behind the SHG algorithm is applicable to sum and difference frequency generation and third harmonic generation. If the coupled-mode equations in the case of multiple modes are solvable, the matrix formalism can be adapted.

In principle, both the SHG and Kerr method can be extended to three dimensions. However, until the 3D mode solvers become more efficient, it seems most feasible for SHG, because less modes have to be calculated.

We mention the metal-dielectric system as a promising new way to obtain nonlinear effects [108]. Indeed, plasmon resonances dramatically increase the local field strength. Because metals can also be modeled by eigenmodes, the tools are immediately suitable.

The work on intrinsic localized modes is also extendable. In the previous we considered series with identical cavities in or adjacent to the waveguide. Other types of resonators, e.g. exhibiting a Fano resonance, can be envisaged. Moreover, nonuniform series, e.g. with apodization, present new filtering and switching opportunities.

Finally, the SHG calculations with pump depletion offer the possibility to examine quadratic localized modes. Waves with interlocked fundamental and second harmonic, similar to the Kerr self-localized waveguides, may be uncovered. We can possibly extend the semi-analytical strip Green method for this case.

In conclusion, with the techniques we developed a large class of devices and phenomena can be examined. Further innovations and other systems will present us with new and unexpected nonlinear concepts.

Bibliography

[1] T. H. Maiman. Stimulated optical radiation in ruby. *Nature*, 187:493, 1960.

[2] P. A. Franken, A. E. Hill, C. W. Peters, and G. Weinreich. Generation of optical harmonics. *Physical Review Letters*, 7:118, 1961.

[3] C. J. Koester, E. Snitzer, C. J. Campbell, and M. C. Rittler. Experimental laser retina photocoagulation. *Journal of the Optical Society of America*, 52:607, 1962.

[4] L. Reinisch, M. H. Mendenhall, and R. H. Ossoff. Precise laser incisions: Corrected for patient respiration with an intelligent aiming system. *Lasers in Surgery and Medicine*, 20:210–215, 1997.

[5] http://www.ligo.caltech.edu/.

[6] L. F. Mollenauer, R. H. Stolen, and J. P. Gordon. Experimental observation of picosecond pulse narrowing and solitons in optical fibers. *Physical Review Letters*, 45:1095, 1980.

[7] G. P. Agrawal. *Nonlinear fiber optics*. Academic Press, San Diego, 1989.

[8] S. Trillo and W. Torruellas. *Spatial Solitons*. Springer, Berlin, 2001.

[9] Y. S. Kivshar and G. P. Agrawal. *Optical Solitons: From Fibers to Photonic Crystals*. Academic Press, San Diego, 2003.

[10] W. Bogaerts. *Nanophotonic waveguides and photonic crystals in silicon-on-insulator*. PhD thesis, Ghent University, 2004.

[11] D. K. Campbell, S. Flach, and Y. S. Kivshar. Localizing energy through nonlinearity and discreteness. *Physics Today*, 57:43–49, 2004.

[12] E. Yablonovitch and T. J. Gmitter. Photonic band structures: The face-centered cubic case. *Physical Review Letters*, 63:1950–1953, 1989.

[13] W. Bogaerts, V. Wiaux, D. Taillaert, S. Beckx, B. F. J. Luyssaert, P. Bienstman, and R. Baets. Fabrication of photonic crystals in silicon-on-insulator using 248-nm deep UV lithography. *IEEE Journal on Selected Topics in Quantum Electronics*, 8:928–934, 2002.

[14] J. D. Joannopoulos, R. D. Meade, and J. N. Winn. *Photonic crystals: molding the flow of light*. Princeton University Press, Princeton, 1995.

[15] P. Yeh, A. Yariv, and E. Marom. Theory of Bragg fiber. *Journal of the Optical Society of America*, 68:1196–1201, 1978.

[16] J. N. Winn, Y. Fink, S. H. Fan, and J. D. Joannopoulos. Omnidirectional reflection from a one-dimensional photonic crystal. *Optics Letters*, 23:1573–1575, 1998.

[17] C. M. Smith, N. Venkataraman, M. T. Gallagher, D. Muller, J. A. West, N. F. Borrelli, D. C. Allan, and K. W. Koch. Low-loss hollow-core silica / air photonic bandgap fibre. *Nature*, 424:657–659, 2003.

[18] W. J. Wadsworth, A. Ortigosa-Blanch, J. C. Knight, T. A. Birks, T. P. M. Man, and P. S. Russell. Supercontinuum generation in photonic crystal fibers and optical fiber tapers: a novel light source. *Journal of the Optical Society of America B*, 19:2148–2155, 2002.

[19] M. Soljacic, M. Ibanescu, S. G. Johnson, Y. Fink, and J. D. Joannopoulos. Optimal bistable switching in nonlinear photonic crystals. *Physical Review E*, 66:055601, 2002.

[20] M. Soljacic and J. D. Joannopoulos. Enhancement of non-linear effects using photonic crystals. *Nature Materials*, 3:211–219, 2004.

[21] K. Kawano and T. Kitoh. *Introduction to optical waveguide analysis: solving Maxwell's equations and the Schrödinger equation*. Wiley, New York, 2001.

[22] V. Janyani, A. Vukovic, J. D. Paul, P. Sewell, and T. M. Benson. Time domain simulation of all-optical limiter using Kerr and

Duffing models. *Proceedings of Optical Waveguide Theory and Numerical Modelling, Ghent*, page 39, 2004.

[23] A. Taflove. *Advances in Computational Electrodynamics: The Finite-Difference Time-Domain Method*. Artech House, Boston, 1998.

[24] R. Scarmozzino, A. Gopinath, R. Pregla, and S. Helfert. Numerical techniques for modeling guided-wave photonic devices. *IEEE Journal of Selected Topics in Quantum Electronics*, 6:150–162, 2000.

[25] F. Raineri, Y. Dumeige, A. Levenson, and X. Letartre. Nonlinear decoupled FDTD code: phase-matching in 2D defective photonic crystal. *Electronics Letters*, 38:1704–1706, 2002.

[26] A. Locatelli, D. Modotto, C. De Angelis, F. M. Pigozzo, and A.-D. Capobianco. Nonlinear bidirectional beam propagation method based on scattering operators for periodic microstructured waveguides. *Journal of the Optical Society of America B*, 20:1724–1731, 2003.

[27] P. Bienstman and R. Baets. Optical modelling of photonic crystals and vcsels using eigenmode expansion and perfectly matched layers. *Optical and Quantum Electronics*, 33:327–341, 2001.

[28] CAMFR simulation software is freely available from http://camfr.sourceforge.net/.

[29] W. Bogaerts, P. Bienstman, D. Taillaert, R. Baets, and D. De Zutter. Out-of-plane scattering in photonic crystal slabs. *IEEE Photonics Technology Letters*, 13:565–567, 2001.

[30] R. Menzel. *Photonics: Linear and Nonlinear Interactions of Laser Light and Matter*. Springer-Verlag, Berlin, 2001.

[31] R. W. Boyd. *Nonlinear Optics*. Academic Press, San Diego, second edition, 2003.

[32] P. Bienstman. *Rigorous and efficient modelling of wavelength scale photonic components*. PhD thesis, Ghent University, 2001.

[33] C. Manolatou, M. J. Khan, S. Fan, P. R. Villeneuve, H. A. Haus, and J. D. Joannopoulos. Coupling of modes analysis of resonant channel add-drop filters. *IEEE Journal of Quantum Electronics*, 35:1322–1331, 1999.

[34] S. Fan, W. Suh, and J. D. Joannopoulos. Temporal coupled-mode theory for the fano resonance in optical resonators. *Journal of the Optical Society of America A*, 20:569–572, 2003.

[35] C. Jin, S. Fan, S. Han, and D. Zhang. Reflectionless multichannel wavelength demultiplexer in a transmission resonator configuration. *IEEE Journal of Quantum Electronics*, 39:160–164, 2003.

[36] M. F. Yanik, S. Fan, and M. Soljacic. High-contrast all-optical bistable switching in photonic crystal microcavities. *Applied Physics Letters*, 83:2739–2741, 2003.

[37] M. Soljacic, C. Luo, J. D. Joannopoulos, and S. Fan. Nonlinear photonic crystal microdevices for optical integration. *Optics Letters*, 28:637–639, 2003.

[38] M. F. Yanik, S. Fan, M. Soljacic, and J. D. Joannopoulos. All-optical transistor action with bistable switching in a photonic crystal waveguide geometry. *Optics Letters*, 28:2506–2508, 2003.

[39] H. M. Gibbs. *Optical Bistability: Controlling Light with Light*. Academic Press, London, 1985.

[40] K. C. Huang, P. Bienstman, J. D. Joannopoulos, K. A. Nelson, and S Fan. Field expulsion and reconfiguration in polaritonic photonic crystals. *Physical Review Letters*, 90:196402, 2003.

[41] W. Chen and D. L. Mills. Gap solitons and the nonlinear optical-response of superlattices. *Physical Review Letters*, 58:160–163, 1987.

[42] M. Bahl, N. C. Panoiu, and R. M. Osgood. Nonlinear optical effects in a two-dimensional photonic crystal containing one-dimensional kerr defects. *Physical Review E*, 67:056604, 2003.

[43] U. Fano. The theory of anomalous diffraction gratings and of quasi-stationary waves on metallic surfaces. *Journal of the Optical Society of America*, 31:213–222, 1941.

[44] V. Lousse and J. P. Vigneron. Use of fano resonances for bistable optical transfer through photonic crystal films. *Physical Review E*, 69:155106, 2004.

[45] A. R. Cowan and J. F. Young. Optical bistability involving photonic crystal microcavities and fano line shapes. *Physical Review E*, 68:046606, 2003.

[46] P. Tran. Photonic-band-structure calculation of material possessing kerr nonlinearity. *Physical Review B*, 52:10673–10676, 1995.

[47] V. Lousse and J. P. Vigneron. Self-consistent photonic band structure of dielectric superlattices containing nonlinear optical materials. *Physical Review E*, 63:027602, 2001.

[48] A. Huttunen and P. Törmä. Band structures for nonlinear photonic crystals. *Journal of Applied Physics*, 91:3988–3991, 2002.

[49] N. C. Panoiu, M. Bahl, and R. M. Osgood. Ultrafast optical tuning of a superprism effect in nonlinear photonic crystals. *Journal of the Optical Society of America B*, 21:1500–1508, 2004.

[50] A. Yariv, Y. Xu, R. K. Lee, and A. Scherer. Coupled-resonator optical waveguide: a proposal and analysis. *Optics Letters*, 24:711–713, 1999.

[51] T. Fujisawa and M. Koshiba. Time-domain beam propagation method for nonlinear optical propagation analysis and its application to photonic crystal circuits. *OSA Technical Digest, Integrated Photonics Research, Washington DC*, 23:IME5, 2003.

[52] C. T. Seaton, J. D. Valera, R. L. Shoemaker, G. I. Stegeman, J. T. Chilwell, and S. D. Smith. Calculations of nonlinear TE waves guided by thin dielectric films bounded by nonlinear media. *IEEE Journal of Quantum Electronics*, 21:774–783, 1985.

[53] M. A. Gubbels, E. M. Wright, G. I. Stegeman, C. T. Seaton, and J. V. Moloney. Numerical study of soliton emission from a nonlinear waveguide. *Journal of the Optical Society of America B*, 4:1837–1842, 1987.

[54] S. D. Gupta and G. S. Agarwal. Dispersive bistability in coupled nonlinear fabry-perot resonators. *Journal of the Optical Society of America B*, 4:691–695, 1987.

[55] H. A. Haus and Y. Lai. Theory of cascaded quarter wave shifted distributed feedback resonators. *IEEE Journal of Quantum Electronics*, 28:205–213, 1992.

[56] Y. Xu, Y. Li, R. K. Lee, and A. Yariv. Scattering-theory analysis of waveguide- resonator coupling. *Physical Review E*, 62:7389–7404, 2000.

[57] J. E. Heebner, R. W. Boyd, and Q. H. Park. Scissor solitons and other novel propagation effects in microresonator-modified waveguides. *Journal of the Optical Society of America B*, 19:722–731, 2002.

[58] S. F. Mingaleev, Y. S. Kivshar, and R. A. Sammut. Long-range interaction and nonlinear localized modes in photonic crystal waveguides. *Physical Review E*, 62:5777–5782, 2000.

[59] S. Mookherjea and A. Yariv. Kerr-stabilized super-resonant modes in coupled-resonator optical waveguides. *Physical Review E*, 66:046610, 2002.

[60] S. Pereira, P. Chak, and J. E. Sipe. Gap-soliton switching in short microresonator structures. *Journal of the Optical Society of America B*, 19:2191–2202, 2002.

[61] P. Xie and Z. Q. Zhang. Excitation of gap solitons, soliton trains, and soliton sets in finite-sized two-dimensional photonic crystals. *Physical Review E*, 69:036601, 2004.

[62] A. R. McGurn and G. Birkok. Transmission anomalies in kerr media photonic crystal circuits: Intrinsic localized modes. *Physical Review B*, 69:235105, 2004.

[63] S. F. Mingaleev, Y. B. Gaididei, P. L. Christiansen, and Y. S. Kivshar. Localizing energy through nonlinearity and discreteness. *Europhysics Letters*, 59:403–409, 2002.

[64] P. Chak, J. E. Sipe, and S. Pereira. Lorentzian model for nonlinear switching in a microresonator structure. *Optics Communications*, 213:163–171, 2002.

[65] J. E. Sipe, L. Poladian, and C. M. de Sterke. Propagation through nonuniform grating structures. *Journal of the Optical Society of America A*, 11:1307–1320, 1994.

[66] J. E. Heebner, P. Chak, S. Pereira, J. E. Sipe, and R. W. Boyd. Distributed and localized feedback in microresonator sequences for linear and nonlinear optics. *Journal of the Optical Society of America B*, 21:1818–1832, 2004.

[67] P. Dumon, W. Bogaerts, V. Wiaux, J. Wouters, S. Beckx, J. Van Campenhout, D. Taillaert, B. Luyssaert, P. Bienstman, D. Van Thourhout, and R. Baets. Low-loss SOI photonic wires and ring resonators fabricated with deep UV lithography. *IEEE Photonics Technology Letters*, 16:1328–1330, 2004.

[68] V. R. Almeida, C. A. Barrios, R. Panepucci, and M. Lipson. All-optical control of light on a silicon chip. *Nature*, 431:1081–1084, 2004.

[69] P. E. Barclay, K. Srinivasan, and O. Painter. Nonlinear response of silicon photonic crystal microresonators excited via an integrated waveguide and fiber taper. *Optics Express*, 13:801–820, 2005.

[70] S. Noda, M. Imada, M. Okano, S. Ogawa, M. Mochizuki, and A. Chutinan. Semiconductor three-dimensional and two-dimensional photonic crystals and devices. *IEEE Journal of Quantum Electronics*, 38:726–735, 2002.

[71] R. Morandotti, H. S. Eisenberg, Y. Silberberg, M. Sorel, and J. S. Aitchison. Self-focusing and defocusing in waveguide arrays. *Physical Review Letters*, 86:3296–3299, 2001.

[72] H. S. Eisenberg, Y. Silberberg, R. Morandotti, A. R. Boyd, and J. S. Aitchison. Discrete spatial optical solitons in waveguide arrays. *Physical Review Letters*, 81:3383–3386, 1998.

[73] R. Morandotti, U. Peschel, J. S. Aitchison, H. S. Eisenberg, and Y. Silberberg. Dynamics of discrete solitons in optical waveguide arrays. *Physical Review Letters*, 83:2726–2729, 1999.

[74] A. A. Sukhorukov, Y. S. Kivshar, H. S. Eisenberg, and Y. Silberberg. Spatial optical solitons in waveguide arrays. *IEEE Journal of Quantum Electronics*, 39:31–50, 2003.

[75] J. Feng. Alternative scheme for studying gap solitons in an infinite periodic Kerr medium. *Optics Letters*, 18:1302–1304, 1993.

[76] D. Neshev, A. A. Sukhorukov, B. Hanna, W. Krolikowski, and Y. S. Kivshar. Controlled generation and steering of spatial gap solitons. *Physical Review Letters*, 93:083905, 2004.

[77] D. Mandelik, R. Morandotti, J. S. Aitchison, and Y. Silberberg. Gap solitons in waveguide arrays. *Physical Review Letters*, 92:093904, 2004.

[78] S. John and N. Aközbek. Nonlinear optical solitary waves in a photonic band gap. *Physical Review Letters*, 71:1168–1171, 1993.

[79] N. Aközbek and S. John. Optical solitary waves in two- and three-dimensional nonlinear photonic band-gap structures. *Physical Review E*, 57:2287–2319, 1998.

[80] N. K. Efremidis, S. Sears, D. N. Christodoulides, J. W. Fleischer, and M. Segev. Discrete solitons in photorefractive optically induced photonic lattices. *Physical Review E*, 66:046602, 2002.

[81] J. W. Fleischer, T. Carmon, M. Segev, N. K. Efremidis, and D. N. Christodoulides. Observation of discrete solitons in optically induced real time waveguide arrays. *Physical Review Letters*, 90:023902, 2003.

[82] Z. Chen, H. Martin, E. D. Eugenieva, J. Xu, and J. Yang. Formation of discrete solitons in light-induced photonic lattices. *Optics Express*, 13:1816–1826, 2005.

[83] A. W. Snyder, D. J. Mitchell, L. Poladian, and F. Ladouceur. Self-induced optical fibers - spatial solitary waves. *Optics Letters*, 16:21–23, 1991.

[84] D. Cai, A. R. Bishop, and N. Gronbech-Jensen. Localized states in discrete nonlinear Schrödinger equations. *Physical Review Letters*, 72:591–595, 1994.

[85] R. Y. Chiao, E. Garmire, and C. H. Townes. Self-trapping of optical beams. *Physical Review Letters*, 13:479–482, 1964.

[86] K. Busch and S. John. Liquid-crystal photonic-band-gap materials: The tunable electromagnetic vacuum. *Physical Review Letters*, 83:967–970, 1999.

[87] E. Yablonovitch. Liquid versus photonic crystals. *Nature*, 401:539–540, 1999.

[88] I. M. Merhasin and B. A. Malomed. Four-wave solitons in Bragg cross-gratings. *Journal of Optics B*, 6:S323–S332, 2004.

[89] I. M. Merhasin and B. A. Malomed. Four-wave solitons in waveguides with a cross-grating. *Physics Letters A*, 327:296–311, 2004.

[90] T. Mayteevarunyoo, B. A. Malomed, P. L. Chu, and A. Roeksabutr. Stability and collisions of moving semi-gap solitons in Bragg cross-gratings. *Physics Letters A*, 332:220–229, 2004.

[91] H. Ammari and F. Santosa. Guided waves in a photonic bandgap structure with a line defect. *SIAM J. Appl. Math.*, 64:2018–2033, 2004.

[92] W. H. Press, S. A. Teukolsky, W. T. Vetterling, and B. P. Flannery. *Numerical recipes in C : The Art of Scientific Computing*. Cambridge University Press, Cambridge, second edition, 1992.

[93] C. M. Anderson and K. P. Giapis. Symmetry reduction in group 4mm photonic crystals. *Physical Review B*, 56:7313–7320, 1997.

[94] T. Suhara and M. Fujimura. *Waveguide Nonlinear-Optic Devices*. Springer, Berlin, 2003.

[95] Y. Jeong and B. Lee. Matrix analysis for layered quasi-phase-matched media considering multiple reflection and pump wave depletion. *IEEE Journal of Quantum Electronics*, 35:162–172, 1999.

[96] M. Centini, C. Sibilia, M. Scalora, G. D'Aguanno, M. Bertolotti, M. J. Bloemer, C. M. Bowden, and I. Nefedov. Dispersive properties of finite, one-dimensional photonic band gap structures: Applications to nonlinear quadratic interactions. *Physical Review E*, 60:4891–4898, 1999.

[97] C. De Angelis, F. Gringoli, M. Midrio, D. Modotto, J. S. Aitchison, and G. G. Nalesso. Conversion efficiency for second-harmonic generation in photonic crystals. *Journal of the Optical Society of America B*, 18:348–351, 2001.

[98] Y. Dumeige, F. Raineri, A. Levenson, and X. Letartre. Second-harmonic generation in one-dimensional photonic edge waveguides. *Physical Review E*, 68:066617, 2003.

[99] W. Nakagawa, R. C. Tyan, and Y. Fainman. Analysis of enhanced second-harmonic generation in periodic nanostructures using modified rigorous coupled-wave analysis in the undepleted-pump approximation. *Journal of the Optical Society of America A*, 19:1919–1928, 2002.

[100] B. Shi, Z. M. Jiang, X. F. Zhou, and X. Wang. A two-dimensional nonlinear photonic crystal for strong second harmonic generation. *Journal of Applied Physics*, 91:6769–6771, 2002.

[101] A. Locatelli, F.-M. Pigozzo, F. Baronio, D. Modotto, A.-D. Capobianco, and C. De Angelis. Bidirectional beam propagation method for second-harmonic generation in engineered multilayered waveguides. *Optical and Quantum Electronics*, 35:429–452, 2003.

[102] J. A. Armstrong, N. Bloembergen, J. Ducuing, and P. S. Pershan. Interactions between light waves in a nonlinear dielectric. *Pysical Review*, 127:1918–1939, 1962.

[103] A. Yariv. *Introduction to Optical Electronics*. Holt, Rinehart and Winston, New York, 1976.

[104] C. De Angelis, G. Nalesso, D. Modotto, M. Midrio, A. Locatelli, and J. S. Aitchison. Multiple-scale coupled-mode theory for second-harmonic generation in one-dimensional periodic structures. *Journal of the Optical Society of America B*, 20:1853–1865, 2003.

[105] P. Lalanne. Electromagnetic analysis of photonic crystal waveguides operating above the light cone. *IEEE Journal of Quantum Electronics*, 38:800–804, 2002.

[106] J. Ctyroky, S. Helfert, R. Pregla, P. Bienstman, R. Baets, R. De Ridder, R. Stoffer, G. Klaasse, J. Petracek, P. Lalanne, J. P. Hugonin, and R. M. De La Rue. Bragg waveguide grating as a 1d photonic band gap structure: Cost 268 modelling task. *Optical and Quantum Electronics*, 34:455–470, 2002.

[107] S. G. Johnson and J. D. Joannopoulos. Block-iterative frequency-domain methods for maxwell's equations in a planewave basis. *Optics Express*, 8:173–190, 2001.

[108] W. L. Barnes, A. Dereux, and T. W. Ebbesen. Surface plasmon subwavelength optics. *Nature*, 424:824–830, 2003.